

"Quantitative Determination of Conformational Dynamics of Nucleic Acids Duplexes"

Dissertation
for attaining the PhD degree
of Natural Sciences

by

Nicole Erlenbach

from Offenbach am Main, Germany

Frankfurt am Main 2019

Institute of Physical and Theoretical Chemistry
Faculty Biochemistry, Chemistry and Pharmacy
Goethe University Frankfurt am Main
(D30)

Nicole Erlenbach

born at 19.05.1988 in Offenbach am Main

Dean: Prof. Clemens Glaubitz

First expert assessor: Prof. Thomas F. Prisner

Second expert assessor: Prof. Gerhardt Hummer

Das Liebesleben der Pflastersteine unter
Berücksichtigung
des Sonnenfleckensminimums und -maximums.
*Horst Heine, mein Opa,
und seine Vorstellung über meine Doktorarbeit*

Contents

1	Introduction and Motivation	1
1.1	Motivation and Aim	3
2	Theoretical Framework	7
2.1	Structure and Function of Nucleic Acids	7
2.1.1	Structure of Nucleic Acids	7
2.1.2	Biological Function of Nucleic Acids	10
2.2	Structure and Dynamic Determination for Nucleic Acids	11
2.3	Molecular Dynamics Simulation	14
2.3.1	Force Field Development for Nucleic Acids	16
2.4	Electron Paramagnetic Resonance Spectroscopy	19
2.4.1	Spin Labels for EPR	19
2.4.2	Theoretical Principles of EPR Spectroscopy	20
2.4.3	Spin Interactions in EPR Spectroscopy	21
2.4.4	CW-EPR Spectrum of Nitroxide Radicals	25
2.5	Introduction to Pulsed Dipolar Spectroscopy	27
2.5.1	Introduction to Pulsed EPR	27
2.5.2	Pulsed Electron-Electron Dipolare Resonance Spectroscopy	29
2.5.3	A Mathematical Description of PELDOR	30
2.5.4	Orientation Selective PELDOR	33
2.5.5	PELDOR of Flexible Systems	36
2.5.6	CP-PELDOR	38
3	Results and Discussion	41
3.1	PELDOR Spectroscopy on Nucleic Acids - A Short Introduction	41
3.2	Intermolecular Interaction - 'End-to-End' Stacking of dsRNA	44
3.3	Flexibility of Spin Label - A Semi-Rigid Approach	49
3.4	Study of an Intercalating Spin Label	53
3.5	Orientation-Selective 2D-SIFTER Simulations	57
3.6	Conformational Dynamics of DNA by PELDOR and MD	62
3.7	Analysis of Room Temperature PELDOR Measurements	67

4	Summary and Outlook	71
5	Deutsche Zusammenfassung	74
6	List of Scientific Contributions	79
7	List of Collaborator Contributions	82
	Bibliography	86

CHAPTER 1

Introduction and Motivation

The structure-function paradigm claims that the function of proteins and nucleic acids can be understood with the knowledge of their three-dimensional structure. With this motivation, several biophysical methods are available giving access to the structure of biological polymers. With the help of crystallography,^[1] nuclear magnetic resonance (NMR)^[2,3] and nowadays additionally cryo-electron microscopy^[4,5] the data bank of protein and nucleic acid structures^[6] has grown enormously within the last decades.

Nevertheless, even if a perfect three-dimensional picture of the whole cell could be obtained, this static picture would be incapable of explaining all the mechanisms of and interactions between the different kinds of biomolecules. More specifically, macromolecules possess exceptionally fast, local fluctuations and slow, concerted structural motions. A deep understanding of all the processes in the cell can only be achieved with additional knowledge of the dynamics under native conditions. Therefore, biophysics entered the "dynamic age" to tackle these problems. Ensemble methods, like small angle X-ray scattering (SAXS),^[7] cryo-electron microscopy and pulsed electron-electron double resonance (PELDOR)^[8] do not yield temporal information, however could add knowledge about the flexibility of static structures. Moreover, for example magnetic resonance based techniques as electron paramagnetic resonance (EPR)^[9,10] and NMR^[11] as well as optical methods at various wavelength like Förster resonance energy transfer (FRET),^[12,13] fluorescent measurements,^[14] infrared radiation (IR)-^[15,16] and resonance raman (RR)-spectroscopy^[17] have already shown to be suitable tools for dynamical studies. However, even if they encode temporal information, the extraction of this information can be complicated and it is challenging to complement the structural studies with the dynamical ones. Other approaches to reaching an understanding of the dynamics of molecules include computational methods.^[18] Quantum mechanical (QM) calculations explain the behavior of atoms and subatomic particles and their interactions with energy.^[19,20] Wave function-based approaches represent the traditional family of QM methods. They are successful in explaining the structures and dynamics of small molecules like nucleobase.^[21] However, these approaches get time-consuming when molecules exceed several atoms. Even with the coarsest quantum mechanical approximation, the Hartree Fock method,^[22,23] large systems are not accessible. More accurate post-HF methods, including elec-

tron correlation functions like couples cluster (CC)^[24,25] or configuration interaction (CI)^[26] are even more limited. To increase the accessible number of atoms, density functional theory (DFT)^[27,28] calculations, based on the electron density can be used. Nevertheless even here more than several hundreds of atoms are out of the range.

A more empirical approach, molecular dynamic (MD), was developed 50 years ago. This method is based on the empirical description of atom-atom interactions.^[29,30] Force fields,^[31,32] describing bonds, angles and intermolecular interactions, were developed based on quantum mechanical simulations of small moieties and on experimental data. These MD simulations provide a detailed description of the biomolecules with high spatial and temporal resolution. However, their accuracy depends on the specific systems of interest and needs careful evaluation. Especially for nucleic acids, the currently existing force fields still have a lack of accuracy.^[33] The quality of newly developed force fields needs to be assessed against different experimental data to reach trustworthiness.

Both experimental and the computational approaches have their weaknesses as stand-alone strategies. Experimental data does not always produce unambiguous results and theoretical studies condemned as untrustworthy. However, combining the theoretical knowledge of structure and dynamics provided by computational simulations with the empirical structures and dynamics yielded by experiments can answer central questions in biology. Such questions mainly relate to two kinds of biomolecules present in cells. Proteins are the main workers in living tissues. They play a central role in biological processes for example in most catalytic tasks,^[34] in signal transduction^[35] and for transport across the cell membrane.^[36] Most research groups in structural biology focus on this important biological class. Nevertheless nucleic acids are often underestimated in their importance, without them, life would not be possible. DNA stores the genetic information and messenger RNA (mRNA) carries the protein blueprint from a cell's DNA to the ribosome, the "machine" that drives protein synthesis.^[37] Modern research has revealed that in addition to its coding function, RNA plays numerous roles in both normal cellular processes and in disease states.^[38] The focus in structural RNA biology is the understanding of large RNA structures like ribosomes and ribozymes as well as smaller regulatory structural elements like aptamers and riboswitches. These shorter RNAs can be up to 200 nucleotides in length and bind small chemical compounds or peptides specifically, leading to conformational rearrangements.

1.1 | Motivation and Aim

EPR based distance measurements represent an experimental tool to study the conformational rearrangements of doubly spin-labelled biomolecules, here nucleic acids over long-range distances of 2 to (more recently) 12 nm.^[39] These measurements rest on the dipolar coupling of two electron spins', therefore this method is called dipolar spectroscopy. As the dipolar coupling is an anisotropic effect, one feature of such measurements arises for structures where both the biomolecule and the spin label are rigid: in this case even the orientation of the spin labels' to each other can be detected.^[40] As a consequence, more details can be learned about the system of interest. With this ensemble method flexibilities and conformational changes can be studied. This is of interest in reaching a deeper understanding of the details of the rearrangements in DNA and RNA aptamers and riboswitches upon ligand binding.^[41,42] Dipolar spectroscopy of nucleic acids has been performed successfully in the past. These studies range from work with small 12 to 20mer double stranded DNAs^[43,44,45] to research on RNA riboswitches such as tetracycline^[46,42] and will be discussed in section 3.7 in more detail.

However several problems remain unresolved, limiting the range of applicability of such studies. One major aspect of performing such measurements is the introduction of unpaired electron spins, usually with a nitroxide-based spin label. Such labels should neither impede nor destabilise the nucleic acid's structure and the dynamic of the spin label should also be known to be separate from the dynamics of the nucleic acid. For orientation selective studies in particular the dynamics of the spin label must be minimal or negligible in order to maximize anisotropic effects in the resulting dipolar time traces and not to introduce dynamics obscuring the motions of interest.^[47] However, the known spin label **Q**,^[48] which has perfect spectroscopical properties for anisotropic data on nucleic acids, needs a great synthetic effort, and it is challenging to incorporate into nucleic acid motifs. Synthetically less challenging spin labels were developed in the Sigurdsson laboratory,^[49,50,51] replacing the **Q**. However the orientation and dynamics of these new labels could differ from those of the **Q** and this has been examined in this thesis. Traditional dipolar coupling-based studies were performed with the double frequency pulse technique PELDOR;^[52,53,40] however, for the study of the two spin labels' orientation a number of time-consuming multi-frequency/multi-field PELDOR measurements are needed.^[54] Other techniques were supposed to work faster and more efficiently. However, the reliable usage of other pulse techniques based on shaped pulses with broadband excitation was hindered for a long time by hardware limitations. Other limitations include the relaxation based restriction in the time windows, which limited the maximum

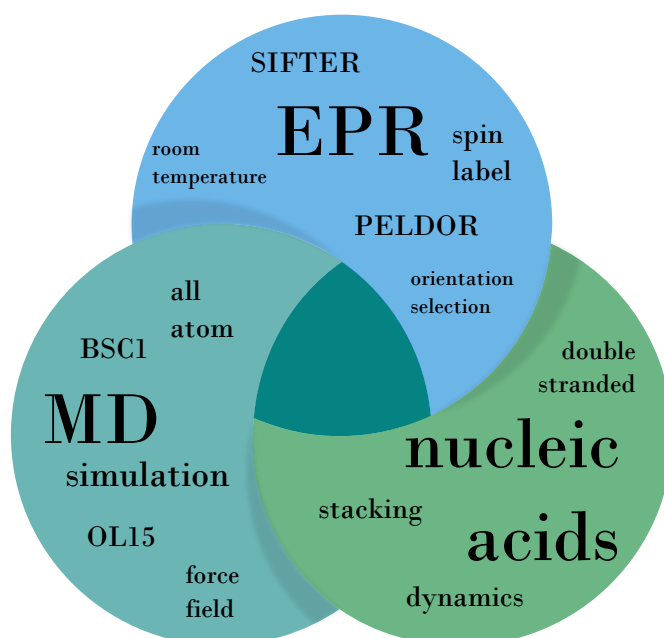
measurable distance.^[55] The development of fast arbitrary waveform generator opened the door for the usage of shaped pulses, such as Gauss pulses and adiabatic pulses.^[39] This resulted in both various new possibilities for the further development of pulsed EPR, such as 7 pulse-Carr-Purcell-PELDOR to increase the maximum time window,^[56] and in the use of new pulse sequences like double quantum coherence (DQC),^[57,58,59,60] relaxation-induced dipolar modulation enhancement (RIDME)^[61,62,63] or single-frequency technique for refocusing dipolar couplings (SIFTER).^[64,65,66] 2D-SIFTER^[67] data could complement or partially replace time-consuming orientation selective PELDOR measurements', hence, in this thesis new simulation protocols for 2D-SIFTER were written and evaluated against known measurements and structures.

Another point is the challenge of archiving an unambiguous interpretation of the data in terms of structure and dynamics. Therefore additional information about static structures or possible dynamics can aid the analysis. Static structures can be either reached by other experiments or by topological knowledge. This is often more difficult dynamical studies. Model-based interpretations can provide many useful hints but can also be challenging in a full analysis if more than one dynamic is present in the sample.^[45] In this respect MD simulations combine a vast amount of knowledge from other experimental methods and from QM simulations. A quantitative comparison of the experiments with these simulations might be helpful but is still challenging in many of the following aspects. As dipolar spectroscopy is measured at cryogenic temperatures, the temperature difference between the measurements and typical room temperature simulations could lead to differences or even artifacts.^[68] Moreover the type and dynamics of the spin labels has to be taken into account. Additional aspects would be the size of the sampling window and artefacts due to the use of force fields not particularly suited to nucleic acids.^[33] In this thesis, sensitive orientation-selective measurements were used to benchmark newly developed force fields for nucleic acids. Only by reaching a quantitative agreement between experiments and MD, the reliability of the nucleic acid dynamics extracted from the MD simulation can be established.

From a more biological point of view, the dipolar measurements are problematic as they do not take place in a native-like environment. The relaxation of the signal by room temperature dynamics cannot be avoided in any measurements at native temperatures and in addition the rotation of the molecule in solution leads to an average of the dipolar coupling.^[69] One of several solution to overcome such drawbacks could be a DNA electrostatically bound to a nucleosil, as this inhibits the rotation and thus enables the measurements of the dipolar coupling.^[69,70] The use of rigid spin labels also leads to the fact that the relaxation of the signal is not

too fast; therefore the first orientation selective PELDOR data are available at room temperature. In this thesis a contribution was made to understanding the differences between measurements at two different temperatures and to confirm the differences with calculations from MD simulations.

One point that has been noticed in the past in various studies on small RNA building blocks is that double-stranded RNA ends tend to stack.^[71,72,73] This leads to chain-like structures in short double-stranded RNA building blocks. This can be observed especially with PELDOR, as additional distances appear in the measurements.^[74,75,76,77,78,79] This can influence the investigations of such building blocks. Therefore, a special aim of this thesis was to prevent this stacking. In addition, measurements under different salt concentrations contributed to a better understanding of these intermolecular interactions.



In summary this thesis focusses on the building of a bridge between, orientation selective dipolar EPR measurements with various pulse techniques, experimental conditions and various spin labels and MD simulations, provided by the group of Prof. Hummer at the Max-Planck Institute of Biophysics. This integrated project works to link the experimental and the computational perspective, to connect the advantages of both and to overcome their disadvantages and limitations when both were used in a standalone way. The third compound of this thesis includes the goal to reach a deeper understanding of the dynamics and properties of small nucleic acid duplexes.

CHAPTER 2

Theoretical Framework

2.1 | Structure and Function of Nucleic Acids

2.1.1 | Structure of Nucleic Acids

Nucleic acids are long, linear chain composed of monomers called nucleotides. These biopolymers contain from twenty nucleotide pairs, as with some micro (mi)RNAs, to 10^8 nucleotide pairs in the case of a chromosome. The monomeric units of nucleic acid are composed of three parts: a nucleobase - either a purine or a pyrimidine isomer - a pentose sugar and a phosphate group.

The central part is the pentose sugar, which is locked into a five-membered furanose ring. The sugars are joined together by phosphate groups that form phosphodiester bonds between the third (3') and fifth (5') carbon atoms of adjacent sugar rings. Each phosphoryl is normally considered to belong to the nucleotide whose 5' carbon forms a bond with it. Any nucleic acid strand therefore normally has one end with a phosphoryl attached to the 5' carbon and another end with a free hydroxyl. The orientation of the 3' and 5' carbons along the sugar-phosphate backbone confers directionality to each nucleic acid strand.

The main difference between DNA and RNA is the sugar. RNA has a D-ribose while DNA has a 2-deoxy-D-ribose. This minor change makes a difference in stability with respect to hydrolysis. Hence the different nucleic acids have different tasks in the biological machinery of the cell.

At the 1' carbon of the sugar ring, one out of four different bases is attached. Both nucleic acids contain the pyrimidine analogue adenine (A) and guanine (G) and the purine analogue cytosine (C). However, RNA has a purine analogue uracil (U), which is replaced by a thymine (T) in the case of DNA. These five nucleobases are referred in their nucleotide form as guanosine, adenosine, cytidine, thymidine and uridine, and their sequence along the backbone encodes biological information.

Nucleic acid polymers, especially RNA, can be found as single strands or, as is often the case for DNA, as anti-parallel double strands. The three-dimensional building blocks of RNA often include double stranded sections and other tertiary motifs like hairpin loops and bulges. The phosphate groups have one negative

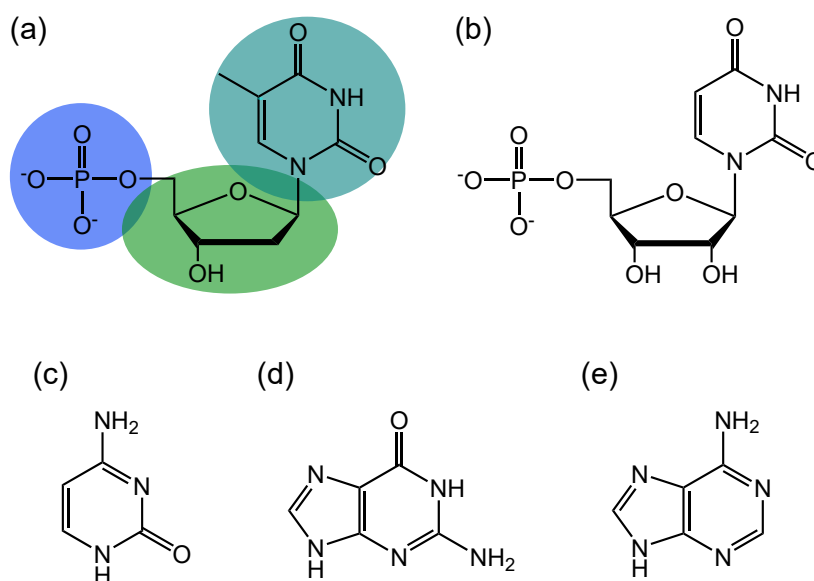


Figure 2.1.1: (a) DNA nucleotide composed of a 2-deoxy-D-ribose (marked in green), a phosphate group (blue) and the nucleobase thymine (turquoise). (b) RNA nucleotide composed a D-ribose, a phosphate residue and the nucleobase uracil. (c) cytosine (d) guanine (e) adenine

charge each, making nucleic acids charged molecules (polyanions). These charges neutralised by the surrounding ions', therefore the kind of salt present and its concentration play a major roles in the folding process and consequently in the three-dimensional structure of nucleic acids.

In double-stranded nucleic acids the two polymer strands bind together in a helical fashion by non-covalent bonding. This double-stranded structure is maintained largely by the intra-strand base-stacking interactions and by hydrogen bonds between the nucleobases of different strands, resulting in a helix with both strands coiled around the same axis. In such a double helix, each type of nucleobase on one strand bonds with just one type of nucleobase on the other strand. This is called complementary base pairing. Here, A bonds only with T/U with two hydrogen bonds, and C bonds only with G with three hydrogen bonds. Thus a G-C pair has more impact on the stability of a double strand than a A-U/T

The helical structure can vary in its geometry. There are three different forms found in nature. DNA is commonly found in the B-helical form, whereas RNA occurs as an A-helix. Both the A- and B-forms are right-handed helices.^[80] Dehydration or protein binding can also force the DNA to form an A helical structure, and alternating poly dG/dC chains at high salt concentrations lead to the left-handed Z-DNA which has a zig-zag backbone and alternating sugar puckers.^[81] As the anti-parallel strands are not directly opposite to each other, the grooves

are unequal in size. The grooves in B-DNA have names with the so-called major groove being wider than the minor groove. Therefore sequence-specific protein interactions mostly happen in the major groove, while small synthetic drugs and organic compounds intercalate in the minor groove.^[82,83] In contrast, the A-form geometry of RNA results in a very deep and narrow major groove and a shallow and wide minor groove. Moreover, the B form is a more compact helical structure whose base pairs are not perpendicular to the helix axis. The two different helical geometries are illustrated in figure 2.1.2, and more structural features of the three naturally occurring helical forms are given in table 2.1

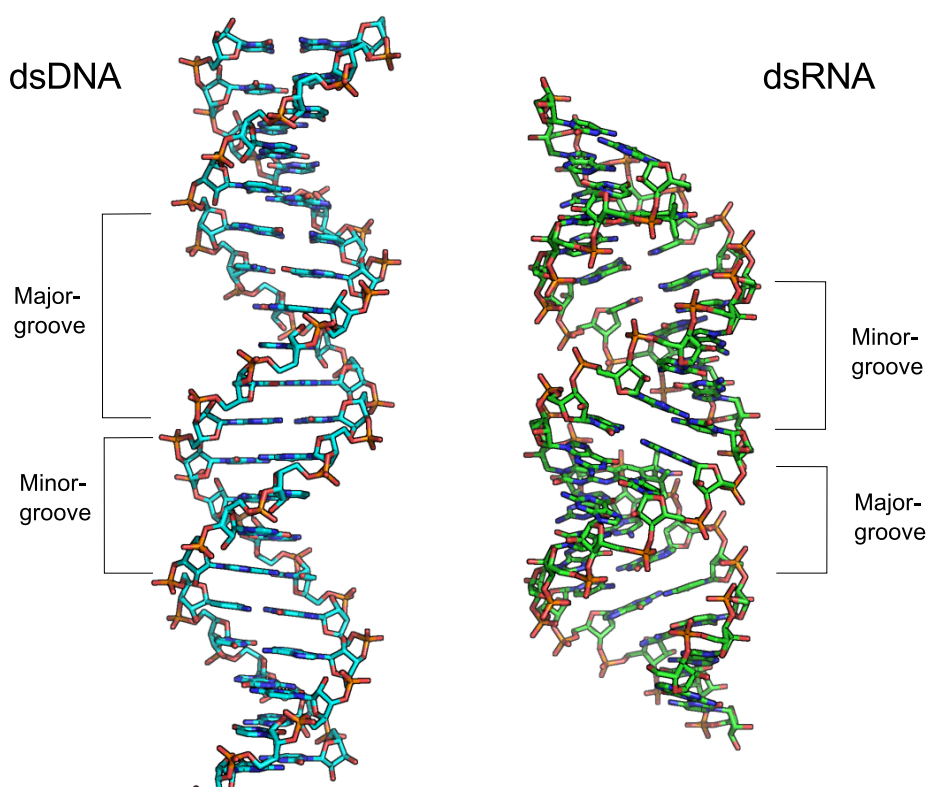


Figure 2.1.2: *Helical structure of B-DNA (left) and A-RNA(right)*

Table 2.1: *Some structural features of the three natural occurrence helical forms.*^[84]

structural feature	A-DNA	B-DNA	Z-DNA
helix handedness	right	right	left
diameter [nm]	$\approx 2,6$	≈ 2	$\approx 1,8$
base pairs/ turn	11,6	10	12
rotation/ base pair [°]	31	33	30
rise/ base pairs [Å]	0,29	0,33	0,44

2.1.2 | Biological Function of Nucleic Acids

RNA and DNA are both major players in the functions of living cells. Yet despite their structural similarity, they have clearly different tasks. DNA is highly stable due to its lack of the ribose hydroxal group, making it well suited to carry the whole genetic instruction, including RNA and protein structures. It occurs mainly as linear chromosomes in eukaryotes and circular chromosomes in prokaryotes. The non-systematic sequence of nucleobases is protected due to the double-stranded structure. Nevertheless, as the interaction between the strands is only based on hydrogen bonds, this structure can be broken easily. This fact is needed to ensure gene expression. The first step thereby is in transcription, where codons, made up of the nucleobase sequence, are copied to a messenger (m)RNA with a complimentary sequence. This mRNA serves as a template for the translation of the genetic sequence into a protein. The whole process takes place in the ribosomal (r)RNA. There transfer (t)RNAs act as adaptors and links each three nucleobase code on the mRNA to a specific amino acid.

In addition to the known roles of mRNA, tRNA and rRNA in the transcription and translation processes, RNA are play parts in catalytic and complex regulatory processes. For example small nuclear (sn)RNAs like miRNAs can repress translation by binding to mRNAs.^[85,86] The so-called riboswitches are also part of gene regulation, when they bind small proteins or organic compounds in the cell or sense pH or temperature changes, they undergo structural changes. Due to these changes gene expression is either started or suppressed. Enzymatic RNAs with catalytic activity are called ribozymes and can be active in replication, mRNA processing and splicing.^[87]

2.2 | Structure and Dynamic Determination for Nucleic Acids

The focus of this thesis is structure elucidation, detecting of structural changes and dynamics of nucleic acids. Today there is no method able to answer the complete spectrum of these questions, therefore it is important that more methods work together, to achieve real understanding of the chemical, physical and biological processes of nucleic acids in cell. This chapter tries to provide an overview of the most important methods without the claim of completeness.

Most methods addressing structural questions are based on spectroscopy or microscopy. Both measure the interaction between energetic radiation and matter. Depending on the energy of the radiation, expressed in the wavelength, it interacts with different particles, as there are atomic nuclei or electrons. While spectroscopy measures the adsorption or emission of energy, microscopy measures the diffraction, transmission or reflection on particles. The following methods were sorted according to their wavelength.

Due to new detector technologies and software algorithms, cryo-electron microscopy (cryo-EM) has made the greatest progress in recent years. Electron radiation has a de-Broglie wavelength in the picometer range. This method allows the determination of biomolecule structures with near-atomic resolution; however in a frozen state as cryo-EM works with rapidly frozen amorphous solids. A series of images of single molecules were taken and processed by a reconstruction software, yielding accurate and detailed 3D models.^[5,88,89]

The method with the most solved high resolution structures is still macromolecular crystallography (MX), which uses X-ray radiation with wavelengths of several Ångström to nanometer. Initially the first DNA structure was solved with help of a X-ray fibre charge density map, measured by Rosalind Franklin and Maurice Wilkins.^[90] With computational help and better instruments, structures of most kind of nucleic acids were solved by crystallography.^[91,92] The main drawback is that all structure are solved in crystals, which give rise to only one single conformer that is not necessary in the same conformation as in native solution. Moreover for RNA most secondary-structural elements tend to appear quite similar, making sequence assignment and backbone tracing challenging. Crystallization of RNAs for X-ray diffraction studies is also far more challenging than for proteins as the RNAs are able to fold into multiple secondary structures.^[93] Interesting are the new achievements in serial femtosecond nanocrystallography (SFX).^[94] There nanocrystals, growing more readily than large crystals required for MX, are used in a liquid fluid. All crystals are measured independently with femtosecond pulses

2.2. STRUCTURE AND DYNAMIC DETERMINATION FOR NUCLEIC ACIDS

to circumvent radiation damage of the crystals, allowing snapshots by 'diffract before destroy'.^[95,96] With this technique also dynamical processes, mainly reaction so far, can be triggered.^[97]

Another technique which relies on X-ray irradiation is called glsaxs^[98,99] Reconstruction of 3-D electron density maps from 1-D scattering profiles made possible to extract diverse global information about the size and shape of biomolecules, intermolecular interactions or linker flexibilities. This can complement the results from other techniques and the interpretation of this 3-D maps are often combined with MD simulations.^[100] This scattering occurs by interaction of $\sim \text{\AA}$ wavelength X-rays probing nanometer-sized biomolecules in solutions. The biggest advantage is that this method works in solutions, however going into cell is problematic, due to crowding of different kind of other proteins. One example for SAXS measurements on nucleic acids are the changes of riboswitches upon ligand binding.^[101]

By extending the wavelength, one arrives in the area of optical spectroscopy. This includes ultraviolet (UV) radiation (10 – 400 nm), visible light (400 – 700 nm) and infrared radiation (IR, $\sim \text{mm}$ to μm). A well-known method in optical spectroscopy for structural information is Förster resonance energy transfer (FRET), which is based on the through-space interaction of two transition dipoles of two fluorophores.^[102] This enables to measure long-range distances in the nm range between two fluorescence labelled sites on a biomolecule. FRET can be performed as an ensemble method in solution or as a single molecule method attached to a solid support.^[12,103] One possibility is the measurement of structural changes and dynamics with a temporal resolution of about one microsecond. However, the bulky labels can influence the result. Classically, two different labels are required, with the exception of HOMO-FRET.^[104] using the difference in emission and excitation of one label. New small labels, like the \mathbf{Q}_m^f have already been used for fluorescence spectroscopy,^[105] but anisotropic effects of this rigid label need to be considered, by using the label for FRET spectroscopy.^[106]

In addition to FRET, there are also other methods in optical spectroscopy. These include fluorescence lifetime and depolarisation measurements. The fluorescence lifetime is sensitive to the environment of the fluorophore and can highlight structural changes as has been reported for the neomycin aptamer upon ligand binding.^[14] With circular dichroism (CD) the secondary structure of the highly chiral nucleic acids can be studied. This method is in particular powerful to follow dynamical changes.^[107,108] With 2D-IR spectroscopy one can determine the vibrational coupling through bonding or through space interaction. With this method basepair formation and the interactions with the surrounding solution can be studied in detail. In addition vibrational backbone dynamics could be detected. The

strength of this technique is the time resolution: while most of the other techniques are able to detect process happening in the nanosecond range or slower, the time resolution of these experiments is around $1 - 2$ ps.^[109]

By lowering the energy of the radiation to microwaves ($1 - 100$ cm), absorption by paramagnetic centers can be detected. This will be discussed in more detail in the following sections. With wavelength above one meter, the radiation is absorbed by nuclei in magnetic fields, used by nuclear magnetic resonance (NMR) spectroscopy. It can be performed on solids as well as in solution, which give a broad range of application. NMR probes the angular momentum of nuclear spins. Short range interaction of bound atoms, but also unbound restraints can be measured and translated into a three-dimensional structure. They can be used to compare structures in crystals to such in solutions.^[110,111,112] With a whole bunch of different experiments one can achieve angles, distances, couplings etc; however, most of this value are short range, beneath 5 \AA .^[113,114] The whole shape and flexibel regions are however hard to reach with NMR. Moreover, when the systems increases, the spectrum complexity increases significant and pulse overlaps decreases the possibility to solve the structure. Subsequently NMR is limited to small systems up to 64 kDa. However, one of the strength of solution NMR is the possibility to adress structural changes due to ligand interaction and other dynamical processes at native conditions. Moreover it has the ability to follow kinetic process in real time, like folding and aggregation.^[115]

Other methods, which are not based on radiation are for example atomic force microscopy (AFM) which can determine the secondary structure of larger RNA viruses. A very thin tip (~ 20 nm radius) scans the surface of the sample to determine it with sub nanometer resolution.^[116] isothermal titration calorimetry (ITC) can be used to determine the thermodynamic parameters of interactions with ligands in solution. Also electrochemistry methods, as scanning tunneling microscope-break junction (STM-BJ) measurements^[117] or gel electrophoresis to study secondary structure based on the charge differences can be used for nucleic acids.^[116,118]

2.3 | Molecular Dynamics Simulation

To study conformational dynamics and energetic properties of biomolecules computationally, quantum mechanical (QM) calculations provide the most accurate description. These calculations are based on the Schroedinger equation, which describes how a physical system changes over time and in which quantum effects, such as wave-particle duality, are significant. Nevertheless, as QM considers all electrons existing in the system, even calculations for very small molecules with less than 100 atoms are extremely time-consuming, as it involves a partial differential equation. For most applications the degree of accuracy provided by QM calculations is unnecessary and more empirical calculations are sufficient.

Such molecular dynamic (MD) simulations allow the calculation of the dynamic evolution of the system over a certain time period, considering intra- and inter-molecular forces. These forces are described in force fields, which are developed based on QM simulations and empirical parameters. A force field consists of classical functions describing the main potential energy (V) functions for the structural parameters. Moreover MD simulations calculate the dynamic of biological systems as a evolution of time. In such force fields the atoms are described as balls and bonds as springs. Newton's equation of motion is solved - the acceleration (a) of each atom (n) is calculated from its mass (m) and the force (F) operating on it.

$$F_n = m_n a_n \quad (2.1)$$

The force can also be expressed as the gradient of the potential energy:

$$F_n = -\nabla_n V \quad (2.2)$$

Combining both equations yields the following equation:

$$\frac{-\partial V}{\partial r_n} = m_n \frac{\partial^2 r_n}{\partial t^2} \quad (2.3)$$

The force on each atom is derived by the empirical potential energy. An equation of motion, a trajectory, describing the position (r), the velocities and the acceleration for each particle for each time point (t). The full potential energy of an molecule can be described by classical physical properties. Therefore all pair-wise interactions between atoms near to each other have to be taken into account, as described in the following equation.

$$V_{pot} = V_{bonds} + V_{angles} + V_{torsions} + V_{non-bonds} \quad (2.4)$$

The first term describes the sum of all bond energies in the molecules. This

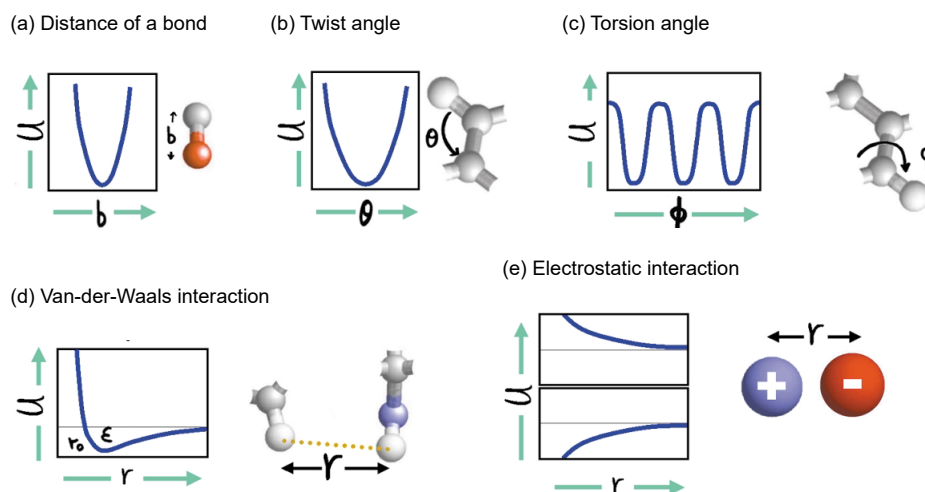


Figure 2.3.1: The total potential energy of any molecule is the sum of terms describing (a) bond stretching, (b) bond angle bending, (c) bond twisting, (d) van der Waals interactions and (e) electrostatics interactions. Modified from M. Levitt.^[119]

potential can be described using the model of harmonic oscillator (eqn. 2.5) as shown in figure 2.3.1 (a) where k_b is the force constant and b_0 the equilibrium bond length.

$$\begin{aligned}
 V_{bonds} &= \sum_{bonds} k_b (b - b_0)^2 \\
 V_{angles} &= \sum_{angles} k_a (\Theta - \Theta_0)^2 \\
 V_{torsion} &= \sum_{dihedrals} \sum_a \frac{v_n}{2} [1 + \cos(a\phi - \gamma)]
 \end{aligned} \tag{2.5}$$

The bend angle between two neighbouring covalently bonded atoms can be described in an analogous fashion with k_a as the force field constant and Θ_0 as the equilibrium angle. The last term for bond interaction describes the potential energy related to the dihedral angle (ϕ). This is called torsion and expressed as a cosine series expansion with the constant v_n . The a is the multiplicity and gives the number of minimums within 360° rotation and γ is the phase angle for the torsion.

The non-covalent interaction of an atom i and a nearby atom j near to each other can be separated into two parts. The van-der-Waals (vdW) interaction can be approximated by a Lennard-Jones potential, which describes the attraction and repulsion between an atom and a nearby atom with which it does not share a bond. The parameters are the equilibrium vdW distance (r_{ij}^0), and the potential well-depth (ϵ_{ij}) as shown in eqn 2.6. The second part is the Coulomb interaction between two charged particles. For calculating the potential the constant for the

permittivity of free space (ϵ_0), the relative permittivity (ϵ_r) as constants and the partial charges q_i and q_j are needed.

$$V_{nb} = \sum_{vdW}^{i<j} \left[\left(\frac{r_{ij}^0}{r_{ij}} \right)^{12} \epsilon_{ij} - 2 * \left(\frac{r_{ij}^0}{r_{ij}} \right)^6 \epsilon_{ij} \right] + \sum_{electrostatics}^{i<j} \frac{q_i q_j}{4\pi\epsilon_0\epsilon_r r_{ij}} \quad (2.6)$$

For accurate MD simulations the interaction with the surrounding solution - also in this case water and salt - also has to be taken into account. As water molecules occupy the majority of the simulations box and have different challenging characteristics, like the hydrogen bond networks and non-additive inductive effects, a description of water with the same accuracy as the biological system would lead in a tremendous increase of computational cost. Therefore different models are introduced, which describe a water molecule a rigid structures with effective point charges. In this thesis the transferable intermolecular potential (TIP)-based models were used. They describe the water either by a three point model (TIP3P) or with an additional displaced point charge for the oxygen (TIP4P) to correct the excessively large dipole moment in TIP3P.^[120] As these water models are problematic to describe disordered biological structures, the TIP4P-D model was introduced by Piana *et al.* with the goal of to approximating the water dispersion interaction more accurately.^[121] This leads to more dynamic simulations it however tends to destabilize folded protein and nucleic acid structures. The accuracy of a force field is strongly dependent on the water model used. As optimisation is always done with one particular water model, it should not be changed extensively afterwards without further testing.

While the protein force fields used today are highly accurate, for a long time the application of MD to nucleic acids has been hindered by the lack of accurate force fields, which resulted in several artefacts.^[33] Experimental results can be used as sensitive benchmark data for the development and evaluation of new force fields for nucleic acids.

2.3.1 | Force Field Development for Nucleic Acids

In this section, a short overview of the development of the force field in the assisted model building with energy refinement (AMBER)^[122] package is given. A short scheme can be found in figure 2.3.2.

The AMBER first force field for biomolecules was developed in the group of Kollman and Weiner published in 1984.^[31,32] They combine the bond parameters already known from literature with the point charge and vdW parameters that they calculated quantum mechanically. However at that time, only small molecules with small basis sets could be addressed with QM. These parameters

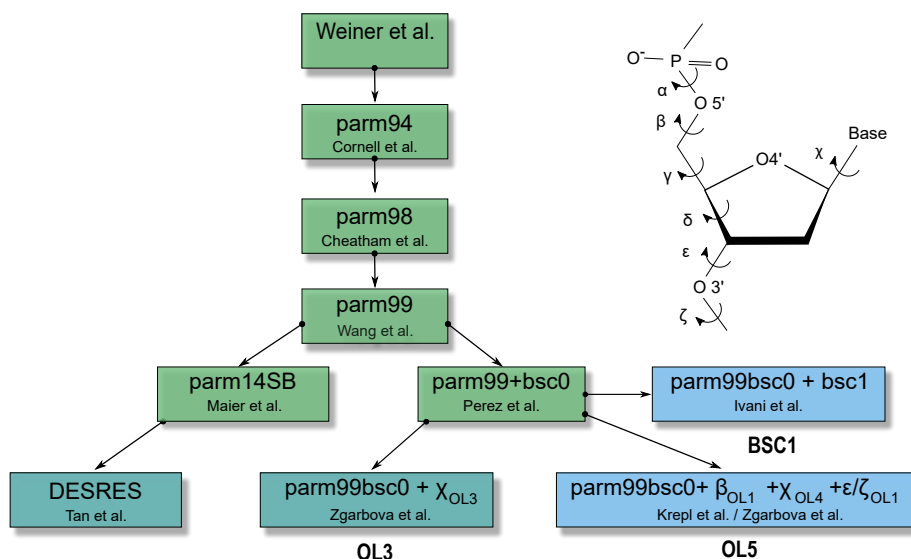


Figure 2.3.2: Historical flowchart of the main forks of the AMBER force field for nucleic acids. Force field for DNA in blue, for RNA in turquoise and for both in green. References in historical order^[32,123,124,125,126,127,128,129,130,131,132,133]. Modified from Galindo-Murillo *et al.*^[134]

were updated by Cornell *et al.* 10 years later, with a new parameter set called 'parm94'.^[123] It adjusted the vdW parameters, which were calculated with QM simulations using new basis sets. It also introduced the restrained electrostatic potential (RESP) charge model which allows the reproduction of the electrostatic potential around the nucleic acid. Cheatham and Wang, both also from the Kollman group, modified the parameter set slightly in the following years to 'parm98',^[124] and '**parm99**',^[125] moderate success, using additional QM calculations to refine the parameter for the dihedral angles and for the charges in order to eliminate the under-twisting of the B-DNA. The main problems for nucleic acids was that severe artifacts arise in simulations longer than 10 ns, while the accuracy seemed to be high for short trajectories.^[135,136] There had been only scarce simulations reaching 100 ns at that time.

These parameter sets were developed for proteins and nucleic acids as well as for small organic compounds. In 2007 Perez, from the Barcelona Supercomputer Center (BSC) in the group of Modesto Orozco, refined the force fields only for nucleic acids, by suppressing non-native conformational transitions of the α and γ torsion angles. He used new QM calculations and was able to perform stable MD simulations over 200 ns, achieving structures at the end that still were comparable with the crystal structures. This set, called 'parmbc0' or simply 'BSC0',^[126] was the reference force field for nucleic acids for a long time.

The main focus for further optimisations was on the dihedral angles of the back-

bone (depicted for nucleic acids in the upper right of figure 2.3.2). Small changes in the shape of the potential surfaces can have a large effect on the stabilisation of the double strands. However, it was seen, that the artefacts change between RNA and DNA. Therefore different parameter optimisations were proposed depending on the system of interest, *e.g.*, both nucleic acids have conflicting requirements in the χ -potentials.

For DNA, many groups worked independently from another on the optimisation process. The Orozco group developed new parameters, called 'parmbsc1', which were published with updated parameter sets evaluated using comparisons with NMR structures.^[132] Stable simulation beyond the microsecond regime were achieved. As an alternative, the group of Prof Šponer from Olomouc (OL) proposed three independent updated parameters: for the backbone dihedrals β_{OL1} ^[131] and ϵ/ζ_{OL1} ^[129] and for the dihedral between the nucleobase and the sugar χ_{OL4} .^[128] All these parameters together are called OL15.

Simulations for RNA proved to be much more complicated. Aside from the χ angle for which the Šponer group proposed an update (OL3)^[127] was the non-bonding interactions presented greatest. The base pair strength, especially for short distances $< 2.7\text{\AA}$ was underestimated. In contrast the stacking behaviour between nucleobases was overestimated. One other severe problem was that the point charges seemed to be well estimated with the RESP approach for the relatively rigid and planar nucleobases, but a fixed set of point charges was too limiting for the description of the flexible region of the backbone, specially for different conformations.^[137] Therefore the David E. Shaw group published an updated parameter set, called DES RES,^[133] which they said to behave as accurately as MD simulations for proteins. This parameter set was updated again based on the parm99, not taking the BSC0 into account. They included interactions with the new water parameter set TIP4P-D, changed the values for the non-bonded interactions and refined the values for the backbone dihedrals γ , ζ and for the χ angle.

2.4 | Electron Paramagnetic Resonance Spectroscopy

Electron paramagnetic resonance (EPR) spectroscopy studies the resonant absorption of microwaves due to unpaired electron spins in an external magnetic field. With this technique the microenvironment of paramagnetic centers can be studied. This absorption was first observed by Jewgeni Zavoisky in Kasan (Russia), who measured a resonant absorption of copper(II) chloride dihydrate.^[138] Twenty-three years earlier the Stern-Gerlach experiment, done at the Goethe University in Frankfurt, had demonstrated electron paramagnetism and discrete spin states.^[139] The following chapter describes briefly the physical principles of the electron paramagnetic resonance (EPR) technique briefly. For a more detailed description standard textbooks are recommended.^[39]

2.4.1 | Spin Labels for EPR

To enter the paramagnetic world with diamagnetic, and thus EPR silent, biopolymers it is necessary to attach radicals or paramagnetic centres (called "spin labels") at distinct positions on the molecule of interest. Spin labels have to fulfill two main criteria to be suitable for EPR. The radical has to be stable - it should not be easily reduced or affected by other chemical reaction which might occur by handling biological samples. Moreover it should disturb neither the structure of the system nor its function. The first point is the most critical point; however, there are two main classes in organic chemistry which stay stable under various biologically relevant conditions. These are carbon-based trityls and aminoxyl (R-N-O)-based spin labels, commonly referred as nitroxides.^[47] Also a number of paramagnetic metal ions (*e.g.*, Mn^{2+} or Gd^{3+}) can be used. They can either naturally occur in biological objects or be site-directed attached with metal containing spin tags like Mn-DOTA.^[140,141,142,143]

Although trityl-based labels have some spectroscopic advantages, *e.g.*, an insignificant amount of hyperfine coupling and long transversal relaxation times, they require a complex synthesis, they are quite bulky with large tethers which restricts the use of these labels for structural studies and they have low solubility in aqueous systems. Therefore nitroxide labels are often preferable as they are comparable small and thus relatively minimal perturbation to the structure and function of most biomolecules. A major advantage for using nitroxides for EPR is their solubility in polar solvents. The rest of this thesis will focus on nitroxides that are classical five- or six-membered heterocycles, *e.g.*, derivatives of piperidine, pyrrolidine or isoindoline. Historically all of these are based on di-*tert*-butyl

nitroxide.^[144] They are by far the class of paramagnetic molecules for biological applications most frequently used. Their paramagnetism originates from the coupled $2p_z$ -orbital of the nitrogen and oxygen, which results in a fully occupied π orbital and a half-occupied anti-bonding π^* -orbital, with the spin density is delocalized over both atoms. The radical is further stabilised by steric shielding from four alkyl groups at the α positions. This lack of protons prevents decomposition, which would otherwise occur due to the low delocalization energy.

More details about spin labelling techniques for nucleic acids as well as information on the important aspect of the flexibility of spin labels from spectroscopic perspective can be found in the result section.

2.4.2 | Theoretical Principles of EPR Spectroscopy

EPR techniques study the behaviour of unpaired electrons. They have a spin angular momentum quantum number of $S = \frac{1}{2}$, and, in the absence of a magnetic field, two degenerated quantum states. When a magnetic field is applied, the electron spins start to precess with their Larmor frequency around the magnetic field, resulting in a net alignment along the magnetic field lines. This alignment is based on their spin and can be either in the α -state or in the opposite direction, the β -state. A magnetic moment ($\hat{\mu}_e$) proportional to this angular momentum and parallel to the spin vector operator $\hat{\mathbf{S}} = (\hat{S}_x, \hat{S}_y, \hat{S}_z)$ occurs

$$\hat{\mu}_e = g\mu_B\hat{\mathbf{S}} \quad (2.7)$$

where g is the Landé or gyromagnetic factor of the electron and μ_B is the Bohr magneton which is given by

$$\mu_B = \frac{e\hbar}{2m_e} \quad (2.8)$$

where m_e is the mass of the electron and e its charge. \hbar is the reduced Planck constant. The exact g -value for a free electron of $g = 2.0023193043617(15)$ is predicted by quantum electrodynamics and an accurately determined fundamental constant.^[145]

The energy of the spin states is described as follows:

$$E = h\nu = \hat{\mu}_e \cdot \tilde{\mathbf{B}} = g\mu_B B_0 \hat{S}_z = m_s g\mu_B B_0 \quad (2.9)$$

where h is the Planck's constant and ν the microwave irradiation frequency. The energy is the scalar product of the magnetic moment and the magnetic field vector $\tilde{\mathbf{B}}$, which is orientation dependent. As a convention the magnetic field $\tilde{\mathbf{B}} = (0, 0, B_0)$ is aligned along the z-axis of the laboratory system. The projection of the spin vector onto this z axis is the spin quantum number m_s . The energy levels

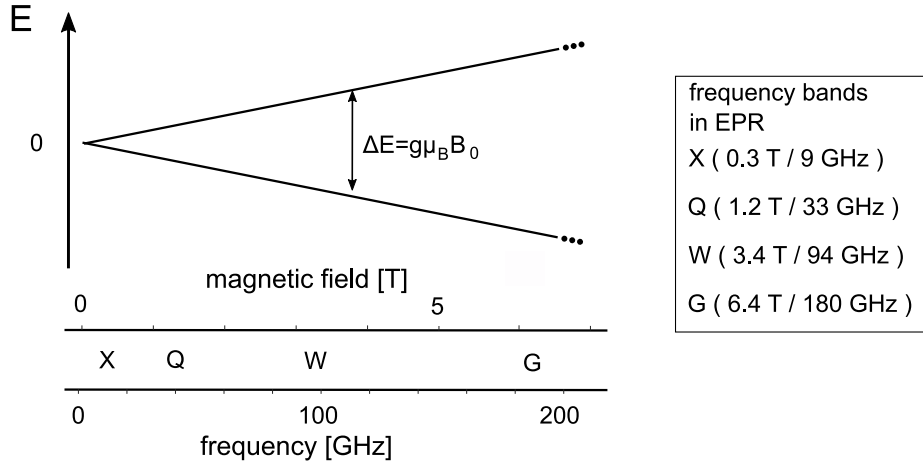


Figure 2.4.1: Energy splitting of an electron spin in relation to an external magnetic field. The typically used frequency bands with their frequencies and magnetic fields given in the gray box on the right.

of the degenerate spin states split depending on their magnetic quantum number $m_S = \pm\frac{1}{2}$.

According to equation 2.9 the differences between the energies of the two states are relative to the external magnetic field as shown in figure 2.4.1. A microwave resonant to this energy difference can induce a spin transition, which can be measured and analysed.

2.4.3 | Spin Interactions in EPR Spectroscopy

An EPR spectrum reflects the energies of the spin states. The energy of quantum states can be described according to the Schrödinger equation with the Hamiltonian \hat{H} and the wave function Ψ

$$\hat{H}\Psi = E\Psi \quad (2.10)$$

For paramagnetic spin centres the energies depend on the different interactions among the electron spins, nuclear spins and the magnetic field present under the conditions of the experiment. The effective Hamiltonian is given by

$$\hat{H} = \hat{H}_{EZ} + \hat{H}_{NZ} + \hat{H}_{HF} + \hat{H}_{DD} + \hat{H}_{NQ} + \hat{H}_{ZFS} \quad (2.11)$$

The first two terms of the sum give the Zeeman interaction of the external magnetic field to the unpaired electron spin and at the nuclear spins, respectively. The third term describes the interaction between the electron spin and nearby

nuclear spins, the hyperfine interaction (HF). In the presence of another unpaired electron, their interaction is described by the dipolar coupling (DD) term \mathcal{H}_{DD} . The last two terms are the nuclear quadrupole interactions (NQ) for spins with $I > \frac{1}{2}$ and the zero field splitting (ZFS) for electron spins with $S > \frac{1}{2}$. In the remainder of this thesis, the discussion of spin Hamiltonian terms is limited to interactions relevant for the presented work, for simplification, a system consisting only one electron interacting with one nuclear spin is considered.

For a nitroxide system with an electron spin quantum number of $S = \frac{1}{2}$ and nuclear spin number of $I = 1$ for the nitrogen, the interaction of the electron spin with the magnetic field is given by the electron Zeeman interaction.

$$\hat{\mathcal{H}}_{EZ} = \mu_B \cdot \hat{\mathbf{S}} \cdot \bar{\mathbf{g}} \cdot \hat{\mathbf{B}} \quad (2.12)$$

For a free electron in vacuum the g is a scalar; however, this interaction is anisotropic for interacting radicals, which is expressed by a (3x3) g -interaction matrix. In general the g -matrix is orthorhombic and is expressed in its principal axes system (PAS) as

$$g_{PAS} = \begin{pmatrix} g_{xx} & 0 & 0 \\ 0 & g_{yy} & 0 \\ 0 & 0 & g_{zz} \end{pmatrix} \quad (2.13)$$

The geometric interpretation of the g -tensor is an ellipsoid, where the effective g -value g_{eff} for an arbitrary orientation of the magnetic field is the distance from the origin to the surface of the ellipsoid. In the special case of nitroxides the definition of the main axes is set in such a way that the g_{xx} points along the N-O bond and g_{zz} is the plane perpendicular to the nitroxide ring. According to its orientation to the external magnetic field the effective g -value can be calculated as following

$$g_{eff}(\Theta, \Phi) = \sqrt{\sin^2(\Theta)\cos^2(\Phi)g_{xx}^2 + \sin^2(\Theta)\sin^2(\Phi)g_{yy}^2 + \cos^2(\Phi)g_{zz}^2} \quad (2.14)$$

with Θ and Φ the polar angles relative to the magnetic field. For the g -tensor anisotropy the differences in the resonance frequencies for two transitions with different orientations is

$$\Delta B = \frac{h\nu_{mw}}{\mu_B} \left(\frac{1}{g_1} - \frac{1}{g_2} \right) \quad (2.15)$$

With this equation it can be seen that the spectral resolution scales linearly with the microwave frequency ν_{mw} . As a result anisotropic interactions are better resolved at higher magnetic fields. The deviation of the g -tensor from the value of the free electron in vacuum (2.002319^[146]) can yield informations about the direct environment. For organic radical the deviation is due to the spin orbit coupling

and is in the per thousand range, while the deviations can be much higher for metal ions.

In an external magnetic field, nuclear energies split into $(2I+1)$ energy levels in a manner analogous to the splitting of the electron energies. This so-called nuclear Zeeman interaction is described as:

$$\hat{\mathcal{H}}_{NZ} = \mu_N \cdot \hat{\mathbf{I}} \cdot \bar{\mathbf{g}}_N \cdot \mathbf{B} \quad (2.16)$$

g_N can have a positive or negative value. For most EPR experiments $\hat{\mathcal{H}}_{NZ}$ can be considered isotropic. The nuclear Zeeman interaction is usually much smaller than the electron Zeeman interaction and it is not considered since $\Delta m_I = 0$.

The hyperfine interaction describes the interaction between the magnetic moment of a nuclear spin ($\hat{\mathbf{I}}$) and an electron spin ($\hat{\mathbf{S}}$). The electron spin experiences the local magnetic fields built up by the nuclei close to it.

$$\hat{\mathcal{H}}_{HF} = \hat{\mathbf{S}} \cdot \bar{\mathbf{A}} \cdot \hat{\mathbf{I}} = \hat{\mathbf{S}} \cdot \bar{\mathbf{A}}' \cdot \hat{\mathbf{I}} + A_{iso} \cdot \hat{\mathbf{S}} \cdot \hat{\mathbf{I}} \quad (2.17)$$

The hyperfine interaction can be divided into two mechanism with different physical origins. The isotropic part, the Fermi contact interaction, describes the finite electron density at the nuclei. The isotropic hyperfine coupling constant A_{iso} can be derived as following:

$$A_{iso} = \frac{2}{3} \mu_0 \mu_B \mu_N g_e g_N |\Psi(0)|^2 \quad (2.18)$$

This interaction is isotropic since the only orbital having a non-zero density at the nucleus $|\Psi_0(r=0)|^2 > 0$ is the s-orbital, which is spherically symmetric.

The second part is the classical electron nuclear dipole-dipole interaction which depends on the relative orientation of the two magnetic moments to each other and is therefore anisotropic. The hyperfine tensor $\bar{\mathbf{A}} = A_{iso} + \bar{\mathbf{A}}'$, and the g-tensor are usually not collinear. However for the calculations of EPR spectra typically the effective \bar{A} tensor is used. This effective A-tensor can be described in a manner analogous description of the g tensor in its orientation relative to the B_0 -field

$$A'_{eff}(\Theta, \Phi) = \sqrt{\sin^2(\Theta)\cos^2(\Phi)A_{xx}^2 + \sin^2(\Theta)\sin^2(\Phi)A_{yy}^2 + \cos^2(\Phi)A_{zz}^2} \quad (2.19)$$

For nitroxides the principal axis system of this interaction is approximately the same as for the g tensor. The dipolar part of the hyperfine interaction is strong when the z-axis is parallel to the external magnetic field, while a perpendicular alignment results much weaker interaction. Therefore $A_{xx} \approx A_{yy} < A_{zz}$ is valid. Between the nirtrogen and the oxygen, only the interaction to the nitrogen ($I = 1$) plays a role in the hyperfine interactions of nitroxides, as ^{16}O has a zero spin.

2.4. ELECTRON PARAMAGNETIC RESONANCE SPECTROSCOPY

The methods used in this thesis are all based on the interacting of two electron spins. For this case, electron-electron interactions occur, in addition to the mentioned ($\hat{\mathcal{H}}(\hat{\mathbf{S}})$).

$$\hat{\mathcal{H}}(\mathbf{S}_A, \mathbf{S}_B) = \hat{\mathcal{H}}(\hat{\mathbf{S}}_A) + \hat{\mathcal{H}}(\hat{\mathbf{S}}_B) + \hat{\mathcal{H}}_{exch} + \hat{\mathcal{H}}_{DD} \quad (2.20)$$

For the nitroxide spin labels studied, the third term, corresponding to the Heisenberg exchange coupling, also called the J-coupling, can be neglected since the spin orbitals do not overlap significantly. This term does need to be considered at distances shorter than 1.5 nm or for strongly delocalised electron densities. For the current work the most relevant contribution is the magnetic dipole-dipole interaction between the electron spins which is dependent on the distance (r). This can be described as follows

$$\hat{\mathcal{H}}_{DD} = \hat{\mathbf{S}}_A \cdot \bar{\mathbf{D}} \cdot \hat{\mathbf{S}}_B = -\frac{\mu_0 \mu_b^2 g_A g_B}{4\pi \hbar r^3} (\hat{A} + \hat{B} + \hat{C} + \hat{D} + \hat{E} + \hat{F}) \quad (2.21)$$

The so-called dipolar alphabet in table 2.2 gives the product of the spin operators and angular expressions in spherical coordinates Θ and Φ .

Table 2.2: *dipolar alphabet with the related spin operator and angular expression*

Term	spin operators	angular expression
\hat{A}	$\hat{\mathbf{S}}_{zA} \hat{\mathbf{S}}_{zB}$	$(1 - 3 \cos^2 \Theta)$
\hat{B}	$-\frac{1}{4}(\hat{\mathbf{S}}_{+A} \hat{\mathbf{S}}_{-B} + \hat{\mathbf{S}}_{-A} \hat{\mathbf{S}}_{+B})$	$(1 - 3 \cos^2 \Theta)$
\hat{C}	$-\frac{3}{2}(\hat{\mathbf{S}}_{+A} \hat{\mathbf{S}}_{zB} + \hat{\mathbf{S}}_{zA} \hat{\mathbf{S}}_{+B})$	$\sin \Theta \cos \Theta \cdot \exp^{-i\Phi}$
\hat{D}	$-\frac{3}{2}(\hat{\mathbf{S}}_{-A} \hat{\mathbf{S}}_{zB} + \hat{\mathbf{S}}_{zA} \hat{\mathbf{S}}_{-B})$	$\sin \Theta \cos \Theta \cdot \exp^{i\Phi}$
\hat{E}	$-\frac{3}{4} \hat{\mathbf{S}}_{+A} \hat{\mathbf{S}}_{+B}$	$\sin^2 \Theta \cdot \exp^{-2i\Phi}$
\hat{F}	$-\frac{3}{4} \hat{\mathbf{S}}_{-A} \hat{\mathbf{S}}_{-B}$	$\sin^2 \Theta \cdot \exp^{2i\Phi}$

Here $\hat{\mathbf{S}}_{\pm}$ is the raising or lowering operator, with $\hat{\mathbf{S}}_{\pm} = \hat{\mathbf{S}}_x \pm i\hat{\mathbf{S}}_y$. All measurements are performed in situations where the high-field approximation is valid. This means that the electron Zeeman interaction is much larger than the dipolar interaction, which results in a quantization of the spins along \mathbf{B}_0 . Therefore only the secular term \hat{A} and the pseudo-secular term \hat{B} have to be retained. For two interacting nitroxides, within the weak coupling limit and the quantization of the two electron spins along the direction of B_0 , only the term \hat{A} has to be taken into account. This leads to

$$\hat{\mathcal{H}}_{DD} = \omega_{dd} \hat{\mathbf{S}}_{zA} \hat{\mathbf{S}}_{zB} \quad (2.22)$$

with

$$\omega_{dd} = \frac{D_{dip}}{r^3} (3 \cos^2 \Theta - 1) \quad (2.23)$$

where

$$D_{dip} = \frac{\mu_0 \mu_b^2 g_A g_B}{4\pi \hbar} \approx 2\pi \cdot 52.04 \text{ MHz} \cdot \text{nm}^3 \quad (2.24)$$

is.

2.4.4 | CW-EPR Spectrum of Nitroxide Radicals

In continuous wave (CW) EPR the resonance absorption frequencies at various magnetic field strength are measured. Due to technical reasons, these spectra are obtained by varying the magnitude B_0 of the external magnetic field, while the microwave frequency is kept constant. For a single electron, only one resonant frequency is expected. Nevertheless a radical attached to a biomolecule with a coupled electron spin \mathbf{S} and nuclear spin \mathbf{I} shows multiple absorptions frequencies depending on the first three terms of the Hamiltonian described in the last section. CW-EPR spectra of liquid solutions show an average of the anisotropic interactions, whenever the tumbling of the molecule exceeds several orders of magnitude of the spectral anisotropy (rotational correlation time $\tau_r < 100$ ps). Due to the energy level diagram of a radical coupled with a nitrogen ($S = \frac{1}{2}$ and $I = 1$) depicted in figure 2.4.2, a nitroxide spectrum contains three symmetric, narrow lines with equal intensities. Thereby is the spectral field position for $\Delta m_I = 0$ is given by the isotropic g value ($\beta_e g_{iso} B / \hbar$), and the splitting corresponds to the isotropic A. The recorded first deviation and absorption spectrum for such an experiment are shown in figure 2.4.2 (bottom right and upper right, respectively). When the

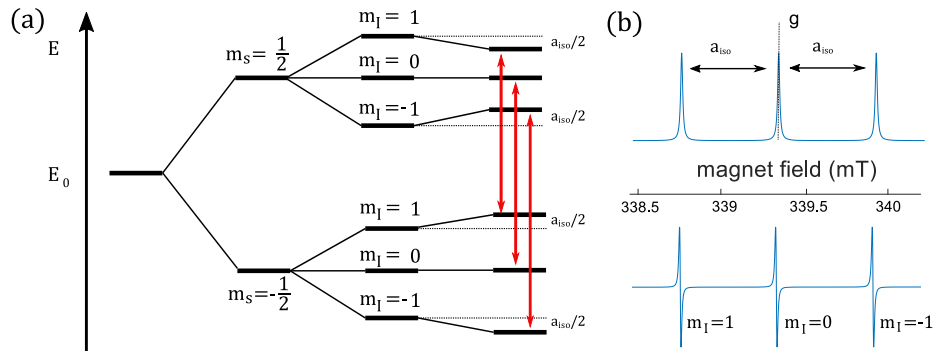


Figure 2.4.2: (a) Energy level diagram for a nitroxide ($S = \frac{1}{2}, I = 1$) (b) CW-EPR spectrum of nitroxides in solution. The bottom spectrum gives the measured first derivative, and the upper spectrum give the resonant absorption.

tumbling of a molecule decreases, the rotational correlation time increases, and

2.4. ELECTRON PARAMAGNETIC RESONANCE SPECTROSCOPY

spectral lines broadens. This can be used to investigate dynamic processes in biological systems to study or the rigidity of spin labels.

A powder or a frozen solution is a collection of randomly oriented micro crystals. Their spectra are therefore superpositions of the resonant absorptions of all possible orientations of the molecule with respect to the magnetic field. In figure 2.4.3 such powder spectra for nitroxides at two different magnetic fields are shown. At lower fields the spectrum is dominated by the ^{14}N -hyperfine interaction, especially by the A_{zz} component (red marks). The g tensor anisotropy is unresolved in the inhomogeneous linewidth of the central peak. Increasing the magnetic field resolves the g tensor, which dominates the shape of the CW spectrum at high frequency.

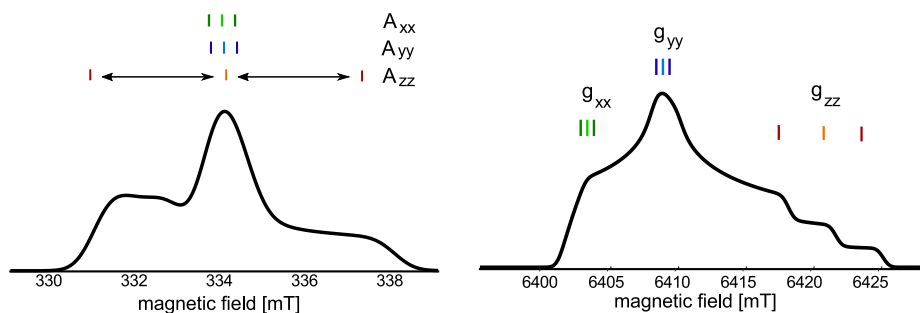


Figure 2.4.3: Simulated CW-EPR powder spectrum of nitroxides at different magnetic field strengths. (left) X-band (9 GHz/0.3 T), (right) at G-band (180 GHz/6.4 T). The coloured marks represent the g tensor (light blue g_{yy} /light green g_{xx} / light red g_{zz}) and the related A -tensor

2.5 | Introduction to Pulsed Dipolar Spectroscopy

2.5.1 | Introduction to Pulsed EPR

A deeper insight into the structures, flexibility, folding and conformational rearrangements of larger biomolecules can be reached by using the more sophisticated pulsed EPR spectroscopy as in CW EPR this information is hidden in the inhomogeneous linewidth. In pulsed EPR spectra are recorded by exciting spin ensembles with high-power microwave pulses at a given carrier frequency ν and a constant magnetic field B_1 . One can then measure the emitted microwave signal created by the sample's transversal magnetization. The pulses are named according to the rotation of the magnetization M_0 that they cause and the direction from which they come. A $\frac{\pi}{2}$ -pulse (also called 90° -pulse) with a magnetic field along x rotates the magnetisation coming from z-axis to the y-axis, while a π -pulse (180°) rotates to -z. Notably the nutation angle Θ depends not only on the pulse length t_p of the pulse but also on the magnetic pulse strength γB_1 .

$$\Theta = \gamma B_1 t_p \quad (2.25)$$

One can differentiate between selective pulses, which excite only a defined spin ensemble, and broadband non-selective pulses, which excite all spins simultaneously. The excited fraction is defined by the inversion profile in the frequency domain of the pulse. In the case of a rectangular pulse this is a sinc function (fig. 2.5.1).

Historically most pulsed applications were based on, for nitroxides selective, rectangular pulses. However, they had some major disadvantages, namely the relatively small bandwidth of approximately $\Delta\nu_\pi = \frac{0.8}{t_p}$ for π -pulses and the inhomogeneous inversion profile stemming from the existence of sidebands and from an offset-dependent orientation of the magnetisation at the end of the pulse. Thanks to the development of arbitrary waveform generator (AWG) which are now fast enough even for EPR experiments, shaped pulses are able to overcome these drawbacks. Shaped pulses are pulses with altered amplitude, phase or frequency within the length of pulse.^[39] Adiabatic pulses and Gaussian pulses are among the shaped pulses often used for EPR. Gaussian pulses can be used for selective excitation without creating side-bands (fig. 2.5.1 (b)) and adiabatic pulses for broadband excitation. Adiabaticity means that the magnetization follows the effective field and is relatively insensitive to inhomogeneities in the driving field. wideband, uniform rate, smooth truncation (WURST) and sech/tanh pulses belong to the

class of chirp pulses. It should be mentioned that adiabatic pulses have an intrinsically longer pulse duration lasting for hundreds of nanoseconds. In figure 2.5.1 the pulse amplitude (c), frequency modulation (d) and the excitation profile (e) for a sech/tanh pulse with 400 ns pulse length is shown with $\beta=8$, the truncate factor to reach a certain B_1 . Pulse methods can be divided according to

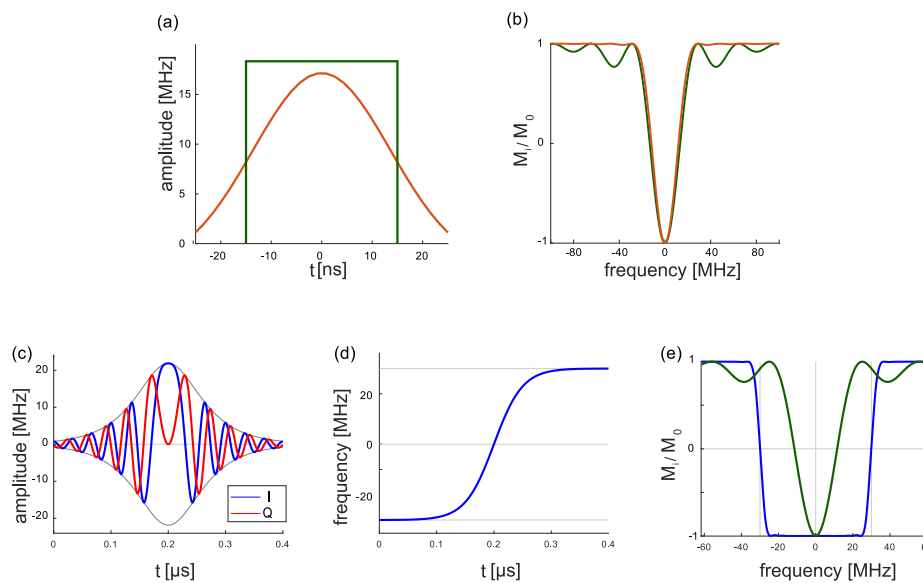


Figure 2.5.1: (a) The pulse amplitude of a rectangular (green, $t_p = 32$ ns) and of a Gaussian pulse (orange, $t_p = 50$ ns and $FWHM = 32$ ns). (b) the resulting excitation profile of both pulses (c) the puls amplitude of a sech/tanh pulse, with $t_p = 400$ ns, $\beta = 8$ (d) the frequency modulation (e) the resulting excitation profile in comparison to the rectangular pulse of (a). Simulations made with EasySpin.^[147]

their detectable interactions. Among others hyperfine spectroscopy, *e.g.*, electron nuclear double resonance (ENDOR), can be used elucidate the molecular and electronic structure of paramagnetic species by measuring the hyperfine interactions, and pulsed dipolare spectroscopy (PDS) techniques measure the dipolar interactions of two paramagnetic centers. The most established type of PDS measurements is pulsed electron-electron double resonance (PELDOR), also called dipolar electron-electron resonance (DEER).^[52,53,40] The four pulse variant is routinely used, although pulse sequences with more pulses like five or even seven pulses are now also used.^[56,148] Other approaches include the single frequency techniques such as relaxation-induced dipolar modulation enhancement (RIDME),^[61,62,63] single-frequency technique for refocusing dipolar couplings (SIFTER)^[64,65,66,67] or double quantum coherence (DQC).^[57,58,59,60] However, their feasibilities have long been time limited by the hardware available. With the introduction of non-selective broadband shape pulses, such measurement types have become the focus of recent research.

In pulsed NMR spectroscopy macroscopic magnetisation gets directly measured after the last pulse, resulting in a free induction decay (FID). Fourier transformation of the FID, a time domain signal, produces the frequency domain NMR spectrum. In EPR the sensitive detector must be protected during and immediately after the microwave pulse from the high microwave power in the resonator. Therefore direct signal recording is not possible. To overcome this limitation, all pulse experiments are measured with their echo. The idea can be shown with a basic pulse experiment, the Hahn echo. It can be used for studying the transversal relaxation T_2 and is the basis of other pulsed experiments.

The Hahn echo experiment starts with a $\frac{\pi}{2}$ -pulse to generate transversal magnetisation, but due to the dead time, the FID cannot be recorded directly after the pulse. After this the inhomogeneity of the magnetic field introduces spin flip flop processes and results in a dephasing of the signal. An additional π -pulse after a delay time τ refocuses the dephasing due to the inhomogeneity after a second time delay τ , producing an echo. One special case for an echo results from the

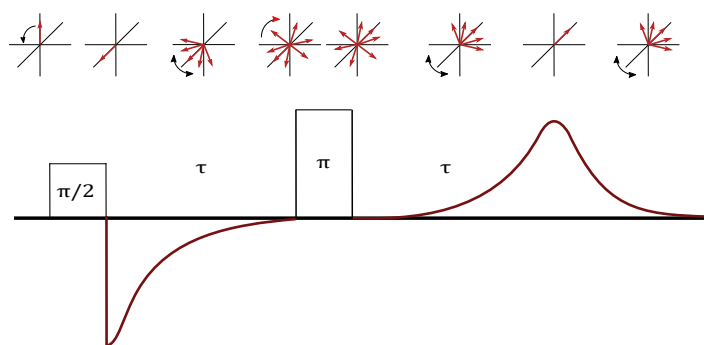


Figure 2.5.2: *Pulse sequence of the Hahn echo experiments with the magnetisation shown in red. Above are the magnetisation vector at the specific sequence position.*

use of broadband pulses that excite the whole nitroxide spectrum. Fourier transformation of these broadband excited echoes allows the recovery of their full EPR spectral shape of nitroxides and other paramagnetic species with narrow EPR lines.

2.5.2 | Pulsed Electron-Electron Dipolare Resonance Spectroscopy

The most frequently used pulsed technique is called PELDOR,^[52] or DEER.^[40] As it belongs to the pulsed techniques that measure dipolare interactions, PELDOR relies on the magnetic dipole-dipole interaction between two electron spins. This

interaction is inversely proportional to the cube of the distance and also depends on the orientation of the spin label relative to the external magnetic field. This method was first proposed by Milov and co-workers in the year 1981 as a three pulse sequence.^[52] However, due to the dead-time, this application of this techniques remained problematic until 1998, when the four pulse PELDOR sequence, which is echo-based, was proposed and first used in the Spiess group.^[149,53] The such measurements from this new pulse sequence were feasible and reliable.

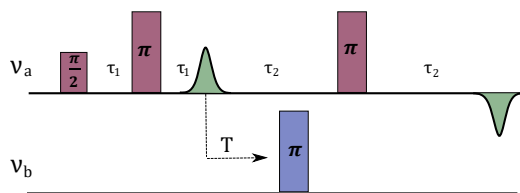


Figure 2.5.3: *4-pulse PELDOR Sequence*

PELDOR is a double-frequency method in which microwave pulses are applied at two different frequencies to excite different sub-ensembles of spins independently. First a Hahn echo experiment is performed the (detection) pulses are resonant to the first spins (spin A) with a frequency ν_A . After a time delay t after the Hahn echo signal, the pump pulse is applied in the resonant frequency ν_B of the second spin (B). This reverses the magnetisation of spins B but does not affect directly the spin A. However, a spin flip changes the sign of the dipolar coupling. This changes the local magnetic field at these spins, which now precess with an altered frequency in the transversal plane. This leads to an imperfect refocussing by the last π -pulse and dephases the echo signal by the dipolar coupling frequency of $\pm\omega_{dip}$ (eqn. 2.23) depending on the spin state of the B-spin before the inversion pump pulse. The net magnetisation of the spins A in the whole ensemble after the pump pulse is a sum of both, equally present, inversions.

$$M(T) = \frac{1}{2}(e^{i\omega_{dd}T} + e^{-i\omega_{dd}T} = \cos(\omega_{dd}T) \quad (2.26)$$

2.5.3 | A Mathematical Description of PELDOR

To aid in the understanding of the origin of orientation selection and distance dependence in PELDOR time traces the mathematics PELDOR will be discussed. More details can be found in previous publication of Andriy Marko.^[150,151,54]

First an appropriate coordinate frame for the orientation of spin labels needs to be defined. In the main axis system of the nitroxide spin label, the x-axis is parallel to the N-O bond, with the z-axis is normal to the nitroxide plane, as depicted in 2.5.4 (a). For both spin labels the principal axis system is used as described before

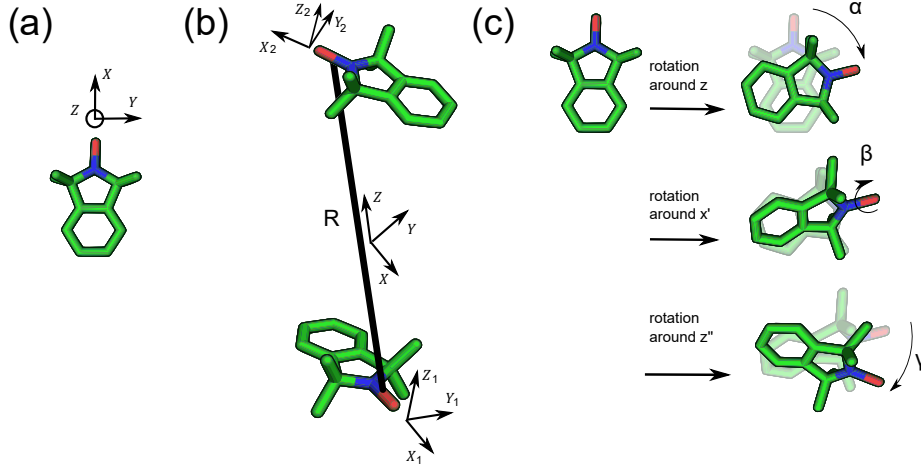


Figure 2.5.4: (a) Orientation of the axis system of a nitroxide spin label $\{x, y, z\}$. (b) The three coordinate systems for the description of a rigid biradical. $\{x_1, y_1, z_1\}$ and $\{x_2, y_2, z_2\}$ frames correspond to the axes of the first and the second nitroxide, respectively. The z axis of $\{x, y, z\}$ coincides with the interspin axis r and the x axis is perpendicular to both vectors z and z_1 (c) rotation of the Euler angles (α, β, γ) in the z, x', z'' convention

with $\{x_a, y_a, z_a\}$ for $a = 1, 2$ for the first and the second nitroxide, respectively. Furthermore, the dipolar coordinate system needs to be defined with the unit vectors $\{x, y, z\}$. For this system the z -axis corresponds to the interspin vector R , and the x -axis is oriented orthogonally to the plane of the two vectors z and z_1 . In this coordinate system the orientation to the external magnetic field B_0 can be described by the polar Θ and azimuth Φ angles.

The mutual orientation of the spin labels to each other is defined by the Euler angles $(\alpha_a, \beta_a, \gamma_a) = o_a$ (fig. 2.5.4), which describe the orientation of the coordinate axis $\{x_a, y_a, z_a\}$ of the spin label in relation to the main axis system $\{x, y, z\}$. The Euler angles are defined by the rotation around z, x', z'' (depicted in fig. 2.5.4 (c)).

The full mathematical description of a PELDOR time trace for a conformation ensemble of $i = 1, \dots, N$ molecules that have slightly different dipolar coupling is the average sum over all conformations present

$$V(T, \nu_A) = V_0(\nu_A) + \sum_{i=1}^N \int_0^{\pi/2} u(\nu_A, \Theta, o_{i,1}, o_{i,2}) (\cos(\omega_{dd,i}(r, \Theta)T) - 1) \sin\Theta d\Theta \quad (2.27)$$

where V_0 is the unmodulated Hahn echo signal and the function $u(\nu_A, \Theta, o_1, o_2)$ is the signal intensity modulation. In the case of a macroscopically disordered sample (frozen solution), all orientations of the spin pairs relative to the external magnetic field are equally probable. Therefore, the total signal is given as the

sum over the sphere of the contributions of each single molecular orientation. As a simplification the conformational average can be divided in to two independent averages. This decompensation can be done when only a weak correlation between the distance fluctuation to the orientation fluctuation of both labels and results in a product of the distance-dependent Kernel function K and an orientation-dependent pump efficiency function λ . Such a normalized PELDOR description with $S(T, \nu) = V(T, \nu)/V_0(\nu_A)$ is defined as

$$S(T, \nu) = 1 + \int_0^1 K(r, \Theta, T) \lambda(\Theta) \sin \Theta d\Theta \quad (2.28)$$

With the Kernel function the time dependence enters the trace as well as the dependence on distance and on the external magnetic field. There the dipolar coupling is the relation that matters (cf. eqn. 2.23).

$$K(r, \Theta, T) = \langle \cos[\omega_{dd}(r_i, \Theta)T] \rangle_i - 1 \quad (2.29)$$

In contrast to this the pump efficiency function $\lambda(\Theta)$ is time- and distance- independent, but influenced by the orientation of the spin labels. The anisotropic interactions, the electron Zeeman and the hyperfine interaction described in the section 2.4, results in different resonance frequencies for chemically identical nitroxide spins where the labels have different orientations to the external magnetic field B_0 , to the inter spin vector o_a (Θ and Φ) and different nitrogen quantum numbers ($m = -1, 0, 1$).

$$\omega_r(\Theta, \Phi, o, m) = \gamma_e \left(B_0 \frac{g_{eff}(\Theta, \Phi, o_a)}{g_e} + mA_{eff}(\Theta, \Phi, o_a) \right) \quad (2.30)$$

where γ_e is the gyromagnetic ratio of the electron. The functions $g_{eff}(\Theta, \Phi, o_i)$ and $A_{eff}(\Theta, \Phi, o_i)$ are effective values of the g-tensor and of the hyperfine interaction, the A-tensor. They can be expressed as the square root of

$$\begin{aligned} T_{eff}^2(\Theta, \Phi, o) &= T_{xx}^2 + (T_{yy}^2 - T_{xx}^2)[\sin \Theta \sin \gamma \cos(\alpha - \Phi) \\ &\quad + \sin \Theta \cos \gamma \sin(\alpha - \Phi) \cos \Theta \cos \gamma \sin \beta]^2 \\ &\quad + (T_{zz}^2 - T_{xx}^2)[\sin \Theta \sin \beta \sin(\alpha - \Phi) + \cos \Theta \cos \beta]^2 \end{aligned} \quad (2.31)$$

where T_{eff} can be either the g-tensor or the A-tensor.

In PELDOR, a pulse does not excite all spins simultaneously, that is the detection pulses excite only the A spin, while the spin partner gets excited by the pump pulse. The excitation of a pulse depends on the pulse frequency ν_k , which must match the resonance frequencies ω_r of the spins. The Rabi frequency of such an excited electron spin is

$$\Omega_k^2 = \gamma_e^2 B_{1k}^2 + (2\pi\nu_k - \omega_{rk})^2 \quad (2.32)$$

Here $k = A, B$ indicate the detection and pulse frequency, respectively. In a PELDOR experiment, the detection pulses create a spin echo magnetization on the spin A, whose transversal component can be expressed as follows

$$m_x(\omega_{ri}, \nu_A) = \frac{\gamma_0 B_{1A}}{\Omega_A} \sin(\Omega_A t_A) \frac{1}{4} \left[\frac{\gamma_0 B'_{1A}}{\Omega'_A} \right]^4 [1 - \cos(\Omega'_A t_A)]^2 \quad (2.33)$$

where t_A the pulse length of the detection pulses. In practice all pulse lengths are kept constant and the difference between $\frac{\pi}{2}$ and π is achieved by doubling the field strength ($B'_{1A} = 2B_{1A}$). Ω'_{1A} is calculated accordingly. A pump pulse with length t_B and field strength B_{1B} will flip a spin B with a probability p_B . This flip probability is defined by

$$p_B(\omega_{ri}, \nu_B) = \frac{\gamma_0^2 B_{1B}^2}{2\Omega_B^2} [1 - \cos(\Omega_B t_B)] \quad (2.34)$$

A PELDOR time traces includes two different contributions. In one part, spin A will be excited by the first π pulse without excitement of the spin B. Those spin pairs will contribute a constant, time-independent signal $V(\nu_a)$ proportional to $(1 - p_b)$ to the overall echo intensity. When both spins are excited, the intensity of the refocused Hahn echo formed by the probe pulses will be modulated by the dipolar coupling, depending on the delay time T between probe and pump pulses. For this case the pump efficiency λ is an averaged sum of the spin echo magnetization m_x of spin A, weighted by the flip probability of the B-spin p_B due to the excitation by the pump pulse

$$\lambda(\Theta) = \frac{1}{2V(\nu_a)} \sum_{m_1 m_2} \langle m_x(\omega_{r1}, \nu_A) p_B(\omega_{r2}, \nu_B) + m_x(\omega_{r2}, \nu_A) p_B(\omega_{r1}, \nu_B) \rangle_{\Theta} \quad (2.35)$$

with resonance frequencies of $\omega_{r1} = \omega_r(\Theta, \Phi, o_1, m)$ and $\omega_{r2} = \omega_r(\Theta, \Phi, o_2, m)$ for the first and the second spin, respectively. The formulas for the transversal spin echo magnetization m_x and for the spin flip probability p_b both contain the resonance frequency, which depends on the magnetic field orientation with respect to the nitroxide as described by the Euler angles. Thus both functions depend on orientations, and the λ function is also called orientation intensity function.

2.5.4 | Orientation Selective PELDOR

As seen in the last section, there is an orientation dependence encoded in PELDOR time traces, directly dependent on the resonance frequencies excited by the pulses.

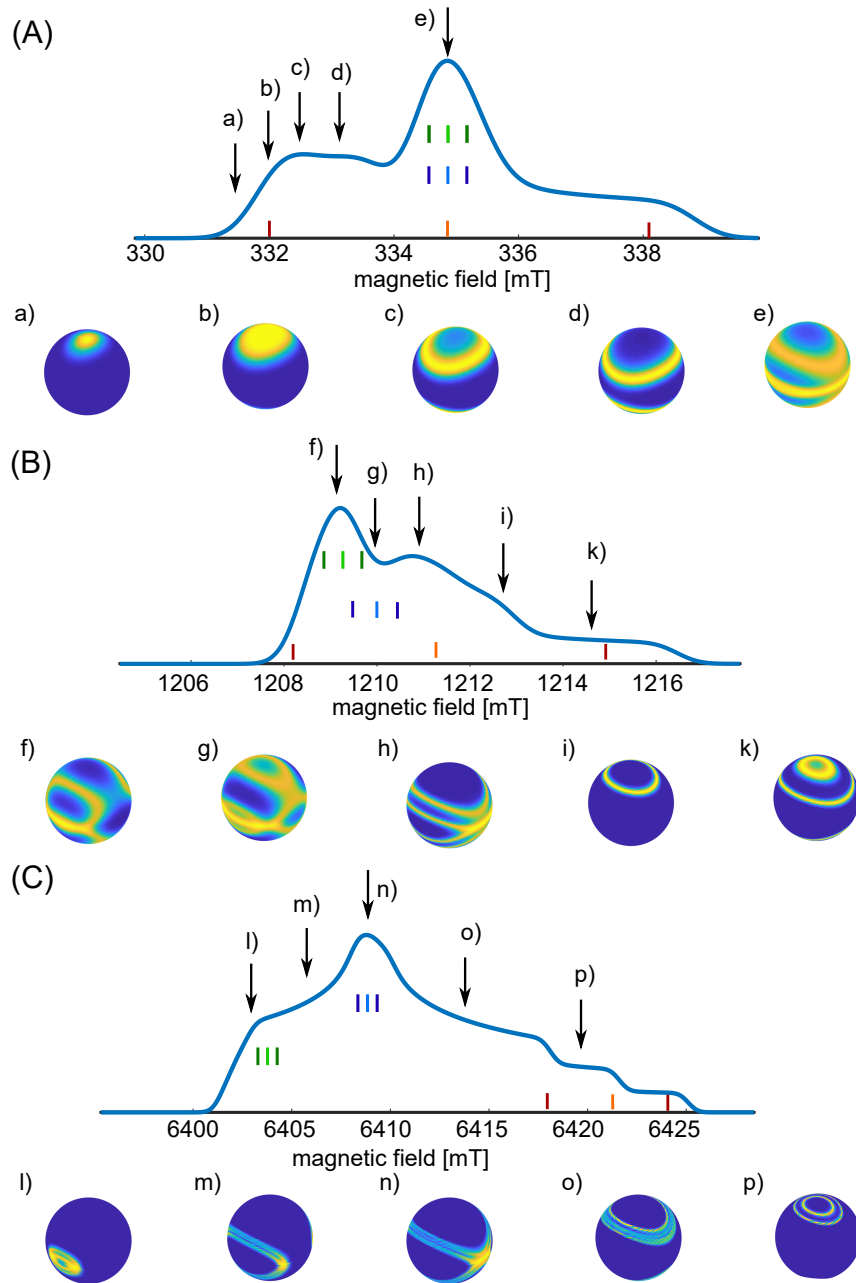


Figure 2.5.5: Simulated field sweep spectra for different magnetic fields. (A) X-band (~ 0.3 T / ~ 6.4 GHz) (B) Q-band (~ 1.2 T / ~ 33 GHz) (C) G-band (~ 6.4 T / ~ 180 GHz). The excited orientations for a 30 ns pulse at different field positions (marked by the arrows) are depicted by the balls. The small alphabet correlate the orientation with the field position. The coloured lines are the g-tensor and A-tensors (cf. fig. 2.4.3)

Thus, the oscillation frequency, dampening and modulation depth of PELDOR time traces can differ when changing the pump or the detection pulse position within the nitroxide spectrum. The different orientation excited by a typically 30 ns long rectangular pulse at different magnetic fields is shown in figure 2.5.5. The X-band is dominated by hyperfine anisotropies, as all three g-tensor are hidden in the inherent linewidth. There are relatively small difference between the orientations parallel to the nitroxide plane (in-plane components) of the hyperfine interaction tensor (A_{xx} and A_{yy}) in comparison to the orientation perpendicular to this plane (out-of-plane component, A_{zz}). Thus, changes in the resonance frequencies ω_r of nitroxide caused by rotation about their z-axis are so small that the variation in the function λ are barely noticeable. Due to this, the orientations which influence the orientation density function are limited to in-plane orientation changes (around the x- or y-axes). Hence, only the β angles of both sets of Euler angles contribute. This reduces the amount of information of a systems, nevertheless it simplifies data analyses. This advantage, or disadvantage, is lost by increasing the magnetic field. At fields above 50 GHz, in our case at G-band (180 GHz), the nitroxide spectrum becomes dominated by the g-tensor anisotropy. This resolves all Euler angles, making the analysis more accurate, though more challenging.

At low fields the pump pulse is set at the maximum of the nitroxide spectrum in order to increase the signal. A typical pulse length of 12 ns will excite all orientations with the quantum number of $m = 0$. This is therefore a state selective but orientation non-selective pulse. As the detection frequencies are commonly varied within an offset range between both frequencies from 40 MHz to 90 MHz a detection selection takes place. At high fields all pulses are orientation selective. Therefore not only does the interspin vector contribute to the signal but the orientations of the two spin labels relative to each other add to the signal. At G-band the magnetic field is shifted, measuring from g_{xx} to g_{zz} with a constant offset between the pulse frequencies.

Independent of the magnetic field, there are some limitations which always have to be taken into account. As shown in the work of Abe *et al.*^[152] equivalent PELDOR traces are caused by symmetry of the magnetic tensor. Hence, the out-of-plane orientation is limited by 180° , having an inversion symmetry, while the in-plane orientation is rotation symmetric on the 4th order (90°). Moreover, there is an invariance for both Euler angles, making both labels indistinguishable. This is due to the fact that both labels give rise to identical nitroxide spectra.

Direct interpretation of the orientation-selective PELDOR data can be ambiguous and challenging. Firstly a single orientation-dependent time trace is not sufficient to distinguish between different orientations. Hence a set of up to six traces equally

distributed of the nitroxide spectrum, were measured. Several fitting algorithm have been published for direct interpretation, for example using a database^[45] or a genetic algorithm.^[153] The database reconstructs the experimental data by fitting a selection of a sub-ensemble out of a set of pre-simulated traces that were derived from a library of possible spin-spin orientations. However, traces with different orientations could be almost identical. Moreover as the measured ensemble increases it becomes more likely that the solution might not be unique, since different ensembles of spin label conformations might represent the same orientation-selective PELDOR data. Another point to consider, is that obtaining a detailed picture of the molecule of interest from the Euler angles alone may be challenging. A more reliable method of the interpretation is simulation of the orientation selective PELDOR traces, as the simulation procedure using equation 2.28 through 2.35 are almost parameter-free. For this reason it is preferable to evaluate the experimental data relative to a biologically acceptable model; this increases the likelihood of determining a reasonable and unique solution. For the simulation one can either use a educated guess, *e.g.*, using simple three dimensional models of the studied molecule by taking other experimental data into account^[41] or from known geometry.^[45,154] Moreover by using structures from MD or QM simulations knowledge derived from other experiments and from quantum mechanical calculations can be combined with PELDOR spectroscopy.

2.5.5 | PELDOR of Flexible Systems

For the case that the orientation of the labels are randomly distributed, the λ function results in an average value. For such flexible systems all anisotropy related effects are cancelled out. Hence only the pulse length and the magnetic field strength B_1 contribute to the pump pulse efficiency λ . The signal can be therefore described by

$$\begin{aligned} S(t) &= 1 - \lambda + \lambda \int_0^{\frac{\pi}{2}} \cos(\omega_{dd}T) \sin\Theta d\Theta \\ &= 1 - \lambda + \lambda \int_{r_{min}}^{r_{max}} K(t, r) p(r) dr \end{aligned} \quad (2.36)$$

Either for a single distance or more realistically, for a distance distribution $p(r)$. Experimental parameters do not affect the oscillations of the traces, they only affects the modulations depth Δ (depicted in fig. 2.5.6 (b)), which is dependent on the pump pulse length. Thus, traces from different magnetic field and with different pulse excitation frequencies are identical.

The calculation of those PELDOR signals from a known distance distribution

is straightforward using equation 2.36, whereas the extraction of distances from the PELDOR time trace, the inverse problem, does not yield a unique solution, especially considering the presence of noise in the experimental time trace. The common strategy is to perform a Tikhonov regularisation a method proposed in the Jeschke lab. This regularisation, implemented in the data processing software DeerAnalysis,^[155] tries to stabilize the solution of this ill-posed problem. The solution is given by the root mean square deviation between a simulated trace ($K(t, r)P(r)$) and the experiment trace ($S(t)$) with a regularisation term:

$$G_\alpha = |S(t) - K(t, r)P(r)|^2 + \alpha|LP(r)|^2 \quad (2.37)$$

The regularisation is given by the α -weighted squared and normalised second derivative of the distance distribution function ($LP(r) = P(r)''$). This term gives the smoothness of the distance distribution so that noise is not later fitted as distances. Nevertheless, a high α can broaden the distribution and decrease the resolution, while a low α create 'artefact' peaks. The estimation of the correct α parameter is done with an L-criterion, which gives the smoothness (logarithms of the second term) against the logarithm of the mean square deviation between the simulation and experiment (first term). The most probably valid parameter gives a compromise between smoothness and resolution and could be found in the kink of the curve.

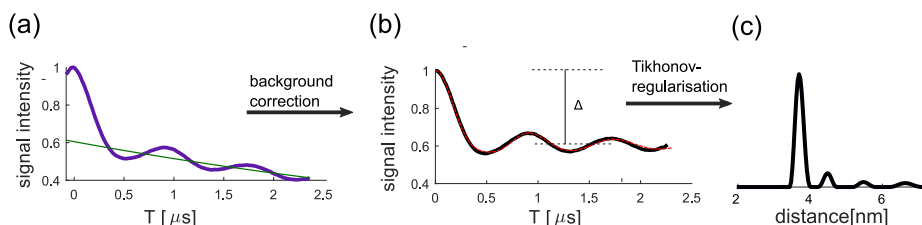


Figure 2.5.6: Data procession for distance based PELDOR measurements. (a) The raw data (violet) include the intermolecular background (green). (b) By background correction the black trace results with only intramolecular interactions. Δ gives the modulation depth. (c) Via Tikhonov regularisation the distance distribution could be determined.^[155] The resulting fit of the data is shown as a red dotted line in (b).

Up to this point, only the dipole-dipole coupling of two distinct spin pair has been discussed. However the A spin also couples with the randomly distributed electron spins of the surrounding molecules. For a homogeneous spatial three-dimensional distribution, such spin-spin interactions can be approximated by a monoexponential decay of the signal, depending on the local spin concentration

c:

$$V_{inter}(t) = e^{\left(-\frac{2\pi g_A g_B \mu_B^2 \mu_0}{9\sqrt{3}\hbar} c\lambda t\right)} \quad (2.38)$$

Hence, the measured raw PELDOR traces can be decomposed to the intra- and inter-molecular dipolar coupling.

$$V(t) = V_{inter}(t) \cdot V_{intra}(t) \quad (2.39)$$

The separation of the two components, the background correction, is usually done by fitting a monoexponential decay at the end of the PELDOR traces, using the DeerAnalysis Software.^[155] Depending on the distance and the length of the traces this can lead to an ambiguous solution. Thus, one has to ensure that all the dipolar oscillation is either fully gone or at least two pronounced oscillations are present for a reliable background correction.

2.5.6 | CP-PELDOR

The length of PELDOR time traces is restricted by the relaxation times of the measured system. This limits the distance accessible with the 4P-PELDOR experiment. There are two ways to overcome this problematic. On the one hand one can try to diluting the sample and using deuterated solutions to prolong the relaxation time. On the other hand one can use a new pulse sequence (see fig. 2.5.7) which was developed in our lab.^[56]

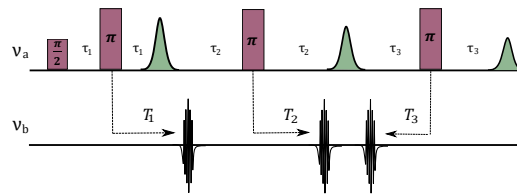


Figure 2.5.7: 7-pulse CP-PELDOR Sequence. The pump pulse sequence with the frequency ν_b consist of three sec/tanh pulses (black)

This pulse sequences is based on the Carr-Purcell (CP) sequence,^[156] which was developed to minimize the translational diffusion effect on the phase memory time in solution NMR by applying several refocusing pulses. Using this idea for dipolar spectroscopy, a number of refocusing pulses can be used in the observer frequency of spin A. However, the number of pump pulses must be chosen in such a way, that the dipolar interaction gets refocussed. Thus, an odd number of pump pulse is necessary. Hence, a 7-pulse CP-PELDOR method has been established in our laboratory

This new sequence benefits from the newly available fast AWG for EPR experiments. The pump sequence consists of three sech/tan pulses (fig. 2.5.1), which accompany the three refocussing pulses of the detection sequence. Since non-uniform inversion of multiple pump pulses can create artefacts, adiabatic sech/tanh pump pulses are needed as they offer high inversion efficiency for a given bandwidth. For a maximal intensity of the refocussed echo at the end of the CP sequence the delay times τ_1, τ_2, τ_3 are of approximately the same length. The time axis, T , of the experiment is given as:

$$T = \tau_1 + \tau_2 + \tau_3 = T_1 + T_2 + T_3 \quad (2.40)$$

Nevertheless even these pulses can show a non-quantitative inversion. Hence, an additional parameter p is defined to describe the probability that all spins are inverted by two subsequent pump pulses. If the parameter p is less than one, the derived signal is a superposition of 8 different dipolar signals with different characteristics weighted by their respective probabilities and thus a complicated intermolecular decay function. Practically, p must be greater than 0.7 to obtain a major contribution of the desired dipolar signal.

CHAPTER 3

Results and Discussion

This chapter summarizes the most important results of this thesis, which were previously published in peer-review journals previously^[157,158,159,160,161] or present as manuscript. Each section starts with a short historical reappraisal including the motivation behind this study. Following a summary of the major findings regarding the author's work is given with a short conclusion.

3.1 | PELDOR Spectroscopy on Nucleic Acids - A Short Introduction

In the last two decades, several works has been published in the EPR community for studying structures, conformational changes and flexibilities of nucleic acids by means of PELDOR spectroscopy. This method was first proposed by Milov and co-workers in the year 1981.^[52] However, the dead-time problematic remained problematic until 1998 when the four-pulse PELDOR sequence was proposed and first used in the Spies group.^[53,149] Since then measurements have become feasible and reliable for structural biology.

These first measurements were done on biradical model systems, and afterward several groups started to use the methods on various polymeric and biological systems. Jeschke showed a first study of polymer chain conformations,^[162] and Persson from the Eaton group compared PELDOR measurements with distances reached from CW spectra and Fourier deconvolution of line shape broadening. Here a large protein system, the human carbonic anhydrase II (HCAII) could be studied.^[163] This was the first example of a PELDOR measurement on a doubly spin-labelled protein.

At the beginning of this century feasibility studies for the usage of PELDOR spectroscopy on nucleic acids were done. For RNA the three pulse PELDOR sequence was used in the Prisner group by Schiemann *et al.* to measure distances on small 12mer dsRNAs. The nitroxide spin labels were covalently bound to the 2'-carbon via a urea linker.^[43] Bowman *et al.* performed 4P-PELDOR distance measurements on C2'-labeled RNA duplexes using amide groups as linkers to the spin label.^[164] Schiemann showed in the same year that DNA labelled with TPA (structure fig. 3.3.1) can be used as a model-free PELDOR-based nanometer

3.1. PELDOR SPECTROSCOPY ON NUCLEIC ACIDS - A SHORT INTRODUCTION

distance ruler, when the spin labels' positions are systematically varied.^[75]

Following, PELDOR measurements on several NA systems were performed. In the study of distances on short DNA duplexes were compared with a geometrical model of a double helix by Ward *et al.*^[165] In the group of Qin the R5 Spin label was introduced with a phosphorothiate linkage.^[166] This spin label could be introduced in an efficient manner; however, the spin label could occur with two diastereomers and show a large distribution. But nonetheless several PELDOR data show clear distances with this spin label in dsRNA.

As a next step, small nucleic acid duplexes with covalently attached **C**, were studied. This rigid spin label showed no flexibility additional to the intrinsic motions of the DNA and the nucleobase itself. The label is a cytidine analogue introduced by Barhate from the Sigurdsson laboratory in 2007 and further studied by Cekan.^[48] Having this special label in hand, first orientation selective PELDOR measurements on nucleic acids were achieved in the Prisner group. Systematic work with these biological samples was evaluated qualitatively by their orientation relative to the interspin vector.^[44] Based on further high field measurements Marko and co-workers proposed a model for the backbone dynamics of small dsDNA motifs.^[167]

In the following years the field of nucleic acid related PELDOR spectroscopy became more widespread. Small dsDNA and dsRNA motifs and their hybrids were studied by Romainczyk *et al.*^[76] In this study the surprising finding was made that the labeling position influences the helical geometry of both B and A forms. Sicoli had a deeper look at the transitions of both helical geometries of dsDNA^[168] and in the Steinhoff group Wunnicke studied non-standard DNA duplexes. They were able to detect local changes due to the introduction of single mis-matched pairs^[169] as well as the difference between antiparallel and parallel dsDNA.^[170] Another paper from the Milov group showed that having a nucleotide missing in a duplex leads to a bending of the structure.^[171] In addition to these small duplexes, motifs like bended DNA structures, studied by Grytz,^[154] pRNA three way junctions^[172] and G-quadruplexes with di-copper labels have come into recent research.

As stated in the introduction structural biologists in the RNA field are particularly interested in structures and structural rearrangement of riboswitches and of aptamers. Several motifs have already been studied by the means of PELDOR spectroscopy. Wunnicke studied the tetracycline aptamer,^[46] Krstic the preorganisation of the neomycin aptamer,^[173] and Grytz, with orientation selective PELDOR restraints, the cocaine aptamer.^[41] Moreover Nak-Kyoon Kim investigated the folding of a hammerhead ribozyme in relation to Mg^{2+} concentration.^[174]

Beside structural studies of isolated nucleic acids, experiments on protein-RNA interactions^[175] and the first in-cell measurements have already been performed.^[74] As mentioned previously, several studies have already been done on small DNA and RNA duplexes of 12 to 25 nucleotides in length. As a result these sequences seem to be well understood in terms of structure and dynamics. On the one hand this makes these motifs interesting for method development and for evaluation of new spin label. On the other hand, with the development of new, more sensitive experimental methods, spin labels and computational possibilities, the previous studies can be refined to reach a more detailed view of this motif; this knowledge could later be transferred to more complex systems. This thesis studied exclusively small nucleic acids duplexes in both ways. Primarily with help of advanced computational MD simulations detailed knowledge of the dynamics of dsDNA could be achieved. These simulations were evaluated against orientation-selective PELDOR measurements on dsDNA. Based on these results methods and spin label development were completed. New technical developments allowed an increase in the applicability of single frequency techniques for orientation-selective studies like 2D-SIFTER. There, simulation procedures were evaluated against known orientation selective PELDOR measurements. To decrease the laboratory effort for synthesizing spin-labelled duplexes the semi-rigid spin label ^{Im}U and the non-covalent bound \acute{G} was studied further. Additionally the effect of room temperature PELDOR on the measured time traces was studied in detail. Finally, artefacts from small RNA duplexes, based on $\pi - \pi$ interaction at the end of the strands were investigated.

3.2 | Intermolecular Interaction - 'End-to-End' Stacking of dsRNA

This chapter is based on the publication Erlenbach *et al.* RNA (2019) 25, 239. The work was prepared in a collaborative manner. The contribution of the author was the performing of all experiments and the following analysis of the PELDOR data. The samples were synthesized by Bizera Krstic and Dr. Christian Grünwald from the group of Prof. Heckel.

One artifact in PELDOR studies of small dsRNA is found several time in literature. Time traces with additional distances were found not only in the Prisner lab^[74,75,76,77] but also the Bennati lab^[78] and in Qin's lab.^[79] Also recent unpublished measurements showed systematic additional distances for RNA duplexes as well as on the tetracycline aptamer.^[42] Initially multiple distances for a doubly-labelled small dsRNA were observed by Cai *et al.*^[79] However, as they were only interested in the single main distance, they exclude minor peaks. In the work of Romainscysk these peaks were also found but not further studied.^[76] The first potential explanation was proposed by Halbmaier and co-workers, who showed in their supplementary information that the derived additional differences agree with 'end-to-end' stacking of two helices,^[78] and Weinrich *et al.* attributed the additional distances to this intermolecular interaction.^[77] However, such a intermolecular interaction is expected to influence both the structure and the dynamics of small RNA duplexes. Further, possible multi-spin interactions complicate the analysis of PELDOR measurements.^[176] As a consequence this interaction had to be characterized and afterwards hindered.

The proposed 'end-to-end' stacking might be due to $\pi - \pi$ interaction between two base pairs, first recognized in 1958 as a stabilisation force in nucleic acids duplexes.^[177] This interaction was studied multiple times as an intramolecular attraction.^[178,179,180] The occurrence of this interresidue effect between different molecules was initially found in crystallography.^[71] Here the dsDNA aggregates spontaneously into rod-like structure, this can only be explained by axial stacking. This 'end-to-end' attraction in dsDNA and in dsRNA was further studied by the Pollack group with SAXS.^[72,73,181] With this method attraction and repulsion between small biomolecules can be measured. They studied the dependence of this 'end-to-end' interaction in dsDNA on the sequence length and at different divalent and higher-valent salt concentrations. They were able to see that this interaction is much more pronounced in the case of dsRNA, due to the greater number of nearby ions on dsRNA, which enables a more effective shielding of the repulsing interactions between the negatively charged backbones.

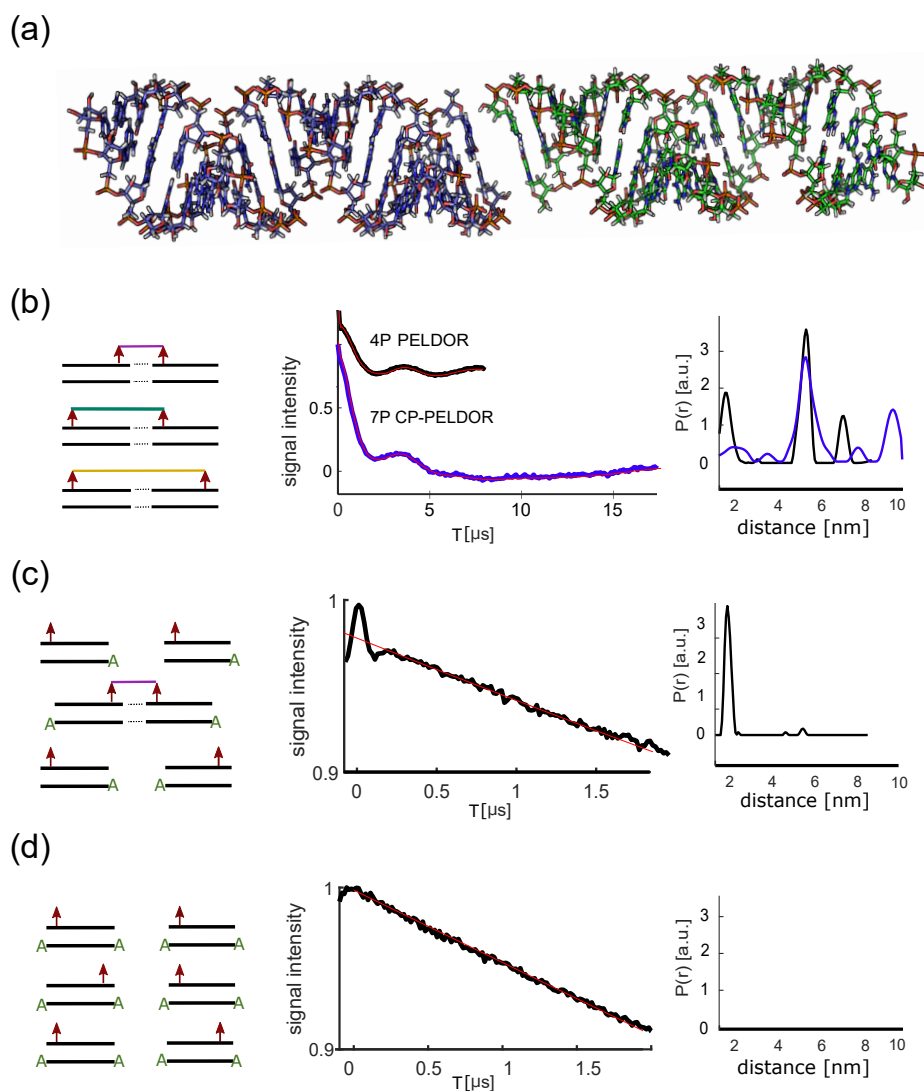


Figure 3.2.1: (a) Two dsRNAs stacked 'end-to-end' (b) (left) Schematic picture of stacking possibilities for singly labelled dsRNA without overhang. (middle) Background corrected 4P-PELDOR time trace (black) and 7PnCP-PELDOR traces (blue) with (right) the related distance distribution calculated with Tikhonov regularisation. (c) Schematic picture of stacking possibilities for dsRNA with a single base overhang at one end and their raw 4-pulse PELDOR data and the related Tikhonov derived distance distribution. (d) Schematic picture of stacking possibilities for dsRNA with a two nucleobase overhang, their raw 4-pulse PELDOR data and the related Tikhonov derived distance distribution. Modified from Erlenbach et al. 2019.^[161]

3.2. INTERMOLECULAR INTERACTION - 'END-TO-END' STACKING OF DSRNA

To work further on this topic with PELDOR spectroscopy, singly labelled dsRNA carrying the TPA spin label were synthesized by Dr. Christian Grünewald and Bisera Krstic. These samples have the advantage that the dipolar coupling, detected by PELDOR, can be exclusively related to interactions between nucleic acids and is not distorted by multi-spin effects.^[176]

PELDOR measurements clearly show dipolar coupled spin pairs, indicating a defined intermolecular interaction. The derived distances correspond to the expected distances for dsRNA 'end-to-end' stacking via $\pi - \pi$ -interaction of nucleobases at the end of strands as depicted in figure 3.2.1 (a). As 4-pulse PELDOR is limited in the distances measurable due to the phase memory time of the spins, the maximum distance which can be reliably derived from these samples is around 7 nm in deuteriated solution. However, one distance was expected around 9 nm. To also observe this long distance with high accuracy additional 7-pulse CP-PELDOR measurements were performed, allowing expansion of the time window to up to 17 μs . By taking the advantage of this, the longest distance could be reliably identified. Both measurements with their corresponding distances, derived by Tikhonov regularisation, are shown in figure 3.2.1.

To prevent the 'end-to-end' interaction one needs to add bulky ends, which sterically inhibit the electrostatic attraction. Therefore, an additional nucleotide was added to the ends of a strand during the solid phase synthesis, to exclude the possibility of $\pi - \pi$ stacking between the dsRNAs. PELDOR measurements with an overhang at one side of the duplex show only an oscillation with a high frequency, as depicted in figure 3.2.1 (b), that is related to a 2 nm distance. This meets the expectations that only dimerisation is still possible. Subsequently, single nucleotides were added at both ends of one strand. This leads to the absence of any distinct distance, which proves the absence of any defined intermolecular interaction. All contributions to the PELDOR signal exclusively relate to the background of randomly distributed RNA duplexes.

The modulation depth of PELDOR measurements for dimers reports directly on the number of spin pairs relative to the overall number of spin labels,

$$\Delta = \lambda p \tag{3.1}$$

with the pump pulse efficiency λ (see sec. 2.5.2) and the stacking probability p defined as

$$p = \frac{2[Dimer]}{[Monomer] + 2[Dimer]} = \frac{2[Dimer]}{[RNA]} \tag{3.2}$$

Measurements at different Na^+ concentrations revealed an increased stacking probability, previously found for divalent ions by Pollack (fig. 3.2.2 (a)). This was first found with samples with one overhang, where only dimerisation is pos-

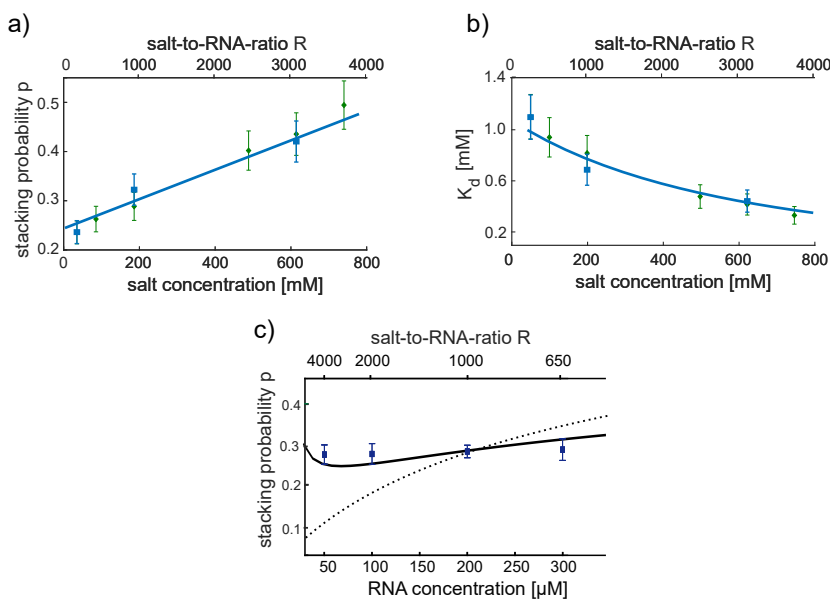


Figure 3.2.2: (a) Stacking probability of dsRNA in relation to the monovalent salt concentration of NaCl and to the salt-to-RNA ratio, for a RNA concentration of 200 μ M. (b) Dimerisation constant for the ‘end-to-end’ stacking for different salt-to-RNA ratios. For both, (a) and (b) in blue samples with one overhang and in green samples without overhang, taking trimers and multi-spin effects into account. (c) Stacking probability of dsRNA in relation to the RNA concentration and the respective salt-to-RNA ratio for 200 mM NaCl (blue data points). The dotted points indicate the expected stacking probability for only a change in RNA concentration. In black the compensated stacking probability is shown in black. Modified from Erlenbach et al. 2019.^[161]

sible. However PELDOR data of samples without overhang, gives rise to the same trend, but the modulation depths from these data reveals the possibility of oligomers. Taking statistics of these oligomers explicitly into account, the same stacking probability was found. Given the known definition of the K_d value in relation to the stacking probability,

$$K_d = \frac{[Monomer]^2}{[Dimer]} = 2[RNA] \frac{(1-p)^2}{p} \quad (3.3)$$

the K_d value for the equilibrium reaction of the dimerisation of two dsRNAs could be calculated, varying between 0.2 – 1.2 mM. These values show a strong dependency on the salt-to-RNA ratio in the measured range as depicted in figure 3.2.2 (b).

Though the dimerisation is an equilibrium reaction, the stacking probability does not show a increase with increasing the RNA concentration. However as the total salt concentration was kept constant in these experiments, the salt-to-RNA ratio R was decreased significantly within this series. That p does not vary with RNA

3.2. INTERMOLECULAR INTERACTION - 'END-TO-END' STACKING OF DSRNA

concentration can be explained by two counteracting effects. On the one hand p increases with the RNA concentration (dotted line in figure 3.2.2), but on the other hand p decreases due to the strongly reduced salt-to-RNA ratio. (see fig. 3.2.2 (c))

With this work we showed that PELDOR is a valid method not only to study, structure and dynamics, but also for investigating intermolecular interactions. By careful evaluation of the modulations depth, the effect of parameters such as concentration on these interactions can also be detected, theories proposed to avoid such interactions can be tested.

3.3 | Flexibility of Spin Label - A Semi-Rigid Approach

This chapter is based on the publication Erlenbach *et al.* Physical Chemistry Chemical Physics (2016) 18,16196. This work was prepared in a collaborative manner. The contribution of the author was the performance of 50 % of the experiments, the remaining experiments were performed by Dr. Burhhard Endeward. The author also performed the analysis of the orientation selective PELDOR data. The samples were synthesized in the group of Prof. Sigurdsson by Dr. Gophane from the University of Iceland Science Institute, Reykjavik.

One crucial step for PDS measurements for the study of the structures and flexibilities of nucleic acids is the usage of spin labels. From a spectroscopic point of view a direct translation of PDS measurements to structure and flexibility is desired. In these experiments the tether between the molecule of interest and the nitroxide moiety plays an important role.

In the case of protein research, the commonly used nitroxide spin label is MTSSL. The tether of MTSSL has several free rotations which broaden the measured distance distribution.^[182] Hence, it is complicated to disentangling the distribution of the label and the biomolecule and translate the distance information to protein flexibility. The different conformations of the spin label possible for one single protein structure are often depicted as a flower pocket, which give rise to all possible radical positions.^[183]

On nucleic acids, 2,2,5,5-tetramethyl-pyrrolin-1-yloxy-3-acetylene (TPA) is a prominent spin label for distance determination (fig. 3.3.1 (a)). There the radical lies on a cone for the rotation of the label around the tether, as the N-O bond is not aligned with the tether. Nevertheless the broadening is minor compared to MTSSL as the acetylene bridge to the nucleobase is short. For more accurate distance determination the usage of a conformationally unambiguous spin labels is preferred. These are labels without any distance broadening due to label flexibility at the same time they do not show any orientation-selective effects on the PELDOR time traces, which would complicate data analysis. In the best case the N-O bond of the nitroxide would align with the tether because rotation around the single bond does not cause displacement of the nitroxide relative to the DNA^[184] and the orientation effects would be rather efficiently averaged out by the rotation. In the Gannett lab a conformationally unambiguous TPA analogue spin label with a six-membered ring was developed.^[185]

The ideal spin label for studies of nucleic acid structures and inherent flexibilities is totally rigid. A direct translation of the measured data to the nucleic acids' prop-

3.3. FLEXIBILITY OF SPIN LABEL - A SEMI-RIGID APPROACH

erties would then be possible, and moreover anisotropic effects could be analysed for even more details regarding the structure and dynamics of nucleic acids. The first totally rigid spin label reported for DNA is known as **Q** and came from the Hopkins laboratory (structure shown in fig. 3.3.1).^[186,187] **Q** is, a five-membered nitroxide and is directly fused to a non natural nucleobase, forming a base pair with 2-amino purine. Later on, **Ç** was developed in the Sigurdsson laboratory; this is an prolonged cytidine analogue and forms a base pair to guanine without structural perturbations.^[48,105,188] The spin label points inside the major grooves. A modified spin label **Çm** can also be used for RNA.^[189]

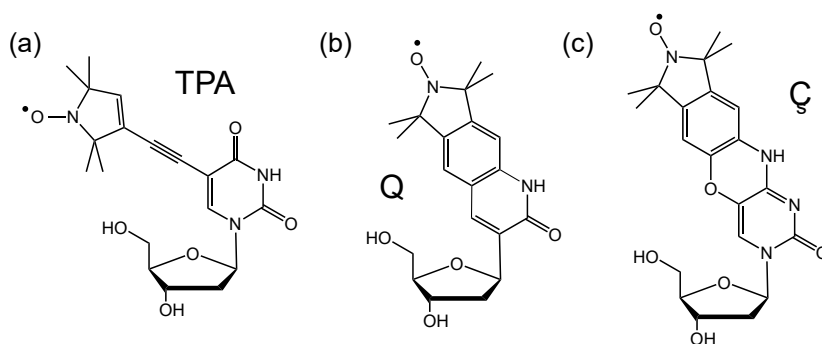


Figure 3.3.1: Spin label structures for nucleic acids (a) TPA (b) **Q** (c) **Ç**

Under consideration of this aspect for spin label attractivity, **Ç** has perfect spectroscopic properties; however, it is synthetically very demanding. Hence, semi-rigid spin labels were introduced. Two of these are the isoindoline derivate spin labels ^{Im}U and ^{Ox}U . The structures of both are reported in fig. 3.3.2 (a). They are restricted in rotation around the single bond linking them to the uridine nucleobase.^[49] In particular ^{Im}U forms an intramolecular hydrogen bond between the NH of the benzimidazole and O4 of the nucleobase. Both labels show orientation-dependent changes in PELDOR time traces although they are less rigid than **Ç**. To gain an in-depth knowledge about a spin label is own mobility it is important to be able to disentangle the intrinsic motion of the nucleic acids from the spin label's flexibility.

Simulations were made on the basis of a dynamical three dimensional model. For every simulation, an ensemble of 500 conformers was calculated to represent the conformational ensemble in the frozen solution. Each DNA duplexes was represented as a helix through the 1' carbon of the sugar and the dynamical parameter of the internal motion of the DNA was taken. This dynamic was found in previous studies by Marko *et al.* using the same DNA sequence spin labelled at various positions with the **Ç**.^[167] Accordingly, a change in the radius of the DNA cylinder without any change of the helix pitch was utilized. In addition to this DNA

twist-stretch motion, the electron spin position of the spin label and their mutual orientation was constructed from the helix. To calculate the intrinsic internal mobility of the spin labels, we introduced additional rotational motions around the spin label molecular axes. The first one is a rotation around the linker between the spin label and the nucleic acid base. This is calculated as a rotation around the x-axis of the spin label (see fig. 3.3.2 (b)). To model any remaining flexibility of the spin label to describe change in the spatial position relative to the DNA small angle fluctuation about the other two axes (y and z) were introduced. All motions were calculated independently from each other and based on Gaussian-distributed angle variations. More details regarding the simulations procedure can be found in Erlenbach *et al.*^[157] Simultaneous simulations of orientation-selective PELDOR data at three different magnetic fields provide excellent fittings, as shown in figure 3.3.2. The analysis proves the semi-rigidity of the isoindoline spin label and gives quantitative values for the internal mobility of these labels. ImU is limited to a x-rotation of 5° , while the OxU label has twice the rotational freedom regardless of the position of the spin label, due to the lack of the hydrogen bond. The other two rotations, reflecting the overall residual flexibility, should be as small as possible for orientational dependent flexibility studies of nucleic acids. The two spin labels had similar amounts of y-rotation (about $15^\circ - 20^\circ$), and their z-rotation was fixed at 5° .

An analogous study was performed for the conformationally unambiguous spin label $ExImU$, which was again proposed by the Sigurdsson lab.^[50] It is a isoindoline-based spin label with a rather long tether, where a free rotation around the triple bond of this tether is possible. Orientation-selective PELDOR measurements at low field (X-band) did not show any anisotropic effects, while at high field slight differences between the traces with a changing magnetic field could be obtained. The three-dimensional model simulations explained above confirm the free rotation around the tether; however owing to the rather long linker this label show increased in-plane motion, which complicates the separation of the label and the nucleic acid proportion in the distance distribution. All simulations are depicted in figure 3.3.2(e).

These detailed analyses of the dynamics of ImU , OxU and $ExImU$ will facilitate the use of these spin labels for further studies of nucleic acid motifs.

3.3. FLEXIBILITY OF SPIN LABEL - A SEMI-RIGID APPROACH

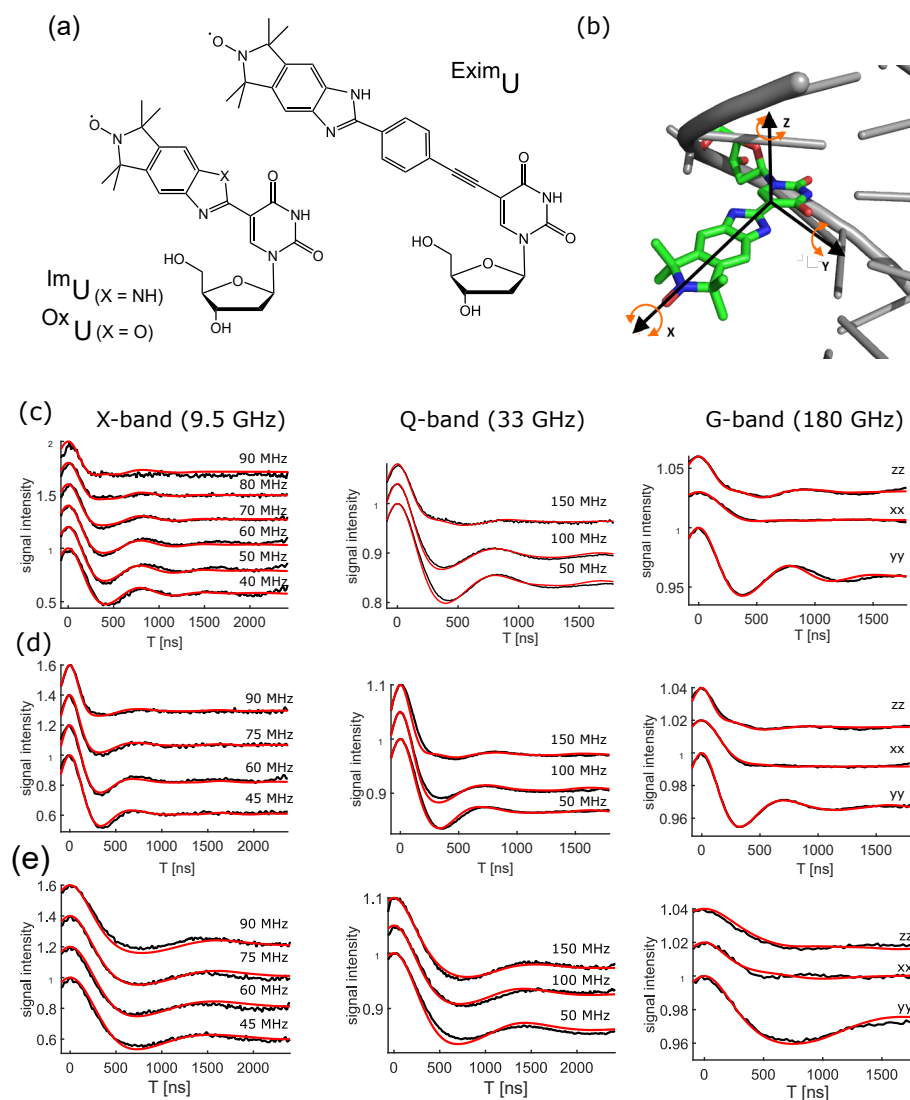


Figure 3.3.2: (a) Chemical structures of the isoindoline derivatives spin labels ImU / OxU and $ExImU$ (b) Modes of spin label motions shown for the ImU -labelled duplex DNA. Experimental (black) and simulated (red) PELDOR time traces with (c) ImU , (d) OxU and with (e) $ExImU$ label. For X-band (left) and Q-band (middle) different offsets ν_n (in MHz) were set between probe and pump pulse frequency. In both magnetic fields, the pump pulse was fixed at the maximum of the nitroxide spectrum. The G-band (right) PELDOR time traces were shown at the three magnetic field positions corresponding to the main g-tensor components. In these experiments the difference between pump and probe frequency was kept constant at $\nu_n = 60$ MHz. Modified from Erlenbach et al. 2016.^[157]

3.4 | Study of an Intercalating Spin Label

This chapter is based on the attached manuscript Heinz *et al.* This work was prepared in a collaborative manner. The contribution of the author was the performing of all experiments and the analysis as well as the calculations of the orientation-selective PELDOR data with help of MD simulations provided by Marcel Heinz und Dr. Lukas Stelzl from the group of Prof. Hummer from the MPI of Biophysics, Frankfurt am Main. The samples were synthesized in the group of Prof. Sigurdsson by Nilesh Kamble from the University of Iceland Science Institute, Reykjavik.

In addition to the relevant rigidity of the spin label, the site specific incorporation of a spin label^[190] to a biomolecule, plays a major role. While spin labelling on proteins is mainly done with the specific reaction of MTSSL with the thiol groups of cysteine amino acids post-synthetically,^[191] the methods of spin labelling for nucleic acids are much more diverse. Particularly in the Sigurdsson lab, but also from others, a broad range of spin labelling strategies were developed in the last years.

From the synthetic point of view, there are three main labelling strategies. For all of them the main challenge is the stability of the radical moiety during incorporation of the spin label. One method is the usage of spin labelled phosphoramidites directly via solid phase synthesis. This approach was first reported by Hopkins and co-workers in 1988.^[192] The spin label TPA^[193] as well as the rigid \mathcal{C} have to be synthesized this way. This method has a few drawbacks, as the synthesis of those phosphoramidites with the spin label requires a significant effort. Also the synthesis conditions for the solid phase synthesise have to be adapted in a way that it is non-reducing. Nevertheless it has also been shown that protection groups can be added at the N-O and after the full synthesis successfully removed, *e.g.*, with light.^[77,194]

Another way is to use modified nucleotides which contain unique reactive functional groups. These phosphoramidites are commercially available, and it is possible to attach the spin label post-synthetically with different possible reactions, for example with click chemistry.^[195,196] This approach is less synthetically demanding, and the spin label is not exposed to the reductive conditions of the solid phase synthesis and purification. Nonetheless incomplete labelling or possible side reactions are still drawbacks for this method. Furthermore care has to be taken that the spin label does not get reduced by the reaction conditions.

The last way is non-covalent site directed spin labelling. On the one hand there are several RNA and DNA motives which have well defined binding pockets and can be involved in ligand receptor interactions. There the small chemical compound

3.4. STUDY OF AN INTERCALATING SPIN LABEL

itself can be spin labelled as done with the malachite green from Sigurdsson and co-workers.^[197] The interaction of the label often takes place through intercalation or groove binding.^[198,199] So far these labels have not been sequence selective, and therefore have a limited usefulness in site-directed spin labelling (SDSL).

In this thesis the $\dot{\mathbf{G}}$ (G-spin) spin label was studied which intercalates in an abasic site in a double-stranded nucleic acid motif, using hydrogen bonds and the $\pi - \pi$ interaction of nucleobases.^[200] Kamble and co-workers were able to show via CW measurements that $\dot{\mathbf{G}}$ intercalates specifically in an abasic site of a nucleic acid duplex with a cytidine as base pairing partner.^[51] The advantage is that one can synthesize the spin label and the strand independently and mix the two afterwards. For RNA duplexes stable $\dot{\mathbf{G}}$ incorporation was established at room temperature, while for the DNA the intercalation takes place by lowering the temperature. First orientation selective PELDOR traces reveal a rigid incorporation of the spin label into the structure. Nevertheless DFT calculations in vacuum, performed by Marcel Heinz, show that a rotation around the tether between the nucleobase analogue part and the isoindoline (fig. 3.4.1 (a) red dihedral angle **d1**) results in two preferred orientations. Whether such a rotation is also possible when the molecule is bound to a nucleic acid was investigated using orientation selective PELDOR measurements and MD simulations. These simulations were also performed by Marcel Heinz.

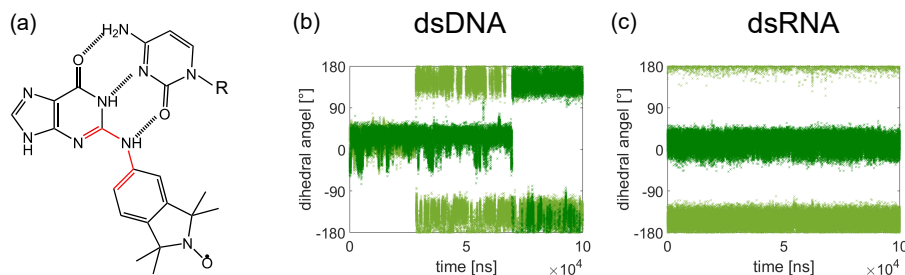


Figure 3.4.1: (a) Structure of the intercalating $\dot{\mathbf{G}}$ spin label base pairing with a cytidine. The dihedral angle **d1** is marked in red. Dihedral angle **d1** between the aromatic purine scaffold and the isoindoline nitroxide plane of the two $\dot{\mathbf{G}}$ s in dsDNA (b) and dsRNA (c) during the molecular dynamic simulations.

In the case of dsDNA the spin label points inside the minor groove, which sterically restricts the rotation around the tether. Nevertheless a 1 μ s simulations shows one $\frac{\pi}{2}/90^\circ$ flip for each spin label. (fig. 3.4.1 (b)) Also the PELDOR measurements with different frequency offsets at the X-Band do not show any orientation-selectivity, while at high field orientation selective effects are observable. This is consistent with the observation of the MD simulations, since in lower fields only the out-of-plane orientation can be resolved, which are no longer selective due to the

rotation. On the other hand, this rotation does not change the orientation of the spin label in the other dimensions. These are additionally resolved in the high field, thus preserving an orientation selection. Quantitative comparison of the MD simulations and PELDOR traces show strong agreement for the X-band as well as for the high field measurements at 180 GHz. The distance distribution shows a comparable width to the distance width obtained from \mathbf{C} measurements on the identical DNA duplex, which makes it a very promising unambiguous label for DNA duplexes for reliable distance measurements at low fields.

In the case of a doubly labelled RNA duplex with the \mathbf{G} things change. The PELDOR traces at both magnetic field show high orientation-selective effects. This already indicates a more rigid incorporation of the spin label in the duplexes. This gets revealed by the MD simulation, where no rotation around the tether was observed as the label is sterically hindered in the deep but narrow major groove. (fig. 3.4.1 (c)) These results give rise to the conclusion that in contrast to \mathbf{G} incorporated in a dsDNA this label paired with dsRNA can be used for accurate orientation-selective PELDOR measurements.

Quantitative simulation of the orientation-selective PELDOR time traces taking the coordinates of the \mathbf{G} from the MD simulation shows a small shift in the distances; however a strong agreement in the overall orientation selective PELDOR pattern was found, as depicted in figure 3.4.2.

The presented work not only enables the direct comparison of PELDOR measurements to MD simulations, it allows also a conclusion of the current state-of-the-art force fields for nucleic acids. Both force fields, ParmBSC1 for DNA and ParmBSC0+ χ_{OL3} for RNA, are able to describe double stranded, helical nucleic acids well. Only some small discrepancies observed between experiment and simulation for dsRNA. The well-established ParmBSC0+ χ_{OL3} force field for RNA seems to describe the dynamics of dsRNA well to completely recapture the PELDOR data. The MD interspin distance distribution is slightly shifted by 1.8 Å towards longer distances and the calculated PELDOR time traces from the MD simulations matches well with the PELDOR data, but still could be improved for an almost perfect match.

3.4. STUDY OF AN INTERCALATING SPIN LABEL

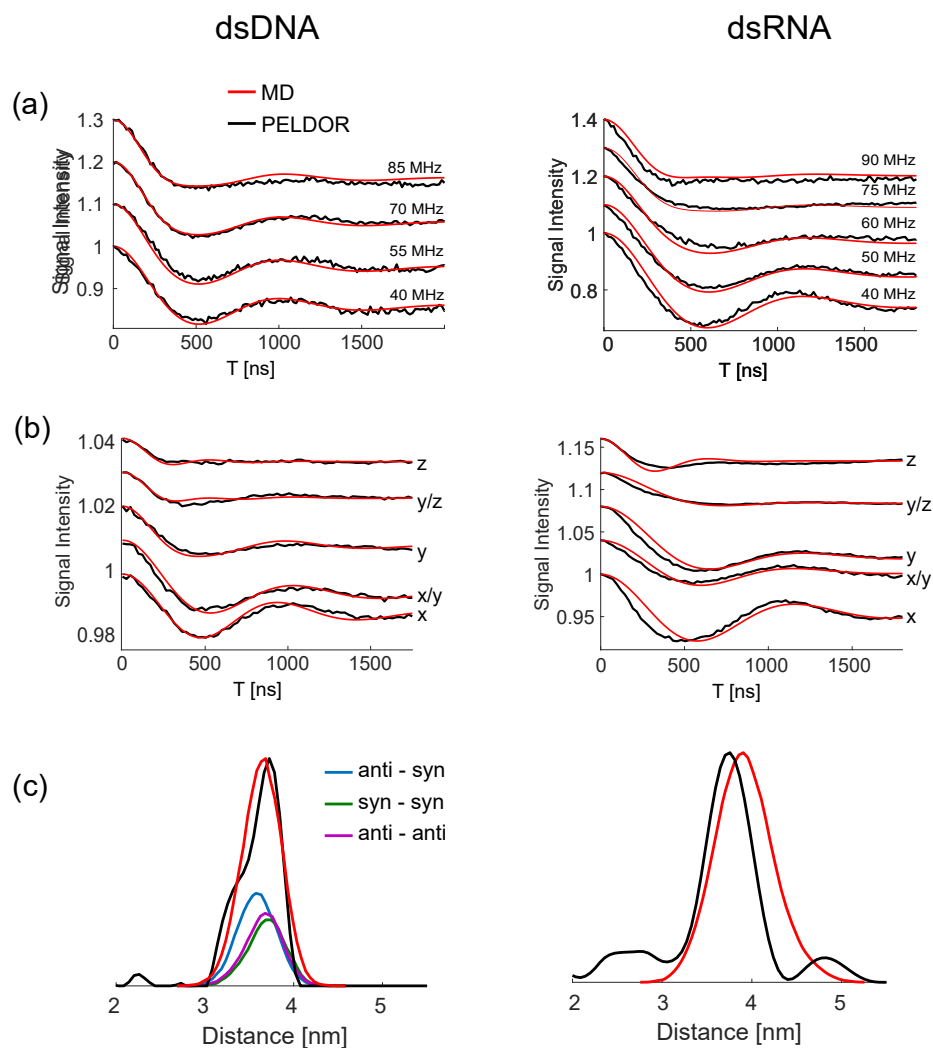


Figure 3.4.2: (a) X-band PELDOR time traces with different offsets ν_n (in MHz) between probe and pump pulse frequency as indicated for dsDNA (left) and dsRNA (right) $\dot{\mathbf{G}}$ labelled. (b) G-band PELDOR time traces at different magnetic field positions corresponding to the main g-tensor components. In these experiments, the difference between pump and probe frequency was kept constant at $\nu_n = 60$ MHz. (c) Distance distribution from the summed X-band PELDOR time traces derived via Tikhonov regularisation. The coloured lines are the distance distribution for different rotational states of the spin label.

3.5 | Orientation-Selective 2D-SIFTER Simulations

This chapter is based on the publication Bowen *et al.* Applied Magnetic Resonance (2018) 49, 1355-1368. The work was prepared in a collaborative manner. The contribution of the author was to further develop a simulation protocol for 2D-broadband SIFTER based on the PELDOR simulation protocol written by Dr. Andriy Marco. Furthermore the author evaluated the simulation procedure for two samples with known geometries and dynamics in comparison to orientation-selective PELDOR measurements. The SIFTER measurements were performed by Dr. Alice Bowen and Dr. Philip van Os (née Schöps).

PELDOR spectroscopy is still the gold standard among all different kinds of PDS techniques to measure interspin distances. It is very robust and widely used for long range distance measurements from 2 to 8 nm. As explained in the theoretical background, another advantage of PELDOR occurs whenever both spin labels have a fixed relative orientation, as anisotropic interactions allow the specific excitation of defined orientation of the label to the external magnetic field B_0 . Therefore only parts of the conformational ensemble contribute to the PELDOR signals. This varies when the pump and/or probe frequencies change and affects the orientation intensity function for each time trace. However, this way to measure the orientation-dependent dipolar coupling is highly time-consuming and the combinations of different pulse positions is limited due to bandwidth limitation in the resonator and to possible pulse overlap.

Next to PELDOR, different single frequency techniques were developed such as DQC,^[57,58,59,60] RIDME^[201,62,63] or SIFTER.^[64,65,66] Nevertheless, they have been less frequently used in the last decades. The reason for this is that the non-selective excitation of the whole resonance spectrum is necessary for these methods. This can be achieved with typical rectangular pulses for trityl- but not for nitroxides based spin labels. As a result, inefficient inversion of spins reduces the sensitivity, decreases the modulation amplitude and furthermore introduces artifacts. Rectangular pulses would need very high microwave field strengths and short pulse lengths. However, by modulating the amplitude or phase of the pulse, the excitation bandwidth can be increased, which was not possible in EPR due to hardware limitation. As faster AWGs were developed in the last years, such single frequency methods have become feasible for EPR.

This allows, *e.g.*, the measurements of artifact-free SIFTER traces with high modulation depth and high sensitivity.^[64] SIFTER is a single frequency technique, which is based on a solid echo and the Jeener-Broekaert sequence.^[202] The pulse

3.5. ORIENTATION-SELECTIVE 2D-SIFTER SIMULATIONS

sequence of SIFTER is shown in figure 3.5.1. The time steps are measured as function of $\tau_1 - \tau_2$ while the sum of both time offsets is kept constant. As SIFTER is also a PDS technique, the time trace retains the same dipolar coupling as PELDOR time traces.

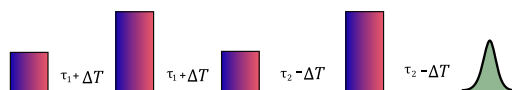


Figure 3.5.1: *SIFTER pulse sequence*

In an echo-based pulse technique, the integration of an echo will often be recorded against the time delay. Subsequently, in the one-dimensional form, by integrating over the echo signal, all anisotropic information gets averaged. Though, Dr. Philip van Os (née Schöps) was able to show that the Fourier transform of the transient echo, derived from a non-selective broadband pulse and simultaneously exciting all orientations, recovers the full EPR spectra of the nitroxide.^[64] Owing to this, recording the transient echo instead of the integrated area at different time point and Fourier transform this echo, achieves a single two-dimensional experiment in which the full spectrally resolved dipolar time traces can be detected simultaneously.^[67] Such time traces encode, in the case of two correlated spin label orientations, an amount of similar orientation content similar to multiple orientation-selective PELDOR time traces, but with less laborious and time-consuming effort.

The differences between orientation-selective PELDOR and 2D-SIFTER occur for two different reasons. SIFTER relies only on the detection selection of the inhomogeneous linewidth as the broadband (pump) pulse excites all orientation present. This makes it impossible to measure the relative orientations of the two spin labels to each other and reduces the number of observable parameter to five. At X-band a typical PELDOR pump pulse at the maximum of the spectrum is hyperfine transition selective ($m = 0$); however it excites almost all orientations simultaneously. Therefore it is a comparable situation to a 2D-SIFTER experiment. In contrast to this, at higher fields PELDOR has a pump- and detection-selection, as both pulses excite only part of the orientations present in the sample, enabling the study of the relative orientations of the two labels.

The second difference occur due to different pulse excitations. The excited fraction for SIFTER as well as the comparison with a standard detection pulse in PELDOR measurements is shown in figure 3.5.2. Therefore the simulations process has to be adjusted and revealed with known models against orientation-selective PELDOR. Fourier transformed 2D-SIFTER traces of a bis-nitroxide model system and with

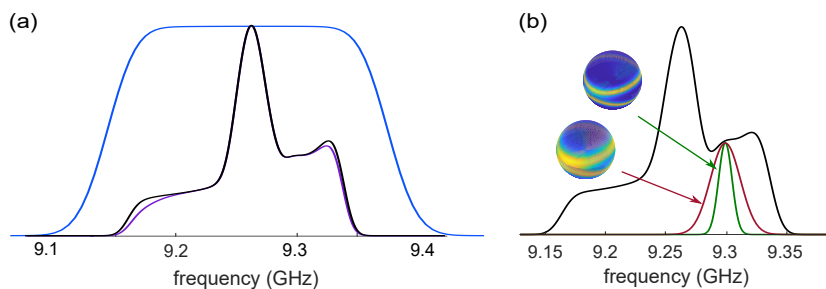


Figure 3.5.2: (a) Excitation profile of a 200 ns WURST pulse (blue) in comparison to a nitroxide spectrum in black. The excited fraction given is shown in violet. (b) Comparison of the excitation of a simulated 32ns rectangular pump pulse with 25 MHz offset (red) and the inhomogeneous linewidth in SIFTER with 20 MHz (green). The spheres represent the excited orientations.

a \mathcal{C} double labelled small 20mer dsDNA, recorded by Dr. Alice Bowen and Dr. Philip van Os (née Schöps), were used to validate the simulations procedure. For both datasets, additional orientation-selective PELDOR traces already existed. For the analytical simulations of the PELDOR and SIFTER dipolar time traces, the relative orientation of the nitroxide moieties as well as their distance distribution are required. A conical model simulating the allowed rotation of the nitroxide moieties and the bending of the linker unit was used to derive the conformational ensemble of the model system. For the doubly labelled dsDNA structures, a MD simulation was used.^[158] The 200 ns long MD trajectory, provided by Dr. Lukas Stelzl, gives rise to an ensemble of 2000 structures, without explicitly simulating the spin label. However, as the \mathcal{C} is totally rigid, the inter spin distance and the orientation of both spin label could be extrapolated for a quantitative simulation of the PELDOR and SIFTER time traces. More details are described in section 3.6.

When using the analytical protocol described in section 2.5.2 the pump pulse efficiency for non-selective WURST-based broadband excitation was modelled according to Kupce *et al.*^[203] In figure 3.5.2 (a) the excitation profile is shown, and the excited fraction of the nitroxide spectrum is depicted in violet. The 'detection pulse bandwidth' was selected to correspond to the inhomogeneous linewidth of the spectrum, which was 20 MHz. This was determined from fitting the the nitroxide spectrum found by Fourier transform of the solid echo and validated by fitting the the field-sweep spectrum. This inherent linewidth is smaller than the bandwidth of the 32 ns detection pulses (25 MHz) commonly used in PELDOR, as seen in figure 3.5.2 (b). As a smaller fraction of orientation gets excited, it ends up with a more pronounced orientation dependence.

Using this simulation method with the pulse parameters derived above and the

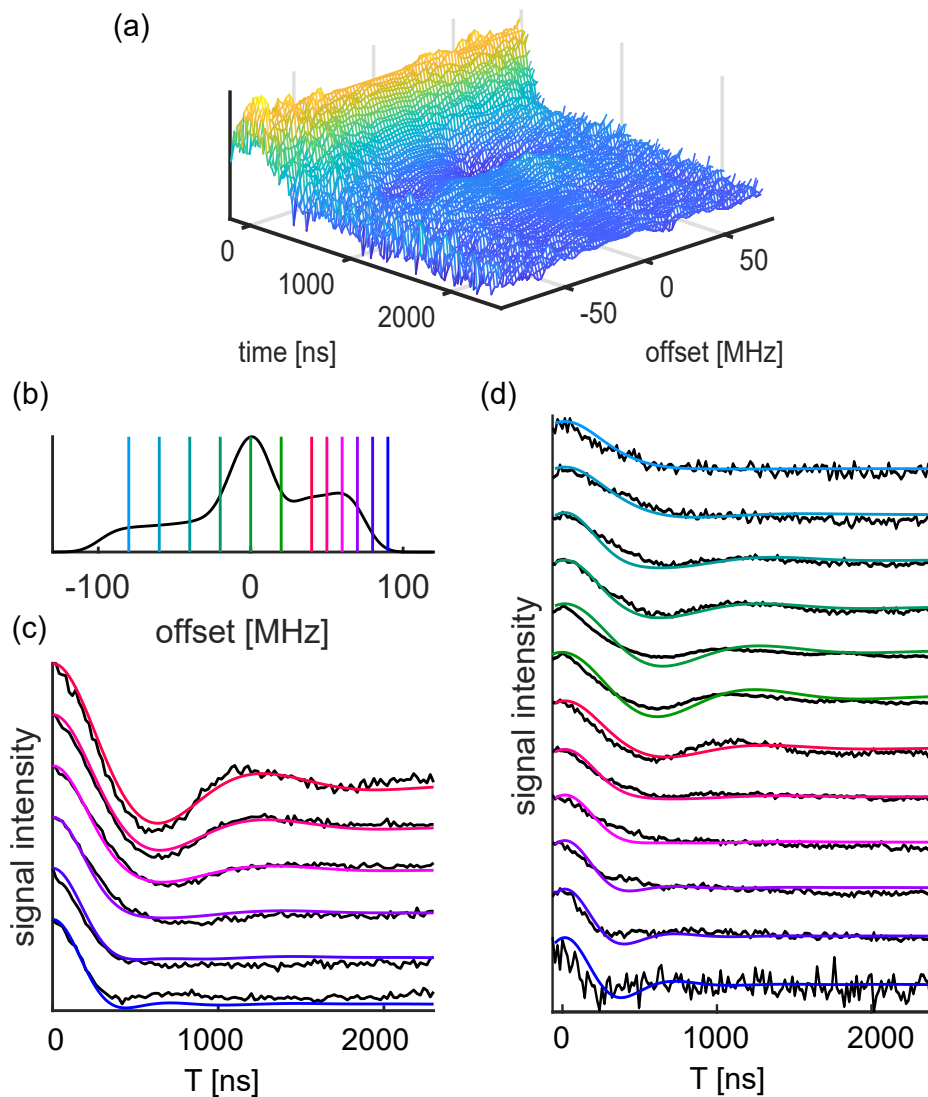


Figure 3.5.3: Results for the DNA duplex double labelled with the C label. (a) Normalised frequency correlated SIFTER dataset presented in the time domain of the dipolar dimension; time is $\tau_1 - \tau_2$. (b) Echo detected field sweep presented in the frequency domain relative to the spectral maxima. The coloured lines show the detection positions offsets for the PELDOR data presented in (c) and the frequency slice of the frequency correlated SIFTER data presented in (d). (c) PELDOR time traces, experimental data (black lines) with corresponding simulations from molecular dynamics (MD)(coloured lines) (d) Slices from the frequency correlated SIFTER experiment (black lines) with corresponding simulations (coloured lines). Modified from Bowen et al.^[160]

models calibrated by the PELDOR data it was possible to simulate the 2D-SIFTER data successfully. They show strong agreement with the experimental data presented in figure 3.5.3 for the DNA. There, for a direct comparison, the related PELDOR traces were also shown, these traces have the same frequency differences to the maximum of the nitroxide spectrum (blue to red traces). Additional traces, which were either not accessible with PELDOR due to overlap of both pulses (-30 to 30 MHz offset, green traces) or had a low efficiency (-30 MHz offset, light blue traces) were additionally shown for SIFTER.

In conclusion, 2D-SIFTER is an effective way to measure dipolar coupling of two nitroxide moieties with a fixed relative orientation. These data can be analysed in an equally effective analytic manner, as done for orientation-selective PELDOR traces in our laboratory in the recent years.^[44,45,167] However, several aspects must be considered, before this method can replace orientation-selective PELDOR. The optimisation for the broadband pulses has to be done carefully and is the most crucial step to avoid unwanted features in the recorded echo. This optimisation takes time. Additionally the net measurement time reduction might be also less effective, as recording of the transient echo is much more time-consuming than measuring the integrated area, at least with Bruker software. Additionally a SIFTER sequence with around 200 ns long broadband pulses is considerably longer, which has an effect on the signal-to-noise ratio. As a result the signal-to-noise is much lower in comparison to PELDOR, especially at the edge of a nitroxide spectrum. From a spectroscopic point, the most interesting orientation content collected from a X-Band spectrometer is encoded in the difference between a 40 MHz trace (x- and y-axes orientation) to 90 MHz trace (z-axes) at the edge of the spectrum. Therefore at least an additional PELDOR traces recorded at this edge might be necessary in order to fully resolve the orientation dependence. Another point to be considered is that modulated pulses, that are broad enough to excite the whole nitroxide spectrum are only feasible for low field measurements, up to 33 GHz. For measurements at high field, orientation-selective PELDOR is still the method of choice.

3.6 | Conformational Dynamics of DNA by PELDOR and MD

This chapter is based on the publication Stelzl *et al.* Journal of the American Society (2017) 30, 129. The work was prepared in a collaborative manner. The contribution of the author was the simulation of the orientation-selective PELDOR time traces using the MD simulations performed by Dr. Lukas Stelzl from the group of Prof. Hummer from the MPI of Biophysics, Frankfurt am Main. The measurements were already published.^[45]

One central aspect of this thesis is related to the quantitative comparisons between orientation-selective PDS measurements and MD simulations on nucleic acids. As already mentioned in section 3.6, MD simulation of nucleic acids lacked of accuracy for a long time, *e.g.*, the dihedral angles of the backbone and between the sugar and the nucleobase had to be adjusted several times. From the traditional computational point, force field development is done based on NMR and crystallography data. Classical crystallography encodes static structures, and also NMR provides only bundles of average structures. Therefore comparison with these more static structures reports over the stability of MD trajectories over time. Hence, evaluation against experimental ensemble methods, like SAXS and PELDOR could be beneficial for evaluation of different force fields, not only check for artifacts but also to evaluate dynamical properties.

When working with MD simulations one has to overcome several challenges for quantitative comparisons with PDS time traces. In the last decades MD simulations were limited by the sampling problem, as exhaustive sampling of the conformational space of even relatively small molecules (as nitroxide spin labels) couldn't be achieved due to the appearance of artefact, especially for nucleic acids. The accuracy of the MD simulations, which is related to the quality of the available force fields, constitutes another issue. As a consequence the first comparisons between PELDOR measurements and MD simulations were mainly made in a qualitative way by comparing only the distances and the distribution. However, this could be problematic even from the experimental side as depending on the experimental quality the distance distribution, derived by Tikhonov regularisation, is an ill-posed problem, where uncertainties could arise.

In the years around 2007 several studies were done for model systems,^[204] proteins^[205,206,207] and nucleic acids,^[75,193] correlating PELDOR distances with MD simulations performed with the AMBER 98 and CHARMM19 force fields. For all these simulations the mean distance was usually in a good agreement with the PELDOR distances, while the distribution, whenever compared, was more prob-

lematic. More comprehensive, MD simulations were used for the analysis of the MTSSL spin label on proteins. Although this spin label can be easily attached to a broad range of proteins, it shows high flexibility. Hence, for separating the effects of the protein and the spin label on the distance distribution MD simulations of the spin labels were performed. The first simulations were done by Robinson in 1992 using Brownian dynamics trajectories and by Steinhoff *et al.* 1996 for a poly-leucine trimer.^[208,209] Several groups followed using more and more advanced trajectories.^[183,210,211,212,213,214,215] However not only was the MTSSL spin label studied with the help of MDs, but the Rx spin label was also studied in such a way.^[216] Here a first quantitative comparison of simulated orientation selective PELDOR traces and MD simulations were shown, however with moderate success. Furthermore MD simulations can also be used for computational biology, *e.g.*, the Rosetta software suite includes algorithms for MD based computational modelling and analysis of protein structures which is also usable with PELDOR restraints.^[217,218,219]

The most recent work on nucleic acids, was done in the Benatti laboratory, where work has been done *ab initio* calculations of the conformation of a new restricted spin label and where qualitative comparisons studies of duplex behaviour have been performed with MD.

MD simulations with different force fields were performed in the Hummer group by Lukas Stelzl for two DNA sequences. Ten different orientation-selective PELDOR sets for these short 20mer double-stranded DNAs were measured previously.^[44,45] The spin labelling positions were varied by leaving the first spin label at the third position of one strand (this position is called '1st') and placing the second spin label at various locations from the 8th to the 18th position (called '5th' to '15th'). These data were previously used for first studies of orientation-selective PELDOR traces and to interpret the DNA in terms of backbone dynamics. Comparisons of the above mentioned MD simulations with these orientation-selective PELDOR datasets clearly distinguish between the older (BSC0) and the newer DNA force fields (OL15 and BSC1). Qualitative comparisons of distances from experiments with PELDOR traces calculated by MD simulation using the BSC0 force field show deviation, while both recent force fields gives equally strong agreement. Nevertheless the concurrence between these simulated results and the experimental data changes with varying spin label position, which may be explained by interaction of the spin label with the DNA or influence of a nearby position of the spin label, as the most obvious differences are found for the samples with the lowest distance between spin labels. An additional comparison can be made for the experimentally determined angle β of the spin labels relative to the spin-spin vector. This angle is also well described by the simulations. All these agreements

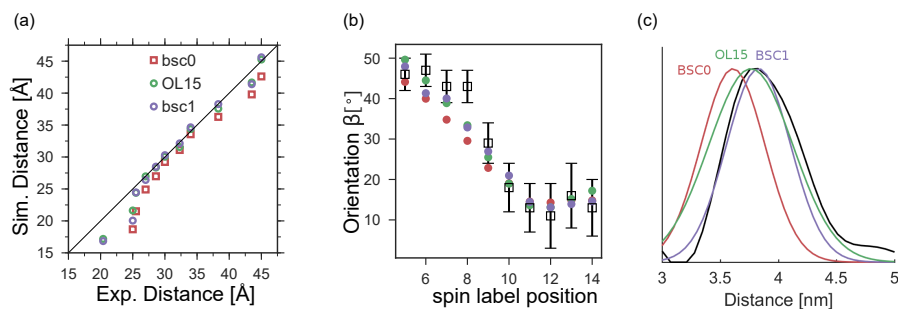


Figure 3.6.1: Comparison between orientation-selective PELDOR experiments (black) and MD simulations (a) PELDOR experiments with eleven spin-label pairs and compared distances from experiments and MD (b) Spin-label orientations from MD and PELDOR. The angle β describes the orientation between the vectors normal of the spin-label plane and the dipole-dipole vector. (c) Spin-spin distance distributions for DNA(1,13) from Tikhonov regularization of PELDOR time traces and MD. Modified from Stelzl et al.^[158]

are depicted in figure 3.6.1.

The way to gain the most honest quantitative comparison between MD simulations and PELDOR time traces is to calculate the experimental traces directly from the distances and spin label orientations achieved from the structural ensemble calculated by the MD simulations. As already mention, gaining a distance distribution is an ill-posed problem, while simulations from known distributions are parameter free. This is even more true for orientation-selective PELDOR, as the model free extraction of orientations can only be archived by different fitting algorithms^[45,153] but is not unique, depending on the orientation and on the orientation distribution.

Therefore PELDOR traces were calculated using 2000 structures from a 200 ns long MD simulation. The spin label positions were extrapolated using the DFT structure and fitting this structure on the nucleobases. An overall strong agreement was also found for direct comparison of X-band data as shown for the different samples in figure 3.6.2. Some additional comparisons with high field G-band measurements show an equally strong agreement, meaning that the additional angles, which could be derived at higher fields, were also well sampled in the MD simulations. With this agreement one can now interpret the MD simulations with the new force fields in more detail. As an example a principal component analysis (PCA) gives rise to all dynamical modes presents in the MD trajectories weighted by the related mean squared displacement. Backbone dynamics were previously discussed in literature. Rotor bead tracking experiments give rise to a twisting of the backbone with a constant helix pitch and changing radius.^[220] The findings from SAXS data with gold crystals at both sides of the strands yielded the opposite

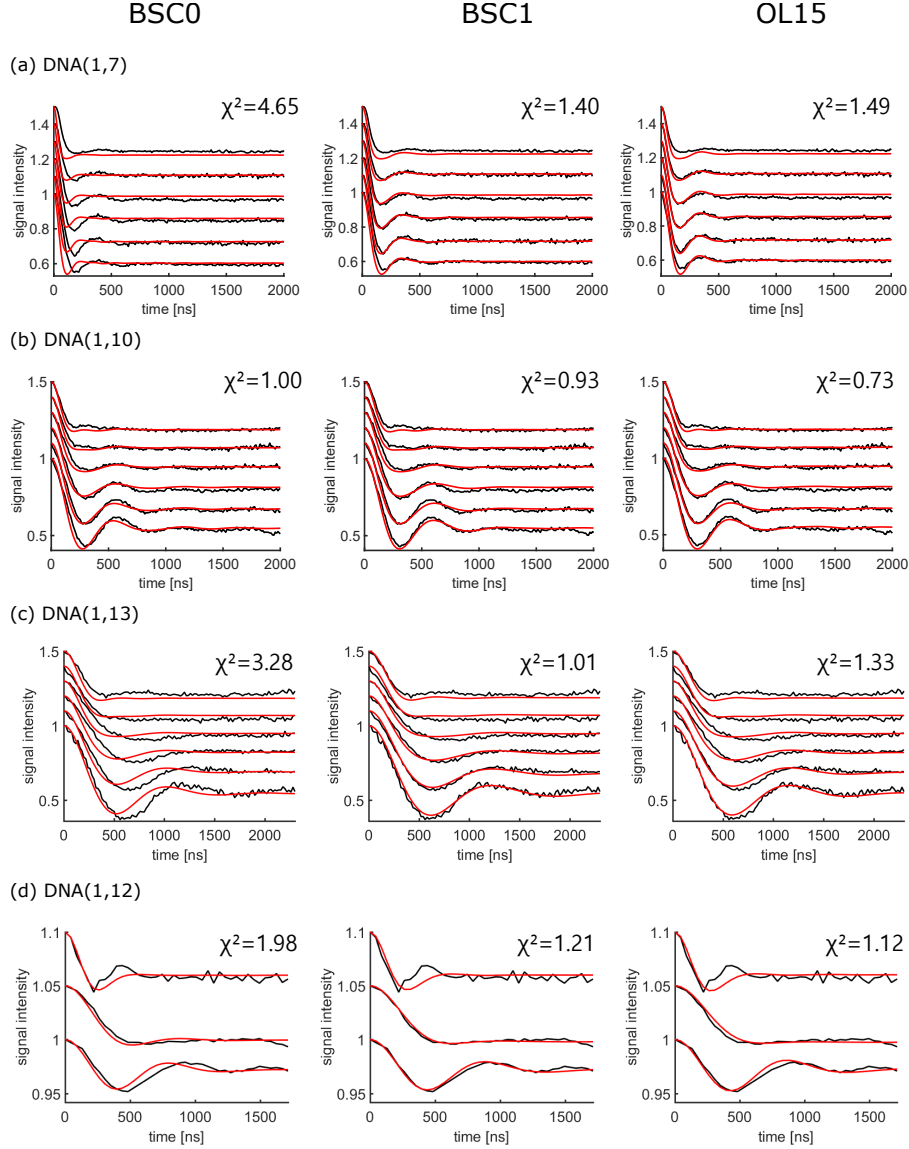


Figure 3.6.2: (a)-(c) Comparison between X-band PELDOR signals calculated from MD simulations (red) and collected experimentally (black). The PELDOR time traces were measured with different offsets ν_n between probe and pump pulse frequency from 40 MHz (lower) to 90 MHz (upper time trace). (d) Comparison between G-band PELDOR signals calculated from MD simulations (red) and collected experimentally (black). The PELDOR time traces were measured at different field position, corresponding to $B \parallel g_{xx}$, $B \parallel g_{yy}$ and $B \parallel g_{zz}$ positions (top to bottom). Simulations with the BSC0, BSC1 and OL15 force fields are shown in the left, center and right panels, respectively. Each panel lists the χ^2 deviations averaged over the three traces. Modified from Stelzl et al.^[158]

results. These data were interpreted as a stretching with a change in the helical pitch with constant helical radius or by a bending mode.^[221] An interpretation with a vectorial model of the orientation-selective PELDOR traces emphasises the twisting mode. This mode was also found previously MD simulations; however, these simulations were restricted to motion along the helical axes.^[222] Therefore, the most prominent mode, found in the present MD simulations, where hindered. The two most important motions, according to the principal component analysis, were bending modes, which have also been found in very long MD simulations. The third most important mode is a twisting motion.

Table 3.1: *The dynamics of DNA from MD simulations and the analysis of PELDOR experiments. Marko et al.^[45] analysed PELDOR experiments in terms of changes in helical pitch (model A), helical radius (model B) and bending (model C). Helical pitch, helical radius and bending were extracted from a 200 ns trajectory (with the BSC1 force field).*

	Marko et al. ^[45]	MD
Helical pitch	$33 \pm 3.68 \text{ \AA}$ (A)	$33 \pm 1 \text{ \AA}$
Helical radius	$5.85 \pm 0.65 \text{ \AA}$ (B)	$6.3 \pm 0.3 \text{ \AA}$
Helical bending	28° (C)	$\approx 23^\circ$

With this work, light was shed on the differences between different force fields, and one can conclude that the recent force field developments in Barcelona and Olomuc both can describe the orientation selective PELDOR traces with high accuracy. This enables to interpret MD simulation of small nucleic acids motifs. Moreover MD simulation of systems of increasing size may be possible; nonetheless, this still should be confirmed with experimental data.

3.7 | Analysis of Room Temperature PELDOR Measurements

This chapter is based on the publication Gränz *et al.* *Angewandte Chemie* (2018) 57, 10540–10543. The work was prepared in a collaborative manner. The contribution of the author was the analysis of the data. The sample preparation was done by Markus Kallis (née Gränz), and the PELDOR measurements were performed by Dr. Philip Spindler. The samples were synthesized in the group of Prof. Sigurdsson by Dr. Gophane from the University of Iceland Science Institute, Reykjavik.

PELDOR spectroscopy yields information about structure, conformational changes and flexibility. However one has to deal with the major drawback that all samples must be frozen prior to measurements. For this reason the considerations must be made for all results as they agree with the situation at room temperature. Usually there are several reasons for an agreement; nevertheless the comparison done by Krstic *et al.* between room temperature CW measurements and cold temperature PELDOR time traces of the neomycin aptamer demonstrated certain changes in flexibility.^[173] Therefore several attempts were done in the recent years to do PDS measurements at ambient temperatures.

There are two main reasons why the commonly used temperature for PDS is beneath 60 K. First of all, the phase memory time T_2 limits the maximum PDS trace length. Traditional nitroxides show a tremendous decrease in this relaxation time when the temperature rises above 65 – 80 K due to the gem-dimethyl groups flanking the N-O radical moiety. These methyl groups provide kinetic stability but start to rotate above a certain temperature which averages nonequivalent couplings of the unpaired electron to the protons.^[223] One can overcome this issue by substituting the methyl groups with spirocyclohexyl groups, which can increase the phase memory time at 150 K more than four fold, as showed by the Eaton group.^[224] Nevertheless, at ambient temperature gem-spiroxyl-based spin labels also have rather short T_2 -times, as these substituents start to show increased dynamics. As a consequence the effect of these substitutions is negligible at room temperature. It should be noted that spin labels based on gem-spiroxyl nitroxides are relatively hydrophobic, which makes site-directed spin labelling of biomolecules difficult. Nevertheless, a doubly labelled t4 lysozyme with gem-spiroxyl nitroxide labels was also measured at room temperature with a total trace length of at least 1.4 μ s.^[225]

Another way to prolong the phase memory time is to replace at least one spin label with a trityl-label. These labels were widely used in oxymetry and EPR

3.7. ANALYSIS OF ROOM TEMPERATURE PELDOR MEASUREMENTS

imaging.^[226] In the last years the Bagryanskaya lab studied these labels due to their T_2 -time and conformational influences.^[227,228] The phase memory time at room temperature for these labels is in the order of microseconds, which make them promising candidates for PDS at higher temperatures. However several drawbacks limit their usability, as the synthesis is time demanding and for nucleic acids, only the attachment at the end of the oligonucleotides were possible yet. Moreover, their bulky structure, which is at the same size than a Alexa fluorophore commonly used for FRET measurements, as well as their high hydrophobicity may influence the stability of native structures of biomolecules.

The second issue one has to overcome for measuring at room temperature is due to the fact that rotational diffusion of the sample leads to averaging of the anisotropic dipolar coupling. As this is the interaction of interest for PDS measurements, one has to slow this rotation. This requirement is automatically satisfied at cryogenic temperatures. At 295 K, this can happen naturally, for example in RNA-protein complexes or by the usage of the natural rotational restriction found in membrane proteins.^[229] For small biological model systems or natural motifs one needs an immobilisation approaches that does not influence the conformation of the molecule. Some biomolecules can be attached on a solid support, as it was done for the T4 lysozyme.^[225] As this is a covalent attachment, it could introduce structural perturbation. Another approach uses dehydrated disaccharides such as there is trehalose, glucose and sucrose.^[225,230,231] In particular trehalose is able to mimic the presence of water and used for studies on the photosynthetic system^[232] as well as for the storage of proteins.^[233] Slow drying preserves the natural states of proteins; their functions are fully restored after rehydration.^[234] DsDNA in glassy trehalose tends to denaturate, this must be avoided by careful sample preparation.^[230] Another approach for nucleic acids is to use the electrostatic interaction of the anionic phosphate groups of a nucleic acids with the cationic charge of NucleosilDMA, which holds the DNA on the particle's surface.^[70] This is a known interaction, typically used for ion exchange chromatography.

All published room temperature PDS traces, both for a small double stranded DNA and for the T4 lysozyme, show that the measured distance distribution at ambient temperature reproduces the cryogenic measurements. However the sensitivity is much lower at room temperature, and all measurements were performed with either TAM- or spiroxyl-based spin labels having a long, flexible tether. Therefore it might be interesting to measure more defined model systems with the advantage of orientation selection, in order to study possible differences between measurements at the two temperatures.

Room temperature measurements with double labelled dsDNA labelled with \mathcal{C} were successfully performed by Dr. Philip Spindler under orientation-selective

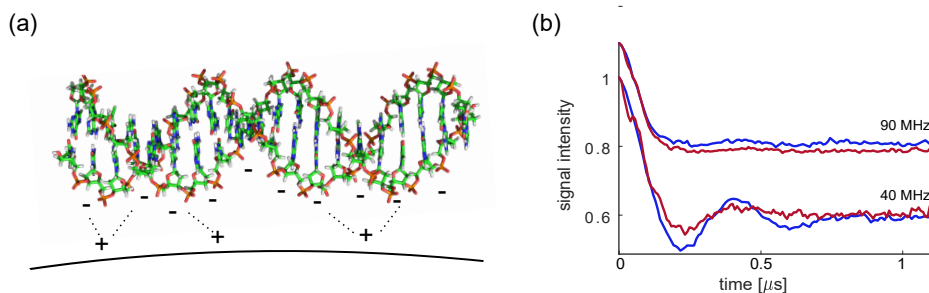


Figure 3.7.1: (a) Molecular model of the dsDNA molecule with an electrostatic interaction with the silica beads (Nucleosil surface). (b) PELDOR time traces at 50 K of dsDNA in a 20 % glycerol/water mix (blue) and attached on Nucleosil surface (red). Traces were recorded with 40 MHz (lower trace) and 90 MHz (upper trace) frequency offsets between pump and probe pulse. The pump pulse was set to the maximum of the nitroxide spectrum. Modified from Gränz et al.^[159]

conditions with two different frequency offsets. The sample preparation, done by Markus Kallis (née Gränz), uses the electrostatic interaction with a Nucleosil surface, shown in figure 3.7.1. Calculations using the expected cation density reveal an interaction at around three point per molecule. This is expected to be enough to fully inhibit free rotation, while it should not disturb the conformational space excessively. However, cryogenic PELDOR measurements with and without absorption on the Nucleosil show differences, which can be seen in figure 3.7.1, presumably as a consequence of this electrostatic interaction.

The PELDOR comparison between cryogenic and physiological temperature measurements of the dsDNA immobilized on Nucleosil shows clear differences in the damping of the signal. Using the MD trajectories described in the section 3.6, simulations can reproduce the changes. The situation for the samples at frozen solution is well known. The derived signal is a superposition of all conformations present in the sample. Due to this, one can extract beside to the mean structure, the distribution and with it the flexibility of the molecule at the glass temperature. PDS in frozen solution is therefore called an ensemble method. Moreover the molecules do not change their conformation during the measurements. This is not the case at higher temperatures. Although the molecule is electrostatically immobilised on a solid support, this 'soft' fixation still allows dynamics of the molecule. As a consequence the Larmor frequency of the spins is modulated the spins' evolution time and the observed PELDOR time trace is affected. This can lead to three different outcomes, depending on the correlation times of the dynamics present in the sample. For dynamics whose correlation time is orders of magnitude slower than the dipolar coupling frequency, no influence due to the dynamic is expected to occur in the time traces. Whenever the time ranges over-

3.7. ANALYSIS OF ROOM TEMPERATURE PELDOR MEASUREMENTS

lap, unusual behaviour might appear, which might be challenging to interpret. The third situation appears when the dynamics are orders of magnitude slower than the dipolar frequency dynamics. In this situation no change between the two measurements will appear.

In the present sample the correlation times extracted from the MD simulations, are considerably shorter than a nanosecond, so the effect of dynamic averaging of fast internal motions occurs. As a consequence, the resulting dipolar interaction is a conformational average. From the mathematical point of view, simulation has to be done as an integral of the delay time of the pulse

$$S(T) = \langle 1 + \int_0^{\pi/2} \lambda(\Theta(T)) (\cos(\int_0^T \omega_{dd}(t) dt) - 1) \sin\Theta d\Theta \rangle_N \quad (3.4)$$

Using the MD trajectory, with different starting points mimicking different molecules present in the sample and essentially using equation 3.4 one can directly compare the measured and simulated traces. Nevertheless one has to be aware that the MD simulations were done without the nucleosil, which leads only to a qualitative comparisons, those these comparisons show strong agreement.

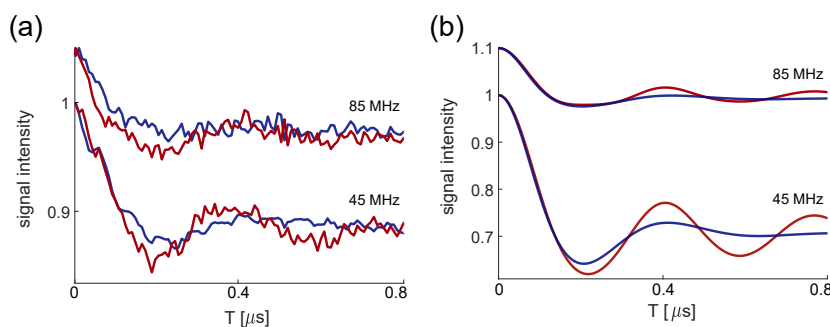


Figure 3.7.2: (a) *Experimental PELDOR time traces at 50 K (blue) and at RT (red) of the dsDNA adsorbed on Nucleosil. The traces were recorded with 45 MHz (lower traces) and 85 MHz (upper traces) offset between pump and probe pulses. The probe pulse was set to the maximum of the nitroxide spectrum to achieve higher signal to noise (S/N).* (b) *Calculated PELDOR time traces from MD trajectories as a conformational ensemble (blue) and with a dynamical average (red). The traces were calculated with 45 MHz (lower traces) and 85 MHz (upper traces) offset between pump and probe pulses. The probe pulse was set to the maximum of the nitroxide spectrum. Modified from Gränz et al. [159]*

CHAPTER 4

Summary and Outlook

The main focus of this thesis was to combine experimental PDS measurements with theoretical MD simulations to overcome disadvantages and limitations which occur when using each methods in a stand-alone way. With this two methods combined a dynamical description of nucleic acids duplexes and their spin label was reached.

Motivated by the challenge to gain a unique and detailed interpretation of 10 sets of highly sensitive orientation selective PELDOR time traces of a 20mer double stranded DNA, MD simulations were performed in the group of Prof. Hummer. However, a evaluation of the different force fields was first necessary, as the established force fields were known to a have lack of accuracy for nucleic acids. Quantitative comparisons using the established simulation protocol^[151] and structures from the MD simulation were able to rank the quality of force fields and showed that the recently developed BSC1 and OL5 force field parameters deliver an adequate description of the DNA ensembles for small duplexes. This agreement strengthens confidence in interpretation of the MD simulations in a more detailed biological sense. It was found in contrary to previous work,^[45] that the principle dynamic of the dsDNA background is comprised of a bending mode and the proposed twisting mode. Twisting means a change in the helical radius without a change in the helical pitch. In addition to the possibility of obtaining new biological knowledge about dynamics and flexibilities, the agreement of the dsDNA simulations with PELDOR data enables us to use the MDs to interpret and elucidate new measurements done by other group members to further develop the usage of dipolar-based spectroscopy.

One example is 2D-Sifter measurements performed by Dr. Alice Bowen and Dr. Philip van Os (née Schöps). They have mostly the same information content as a set of orientation-selective PELDOR data. The usage of this new pulse sequence was possible due to new hardware developments, in this case the faster AWG. Broadband pulses lead to time traces without interfering artifacts caused by inefficient excitation of spin packages. Both the PELDOR and the SIFTER methods measure the dipolar coupling of two electron spins; however as the excitation of the spins differ between the two experiments, the simulation protocol has to be adjusted for each method. This procedure was evaluated by the previ-

ously mentioned MD simulations. Combinations of new orientation-selective PDS techniques like SIFTER with orientation-selective PELDOR increase the effective information content.

In addition to new pulse sequences, one goal in the last years has been to perform PDS measurements at higher temperatures. Markus Kallis (née Gränz) succeeded in overcoming the decrease in relaxation time at higher temperatures by using the rigid \mathbf{C} -label and electrostatically bound the dsDNA on a nucleosil to prevent a dipolar average due to fast rotation. Nevertheless measurements, performed by Dr. Philip Spindler, of the same sample show significant differences when measured at two different temperatures, at 50 K and at room temperature. For the interpretation reached in this thesis, simulations with MD trajectories were used to prove the assumption of a dynamic time average at higher temperatures. At cryogenic temperatures, a PDS signal is a superposition of all structural conformations existing in the sample. The result is an ensemble measurement, allowing interpretation of flexibilities. However as the structures are frozen, PDS could only provide flexibilities. At room temperature, in contrast, the present dynamics of the molecule modulate the Larmor frequency during the measurements and therefore affect the resulting time trace. Couplings modulated by the dynamics faster than their coupling strength are averaged out. However, these measurements could yield a first look into the time-scale of the dynamics. A interesting goal for the next years would be the development of room temperature measurements with more native immobilisation techniques. Protein-RNA complexes could provide an interesting platform for natural immobilization. Additionally samples with dynamics on different time-scale could be very interesting to further elaborate the effect of dynamical averaging at room temperature.

Another crucial step for orientation-selective PDS measurements is the need of nucleic acid samples with rigid spin labels. As the most commonly used spin label \mathbf{C} is synthetically very demanding, the Sigurdsson group developed different semi-rigid and intercalating spin labels for further nucleic acid studies. In this thesis the flexibilities of ^{IM}U , ^{OX}U and ^{EXIM}U were studied, using a three-dimensional model of a helix with additional rotational flexibilities for the isoindoline derivative spin labels. We were able to show, that ^{IM}U is less flexible than the other two labels, due to its ability of forming a hydrogen bond to the nucleobase. Another label was $\hat{\mathbf{G}}$, which could intercalate into abasic sites, base pairing with an adenine. This spin label was studied again with help of MD simulations, provided by Marcel Heinz, and showed strong agreement with the orientation-selective PELDOR traces recorded at low (9 GHz) and high field (180 GHz). The label react differently for each nucleic acids. In DNA, the label does not show orientation selection at low fields but a rather narrow distance distribution. This allows very

precise studies of nucleic acids when only distances are of interest. For the RNA the label shows highly orientation-selective PELDOR traces, due to the sterically inhibited rotation around the N-O bond of the nitroxide. Both are in qualitative and quantitative agreement with the MD simulations.

A next step would be to reconsider the first projects on the dynamics for dsDNA also for dsRNA. The comparison of MD simulation to a set of PDS measurements might reveal MD force fields for RNA. This is expected to be more difficult, as it is known that force fields for RNA are less stable and adequate than dynamic descriptions of DNA. A first comparison showed differences for the OL3, however a stronger agreement with the DES RES force field. As no full set of samples with a systematic variation of the position of one spin label along the sequence for RNA was available, this should be evaluated more carefully with more samples in the near future.

One main problem in working towards this description of RNA, has been the tendency of small dsRNA to form rod-like structures, due to $\pi - \pi$ interactions between base pairs at the end of strands. This intermolecular interaction causes multi-spin effects in the dipolar traces and results in multiple distance peaks. Therefore accurate interpretations of the orientation-selective PELDOR data are infeasible. This 'end-to-end' stacking was studied with singly labelled dsRNA in more detail, as such samples have the advantage of only showing intermolecular interactions. Bulky ends at the end of the strands, in this case added nucleobases, inhibit this interaction. Moreover an increasing stacking possibility was found for an increased amount of monovalent salt concentration.

In the future orientation-selective PDS can be used to address several different questions about nucleic acids. From the biological perspective, the $\dot{\mathbf{G}}$ label makes it more feasible to study more complex systems that would be synthetically challenging to synthesize with an covalently bound spin label. Instead having an abasic site inside a double stranded motif takes much less effort. This increases the applicability of these methods to nucleic acids with increased sizes.

In summary, this work deals with different aspects of method development within pulsed dipolar spectroscopy. Flexibility studies have been performed with different spin labels, new simulation procedures were explored for new pulse sequences and the differences between the measurements at 50 K and at room temperature were investigated by means of simulations. The focus here is on the interaction between very precise orientation-selective PDS measurements and MD simulations with new force fields. On the one hand different force fields were evaluated with the help of the measurements. On the other hand, MD simulations of good quality can help in the understanding of PDS measurements in detail, which is often difficult and ambiguous without additional knowledge about the biochemical system.

CHAPTER 5

Deutsche Zusammenfassung

Die Lebensfunktion der Zelle, dem elementaren Baustein des Menschen, beruht auf der Funktion und Wechselwirkung von verschiedenen biologischen Makromolekülen, zu denen die Nukleinsäuren DNA (2'-Desoxyribonukleinsäure) und RNA (Ribonukleinsäure) sowie die Proteine gehören. Lange Zeit lag der Fokus der biochemischen Forschungen auf den Proteinen, da sie einen Großteil der funktionalen Biomoleküle abbildet. Neuere Forschungen zeigen aber die Wichtigkeit von Nukleinsäuren, insbesondere von RNA-Bausteinen, welche vor allem regulatorische Funktionen besitzen. Die Funktionsweise dieser RNAs wird bestimmt durch deren Struktur, deren Dynamik, dem Zusammenspiel untereinander und der Interaktion mit kleinen Molekülen.

Um die Gesamtheit der Zelle mit allen Funktionen und Aufgaben zu verstehen, wird zuerst versucht, die Strukturen der Zellbestandteile zu bestimmen. Dies wird klassischerweise mit den Strukturermittlungsmethoden Kristallographie und NMR (*engl.* 'nuclear magnetic resonance') durchgeführt und heutzutage zusätzlich mittels Kryoelektronenmikroskopie durchgeführt. Diese Methoden haben ein großes Potential, unterschiedlichste Fragestellungen zu beantworten, allerdings treten auch klassische Nachteile auf. So kann die Kristallographie keine Aussagen über Dynamiken treffen. NMR ist begrenzt auf kleine Systeme und kann vor allem flexible Bereiche nur ungenau abbilden, Kryoelektronenmikroskopie arbeitet ausschließlich im gefrorenen Zustand. Um solche Nachteile auszugleichen gibt es unterschiedliche biophysikalische Methoden, die keine komplette Strukturaufklärung bewerkstelligen können. Sie liefern aber zusätzliche Informationen zur Dynamik und zu Strukturänderungen, dem Schwerpunkten der heutigen Zellbiochemie. Zu diesen Methoden gehört z. B. SAXS (*engl.* 'small angle X-ray scattering') und FRET (Förster-Resonanzenergietransfer)-Spektroskopie.

Eine weitere solche Methode, die auf Abstandsbestimmungen innerhalb biologischer Systeme basiert, ist die EPR (*engl.* 'electron paramagnetic resonance')-Spektroskopie. Mit Hilfe von PDS (*engl.* 'pulsed dipolare spectroscopy')-Techniken, einem Teilbereich in der EPR-Spektroskopie, können Abstände in einem Bereich von 2–10 nm zwischen zwei markierten Positionen eines biologischen Makromoleküls bestimmt werden. Diese Methode liefert neben den mittleren Abständen auch Abstandsverteilungen, mit denen auf die Flexibilität des Moleküls geschlossen werden kann. Durch PDS-Messungen eröffnet sich die Möglichkeit, Bewegungen

und Zustandsänderungen zu untersuchen. Die Messung beruht auf der dipolaren Kopplung von Radikalen (Spinlabel). Da die gemessenen dipolaren Kopplungen eine anisotrope Wechselwirkung sind, können an starren Systemen neben den Abstandsinformationen auch die Orientierungen der beiden Spinlabel zueinander bestimmt werden. Diese zusätzliche Information ermöglicht es, mittels orientierungsselektiver PDS-Messungen noch genauer die Geometrie und Flexibilität des Systems zu untersuchen.

Allerdings hat auch PDS Nachteile und Einschränkungen, weshalb unterschiedliche Gruppen daran arbeiten, diese Methode weiterzuentwickeln. Klassischerweise werden alle Messungen mit der Doppelfrequenztechnik PELDOR (*engl.* 'pulsed electron-electron double resonance') durchgeführt, da aufgrund von Techniklimitationen nur selektive Rechteckspulse genutzt werden konnten. Einzelfrequenzmethoden basieren dagegen auf Breitbandanregung, die mit den technischen Gegebenheiten lange nicht möglich war. Eine sehr wichtige Problematik bei PDS-Messungen ist, dass alle Messungen bei nicht-nativen kryogenen Temperaturen durchgeführt werden, da ansonsten die Signale schon vor dem eigentlichen Messen vollständig relaxiert sind bzw. die freie Rotation von verhältnismäßig kleinen biologischen Systemen in der Lösung das dipolare Signal ausmittelt. Eine weitere Schwierigkeit für speziell orientierungsselektive PELDOR-Messungen ist die aufwendige Synthese von mit dem starren ζ -Label markierten Nukleinsäuren. Allerdings ist der Einsatz von starren Spinlabeln nötig, um die anisotropen Effekte zu maximieren und zusätzlich den Beitrag der Flexibilität des Systems und des Labels zuverlässig zu trennen. Zuletzt ist eine große Herausforderung die eindeutige Interpretation von den sensitiven orientierungsselektiven PELDOR-Messungen. In der Vergangenheit wurden dazu oft einfache Modelle genutzt, die aber uneindeutig sind, wenn gleichzeitig mehrere unbekanntes Bewegungen bestimmt werden sollen. Die Alternative, PELDOR-Daten mittels MD(Moleküldynamik)-Simulationen zu beschreiben, war bisher nur qualitativ möglich, da vor allem im Bereich von Nukleinsäuren die Qualität noch nicht so hoch war, dass sie die benötigte Genauigkeit aufweisen. Neue Entwicklungen durch unterschiedliche Gruppen in und außerhalb der EPR-Gemeinschaft machen es möglich, diese unterschiedlichen Problematiken langsam zu überwinden. Sie bieten aber nicht nur Lösungen, sondern werfen oftmals neue Fragestellungen auf. Diese können auf verschiedene Arten gelöst werden. Ein Ansatz kann die Zuhilfenahme von MD-Simulationen sein.

Diese Computersimulationen können ein vollständiges und detailliertes Bild eines biologischen Systems liefern und so genutzt werden, um z. B. orientierungsselektive PDS-Daten zu beschreiben. MD-Simulationen nutzen empirische Kraftfelder, um Atom-Atom-Interaktionen, wie Bindungen, Winkel und Anziehungskräfte durch den Raum, zu beschreiben. Solche Simulationen sind heutzutage sehr leistungsfä-

hig und ergeben eine sehr präzise zeitliche und örtliche Auflösung. Allerdings ist die Qualität stark abhängig von der Güte der Kraftfelder, die in der Vergangenheit für Nukleinsäuren noch nicht sehr hoch war. Aber auch neu entwickelte Kraftfelder sollten sorgfältig an kleineren Systemen evaluiert werden. Dies geschieht üblicherweise mit Hilfe von Kristallstrukturen und NMR-Daten. Diese Messdaten ergeben aber hauptsächlich statische oder gemittelte Strukturen. Damit kann sichergestellt werden, dass die Simulationen über einen bestimmten Zeitraum stabil sind, nicht dagegen aber, dass die Flexibilität des Systems durch die Kraftfelder richtig beschrieben ist. Ensemble-Methoden, wie z. B. orientierungsselektive PELDOR-Messungen, können diese Lücke füllen.

In dieser Arbeit wurden zehn orientierungsselektive PELDOR-Datensätze einer 20mer doppelsträngigen DNA mit unterschiedlichen Labelpositionen mit MD-Simulationen (bereitgestellt durch die Gruppe von Prof. Dr. Hummer) verglichen. Der Vergleich zeigt, dass es offensichtliche Verbesserungen zwischen dem etablierten Kraftfeld BSC0 aus dem Jahr 2007 und den neuen Kraftfeldern OL3 und BSC1 gibt. Diese neuen Kraftfelder beschreiben sowohl den mittleren Abstand als auch die Abstandsverteilung mit hoher Präzision, was quantitative Vergleiche mit den PELDOR-Messungen zeigen. Dies ermöglicht eine genaue Interpretation der Dynamik des dsDNA-Rückgrats, das sowohl die durch dieselben PELDOR-Messungen zuvor postulierte Twist-Bewegung der Helix als auch zusätzlich als Hauptdynamik ein Biegen der dsDNA zeigt.

Genau diese Analyse der Kraftfelderqualität an der dsRNA stellte sich als schwierig heraus. Die kurzen dsRNA-Bausteine tendieren dazu, Oligomere zu bilden, die wiederum zu Multispineffekten führten. Zusätzlich beeinflusst diese Aggregation die Dynamik der einzelnen RNAs. Daher musste dieses *'end-to-end'*-Stacking verhindert werden. Eine Nukleobase an einem Ende der dsRNA führt zu einer Dimerisierung, während eine Nukleobase an beiden Seiten dieses Stacking vollständig verhindert. Messungen mit unterschiedlichen Salzkonzentrationen konnten zusätzlich zeigen, dass die $\pi - \pi$ -Interaktion zweier dsRNAs bei höheren Salzkonzentrationen zunimmt. Erste dsRNA-Proben ohne Stacking ergaben im Vergleich mit MD-Simulationen neuerer Kraftfelder eine Übereinstimmung, die im Verhältnis zu älteren Kraftfeldern verbessert, aber noch nicht so gut wie für die dsDNA ist.

Das gewonnene Wissen einer Übereinstimmung von MD-Simulationen mit bekannten dsDNA-Proben kann für die Interpretation der neuen Entwicklungen im Feld der gepulsten dipolaren Spektroskopie genutzt werden. Technische Neuerungen, die es erlauben, die in der NMR bereits etablierten modulierten Pulse zu nutzen, machen es möglich, neue Pulssequenzen in der EPR anzuwenden. Eine solche Sequenz ist SIFTER (*engl.* 'single frequency technique for refocusing dipolar

couplings'), die mit solchen Breitbandpulsen eine Alternative für dipolar basierte Abstandsbestimmungen darstellt. Da mit Hilfe dieser Methode die anisotrope dipolare Kopplung mit nur einer Messung bestimmt werden kann, ist es möglich, damit zeitaufwendige, aber etablierte orientierungsselektive PELDOR-Messungen zu ersetzen bzw. zu ergänzen. Auch wenn beide Methoden die selbe dipolare Kopplung messen, sind aufgrund unterschiedlicher Pulsanregungen die experimentellen Zeitspuren und der Simulationsprozess nicht identisch. Eine im Rahmen dieser Arbeit von PELDOR ausgehend weiterentwickelte Simulationsprozedur wurde an dem oben beschriebenen biologischen Modellsystem, der doppelsträngigen 20mer DNA, evaluiert und mit orientierungsselektiven PELDOR-Daten verglichen. Es zeigte sich, dass beide Messdaten mit gleicher Qualität simuliert werden können. Eine weitere elementare Bedingung, um EPR-Spektroskopie an biologischen Proben messen zu können, ist das Anbringen von Spinlabeln an spezifischen Stellen innerhalb des Moleküls. Um neue spezifische Spinlabel zu entwickeln, müssen vor allem zwei Aspekte beachtet werden. Zum einen muss aus synthetischer Sicht das Label möglichst einfach, effizient und spezifisch an das Biomolekül angebracht werden können. Zum anderen muss aus spektroskopischer Sicht ein neuer Spinlabel für die in dieser Arbeit genutzten orientierungsselektiven PDS-Techniken besonders starr sein. Spinlabel besitzen allerdings zumeist eine Eigendynamik, die die Abstandsverteilungen der PELDOR-Messungen verbreitern. Diese Starrheit ist ideal im Falle des \mathbf{C} -Labels, der aber synthetisch sehr anspruchsvoll ist. Als Alternative wurde in der Sigurdsson-Gruppe das ^{1M}U -Label entwickelt. Dabei handelt es sich um ein halbstarres Label, bei dem eine Wasserstoffbrücke zum Zuckerbaustein der Nukleinsäure die Beweglichkeit einschränkt. Die Analyse der orientierungsselektiven Daten aus unterschiedlichen Magnetfeldern durch ein dreidimensionales Modell mit der dsDNA-Dynamik von Andriy Marko als Basis bestätigt dies. Dazu zählt eine Rotationsmöglichkeit von 5° um die X-Achse (entlang der N-O Bindung) sowie eine vertikale und horizontale Rotation von $15 - 20^\circ$.

Ein weiterer interessanter Spinlabel ist der \mathbf{G} . Dieser Label ist nicht kovalent gebunden, sondern interkaliert in eine Stelle der Nukleinsäure, in der eine Guanin-Base fehlt. Mit Hilfe von Wasserstoffbrückenbindungen zum gegenüberliegenden Cytidin und $\pi - \pi$ -Interaktionen zu den benachbarten Basen sitzt der Spinlabel fest innerhalb der Nukleinsäure. MD-Simulationen im quantitativen Vergleich mit orientierungsselektiven PELDOR-Messungen an verschiedenen Magnetfeldern ergaben eine hohe Übereinstimmung. Dabei konnte gezeigt werden, dass der Label, interkaliert in eine dsDNA, flippen kann, was zu einer Ausmittelung der Anisotropie führt, allerdings zu keiner Verbreiterung der Abstandsverteilung. Damit ist eine sehr präzise Abstandsbestimmung möglich. In der dsRNA dagegen wird dieses Flippen um die Einfachbindung sterisch gehindert, so dass neben dem Abstand

auch die Orientierung des Labels bestimmt werden kann.

Eine weitere Entwicklung die innerhalb der EPR-Community vorangetrieben wird, ist die Entwicklung von PDS-Messungen bei Raumtemperatur. Dabei müssen zuerst zwei Bedingungen erfüllt sein. Zum einen muss die Eigendynamik des Labels reduziert werden, da diese die Relaxationszeiten bei Temperaturen über der Glastemperatur drastisch kürzt. Daher ist der starre ζ ideal für Messungen bei Raumtemperatur. Zum anderen muss die Rotation des Moleküls in der Lösung verhindert werden. Diese besonders bei kleineren Systemen sehr schnelle Rotation führt zu einem Ausmitteln der dipolaren Kopplung. Dies kann durch elektrostatische Bindung des Moleküls an eine Nukleosil-Oberfläche geschehen. Die kurze dsDNA markiert mit dem ζ , vorbereitet und gemessen von Markus Kallis (geb. Gränz) und Dr. Philip Spindler, zeigte auch bei Raumtemperatur orientierungsselektive Effekte in den PELDOR-Zeitspuren. Die Messungen ergaben allerdings zwei Effekte. Zuerst konnte gezeigt werden, dass die Bindung an das Nukleosil zu einer Verbreiterung des Konformationsensembles führt. Trotzdem führt diese Bindung nicht zur vollständigen Fixierung, so dass die gebundene Struktur weiterhin dynamische Effekte zeigt. Diese Dynamik ist wichtig für den zweiten Effekt. Die Zeitspuren, gemessen bei zwei Temperaturen, unterscheiden sich besonders in ihrer Dämpfung. Der physikalische Unterschied beider Messungen konnte mit Hilfe von Simulationen durch die oben genannten MD-Simulationen qualitativ nachvollzogen werden. Dabei wurde ersichtlich, dass diese Dynamiken, die schneller sind als die Frequenzen der dipolaren Kopplung selbst, sich während der Messung ausmitteln. Das bedeutet, während bei tiefen Temperaturen die Messungen eine Superposition aller Konformere in der Probe sind, kann bei höheren Temperaturen nur das zeitliche dynamische Mittel der Strukturen gemessen werden. Dadurch ist es möglich, erste Aussagen über die Größenordnung der Geschwindigkeit der Dynamik mit Hilfe von PDS-Messungen zu treffen.

Insgesamt befasst sich diese Arbeit mit unterschiedlichen Aspekten der Methodenentwicklung innerhalb der gepulsten dipolaren Spektroskopie. Hierzu wurden Flexibilitätsstudien von unterschiedlichen Spinlabeln gemacht, neue Simulationsprozeduren für neue Pulssequenzen geschrieben und evaluiert sowie die Unterschiede zwischen Messungen bei 50 K und bei Raumtemperatur mittels Simulationen beschrieben. Im Mittelpunkt steht dabei das Zusammenspiel zwischen sehr präzisen orientierungsselektiven PDS-Messungen und MD-Simulationen mit neuen Kraftfeldern. Dabei werden zum einen mit Hilfe der Messungen unterschiedliche Kraftfelder verglichen und evaluiert. Zum anderen können qualitativ gute MD-Simulationen helfen, die PDS-Messungen im Detail zu verstehen, was ohne zusätzliches Wissen über das biochemische System oft schwierig und uneindeutig ist.

CHAPTER 6

List of Scientific Contributions

The results presented in this thesis have been published in peer-reviewed scientific journals and presented at national and international conferences as oral or poster presentations.

The list of publications that are relevant for this thesis:

1. **N. Erlenbach**, B. Endeward, P. Schöps, D. B. Gophane, S. Th. Sigurdsson and T. F. Prisner; 'Flexibilities of Isoindoline-Derived Spin Labels for Nucleic Acids by Orientation Selective PELDOR', *Phys. Chem. Chem. Phys.* 18, 161960 (2016)

The author's contribution was the preparation of the manuscript, performance of 50 % of the measurements and the analysis and the simulations of the PELDOR time traces.

2. L. S. Stelzl¹, **N. Erlenbach**¹, M. Heinz, T. F. Prisner and G. Hummer; 'Resolving the Conformational Dynamics of DNA with Ångstrom Resolution by PELDOR and Molecular Dynamics', *J. Am. Chem. Soc.* 139, 11674 (2017)

The author's contribution was the preparation of 50 % of the manuscript, performance of the calculation of the PELDOR time traces using the provided MD simulation and the analysis of the data.

3. M. Gränz, **N. Erlenbach**, L. S. Stelzl, S. Th. Sigurdsson and T. F. Prisner; 'Dynamics of Nucleic Acids at Room Temperature Revealed by Pulsed EPR', *Ang. Chem. Int. Ed.*, 57, 10540-10543 (2018)

The author's contribution was the preparation of 50 % of the manuscript, the development of the theoretical description for the room temperature data and the simulations of the PELDOR time traces using the provided MD simulations.

4. A. Bowen¹, **N. Erlenbach**¹, P. van Os, L. S. Stelzl, S. Th. Sigurdsson and T. F. Prisner; 'Orientation selective 2D-SIFTER Experiments at X-band Frequencies', *Appl. Magn. Res.*, 49, 1355-1368 (2018)

The author's contribution was preparation of 50 % of the manuscript, performance the simulations of the SIFTER time traces using the provided MD simulation and analysis of the data.

5. **N. Erlenbach**, C. Grünewald, B. Krstic, A. Heckel and T. F. Prisner; 'End-to-End' Stacking of small dsRNA', *RNA*, 25, 239-246 (2019)

The author's contribution was the preparation of the manuscript, performance of the PELDOR measurements and analysis of the data.

The following work is attached as finished manuscript:

M. Heinz¹, **N. Erlenbach**¹, S. Subham, G. Thierolf, S. T. Sigurdsson, T. F. Prisner, L. S. Stelzl, G. Hummer; 'Orientation Selective EPR Distance Measurements on RNA and DNA with Non-Covalent $\dot{\text{G}}$ Spin Label'

The author's contribution was the preparation of 50 % of the manuscript, performance of the PELDOR measurements and the calculation of the PELDOR time traces using the provided MD simulations.

¹*These authors contribute equally to this work.*

Oral presentations given by the author:

1. 'Novel Rigid Spin Label for Nucleic Acids'
The 40th Discussion Meeting of the GDCh-Division of 'Magnetic Resonance' (FGMR), Leipzig, Germany, 2018
2. 'Small dsDNA as Model Systems for Orientation Selective Pulsed EPR'
51st Annual International Meeting of the ESR Spectroscopy Group of the Royal Society of Chemistry, London, Great Britain, 2018
3. 'Conformational Dynamics of DNA by Orientation Selective PELDOR/DEER and MD simulations'
European congress on Magnetic Resonance (EUROMAR), Aarhus, Denmark, 2016
4. 'Conformational Flexibility of the Isoindoline Derived Spin Labels'
Winter School of the IRTG/SFB902 ('Molecular Principles of RNA-based Regulation'), Obergurgl, Austria, 2015
5. 'Conformational Dynamics of DNA by Orientation Selective PELDOR and MD'
Seminar of the Institute for Physical and Theoretical Chemistry, Goethe University Frankfurt, Hirschegg, Austria, 2016
6. 'Conformational Dynamics of Nucleic Acids by Pulsed EPR and MD'
RNA Symposium of the SFB902 ('Molecular Principles of RNA-based Regulation'), Bad Homburg, Germany, 2016

-
7. 'Conformational Dynamics of dsDNA by Orientation Selective PELDOR and MD simulations'
Summer school of the IRTG/SFB902 ('Molecular Principles of RNA-based Regulation'), Hirschegg, Austria, 2016
 8. '"End-to-End" Stacking of Small dsRNA'
Summer school of the IRTG/SFB902 ('Molecular Principles of RNA-based Regulation'), Wernigerode, Germany, 2017
 9. '"End-to-end" Stacking of Small dsRNA Studied by PELDOR'
Seminar of the Institute for Physical and Theoretical Chemistry, Goethe University Frankfurt, Hirschegg, Austria, 2017
 10. 'Room Temperature PELDOR'
Winter school of the IRTG/SFB902 ('Molecular Principles of RNA-based Regulation'), Altglashütten, Germany, 2018

Poster presentations given by the author:

1. 'Conformational Flexibility of the Isoindoline Derived Spin Labels'
The 37th Discussion Meeting of the GDCh-Division of 'Magnetic Resonance' (FGMR), Darmstadt, Germany, 2015
2. 'Conformational Dynamics of Nucleic Acids by Orientation Selective pulsed EPR Spectroscopy'
International Symposium 'Connecting EPR, ssNMR and DNP for the Study of complex Biomolecules', Ringbergmeeting, Kreuth, Germany, 2016
3. 'Conformational Dynamics of Nucleic Acids by Orientation Selective PELDOR/DEER'
Thematic Meeting of the Biophysical Society ('Conformational Ensembles from Experimental Data and Computer Simulations'), Berlin, Germany, 2017
4. '"End-to-End' stacking of small dsRNA by the means of PELDOR/DEER'
The 39th Discussion Meeting of the GDCh-Division of 'Magnetic Resonance' (FGMR), Bayreuth, Germany, 2017
5. 'Development of PELDOR Spectroscopy toward more native Conditions'
RNA Symposium of the SFB902 ('Molecular Principles of RNA-based Regulation'), Frankfurt, Germany, 2018

CHAPTER 7

List of Collaborator Contributions

Except where stated otherwise the work presented was performed by the author under the supervision of Prof. Prisner during her doctoral studies.

All contributions from colleagues and collaborators are explicitly referenced in the thesis. The sections listed below were obtained in the context of collaborative research:

Section 3.2

Intermolecular Interaction - 'End-to-End' Stacking of dsRNA

The samples were synthesised by Bizera Krstic from the group of Prof. Dr. Prisner and Dr. Christian Grünewald from the group of Prof. Dr. Heckel.

Section 3.3

Flexibility of Spin Label - A Semi-Rigid Approach

50 % of the experiments were performed by Dr. Burkhard Endeward from the group of Prof. Dr. Prisner. The samples were synthesized in the group of Prof. Dr. Sigurdsson by Dr. Dnyaneshwar Gophane from the University of Iceland, Science Institute, Reykjavik.

Section 3.4

Study of an Intercalating Spin Label

MD simulations were provided by Marcel Heinz und Dr. Lukas Stelzl from the group of Prof. Dr. Hummer from the MPI of Biophysics, Frankfurt am Main. The samples were synthesised in the group of Prof. Dr. Sigurdsson by Dr. Nilesh Kamble from the University of Iceland, Science Institute, Reykjavik.

Section 3.5

Orientation-Selective 2D-SIFTER Simulations

The 2D-SIFTER measurements were performed by Dr. Alice Bowen and Dr. Philip van Os (née Schöps) from the group of Prof. Dr. Prisner. The PELDOR measurements for the DNA were already published,^[45] while the PELDOR measurements for the model system were performed by Dr. Alice Bowen.

Section 3.6

Conformational Dynamics of DNA by PELDOR and MD

MD simulations were performed by Dr. Lukas Stelzl from the group of Prof. Dr. Hummer from the MPI of Biophysics, Frankfurt am Main. The measurements were already published.^[45]

Section 3.7

Analysis of Room Temperature PELDOR Measurements

The sample preparation and the evaluation of different approaches for Room Temperature PELDOR was done by Markus Kallis (née Gränz), and the final PELDOR measurements were performed by Dr. Philip Spindler. The samples were synthesised in the group of Prof. Dr. Sigurdsson by Dr. Dnyaneshwar Gophane from the University of Iceland, Science Institute, Reykjavik.

Danksagung

Viele Jahre habe ich an dieser Arbeit gearbeitet. Das geht natürlich nicht völlig allein, daher bin ich vielen Menschen dankbar, die mich entweder fachlich oder menschlich in dieser Zeit unterstützt haben.

Anfangen möchte ich mit **Prof. Dr. Thomas Prisner**. Am meisten danke ich ihm für seine Antwort, als ich ihm sagte, dass ich leider noch keinerlei Programmiererfahrung besitze. 'Dann lernst du es' und das habe ich in den letzten Jahren auch getan. Er hat mir die Möglichkeit gegeben, meine mathematische Leidenschaft auszuleben und interessante Projekte zu bearbeiten. Dazu kommt die wissenschaftliche Freiheit und das Vertrauen, dass ich unter ihm genossen habe. Während der ganzen Zeit hat er mir immer mit Rat und Tat zur Seite gestanden und ich konnte viel von seiner großen Erfahrung lernen.

Daneben möchte ich **Dr. Björn Corzilius** danken. Mit ihm konnte ich während der Zeit viele 'fruitfull discussions', wie im Englischen so schön gesagt wird, führen. Er war ein hervorragender Co-Betreuer, auch oder gerade aus menschlicher Sicht. Aus unserer Gruppe besonders hervorheben möchte ich **Dr. Alberto Collauto**, der so manch 'dumme Frage' beantworten musste und mir immer absolut zuvorkommend geholfen hat. Aber noch viel mehr weiß ich es wertzuschätzen, dass er meine gesamte Arbeit inhaltlich Korrektur gelesen hat. Derselbe Dank geht an **Phoebe Young**, die mir nicht nur viel Spass im PC-Praktikum bereitet hat, sondern vor allem sich meinem Englisch in dieser Arbeit angenommen hat.

Der wohl wichtigste Kollaborationspartner während meiner Arbeit war **Dr. Lukas Stelzl**. Mit ihm teile ich die meisten Publikation auf meiner Liste, weshalb wir auch viele Stunden diskutiert haben. Ich war von Anfang an begeistert, dass wir wissenschaftlich tatsächlich die gleiche Sprache sprechen und ich mich immer auf ihn verlassen konnte. Daneben will ich aber auf jeden Fall **Marcel Heinz** nennen, den ich noch als Student kennengelernt habe. Er hat viele Simulationen für unsere Projekte laufen lassen 'müssen'. Aber es gab besonders viele erfrischende Gespräche, vor allem, wenn wir über alte Zeiten als Studenten an der Uni Frankfurt 'geredet' haben.

Wichtig für mich als Spektroskopikerin, die das Labor gerne nur von außen sieht, ist es aber, gute Kollaborationspartner für die Probenvorbereitung zu haben. So

konnte ich mich auf eine gute Zusammenarbeit mit **Prof. Dr. Snorri Sigurdson** und **Anna-Lena Segler** in Island verlassen, ebenso aber auch im Haus auf **Dr. Christian Grünewald**.

Doch auch Projekte mit vorhandenen spektroskopischen Daten waren jederzeit willkommen, weshalb ich sehr gerne mit **Dr. Alice Bowen**, **Dr. Philips van Os (geb. Schöps)**, **Dr. Philip Spindler** und besonders **Markus Kallis (geb. Gränz)** gearbeitet habe. Gerade Markus habe ich meine Spektroskopie-Kenntnisse zu verdanken. Aber auch **Dr. Burkhard Endeward** hat in dem Bereich viel beigetragen. Bekannt als Theoretikerin hatte ich allen Grund regelmässig in sein Büro hereinzuplatzen, weil z. B. Elexsys mal wieder nicht wusste, was ich von ihm wollte. Das gleiche gilt für **Dr. Vasyil Denysenkov**, wenn ich mich am Hochfeldspektrometer versucht habe. Ein anderer Glückstreffer für unsere Gruppe und auch für mich war **Silke Schneider**, die immer für uns alle da war.

Da aber auf der Arbeit nicht nur Fachhilfe benötigt wird, sondern auch das soziale Umfeld extrem wichtig ist, möchte ich mich bei der kompletten Prisner/Corzilius-Gruppe bedanken. Hier möchte ich vor allem **Dr. Dmitry Akhmetzyanov** herausheben, der mir im Büro so sehr fehlt seit seinem Weggang nach Kanada. Daneben habe ich mich aber auch mit **Thilo Hetzke** gerne über Fußball oder andere Themen ausgetauscht oder die Neuigkeiten aus der Gruppe von **Victoria Aladin** erfahren. **Eva Jaumann** hatte immer ein offenes Ohr für mich und mit **Dr. Johannes Wittmann**, auch wenn er nur eine kurze Zeit da war, und **Dr. Monu Kaushik** hatte ich eine gute Zeit.

Allein ein gutes Umfeld in der Uni reicht jedoch nicht für eine Dissertation, dazu braucht es auch andere Unterstützung. Und am meisten leiden musste zuhause mein Freund **Andreas**, der trotz all meiner Macken, vor allem unter Stress, immer für mich da war. Daneben stand aber auch meine Familie immer hinter mir. Egal ob Mama, Papa, Oma, Opa, Cousin oder Tanten, alle waren immer da, wenn ich sie brauchte.

Und falls ich noch jemanden vergessen haben sollte: Danke für alles!

Bibliography

- [1] E Ennifar, editor. *Nucleic Acid Crystallography*. Springer Science, 2015.
- [2] B. Fürtig, C. Richter, J. Wöhnert, and H. Schwalbe. NMR spectroscopy of RNA. *Chem. Bio. Chem.*, 4(10):936–62, 2003.
- [3] S. Zhou, P. Pettersson, J. Huang, J. Sjöholm, D. Sjöstrand, R. Pomès, M. Högbom, P. Brzezinski, L. Mäler, and P. Ädelroth. Solution NMR structure of yeast Rcf1, a protein involved in respiratory supercomplex formation. *Proc. Natl. Acad. Sci.*, 115(12):3048–3053, 2018.
- [4] X. Bai, T. G. Martin, S. H. Scheres, and H. Dietz. Cryo-EM structure of a 3D DNA-origami object. *Proc. Natl. Acad. Sci. U. S. A.*, 109(49):20012–20017, 2012.
- [5] L. A. Earl, V. Falconieri, J. L. S. Milne, and S. Subramaniam. Cryo-EM: beyond the microscope. *Curr. Opin. Struct. Biol.*, 46:71–78, 2017.
- [6] H. M. Berman, J. Westbrook, Z. Feng, G. Gilliland, T. N. Bhat, H. Weissig, I. N. Shindyalov, and P. E. Bourne. The Protein Data Bank. *Nucleic Acids Res.*, 28(1):235–42, 2000.
- [7] J. Li, A. Jiao, S. Chen, Z. Wu, E. Xu, and Z. Jin. Application of the small-angle X-ray scattering technique for structural analysis studies: A review. *J. Mol. Struct.*, 1165, 2018.
- [8] A. D. Milov, A. B. Ponomarev, and Y. D. Tsvetkov. Electron-Electron Double Resonance in Electron Spin Echo: Model Biradical Systems and the Sensitized Photolysis of Decalin. *Lett. Chem. Phys.*, 110:67–72, 1984.
- [9] T. Stockner, A. Mullen, and F. MacMillan. Investigating the dynamic nature of the ABC transporters: ABCB1 and MsbA as examples for the potential synergies of MD theory and EPR applications. *Biochem. Soc. Trans.*, 43(5):1023–32, 2015.
- [10] H. Ghimire, S. Abu-Baker, I. D. Sahu, A. Zhou, D. J. Mayo, R. T. Lee, and G. A. Lorigan. Probing the helical tilt and dynamic properties of membrane-bound phospholamban in magnetically aligned bicelles using electron paramagnetic resonance spectroscopy. *Biochim. Biophys. Acta - Biomembr.*, 1818(3):645–650, 2012.
- [11] R. Ishima and D. A. Torchia. Protein dynamics from NMR. *Nat. Struct. Biol.*, 7(9):740–743, 2000.

BIBLIOGRAPHY

- [12] R. Roy, S. Hohng, and T. Ha. A practical guide to single-molecule FRET. *Nat. Methods*, 5(6):507–516, 2008.
- [13] T. Ha, T. Enderle, D. F. Ogletree, D. S. Chemla, P. R. Selvin, and S. Weiss. Probing the interaction between two single molecules: fluorescence resonance energy transfer between a single donor and a single acceptor. *Proc. Natl. Acad. Sci. U. S. A.*, 93(13):6264–8, 1996.
- [14] H. Gustmann, A.-L. J. Segler, D. B. Gophane, A. J. Reuss, C. Grünewald, M. Braun, J. E. Weigand, S. Th. Sigurdsson, and J. Wachtveitl. Structure guided fluorescence labeling reveals a two-step binding mechanism of neomycin to its RNA aptamer. *Nucleic Acids Res.*, 2018.
- [15] N. T. Hunt. 2D-IR spectroscopy: ultrafast insights into biomolecule structure and function. *Chem. Soc. Rev.*, 38(7):1837, 2009.
- [16] N. Simpson and N. T. Hunt. Ultrafast 2D-IR spectroscopy of haemoproteins. *Int. Rev. Phys. Chem.*, 34(3):361–383, 2015.
- [17] I. López-Peña, B. S. Leigh, D. E. Schlamadinger, and J. E. Kim. Insights into Protein Structure and Dynamics by Ultraviolet and Visible Resonance Raman Spectroscopy. *Biochemistry*, (31):4770–4783, 2015.
- [18] J. Šponer and F. Lankas. *Computational studies of RNA and DNA*. Springer, 2006.
- [19] W. Heisenberg. Über quantentheoretische Umdeutung kinematischer und mechanischer Beziehungen. *Zeitschrift für Phys.*, 33(1):879–893, 1925.
- [20] M. Born, W. Heisenberg, and P. Jordan. Zur Quantenmechanik. *Zeitschrift für Phys.*, 35(8-9):557–615, 1926.
- [21] O. V. Shishkin, L. Gorb, P. Hobza, and J. Leszczynski. Structural nonrigidity of nucleic acid bases. Post-Hartree-Fock ab initio study. *Int. J. Quantum Chem.*, 80(4-5):1116–1124, 2000.
- [22] V. Fock. Näherungsmethode zur Lösung des quantenmechanischen Mehrkörperproblems. *Zeitschrift für Phys.*, 61(1-2):126–148, 1930.
- [23] D. R. Hartree. The Wave Mechanics of an Atom with a Non-Coulomb Central Field. Part I. Theory and Methods. *Math. Proc. Cambridge Philos. Soc.*, 24(1):89, 1928.
- [24] F. Coester and H. Kümmel. Short-range correlations in nuclear wave functions. *Nucl. Phys.*, 17:477–485, 1960.
- [25] J. Čížek. On the Correlation Problem in Atomic and Molecular Systems. Calculation of Wavefunction Components in Ursell Type Expansion Using Quantum Field Theoretical Methods. *J. Chem. Phys.*, 45(11):4256–4266, 1966.

-
- [26] U. Fano. Effects of Configuration Interaction on Intensities and Phase Shifts. *Phys. Rev.*, 124(6):1866–1878, 1961.
- [27] P. Hohenberg and W. Kohn. Inhomogeneous Electron Gas. *Phys. Rev.*, 136(3B):B864–B871, 1964.
- [28] W. Kohn and L. J. Sham. Self-Consistent Equations Including Exchange and Correlation Effects. *Phys. Rev.*, 140(4A):A1133–A1138, 1965.
- [29] M. Levitt and A. Warshel. Computer simulation of protein folding. *Nature*, 253(5494):694–698, 1975.
- [30] B. J. Alder and T. E. Wainwright. Studies in Molecular Dynamics. I. General Method Studies in Molecular Dynamics. I. General Method. *J. Chem. Phys.*, 31(2):459–466, 1959.
- [31] S. J. Weiner, P. A. Kollman, D. A. Case, U. C. Singh, C. Ghio, G. Alagona, S. Proffeta, and P. Weiner. A new force field for molecular mechanical simulation of nucleic acids and proteins. *J. Am. Chem. Soc.*, 106(3):765–784, 1984.
- [32] S. J. Weiner, P. A. Kollman, D. T. Nguyen, and D. A. Case. An all atom force field for simulations of proteins and nucleic acids. *J. Comput. Chem.*, 7(2):230–252, 1986.
- [33] J. Šponer, G. Bussi, M. Krepl, P. Banáš, S. Bottaro, R. A. Cunha, A. Gil-Ley, G. Pinamonti, S. Poblete, P. Jurečka, N. G. Walter, and M. Otyepka. RNA Structural Dynamics As Captured by Molecular Simulations: A Comprehensive Overview. *Chem. Rev.*, 2018.
- [34] T. Palmer and P. L. R. Bonner. *Enzymes: biochemistry, biotechnology and clinical chemistry*. 2008.
- [35] G. Krauss. *Biochemistry of signal transduction and regulation*. Wiley-VCH, 2008.
- [36] N. Vaidehi and J. Klein-Seetharaman. *Membrane protein structure and dynamics: methods and protocols*. Humana Press, 2012.
- [37] J. Lucas-Lenard and F. Lipmann. Protein Biosynthesis. *Annu. Rev. Biochem.*, 40(1):409–448, 1971.
- [38] S. R. Eddy. Non-coding RNA genes and the modern RNA world. *Nat. Rev. Genet.*, 2(12):919–929, 2001.
- [39] D. Goldfarb and S. Stoll, editors. *Handbook of EPR spectroscopy : fundamentals and methods*. EMagnRes Books, 1th edition, 2018.
- [40] R. G. Larsen and D. J. Singel. Double electron-electron measurement of electron disordered solids resonance spin-echo spin pair separations modulation: Spectroscopic in orientationally disordered solids. *J. Chem. Phys.*, 98(1993):5134–5146, 1993.

BIBLIOGRAPHY

- [41] C. M. Grytz, A. Marko, P. Cekan, S. Th. Sigurdsson, and T. F. Prisner. Flexibility and conformation of the cocaine aptamer studied by PELDOR. *Phys. Chem. Chem. Phys.*, 18:2993–3002, 2016.
- [42] T. Hetzke, M. Vogel, D. B. Gophane, J. E. Weigand, B. Suess, S. Th. Sigurdsson, and T. F. Prisner. Influence of Mg²⁺ on the conformational flexibility of a tetracycline aptamer. *RNA*, 25(1):158–167, 2019.
- [43] O. Schiemann, A. Weber, T. E. Edwards, T. F. Prisner, and S. Th. Sigurdsson. Nanometer Distance Measurements on RNA Using PELDOR. *J. Am. Chem. Soc.*, 125, 2003.
- [44] O. Schiemann, P. Cekan, D. Margraf, T. F. Prisner, and S. T. Sigurdsson. Relative orientation of rigid nitroxides by peldor: Beyond distance measurements in nucleic acids. *Angew. Chemie - Int. Ed.*, 48(18):3292–3295, 2009.
- [45] A. Marko, V. P. Denysenkov, D. Margraf, P. Cekan, O. Schiemann, S. Th. Sigurdsson, and T. F. Prisner. Conformational Flexibility of DNA. *J. Am. Chem. Soc.*, 133:13375, 2011.
- [46] D. Wunnicke, D. Strohbach, J. E. Weigand, B. Appel, E. Feresin, B. Suess, S. Muller, and H.-J. Steinhoff. Ligand-induced conformational capture of a synthetic tetracycline riboswitch revealed by pulse EPR. *RNA*, 17(1):182–188, 2011.
- [47] M. M. Haugland, E. A. Anderson, and J. E. Lovett. Tuning the properties of nitroxide spin labels for use in electron paramagnetic resonance spectroscopy through chemical modification of the nitroxide framework. *Electron Paramag. Reson.*, 25, 2017.
- [48] P. Cekan, A. L. Smith, N. Barhate, B. H. Robinson, and S. Th. Sigurdsson. Rigid spin-labeled nucleoside: A nonperturbing EPR probe of nucleic acid conformation. *Nucleic Acids Res.*, 36(18):5946–5954, 2008.
- [49] D. B. Gophane and S. Th. Sigurdsson. Hydrogen-bonding controlled rigidity of an isoindoline-derived nitroxide spin label for nucleic acids. *Chem. Commun.*, 49(10):999–1001, 2013.
- [50] D. B. Gophane, B. Endeward, T. F. Prisner, and S. Th. Sigurdsson. Conformationally Restricted Isoindoline-Derived Spin Labels in Duplex DNA: Distances and Rotational Flexibility by Pulsed Electron-Electron Double Resonance Spectroscopy. *Chem. - A Eur. J.*, 20(48):15913–15919, 2014.
- [51] N. R. Kamble, M. Gränz, T. F. Prisner, and S. Th. Sigurdsson. Noncovalent and site-directed spin labeling of duplex RNA. *Chem. Commun.*, 52(100):14442–14445, 2016.
- [52] A. D. Milov, K. M. Salikhov, and M. D. Shchirov. Application of the double resonance method to electron spin echo in a study of the spatial distribution of paramagnetic centers in solids. *Sov. Phys. Solid State*, 23(4):975–982, 1981.

-
- [53] M. Pannier, S. Veit, A. Godt, G. Jeschke, and H. W. Spiess. Dead-Time Free Measurement of Dipole-Dipole Interactions between Electron Spins. *J. Magn. Reson.*, 142(2):331–340, 2000.
- [54] T. F. Prisner, A. Marko, and S. Th. Sigurdsson. Conformational dynamics of nucleic acid molecules studied by PELDOR spectroscopy with rigid spin labels. *J. Magn. Reson.*, 252:187–198, 2015.
- [55] G. Jeschke. DEER Distance Measurements on Proteins. *Annu. Rev. Phys. Chem.*, 63(1):419–446, 2012.
- [56] P. E. Spindler, I. Waclawska, B. Endeward, J. Plackmeyer, C. Ziegler, and T. F. Prisner. Carr-Purcell Pulsed Electron Double Resonance with Shaped Inversion Pulses. *J. Phys. Chem. Lett.*, 6(21):4331–4335, 2015.
- [57] P. P. Borbat and J. H. Freed. Multiple-quantum ESR and distance measurements. *Chem. Phys. Lett.*, 313:145–154, 1999.
- [58] P. P. Borbat, H. S. Mchaourab, and J. H. Freed. Protein structure determination using long-distance constraints from double-quantum coherence ESR: Study of T4 lysozyme. *J. Am. Chem. Soc.*, 124(19):5304–5314, 2002.
- [59] D. Akhmetzyanov, P. Schöps, A. Marko, N. C. Kunjir, S. Th. Sigurdsson, and T. F. Prisner. Pulsed EPR dipolar spectroscopy at Q- and G-band on a trityl biradical. *Phys. Chem. Chem. Phys.*, 17(37):24446–24451, 2015.
- [60] S. K. Misra, P. P. Borbat, and J. H. Freed. Calculation of double-quantum-coherence two-dimensional spectra: Distance measurements and orientational correlations. *Appl. Magn. Reson.*, 36(2-4):237–258, 2009.
- [61] S. Milikisyants, F. Scarpelli, M. G. Finiguerra, M. Ubbink, and M. Huber. A pulsed EPR method to determine distances between paramagnetic centers with strong spectral anisotropy and radicals: The dead-time free RIDME sequence. *J. Magn. Reson.*, 201(1):48–56, 2009.
- [62] D. Akhmetzyanov, H. Y. V. Ching, V. P. Denysenkov, P. Demay-Drouhard, H. C. Bertrand, L. C. Tabares, C. Policar, T. F. Prisner, and S. Un. RIDME spectroscopy on high-spin Mn²⁺ centers. *Phys. Chem. Chem. Phys.*, 18(44):30857–30866, 2016.
- [63] L. V. Kulik, S. A. Dzuba, I. A. Grigoryev, and Y. D. Tsvetkov. Electron dipole-dipole interaction in ESEEM of nitroxide biradicals. *Chem. Phys. Lett.*, 343(3-4):315–324, 2001.
- [64] P. Schöps, P. E. Spindler, A. Marko, and T. F. Prisner. Broadband spin echoes and broadband SIFTER in EPR. *J. Magn. Reson.*, 250:55–62, 2015.
- [65] G. Jeschke, M. Pannier, A. Godt, and H. W. Spiess. Dipolar spectroscopy and spin alignment in electron paramagnetic resonance. *Chem. Phys. Lett.*, 331(2-4):243–252, 2000.

BIBLIOGRAPHY

- [66] H. Jäger, A. Koch, V. Maus, H. W. Spiess, and G. Jeschke. Relaxation-based distance measurements between a nitroxide and a lanthanide spin label. *J. Magn. Reson.*, 194(2):254–263, 2008.
- [67] A. Doll and G. Jeschke. EPR-correlated dipolar spectroscopy by Q-band chirp SIFTER. *Phys. Chem. Chem. Phys.*, 18(33), 2016.
- [68] G. Jeschke, M. Sajid, M. Schulte, N. Ramezani, A. Volkov, H. Zimmermann, and A. Godt. Flexibility of Shape-Persistent Molecular Building Blocks Composed of p-Phenylene and Ethynylene Units. (22):10107–10117, 2010.
- [69] O. Krumkacheva and E. Bagryanskaya. EPR-based distance measurements at ambient temperature. *J. Magn. Reson.*, 280:117–126, 2017.
- [70] G. Y. Shevelev, O. A. Krumkacheva, A. A. Lomzov, A. A. Kuzhelev, O. Y. Rogozhnikova, D. V. Trukhin, T. I. Troitskaya, V. M. Tormyshev, M. V. Fedin, D. V. Pyshnyi, and E. G. Bagryanskaya. Physiological-Temperature Distance Measurement in Nucleic Acid using Triarylmethyl-Based Spin Labels and Pulsed Dipolar EPR Spectroscopy. *J. Am. Chem. Soc.*, 136(28):9874–9877, 2014.
- [71] M. Nakata, G. Zanchetta, B. D. Chapman, C. D. Jones, J. O. Cross, R. Pindak, T. Bellini, and N. A. Clark. End-to-end stacking and liquid crystal condensation of 6 to 20 base pair DNA duplexes. *Science*, 318(5854):1276–1279, 2007.
- [72] L. Pollack. SAXS Studies of Ion-Nucleic Acid Interactions. *Annu. Rev. Biophys.*, 40(1):225–242, 2011.
- [73] S. A. Pabit, X. Qiu, J. S. Lamb, L. Li, S. P. Meisburger, and L. Pollack. Both helix topology and counterion distribution contribute to the more effective charge screening in dsRNA compared with dsDNA. *Nucleic Acids Res.*, 37(12):3887–3896, 2009.
- [74] I. Krstić, R. Hänsel, O. Romainczyk, J. W. Engels, V. Dötsch, and T. F. Prisner. Long-Range Distance Measurements on Nucleic Acids in Cells by Pulsed EPR Spectroscopy. *Angew. Chemie Int. Ed.*, 50(22):5070–5074, 2011.
- [75] O. Schiemann, N. Piton, Y. Mu, G. Stock, J. W. Engels, and T. F. Prisner. A PELDOR-Based Nanometer Distance Ruler for Oligonucleotides. *J. Am. Chem. Soc.*, 126:5722–5729, 2003.
- [76] O. Romainczyk, B. Endeward, T. F. Prisner, and J. W. Engels. The RNA-DNA hybrid structure determined by EPR, CD and RNase H1. *Mol. Biosyst.*, 7(4):1050–1052, 2011.
- [77] T. Weinrich, M. Gränz, C. Grünewald, T. F. Prisner, and M. W. Göbel. Synthesis of a Cytidine Phosphoramidite with Protected Nitroxide Spin Label for EPR Experiments with RNA. *European J. Org. Chem.*, 2017(3):491–496, 2017.

-
- [78] K. Halbmaier, J. Seikowski, I. Tkach, C. Höbartner, D. Sezer, and M. Bennati. High-resolution measurement of long-range distances in RNA: pulse EPR spectroscopy with TEMPO-labeled nucleotides. *Chem. Sci.*, 17:3172–3180, 2016.
- [79] Q. Cai, A. K. Kusnetzow, K. Hideg, E. A Price, I. S. Haworth, and P. Z. Qin. Nanometer distance measurements in RNA using site-directed spin labeling. *Biophys. J.*, 93(6):2110–7, 2007.
- [80] A. Ghosh and M. Bansal. A glossary of DNA structures from A to Z. *Acta Crystallogr. Sect. D Biol. Crystallogr.*, 59(4):620–626, 2003.
- [81] A. Rich, A. Nordheim, and A. H. J. Wang. The Chemistry and Biology of Left-Handed Z-DNA. *Annu. Rev. Biochem.*, 53(1):791–846, 1984.
- [82] P. L. Privalov, A. I. Dragan, C. Crane-Robinson, K. J. Breslauer, D. P. Remeta, and C. A. Minetti. What drives proteins into the major or minor grooves of DNA? *J. Mol. Biol.*, 365(1):1–9, 2007.
- [83] B. S. Reddy, S. M. Sondhi, and J. W. Lown. Synthetic DNA minor groove-binding drugs. *Pharmacol. Ther.*, 84(1):1–111, 1999.
- [84] S. Neidle. *Principles of nucleic acid structure*. Elsevier, 2008.
- [85] E. Jabri. Small, but in control. *Nat. Rev. Mol. Cell Biol.*, 6(5):361–361, 2005.
- [86] L. He and G. J. Hannon. MicroRNAs: small RNAs with a big role in gene regulation. *Nat. Rev. Genet.*, 5(7):522–531, 2004.
- [87] A. Serganov and D. J. Patel. Ribozymes, riboswitches and beyond: regulation of gene expression without proteins. *Nat. Rev. Genet.*, 8(10):776–790, 2007.
- [88] Y. Cheng. Single-Particle Cryo-EM at Crystallographic Resolution. *Cell*, 161(3):450–457, 2015.
- [89] D. Cressey and E. Callaway. Cryo-electron microscopy wins chemistry Nobel. *Nature*, 550(7675):167–167, 2017.
- [90] J. D. Watson and F. H. Crick. Molecular Structure of Nucleic Acids. *Nature*, 171:737–738, 1953.
- [91] M. M. Woolfson. The development of structural x-ray crystallography. *Phys. Scr.*, 93(3):032501, 2018.
- [92] A. Garg and U. Heinemann. A novel form of RNA double helix based on GU and CA+ wobble base pairing. *RNA*, 24(2):209–218, 2018.
- [93] J. K. Flores, J. L. Walshe, and S. F. Ataide. RNA and RNA-protein complex crystallography and its challenges. *Aust. J. Chem.*, 67(12):1741–1750, 2014.

BIBLIOGRAPHY

- [94] C. Rose-Petruck, R. Jimenez, T. Guo, A. Cavalleri, C. W. Siders, F. Rksi, J. A. Squier, B. C. Walker, K. R. Wilson, and C. P. J. Barty. Picosecond-milliångström lattice dynamics measured by ultrafast X-ray diffraction. *Nature*, 398(6725):310–312, 1999.
- [95] R. Neutze, R. Wouts, D. van der Spoel, E. Weckert, and J. Hajdu. Potential for biomolecular imaging with femtosecond X-ray pulses. *Nature*, 406(6797):752–757, 2000.
- [96] P. Emma, R. Akre, J. Arthur, R. Bionta, C. Bostedt, J. Bozek, A. Brachmann, P. Bucksbaum, R. Coffee, F.-J. Decker, Y. Ding, D. Dowell, S. Edstrom, A. Fisher, J. Frisch, S. Gilevich, J. Hastings, G. Hays, Ph. Hering, Z. Huang, R. Iverson, H. Loos, M. Messerschmidt, A. Miahnahri, S. Moeller, H.-D. Nuhn, G. Pile, D. Ratner, J. Rzepiela, D. Schultz, T. Smith, P. Stefan, H. Tompkins, J. Turner, J. Welch, W. White, J. Wu, G. Yocky, and J. Galayda. First lasing and operation of an ångstrom-wavelength free-electron laser. *Nat. Photonics*, 4(9):641–647, 2010.
- [97] J. C. H. Spence, U. Weierstall, and H. N. Chapman. X-ray lasers for structural and dynamic biology. *Reports Prog. Phys.*, 75(10):102601, 2012.
- [98] J. Lipfert and S. Doniach. Small-Angle X-Ray Scattering from RNA, Proteins, and Protein Complexes. *Annu. Rev. Biophys. Biomol. Struct.*, 36(1):307–327, 2007.
- [99] S. Doniach and J. Lipfert. Use of Small Angle X-ray Scattering (SAXS) to Characterize Conformational States of Functional RNAs. *Methods Enzymol.*, 469:237–251, 2009.
- [100] B. Różycki, Y. C. Kim, and G. Hummer. SAXS Ensemble Refinement of ESCRT-III CHMP3 Conformational Transitions. *Structure*, 19(1):109–116, 2011.
- [101] J. Zhang, C. P. Jones, and A. R. Ferré-D’Amaré. Global analysis of riboswitches by small-angle X-ray scattering and calorimetry. *Biochim. Biophys. Acta - Gene Regul. Mech.*, 1839(10):1020–1029, 2014.
- [102] Th. Förster. Zwischenmolekulare Energiewanderung und Fluoreszenz. *Ann. Phys.*, 437(1-2):55–75, 1948.
- [103] M. Bood, S. Sarangamath, M. S. Wranne, M. Grötli, and L. M. Wilhelmsson. Fluorescent nucleobase analogues for base–base FRET in nucleic acids: synthesis, photophysics and applications. *Beilstein J. Org. Chem.*, 14(1):114–129, 2018.
- [104] I. Gautier, M. Tramier, C. Durieux, J. Coppey, R. B. Pansu, J.-C. Nicolas, K. Kemnitz, and M. Coppey-Moisán. Homo-FRET Microscopy in Living Cells to Measure Monomer-Dimer Transition of GFP-Tagged Proteins. *Biophys. J.*, 80(6):3000–3008, 2001.
- [105] N. Barhate and P. Cekan. A nucleoside that contains a rigid nitroxide spin label: a fluorophore in disguise. *Angew. Int. Ed.*, 46(15), 2007.

-
- [106] M. Khrenova, I. Topol, J. Collins, and A. Nemukhin. Estimating orientation factors in the FRET theory of fluorescent proteins: the TagRFP-KFP pair and beyond. *Biophys. J.*, 108(1):126–32, 2015.
- [107] C. Chen, M. Li, Y. Xing, Y. Li, C.-C. Joedecke, J. Jin, Z. Yang, and D. Liu. Study of pH-Induced Folding and Unfolding Kinetics of the DNA i-Motif by Stopped-Flow Circular Dichroism. *Langmuir*, 28(51):17743–17748, 2012.
- [108] N. J. Greenfield. Applications of circular dichroism in protein and peptide analysis. *TrAC Trends Anal. Chem.*, 18(4):236–244, 1999.
- [109] J. Laane, editor. *Frontiers and Advances in Molecular Spectroscopy*. Elsevier/Academic Press, 2018.
- [110] A. Cavalli, X. Salvatella, C. M. Dobson, and M. Vendruscolo. Protein structure determination from NMR chemical shifts. *Proc. Natl. Acad. Sci.*, 104(23):9615–9620, 2007.
- [111] D. S. Wishart, D. Arndt, M. Berjanskii, P. Tang, J. Zhou, and G. Lin. CS23D: a web server for rapid protein structure generation using NMR chemical shifts and sequence data. *Nucleic Acids Res.*, 36:W496–W502, 2008.
- [112] S. Raman, O. F. Lange, P. Rossi, M. Tyka, X. Wang, J. Aramini, G. Liu, T. A. Ramelot, A. Eletsky, T. Szyperski, M. A. Kennedy, J. Prestegard, G. T. Montelione, and D. Baker. NMR structure determination for larger proteins using backbone-only data. *Science*, 327(5968):1014–8, 2010.
- [113] K. A. Schnorr, D. B. Gophane, C. Helmling, E. Cetiner, K. Pasemann, B. Fürtig, A. Wacker, N. S. Qureshi, M. Gränz, D. Barthelmes, H. R. Jonker, E. Stirnal, S. Th. Sigurdsson, and H. Schwalbe. Impact of spin label rigidity on extent and accuracy of distance information from PRE data. *J. Biomol. NMR*, 68(68):53–63, 2017.
- [114] J. Iwahara, , C. D. Schwieters, and M. G. Clore. Characterization of Nonspecific Protein-DNA Interactions by ^1H Paramagnetic Relaxation Enhancement. *J. Am. Chem. Soc.*, 126(40), 2004.
- [115] C. Helmling, D.-P. Klötzner, F. Sochor, R. A. Mooney, A. Wacker, R. Landick, B. Fürtig, A. Heckel, and H. Schwalbe. Life times of metastable states guide regulatory signaling in transcriptional riboswitches. *Nat. Comm.*, 9(944), 2018.
- [116] D. Klostermeier and C. Hammann, editors. *RNA Structure and Folding*. Walter de Gruyter GmbH, 2013.
- [117] D. N. Beratan, R. Naaman, and D. H. Waldeck. Charge and spin transport through nucleic acids. *Curr. Opin. Electrochem.*, 4(1):175–181, 2017.
- [118] A. L. Feig. Applications of isothermal titration calorimetry in RNA biochemistry and biophysics. *Biopolymers*, 87(5-6):293–301, 2007.

BIBLIOGRAPHY

- [119] M. H. Levitt. The birth of computational structural biology. *Nat. Struct. Biol.*, 8(5):392–393, 2001.
- [120] W. L. Jorgensen, J. Chandrasekhar, J. D. Madura, R. W. Impey, and M. L. Klein. Comparison of simple potential functions for simulating liquid water. *J. Chem. Phys.*, 79(2):926–935, 1983.
- [121] S. Piana, A. G. Donchev, P. Robustelli, and D. E. Shaw. Water Dispersion Interactions Strongly Influence Simulated Structural Properties of Disordered Protein States. *J. Phys. Chem. B*, 119(16), 2015.
- [122] D. A. Case, T. E. Cheatham, T. Darden, H. Gohlke, R. Luo, K. M. Merz, A. Onufriev, C. Simmerling, B. Wang, and R. J. Woods. The Amber biomolecular simulation programs. *J. Comput. Chem.*, 26(16):1668–1688, 2005.
- [123] W. D. Cornell, P. Cieplak, C. I. Bayly, I. R. Gould, K. M. Merz, D. M. Ferguson, D. C. Spellmeyer, T. Fox, J. W. Caldwell, and P. A. Kollman. A Second Generation Force Field for the Simulation of Proteins, Nucleic Acids, and Organic Molecules. *J. Am. Chem. Soc.*, 117(19):5179–5197, 1995.
- [124] T. E. Cheatham, P. Cieplak, and P. A. Kollman. A Modified Version of the Cornell et al. Force Field with Improved Sugar Pucker Phases and Helical Repeat. *J. Biomol. Struct. Dyn.*, 16(4):845–862, 1999.
- [125] J. Wang, P. Cieplak, and P. A. Kollman. How well does a restrained electrostatic potential (RESP) model perform in calculating conformational energies of organic and biological molecules? *J. Comput. Chem.*, 21(12):1049–1074, 2000.
- [126] A. Pérez, I. Marchán, D. Svozil, J. Šponer, T. E. Cheatham, C. A. Laughton, and M. Orozco. Refinement of the AMBER force field for nucleic acids: improving the description of alpha/gamma conformers. *Biophys. J.*, 92(11):3817–29, 2007.
- [127] M. Zgarbová, M. Otyepka, J. Šponer, A. Mládek, P. Banáš, T. E. Cheatham, and P. Jurečka. Refinement of the Cornell *et al.* Nucleic Acids Force Field Based on Reference Quantum Chemical Calculations of Glycosidic Torsion Profiles. *J. Chem. Theory Comput.*, 9:2886–2902, 2011.
- [128] M. Krepl, M. Zgarbová, P. Stadlbauer, M. Otyepka, P. Banáš, J. Koča, T. E. Cheatham, P. Jurečka, and J. Šponer. Reference Simulations of Noncanonical Nucleic Acids with Different χ Variants of the AMBER Force Field: Quadruplex DNA, Quadruplex RNA, and Z-DNA. *J. Chem. Theory Comput.*, 8(7):2506–2520, 2012.
- [129] M. Zgarbová, F. J. Luque, J. Šponer, T. E. Cheatham, M. Otyepka, and P. Jurečka. Toward Improved Description of DNA Backbone: Revisiting Epsilon and Zeta Torsion Force Field Parameters. *J. Chem. Theory Comput.*, 9(5):2339–2354, 2013.

-
- [130] J. A. Maier, C. Martinez, K. Kasavajhala, L. Wickstrom, K. E. Hauser, and C. Simmerling. ff14SB: Improving the Accuracy of Protein Side Chain and Backbone Parameters from ff99SB. *J. Chem. Theory Comput.*, 11(8):3696–3713, 2015.
- [131] M. Zgarbová, J. Šponer, M. Otyepka, T. E. Cheatham, R. Galindo-Murillo, and P. Jurečka. Refinement of the Sugar-Phosphate Backbone Torsion Beta for AMBER Force Fields Improves the Description of Z- and B-DNA. *J. Chem. Theory Comput.*, 11(12):5723–5736, 2015.
- [132] I. Ivani, P. D. Dans, A. Noy, A. Pérez, I. Faustino, A. Hospital, J. Walther, P. Andrio, R. Goñi, A. Balaceanu, G. Portella, F. Battistini, J. L. Gelpí, C. González, M. Vendruscolo, C. A. Laughton, S. A. Harris, D. A. Case, and M. Orozco. Parmbsc: a refined force field for DNA simulations. *Nat. Methods*, 13(1):55–58, 2015.
- [133] D. Tan, S. Piana, R. M. Dirks, and D. E. Shaw. RNA force field with accuracy comparable to state-of-the-art protein force fields. *Proc. Natl. Acad. Sci.*, 115(7):E1346–E1355, 2018.
- [134] R. Galindo-Murillo, J. C. Robertson, M. Zgarbová, J. Šponer, M. Otyepka, P. Jurečka, and T. Cheatham. Assessing the Current State of Amber Force Field Modifications for DNA. *J. Chem. Theory Comput.*, 12(8):4114–4127, 2016.
- [135] D. L. Beveridge, G. A. Barreiro, S. Byun, D. A. Case, T. E. Cheatham, S. B. Dixit, E. Giudice, F. Lankas, R. Lavery, J. H. Maddocks, R. Osman, E. Seibert, H. Sklenar, G. Stoll, K. M. Thayer, P. Varnai, and M. A. Young. Molecular Dynamics Simulations of the 136 Unique Tetranucleotide Sequences of DNA Oligonucleotides. I. Research Design and Results on d(CpG) Steps. *Biophys. J.*, 87(6):3799–3813, 2004.
- [136] S. B. Dixit, D. L. Beveridge, D. A. Case, T. E. Cheatham, E. Giudice, F. Lankas, R. Lavery, J. H. Maddocks, R. Osman, H. Sklenar, K. M. Thayer, and P. Varnai. Molecular Dynamics Simulations of the 136 Unique Tetranucleotide Sequences of DNA Oligonucleotides. II: Sequence Context Effects on the Dynamical Structures of the 10 Unique Dinucleotide Steps. *Biophys. J.*, 89(6):3721–3740, 2005.
- [137] J. S. Richardson, B. Schneider, L. W. Murray, G. J. Kapral, R. M. Immormino, J. J. Headd, D. C. Richardson, D. Ham, E. Hershkovits, L. D. Williams, K. S. Keating, A. M. Pyle, D. Micallef, J. Westbrook, and H. M. Berman. RNA backbone: consensus all-angle conformers and modular string nomenclature (an RNA Ontology Consortium contribution). *RNA*, 14(3):465–81, 2008.
- [138] E. Zavoisky. Spin-magnetic resonance in paramagnetics. *J. Phys. USSR*, 9:211–245, 1945.
- [139] W. Gerlach and O. Stern. Der experimentelle Nachweis der Richtungsquantelung im Magnetfeld. *Zeitschrift für Phys.*, 9(1):349–352, 1922.

BIBLIOGRAPHY

- [140] J. Iwahara, D. E. Anderson, E. C. Murphy, and G. M. Clore. EDTA-Derivatized Deoxythymidine as a Tool for Rapid Determination of Protein Binding Polarity to DNA by Intermolecular Paramagnetic Relaxation Enhancement. *J. Am. Chem. Soc.*, 125(22):6634–6635, 2003.
- [141] Y. Song, T. J. Meade, A. V. Astashkin, E. L. Klein, J. H. Enemark, and A. Rait-simring. Pulsed dipolar spectroscopy distance measurements in biomacromolecules labeled with Gd(III) markers. *J. Magn. Reson.*, 210(1):59–68, 2011.
- [142] T. F. Cunningham, M. D. Shannon, M. R. Putterman, R. J. Arachchige, I. Sengupta, M. Gao, C. P. Jaroniec, and S. Saxena. Cysteine-Specific Cu²⁺ Chelating Tags Used as Paramagnetic Probes in Double Electron Electron Resonance. *J. Phys. Chem. B*, 119(7):2839–2843, 2015.
- [143] D. Goldfarb. Gd³⁺ spin labeling for distance measurements by pulse EPR spectroscopy. *Phys. Chem. Chem. Phys.*, 16(21):9685, 2014.
- [144] A. K. Hoffmann and A. T. Henderson. A new stable free radical: di-*t*-butylnitroxide. *J. Am. Chem. Soc.*, 83(22):4671–4672, 1961.
- [145] B. Odom, D. Hanneke, B. D’Urso, and G. Gabrielse. New Measurement of the Electron Magnetic Moment Using a One-Electron Quantum Cyclotron. *Phys. Rev. Lett.*, 97(3):030801, 2006.
- [146] R. S. Van Dyck, P. B. Schwinberg, and H. G. Dehmelt. Electron magnetic moment from geonium spectra: Early experiments and background concepts. *Phys. Rev. D*, 34(3):722–736, 1986.
- [147] S. Stoll and A. Schweiger. EasySpin, a comprehensive software package for spectral simulation and analysis in EPR. *J. Magn. Reson.*, 178:42–55, 2005.
- [148] P. P. Borbat, E. R. Georgieva, and J. H. Freed. Improved Sensitivity for Long-Distance Measurements in Biomolecules: Five-Pulse Double Electron-Electron Resonance. *J. Phys. Chem. Lett.*, 4(1):170–175, 2013.
- [149] R. E. Martin, M. Pannier, F. Diederich, V. Gramlich, M. Hubrich, and H. W. Spiess. Determination of End-to-End Distances in a Series of TEMPO Diradicals of up to 2.8 nm Length with a New Four-Pulse Double Electron Electron Resonance Experiment. *Angew. Chemie Int. Ed.*, 37(20):2833–2837, 1998.
- [150] A. Marko, D. Margraf, H. Yu, Y. Mu, G. Stock, and T. F. Prisner. Molecular orientation studies by pulsed electron-electron double resonance experiments. *J. Chem. Phys.*, 130(6):064102, 2009.
- [151] A. Marko, D. Margraf, P. Cekan, S. Th. Sigurdsson, O. Schiemann, and T. F. Prisner. Analytical method to determine the orientation of rigid spin labels in DNA. *Phys. Rev. E - Stat. Nonlinear, Soft Matter Phys.*, 81(2):1–9, 2010.

-
- [152] C. Abé, D. Klose, F. Dietrich, W. H. Ziegler, Y. Polyhach, G. Jeschke, and H. J. Steinhoff. Orientation selective DEER measurements on vinculin tail at X-band frequencies reveal spin label orientations. *J. Magn. Reson.*, 216:53–61, 2012.
- [153] D. Abdullin, G. Hagelueken, R. I. Hunter, G. M. Smith, and O. Schiemann. Geometric model-based fitting algorithm for orientation-selective PELDOR data. *Mol. Phys.*, 113(6):544–560, 2014.
- [154] C. M. Grytz, S. Kazemi, A. Marko, P. Cekan, P. Güntert, S. Th. Sigurdsson, and T. F. Prisner. Determination of helix orientations in a flexible DNA by multi-frequency EPR spectroscopy. *Phys. Chem. Chem. Phys.*, 19(44):29801–29811, 2017.
- [155] G. Jeschke, V. Chechik, P. Ionita, A. Godt, H. Zimmermann, J. Banham, C. R. Timmel, D. Hilger, and H. Jung. DeerAnalysis2006 a comprehensive software package for analyzing pulsed ELDOR data. *Appl. Magn. Reson.*, 30(3-4):473–498, 2006.
- [156] H. Y. Carr and E. M. Purcell. Effects of Diffusion on Free Precession in Nuclear Magnetic Resonance Experiments. *Phys. Rev.*, 94(3):630–638, 1954.
- [157] N. Erlenbach, B. Endeward, P. Schöps, D. B. Gophane, S. Th. Sigurdsson, and T. F. Prisner. Flexibilities of isoindoline-derived spin labels for nucleic acids by orientation selective PELDOR. *Phys. Chem. Chem. Phys.*, 18(24):16196–16201, 2016.
- [158] L. S. Stelzl, N. Erlenbach, M. Heinz, T. F. Prisner, and G. Hummer. Resolving the conformational dynamics of DNA with Ångstrom Resolution by PELDOR and Molecular Dynamics. *J. Am. Chem. Soc.*, 30(139):11674–11677, 2017.
- [159] M. Gränz, N. Erlenbach, P. Spindler, D. B. Gophane, L. S. Stelzl, S. Th. Sigurdsson, and T. F. Prisner. Dynamics of Nucleic Acids at Room Temperature Revealed by Pulsed EPR Spectroscopy. *Angew. Chemie - Int. Ed.*, 57:10540–10543, 2018.
- [160] A. M. Bowen, N. Erlenbach, P. van Os, L. S. Stelzl, S. Th. Sigurdsson, and T. F. Prisner. Orientation Selective 2D-SIFTER Experiments at X-Band Frequencies. *Appl. Magn. Reson.*, 49(12):1355–1368, 2018.
- [161] N. Erlenbach, C. Grünewald, B. Krstic, A. Heckel, and T. F. Prisner. End-to-end stacking of small dsRNA. *RNA*, 25:239–246, 2019.
- [162] G. Jeschke. Determination of the Nanostructure of Polymer Materials by Electron Paramagnetic Resonance Spectroscopy. *Macromol. Rapid Commun.*, 23(4):227–246, 2002.
- [163] M. Persson, J. R. Harbridge, P. Hammarström, R. Mitri, L.-G. Mårtensson, U. Carlsson, G. R. Eaton, and S. S. Eaton. Comparison of Electron Paramagnetic Resonance Methods to Determine Distances between Spin Labels on Human Carbonic Anhydrase II. *Biophys. J.*, 80(6):2886–2897, 2001.

BIBLIOGRAPHY

- [164] M. K. Bowman, A. G. Maryasov, N. Kim, and V. J. DeRose. Visualization of distance distribution from pulsed double electron-electron resonance data. *Appl. Magn. Reson.*, 26(1-2):23–39, 2004.
- [165] R. Ward, D. J. Keeble, H. El-Mkami, and D. G. Norman. Distance determination in heterogeneous DNA model systems by pulsed EPR. *Chem. Bio. Chem.*, 8(16):1957–64, 2007.
- [166] Q. Cai, A. K. Kusnetzow, W. L. Hubbell, I. S. Haworth, G. P. C. Gacho, N. Van Eps, K. Hideg, E. J. Chambers, and P. Z. Qin. Site-directed spin labeling measurements of nanometer distances in nucleic acids using a sequence-independent nitroxide probe. *Nucleic Acids Res.*, 34(17):4722–30, 2006.
- [167] A. Marko and T. F. Prisner. An algorithm to analyze PELDOR data of rigid spin label pairs. *Phys. Chem. Chem. Phys.*, 15(2):619–627, 2013.
- [168] G. Sicoli, G. Mathis, O. Delalande, Y. Boulard, D. Gasparutto, and S. Gambarelli. Double Electron-Electron Resonance (DEER): A Convenient Method To Probe DNA Conformational Changes. *Angew. Chemie*, 120(4):747–749, 2008.
- [169] D. Wunnicke, P. Ding, F. Seela, and H.-J. Steinhoff. Site-Directed Spin Labeling of DNA Reveals Mismatch-Induced Nanometer Distance Changes between Flanking Nucleotides. *J. Phys. Chem. B*, 116(14):4118–4123, 2012.
- [170] D. Wunnicke, P. Ding, H. Yang, F. Seela, and H.-J. Steinhoff. DNA with Parallel Strand Orientation: A Nanometer Distance Study with Spin Labels in the Watson-Crick and the Reverse Watson-Crick Double Helix. *J. Phys. Chem. B*, 119(43):13593–13599, 2015.
- [171] N. A. Kuznetsov, A. D. Milov, V. V. Koval, R. I. Samoilova, Y. A. Grishin, D. G. Knorre, Y. D. Tsvetkov, O. S. Fedorova, and S. A. Dzuba. PELDOR study of conformations of double-spin-labeled single- and double-stranded DNA with non-nucleotide inserts. *Phys. Chem. Chem. Phys.*, 11(31):6826, 2009.
- [172] X. Zhang, C.-S. Tung, G. Z. Sowa, M. M. Hatmal, I. S. Haworth, and P. Z. Qin. Global Structure of a Three-Way Junction in a Phi29 Packaging RNA Dimer Determined Using Site-Directed Spin Labeling. *J. Am. Chem. Soc.*, 134(5):2644–2652, 2012.
- [173] I. Krstic, O. Frolov, D. Sezer, B. Endeward, J. E. Weigand, B. Suess, J. W. Engels, and T. F. Prisner. PELDOR Spectroscopy Reveals Preorganization of the Neomycin-Responsive Riboswitch Tertiary Structure. *J. Am. Chem. Soc.*, 132(5):1454–1455, 2010.
- [174] N.-K. Kim, M. K. Bowman, and V. J. DeRose. Precise Mapping of RNA Tertiary Structure via Nanometer Distance Measurements with Double Electron-Electron Resonance Spectroscopy. *J. Am. Chem. Soc.*, 132(26):8882–8884, 2010.

-
- [175] N. A. Kuznetsov, A. D. Milov, N. P. Isaev, Y. N. Vorobjev, V. V. Koval, S. A. Dzuba, O. S. Fedorova, and Y. D. Tsvetkov. PELDOR analysis of enzyme-induced structural changes in damaged DNA duplexes. *Mol. Biosyst.*, 7(9):2670, 2011.
- [176] B. E. Bode, D. Margraf, J. Plackmeyer, G. Dürner, T. F. Prisner, and O. Schiemann. Counting the Monomers in Nanometer-Sized Oligomers by Pulsed Electron-Electron Double Resonance. *J. Am. Chem. Soc.*, 129:6736–6745, 2007.
- [177] J. M. Sturtevant, S. A. Rice, and E. P. Geiduschek. The stability of the helical deoxyribonucleic acid (DNA) molecule in solution. *Discuss. Faraday Soc.*, 25:138–149, 1958.
- [178] C. A. Hunter and J. K. M. Sanders. The nature of pi-pi interactions. *J. Am. Chem. Soc.*, 112(14):5525–5534, 1990.
- [179] F. Häse and M. Zacharias. Free energy analysis and mechanism of base pair stacking in nicked DNA. *Nucleic Acids Res.*, 44(15):7100–7108, 2016.
- [180] J. Florián, J. Šponer, and A. Warshel. Thermodynamic Parameters for Stacking and Hydrogen Bonding of Nucleic Acid Bases in Aqueous Solution: Ab Initio/Langevin Dipoles Study. *J. Phys. Chem.*, 103:884–892, 1999.
- [181] X. Qiu, K. Andresen, L. W. Kwok, J. S. Lamb, H. Y. Park, and L. Pollack. Inter-DNA attraction mediated by divalent counterions. *Phys. Rev. Lett.*, 99:1–4, 2007.
- [182] A. Kniss, D. Schuetz, S. Kazemi, L. Pluska, P. E. Spindler, V. V. Rogov, K. Husnjak, I. Dikic, P. Güntert, T. Sommer, T. F. Prisner, and V. Dötsch. Chain Assembly and Disassembly Processes Differently Affect the Conformational Space of Ubiquitin Chains. *Structure*, 26(2):249–258.e4, 2018.
- [183] Y. Polyhach, E. Bordignon, and G. Jeschke. Rotamer libraries of spin labelled cysteines for protein studies. *Phys. Chem. Chem. Phys.*, 13(6):2356–66, 2011.
- [184] M. Sajid and G. Jeschke. Conformationally unambiguous spin labeling for distance measurements. *Chem. Eur.*, 15:12960–12963, 2009.
- [185] P. M. Gannett, E. Darian, J. H. Powell, and E. M. Johnson. A Short Procedure for Synthesis of 4-Ethynyl-2,2,6,6-Tetramethyl-3,4-Dehydro-Piperidine-1-Oxyl Nitroxide. *Synth. Commun.*, 31(14):2137–2141, 2001.
- [186] T. R. Miller, S. C. Alley, A. W. Reese, M. S. Solomon, W. V. Mccallister, C. Mailer, B. H. Robinson, and P. B Hopkins. A Probe for Sequence-Dependent Nucleic Acid Dynamics. *J. Am. Chem. Soc.*, 117:9377–9378, 1995.
- [187] Todd R. Miller and Paul B. Hopkins. Toward the synthesis of a second-generation nitroxide spin probe for DNA dynamics studies. *Bioorg. Med. Chem. Lett.*, 4(8):981–986, 1994.

BIBLIOGRAPHY

- [188] T. E. Edwards, P. Cekan, G. W. Reginsson, S. A. Shelke, A. R. Ferré-D'Amaré, O. Schiemann, and S. Th. Sigurdsson. Crystal structure of a DNA containing the planar, phenoxazine-derived bi-functional spectroscopic probe C. *Nucleic Acids Res.*, 39(10):4419–26, 2011.
- [189] C. Höbartner, G. Sicoli, F. Wachowius, D. B. Gophane, and S. Th. Sigurdsson. Synthesis and characterization of RNA containing a rigid and nonperturbing cytidine-derived spin label. *J. Org. Chem.*, 77(17):7749–7754, 2012.
- [190] C. Altenbach, S. L. Flitsch, H. G. Khorana, and W. L. Hubbell. Structural studies on transmembrane proteins. 2. Spin labeling of bacteriorhodopsin mutants at unique cysteines. *Biochemistry*, 28(19):7806–7812, 1989.
- [191] L. J. Berliner, J. Grunwald, H. O. Hankovszky, and K. Hideg. A novel reversible thiol-specific spin label: papain active site labeling and inhibition. *Anal. Biochem.*, 119(2):450–5, 1982.
- [192] A. Spaltenstein, B. H. Robinson, and P. B. Hopkins. Sequence- and structure-dependent DNA base dynamics: synthesis, structure, and dynamics of site, and sequence specifically spin-labeled DNA. *Biochemistry*, 28(24):9484–9495, 1989.
- [193] N. Piton, Y. Mu, G. Stock, T. F. Prisner, O. Schiemann, and J. W. Engels. Base-specific spin-labeling of RNA for structure determination. *Nucleic Acids Res.*, 35(9):3128–3143, 2007.
- [194] T. Weinrich, E. A. Jaumann, U. Scheffer, T. F. Prisner, and M. W. Göbel. A Cytidine Phosphoramidite with Protected Nitroxide Spin Label: Synthesis of a Full-Length TAR RNA and Investigation by In-Line Probing and EPR Spectroscopy. *Chem. - A Eur. J.*, 24(23):6202–6207, 2018.
- [195] M. Kerzhner, D. Abdullin, J. Więcek, H. Matsuoka, G. Hagelueken, O. Schiemann, and M. Famulok. Post-synthetic Spin-Labeling of RNA through Click Chemistry for PELDOR Measurements. *Chem. - A Eur. J.*, 22(34):12113–12121, 2016.
- [196] M. Flaender, G. Sicoli, Th. Fontecave, G. Mathis, C. Saint-Pierre, Y. Boulard, S. Gambarelli, and D. Gasparutto. Site-specific insertion of nitroxide-spin labels into DNA probes by click chemistry for structural analyses by ELDOR spectroscopy. *Nucleic Acids Symp. Ser.*, 52(1):147–148, 2008.
- [197] S. Saha, T. Hetzke, T. F. Prisner, and S. Th. Sigurdsson. Noncovalent spin-labeling of RNA: the aptamer approach. *Chem. Commun.*, 54(83):11749–11752, 2018.
- [198] S. Hong and L. H. Piette. Electron spin resonance spin-label studies of intercalation of ethidium bromide and aromatic amine carcinogens in DNA. *Cancer Res.*, 36(3):1159–71, 1976.
- [199] H. Dugas. Spin-labeled nucleic acids. *Acc. Chem. Res.*, 10(2):47–54, 1977.

-
- [200] S. A. Shelke and S. Th. Sigurdsson. Noncovalent and site-directed spin labeling of nucleic acids. *Angew. Chem. Int. Ed. Engl.*, 43:7984–6, 2010.
- [201] S. Milikisyants, E. J. Groenen, and M. Huber. Observer-selective double electron-electron-spin resonance, a pulse sequence to improve orientation selection. *J. Magn. Reson.*, 2:275–9, 2008.
- [202] J. Jeener and P. Broekaert. Nuclear Magnetic Resonance in Solids: Thermodynamic Effects of a Pair of rf Pulses. *Phys. Rev.*, 157(2):232–240, 1967.
- [203] A. Kupce and R. Freeman. Stretched Adiabatic Pulses for Broadband Spin Inversion. *J. Magn. Reson. Ser. A*, 117(2):246–256, 1995.
- [204] Y. Polyhach, A. Godt, C. Bauer, and G. Jeschke. Spin pair geometry revealed by high-field DEER in the presence of conformational distributions. *J. Magn. Reson.*, 185(1):118–129, 2007.
- [205] K. Sale, L. Song, Y.-S. Liu, E. Perozo, and P. Fajer. Explicit Treatment of Spin Labels in Modeling of Distance Constraints from Dipolar EPR and DEER. *J. Am. Chem. Soc.*, 127(26):9334–9335, 2005.
- [206] A. Milov, Y. Tsvetkov, E. Gorbunova, L. Mustaeva, T. Ovchinnikova, J.-W. Handgraaf, and J. Raap. Solvent Effects on the Secondary Structure of the Membrane-Active Zervamicin Determined by PELDOR Spectroscopy. *Chem. Biodivers.*, 4(6):1243–1255, 2007.
- [207] R. Pievo, C. Casati, P. Franchi, E. Mezzina, M. Bennati, and M. Lucarini. End-to-End Distance Determination in a Cucurbit[6]uril-Based Rotaxane by PELDOR Spectroscopy. *Chem. Phys. Chem.*, 13(11):2659–2661, 2012.
- [208] B. H. Robinson, L. J. Slutsky, and F. P. Auteri. Direct simulation of continuous wave electron paramagnetic resonance spectra from Brownian dynamics trajectories. *J. Chem. Phys.*, 96(4):2609–2616, 1992.
- [209] H.-J. Steinhoff and W. L. Hubbell. Calculation of electron paramagnetic resonance spectra from Brownian dynamics trajectories: application to nitroxide side chains in proteins. *Biophys. J.*, 71(4):2201–12, 1996.
- [210] C. Beier and H.-J. Steinhoff. A structure-based simulation approach for electron paramagnetic resonance spectra using molecular and stochastic dynamics simulations. *Biophys. J.*, 91(7):2647, 2006.
- [211] D. E. Budil, K. L. Sale, K. A. Khairy, and P. G. Fajera. Calculating Slow-Motional Electron Paramagnetic Resonance Spectra from Molecular Dynamics Using a Diffusion Operator Approach. *J. Phys. Chem. A*, 110(10), 2006.
- [212] S. C. DeSensi, D. P. Rangel, A. H. Beth, T. P. Lybrand, and E. J. Hustedt. Simulation of Nitroxide Electron Paramagnetic Resonance Spectra from Brownian Trajectories and Molecular Dynamics Simulations. *Biophys. J.*, 94(10):3798–3809, 2008.

BIBLIOGRAPHY

- [213] D. Sezer, J. H. Freed, and B. Roux. Multifrequency Electron Spin Resonance Spectra of a Spin-Labeled Protein Calculated from Molecular Dynamics Simulations. *J. Am. Chem. Soc.*, 131(7):2597–2605, 2009.
- [214] V. S. Oganessian. A general approach for prediction of motional EPR spectra from Molecular Dynamics (MD) simulations: application to spin labelled protein. *Phys. Chem. Chem. Phys.*, 13(10):4724, 2011.
- [215] E. Kuprusevicius, G. White, and V. S. Oganessian. Prediction of nitroxide spin label EPR spectra from MD trajectories: application to myoglobin. *Faraday Discuss.*, 148(0):283–298, 2011.
- [216] M. A. Stevens, J. E. McKay, J. L. S. Robinson, H. EL Mkami, G. M. Smith, and D. G. Norman. The use of the Rx spin label in orientation measurement on proteins, by EPR. *Phys. Chem. Chem. Phys.*, 18(8):5799–5806, 2016.
- [217] S. J. Hirst, N. Alexander, H. S. Mchaourab, and J. Meiler. RosettaEPR: An integrated tool for protein structure determination from sparse EPR data. *J. Struct. Biol.*, 173(3):506–514, 2011.
- [218] N. S. Alexander, R. A. Stein, H. A. Koteiche, K. W. Kaufmann, H. S. Mchaourab, and J. Meiler. RosettaEPR: Rotamer Library for Spin Label Structure and Dynamics. *PLoS One*, 8(9):e72851, 2013.
- [219] R. Dastvan, E.-M. Brouwer, D. Schuetz, O. Mirus, E. Schleiff, and T. F. Prisner. Relative Orientation of POTRA Domains from Cyanobacterial Omp85 Studied by Pulsed EPR Spectroscopy. *Biophys. J.*, 110(10):2195–2206, 2016.
- [220] J. Gore, Z. Bryant, M. Nöllmann, M. U. Le, N. R. Cozzarelli, and C. Bustamante. DNA overwinds when stretched. *Nature*, 442(7104):836–839, 2006.
- [221] R. Mathew-Fenn, R. Das, and P. Harbury. Remeasuring the Double Helix. *Science*, 17(322):447–449, 2008.
- [222] K. Liebl, T. Drsata, F. Lankas, J. Lipfert, and M. Zacharias. Explaining the striking difference in twist-stretch coupling between DNA and RNA: A comparative molecular dynamics analysis. *Nucleic Acids Res.*, 43(21):10143–56, 2015.
- [223] O. A. Shushakov, S. A. Dzyuba, and Y.D. Tsvetkov. Determining methyl-group internal-rotation barriers for nitroxyl-radical paramagnetic-moiety screening by electron spin echo. *Zhurnal Strukt. Khimii*, 30(4):75–80, 1989.
- [224] A. Rajca, V. Kathirvelu, S. K. Roy, M. Pink, S. Rajca, S. Sarkar, S. S. Eaton, and G. R. Eaton. A spirocyclohexyl nitroxide amino acid spin label for pulsed EPR spectroscopy distance measurements. *Chemistry*, 16(19):5778–82, 2010.
- [225] V. Meyer, M. A. Swanson, L. J. Clouston, P. J. Boratyński, R. A. Stein, H. S. Mchaourab, A. Rajca, S. S. Eaton, and G. R. Eaton. Room-Temperature Distance Measurements of Immobilized Spin-Labeled Protein by DEER/PELDOR. *Biophys. J.*, 108(5):1213–1219, 2015.

-
- [226] B. Epel, G. Redler, V. Tormyshev, and H. J. Halpern. Towards Human Oxygen Images with Electron Paramagnetic Resonance Imaging. In *Adv. Exp. Med. Biol.*, volume 876, pages 363–369. 2016.
- [227] R. Owenius, G. R. Eaton, and S. S. Eaton. Frequency (250MHz to 9.2GHz) and viscosity dependence of electron spin relaxation of triarylmethyl radicals at room temperature. *J. Magn. Reson.*, 172(1):168–175, 2005.
- [228] A. A. Kuzhelev, D. V. Trukhin, O. A. Krumkacheva, R. K. Strizhakov, O. Y. Rogozhnikova, T. I. Troitskaya, M. V. Fedin, Vi. M. Tormyshev, and E. G. Bagryanskaya. Room-Temperature Electron Spin Relaxation of Triarylmethyl Radicals at the X- and Q-Bands. *J. Phys. Chem. B*, 119(43):13630–13640, 2015.
- [229] B. Joseph, V. M. Tormyshev, O. Y. Rogozhnikova, D. Akhmetzyanov, E. G. Bagryanskaya, and T. F. Prisner. Selective High-Resolution Detection of Membrane Protein-Ligand Interaction in Native Membranes Using Trityl-Nitroxide PELDOR. *Angew. Chemie Int. Ed.*, 55(38):11538–11542, 2016.
- [230] A. A. Kuzhelev, R. K. Strizhakov, O. A. Krumkacheva, Y. F. Polienko, D. A. Morozov, G. Y. Shevelev, D. V. Pyshnyi, I. A. Kirilyuk, M. V. Fedin, and E. G. Bagryanskaya. Room-temperature electron spin relaxation of nitroxides immobilized in trehalose: Effect of substituents adjacent to NO-group. *J. Magn. Reson.*, 266:1–7, 2016.
- [231] M. Malferrari, A. Savitsky, W. Lubitz, K. Möbius, and G. Venturoli. Protein Immobilization Capabilities of Sucrose and Trehalose Glasses: The Effect of Protein/Sugar Concentration Unraveled by High-Field EPR. *J. Phys. Chem. Lett.*, 7(23):4871–4877, 2016.
- [232] M. Malferrari, A. Savitsky, M. D. Mamedov, G. E. Milanovsky, W. Lubitz, K. Möbius, A. Y. Semenov, and G. Venturoli. Trehalose matrix effects on charge-recombination kinetics in Photosystem I of oxygenic photosynthesis at different dehydration levels. *Biochim. Biophys. Acta - Bioenerg.*, 1857(9):1440–1454, 2016.
- [233] S. D. Allison, B. Chang, T. W. Randolph, and J. F. Carpenter. Hydrogen Bonding between Sugar and Protein Is Responsible for Inhibition of Dehydration-Induced Protein Unfolding. *Arch. Biochem. Biophys.*, 365(2):289–298, 1999.
- [234] L. M. Crowe, J. H. Crowe, A. Rudolph, C. Womersley, and L. Appel. Preservation of freeze-dried liposomes by trehalose. *Arch. Biochem. Biophys.*, 242(1):240–247, 1985.



Cite this: *Phys. Chem. Chem. Phys.*,
2016, **18**, 16196

Flexibilities of isoindoline-derived spin labels for nucleic acids by orientation selective PELDOR†

N. Erlenbach,^a B. Endeward,^a P. Schöps,^a D. B. Gophane,^b S. Th. Sigurdsson^b and T. F. Prisner^{*a}

Pulsed electron double resonance experiments with rigid spin labels can reveal very detailed information about the structure and conformational flexibility of nucleic acid molecules. On the other hand, the analysis of such data is more involved the distance and orientation information encoded in the time domain data need to be extracted and separated. In this respect studies with different spin labels with variable internal mobility are interesting and can help to unambiguously interpret the EPR data. Here orientation selective multi-frequency/multi-field 4-pulse PELDOR/DEER experiments with three recently presented semi-rigid or conformationally unambiguous isoindoline-derived spin labels were performed and simulated quantitatively by taking the spin label dynamics into account. PELDOR measurements were performed for a 20-mer dsDNA with two spin labels attached to two defined uridine derivatives. Measurements were recorded for different spin label positions within the double helical strand and for different magnetic field strengths. The experimental data sets were compared with simulations, taking into account the previously described dsDNA dynamics and the internal motions of the spin label itself, which had shown distinct differences between the three spin labels used. The ^{Exl}mU spin label shows a free rotation around a single bond, which averages out orientation effects, without influencing the distance distribution as it can occur in other spin labels. The ^{lm}U and ^{Ox}U spin label, on the other hand, show distinct orientation behaviour with minimal intrinsic motion. We could quantitatively determine this internal motion and demonstrate that the conformational dynamics of the nucleic acid and the spin label can be well separated by this approach.

Received 13th April 2016,
Accepted 24th May 2016

DOI: 10.1039/c6cp02475k

www.rsc.org/pccp

1. Introduction

Nucleic acids play a fundamental role in all forms of life as they are involved in storing, transmitting and expressing genetic information. Furthermore, they have various other functional roles, such as protein synthesis and regulation of gene expression. Information about nucleic acid structure and dynamics gives insight into how they are able to carry out their functions. Their structures, and to some extent dynamics, can be investigated with the established methods of X-ray crystallography^{1,2} and nuclear magnetic resonance (NMR) spectroscopy.^{3–6} However, for a better understanding of the functions of subtle nucleic acids dynamics, for example sequence dependent internal dynamics of duplexes involved with protein recognition, other

spectroscopic techniques, such as fluorescence-based techniques and electron paramagnetic resonance (EPR) spectroscopy are very useful. Both of these techniques require reporter groups, fluorescence spectroscopy requires fluorescent labels while EPR spectroscopy uses paramagnetic spin labels. When single labels are used, both techniques can give information about dynamics, but for structural studies, the distances between two labels must be measured, either using the Foerster resonance energy transfer^{7,8} (FRET) or pulsed electron-electron double resonance^{9–14} (PELDOR/DEER).

Commonly used reporter groups for EPR spectroscopy are aminoxyl radicals, usually called nitroxides. Nitroxides are relatively stable and can be synthetically manipulated and attached site specifically to nucleic acids, a technique referred to as site-directed spin labeling^{15,16} (SDSL). Most nitroxide spin labels have some inherent mobility due to rotation around the tether between label and nucleic acid, giving rise to imprecision when used for distance measurements. We have developed the rigid spin labels Ç and Çm^{17,18} (Fig. 1a) to circumvent this drawback, in which the nitroxides are fused to a nucleobase and do, therefore, not have motion independent of the base. However, if the intrinsic motion of the spin label is strongly restricted,

^a Institute of Physical and Theoretical Chemistry, Center of Biomolecular Magnetic Resonance, Goethe University, Max-von-Laue-Str. 7, D-60438 Frankfurt am Main, Germany. E-mail: prisner@chemie.uni-frankfurt.de

^b Department of Chemistry, Science Institute University of Iceland, Dunhaga 3, 107 Reykjavik, Iceland

† Electronic supplementary information (ESI) available: Rawdata for the Q- and G-band measurements. Additional comparisons between experimental and simulated data. See DOI: 10.1039/c6cp02475k

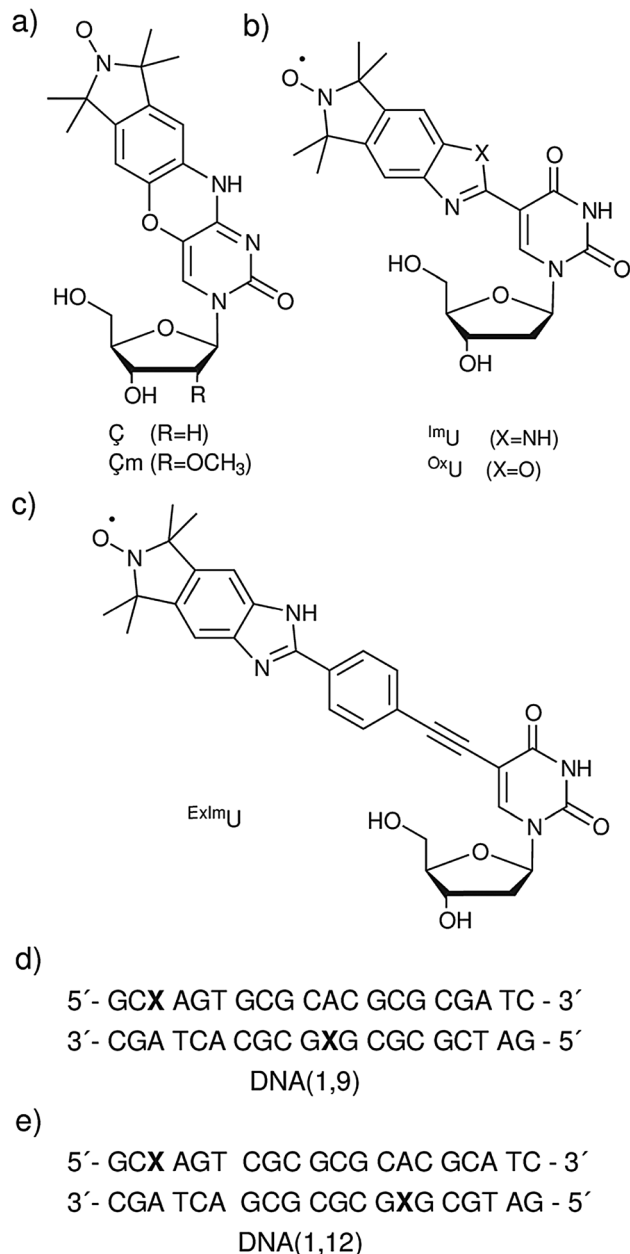


Fig. 1 Spin-labeled nucleosides. (a) Rigid spin labels Ç and Ç_m (b) Isoindoline derived spin labels ^{Im}U and ^{Ox}U. (c) Benzimidazoline spin label Ex^{Im}U. (d and e) The sequence for DNA(1,9) and DNA(1,12), respectively. The X indicates the spin label position. The internal motion of the DNA, found in previous studies, which shows a change in the radius of the DNA cylinder without any change of the helix pitch, was utilized along with a simple three axis model for the internal motion of the spin labels to simulate all PELDOR data sets simultaneously.²¹ Excellent fits of all experimental data could be obtained by assuming rotation of the spin labels around the molecular x-axis of the spin label, which is equal to the N–O bond direction, with different amplitudes for the three spin labels investigated. Our analysis proves the semi-rigidity of the isoidoline spin label and gives quantitative values of the internal mobility of these labels. In the case of ^{Im}U, the rotation around the N–O axis of the nitroxide which has the largest influence on the orientation dependence is around ±5°, whereas for ^{Ox}U it was found to be twice as high. In the case of the Ex^{Im}U the assumption of a free rotation around the tether that reduces orientation effects could be deduced. This detailed analyses of the dynamics of ^{Im}U, ^{Ox}U and Ex^{Im}U will facilitate the use of these spin labels for further studies of nucleic acid motifs.

the common assumption of random orientation distribution, which applies to flexible labels, is no longer correct. Therefore, distance analysis of a single time trace using Tikhonov regularization is not applicable. If only reliable distance information are required, this would be a drawback of rigid spin labels. However, the large advantage of rigid spin labels is the access to information about the relative orientation between spin labels and flexibility of the system under study.^{19,20} We have shown that the analysis of distances and relative orientations between such labels using multi-frequency/multi-field PELDOR data sets can give information about the internal motion of double stranded DNA²¹ and the three-way junction of the cocaine aptamer,²² which would be inaccessible with flexible spin labels.

Although Ç shows a high orientation selection in PELDOR experiments, its preparation is non-trivial. For this reason we have recently introduced isoidoline spin labels that are linked by a single bond to a uridine. The semi-rigid spin labels ^{Im}U and ^{Ox}U (Fig. 1b) are restricted in rotation around the single bond linking them to the nucleobase.²³ In particular the ^{Im}U spin label can form an intramolecular hydrogen bond between the NH of the benzimidazole and O4 of the nucleobase. Both ^{Im}U and ^{Ox}U show orientation-dependent changes in the PELDOR time traces as a function of the chosen probe and pump frequencies, although they are less rigid than Ç. Nevertheless even this small intrinsic motion could have an influence on the analysis of the dynamics of the nucleic acids. Therefore, it is necessary to gain an in depth knowledge about the mobility of the spin label itself to be able to separate this from the motion of the biopolymer.

In addition to ^{Im}U and ^{Ox}U, we have prepared the “conformationally unambiguous spin label”²⁴ Ex^{Im}U (Fig. 1c), which can freely rotate around the single bonds flanking the acetylene.²⁵ Since the N–O bond of the nitroxide aligns to the same axis as these bonds, the displacement of the unpaired electron spin due to this rotation should be negligible. However, the orientation should be rather efficiently averaged out by the rotation and this label could be therefore used for direct distance determinations. It was confirmed that PELDOR of this label does not contain observable orientation information at Q-Band frequencies where such measurements are usually performed.²⁶ Nevertheless at higher frequencies, where the in-ring orientations can be also distinguished, even Ex^{Im}U shows some retained orientation dependence (see below).

In this paper, we describe the detailed analysis of the internal motion of the spin labels ^{Im}U, ^{Ox}U and Ex^{Im}U. Two DNA duplexes (DNA(1,9) and DNA(1,12)), which have already been analyzed with regards to their mobility using the rigid spin label Ç, were spin labeled with ^{Im}U, ^{Ox}U and Ex^{Im}U and measured by multi-frequency/multi-field PELDOR.

2. Experimental

Six different samples were used to analyse the flexibility of isoidoline-derived spin labels. The spin labels, ^{Im}U, ^{Ox}U and Ex^{Im}U, were incorporated pairwise into two DNA duplexes (Fig. 1).

The samples were previously measured at X-band frequencies²⁵ and for this work, they were additionally measured at Q-band (33.8 GHz/1.2 T) and G-band (180 GHz/6.4 T) frequencies. The dead-time-free four-pulse PELDOR sequence¹¹ was used for all experiments. In order to extract the intramolecular PELDOR form factor the raw data were pre-processed using the DeerAnalysis2013 software package,²⁷ with homogenous 3D background correction.

2.1 PELDOR sample preparation

The DNA samples for PELDOR measurement were prepared by annealing 10 nmol of each strand with 10 nmol of its complementary strand in phosphate buffer (100 μ L, pH 7.0, NaCl (100 mM), and EDTA (0.1 mM)), followed by evaporation of the water. The annealed dried samples were subsequently dissolved in 20% ethylene glycol/H₂O (100 μ L). The final spin concentrations for all samples are listed in the ESI.† All samples were rapidly frozen and stored in liquid nitrogen until they were measured.

2.2 Q-band measurements

A Bruker Elexsys E580 X/Q-band spectrometer equipped with an Oxford CF935 cryostat and a phase unlocked PELDOR frequency unit was used. A home built loop-gap Q-band resonator with a larger bandwidth was used to achieve higher offsets between pump and probe pulses. Microwave pulses were amplified by a 10 W solid state Q-band amplifier. 64 ns ($\pi/2$ and π)-pulses were used for detection and a 34 ns (π) pump pulse was used. The delay between the first and second probe pulses was 132 ns. The pulse separation between the second and third probe pulse was typically 2.0 μ s. The frequency of the pump pulse was fixed to the intensity maximum of the nitroxide powder spectrum to obtain maximum pumping efficiency. The probe frequency was chosen to be 50, 100 or 150 MHz below this frequency (Fig. 2). All experiments were carried out at a temperature of 50 K.

2.3 G-band measurements

All G-band EPR experiments were performed with a home built G-band spectrometer equipped with two independent frequency sources.^{28–30} The probe pulse length were between 32–40 ns for the $\pi/2$ -pulse and 60–70 ns for the π -pulse and

the pump inversion pulse was adjusted to be about 60 ns. The pulse separation between the first and second probe pulse was 220 ns and 1.8 μ s between the second and third probe pulse. The repetition time of the experiment was between 6 and 8 ms. All experiments were carried out at a temperature of 40 K. Every set of experiments consisted of around 80 time traces averaged with 100 shots per point and were recorded at different field positions across the EPR spectrum, corresponding roughly to the g_{xx} , g_{yy} , and g_{zz} positions of the spectrum (Fig. 2). The probe frequency was set in all cases at a constant offset of 60 MHz above the pump frequency.

2.4 Simulations

A home-written Matlab® program was used for analysis of the PELDOR data. After generating the positions and orientation of the two unpaired electron spins according to the conformational flexibility of both the helix and the spin label, PELDOR time traces were simulated and compared with experimental data. For every simulation, an ensemble of 500 conformers was calculated, to represent the conformational ensemble in the frozen solution. Each simulation was performed in two steps. First, the DNA helix conformational flexibility was calculated according to the correlated change of the helix radius and the length of the DNA, as described in Marko *et al.*²¹ These calculations were done with two constant helix parameters: the helix of the B form DNA was calculated with a 3.3 nm pitch and a contour length of 0.485 nm, which presents the distance between two base pairs along the helix. The mean radius of the helix cylinder was set to 0.585 nm, with a Gaussian distributed standard deviation of 0.065 nm, which reveals a negative twist-stretch coupling. Each C1' atom of the nucleosides was calculated with these parameters. In a second step, the electron spin position of the spin label and their mutual orientation was constructed from the helix. Two rotations are needed to obtain the angles describing their relative orientation. The first rotation started with the vector between the nucleoside C1a and C1b atom and goes around the z axis with $\alpha = 105^\circ$. Additionally a rotation by $\beta = 10^\circ$ around the normal vector of the plane between the z axis and the new vector was applied (Fig. 3). The resulting vector starts from the C1a-atom in the direction of the electron spin. As the distance between the C1a and the electron

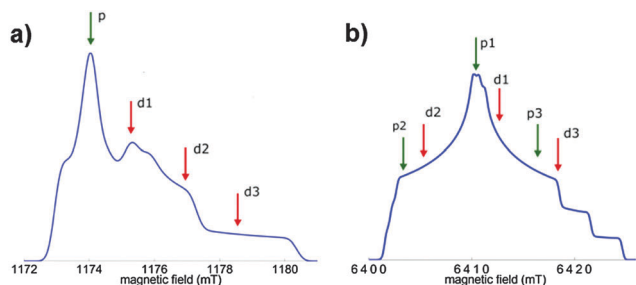


Fig. 2 Simulated field-sweep-spectra at (a) Q-band and (b) G-band frequencies indicating the positions of the PELDOR pump and detection pulses. Green arrows show the position of the pump pulses, the red arrows the detection pulses.

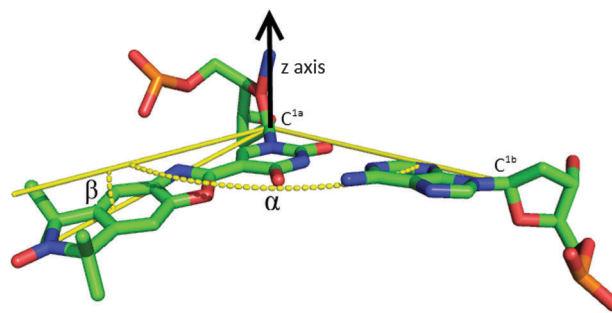


Fig. 3 Isindoline-derived spin label paired to Adenine. The angles between the yellow lines define the rotation angles to calculate the electron spin position with the start C1 coordinates of the paired nucleobases.

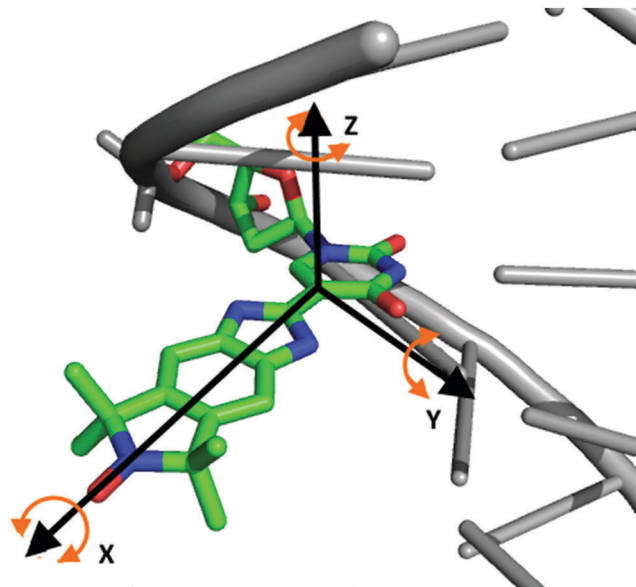


Fig. 4 Modes of spin label motions shown for the ^{1m}U -labelled duplex DNA. In addition to the DNA twist-stretch motions,⁹ rotational variations around the x , y and the z axes were introduced for simulations of the experimental PELDOR time traces.

spin is 1.15 nm for the ^{1m}U and ^{Ox}U spin label and 1.95 nm for the ^{Ex1m}U along this vector, the coordinates of the electron spin could be calculated. These distances and angles are estimated from the model shown in the ESI of Gophane *et al.*²⁵ To allow for the intrinsic internal mobility of the spin labels, we introduced additional rotational motions around the spin label molecular axis. The first one is a rotation around the linker between the spin label and the nucleic acid base. This is calculated as a rotation around the x axis of the spin label (Fig. 4). To model other residual flexibility of the spin label to describe the change of the spatial position of the electron spin relative to the DNA we introduces small angle fluctuation about the other two axis (y and z). All rotations originate at the C5 atom of the uracil.

The y rotation has a more pronounced effect to the damping of the PELDOR oscillation and was adapted to fit the experimental observed damping of the oscillations. The small angle fluctuations around the z -axis have similar effect to the damping but a factor of 10 less. Because it could not be fully distinguished between both fluctuations, the z -rotation were fixed to $\pm 5^\circ$ for all simulations. All three axis motions were calculated independently from each other and are based on Gaussian-distributed angle variations. The calculated electron spin coordinates and the coordinate system of the nitroxide were transformed to distances and Euler angles with respect to a laboratory frame in order to simulate the PELDOR time traces. All optimizations are made by visual comparison of the simulated and experimental time traces as well as by a least square fit procedure. Details regarding our time trace simulation procedure has previously been described.²⁰ Due to poor reproducibility of the modulation depth at G-band, only the frequency of the oscillations and the damping was taken into account for these experiments. Variations in modulation

depths can be caused by uncertainties of the resonator performance and calculation of the excitation profile.

3. Result and discussion

Fig. 5 shows the best simulation results obtained for the three spin labels ^{1m}U , ^{Ox}U and ^{Ex1m}U for the DNA(1,9) construct (see Fig. S5 and S6, ESI† for the corresponding results for the DNA(1,12) construct). In contrast to the spin label ζ , all the three semi-rigid isoindoline spin labels show some intrinsic motion in addition to the mobility of the dsDNA molecule itself. The main internal motion of the spin labels was expected to be around the x -axis of the nitroxide molecular axis system. To simulate the other residual motions of the spin label with respect to the DNA molecular frame, small angle Gaussian distributed fluctuations around the z - and y -axis have been included in our model. The respective angles for all three axis rotations are reported in Table 1.

The rotation around the x axis is of special interest because it directly reflects the expected rotational flexibility around the N-O bond of the spin label. Whereas this rotation is strongly hindered for ^{1m}U and ^{Ox}U , ^{Ex1m}U rotates freely around this bond (a 90° rotation angle distribution reflects a full rotation due to symmetry reasons). For orientation selective measurements, a high rotational freedom is a disadvantage, as it leads to loss of orientation information. On the other hand, the distances from such data might be more easily predicted. Thus ^{Ex1m}U is an almost perfect spin label, for obtaining high-precision distance data alone, although possible structural perturbations in complex folds or in macromolecular complexes must be considered. In comparison the ^{1m}U is limited to an x -rotation of $\pm 5^\circ$, whereas the ^{Ox}U spin label has rotational freedom of $\pm 10^\circ$. These values are independent of the spin label position. Thus, the determined x -axis rotational freedom of the spin labels are in very good agreement with the expectations and fully support the influence of a hydrogen bond between the spin label and the nucleobase in the case of the ^{1m}U spin label. The other two rotations reflect the overall residual flexibility of the spin label. These values should be as small as possible to allow a detailed study of the dynamic of the DNA molecule itself. They are rather similar for all three spin labels investigated, demonstrating that the main difference in the motion of the three spin labels can indeed be described by their rotational freedom around the x -axis. The rotation around the y axis, which correspond to an up and down movement in direction of the helix axis, results for the isoindoline derived spin labels to rotation angles between $\pm 14^\circ$ to $\pm 22^\circ$. These values can be compared to the fluctuations found for the ζ spin label (Fig. S3, ESI†). This rigid spin label shows a small fluctuation with 6° for the y -rotation, while no x -rotation could be observed. These small vibration, could be interpreted as DNA dynamics, that are not explicitly described by our physical model.

These best fit parameters are slightly larger for ^{Ox}U . Additionally these values are slightly larger for the DNA(1,12). This could be caused by a higher mobility at the end of the DNA strand and thus reflect also partly motion of the DNA itself. More systematic studies, including the rigid spin label ζ , have

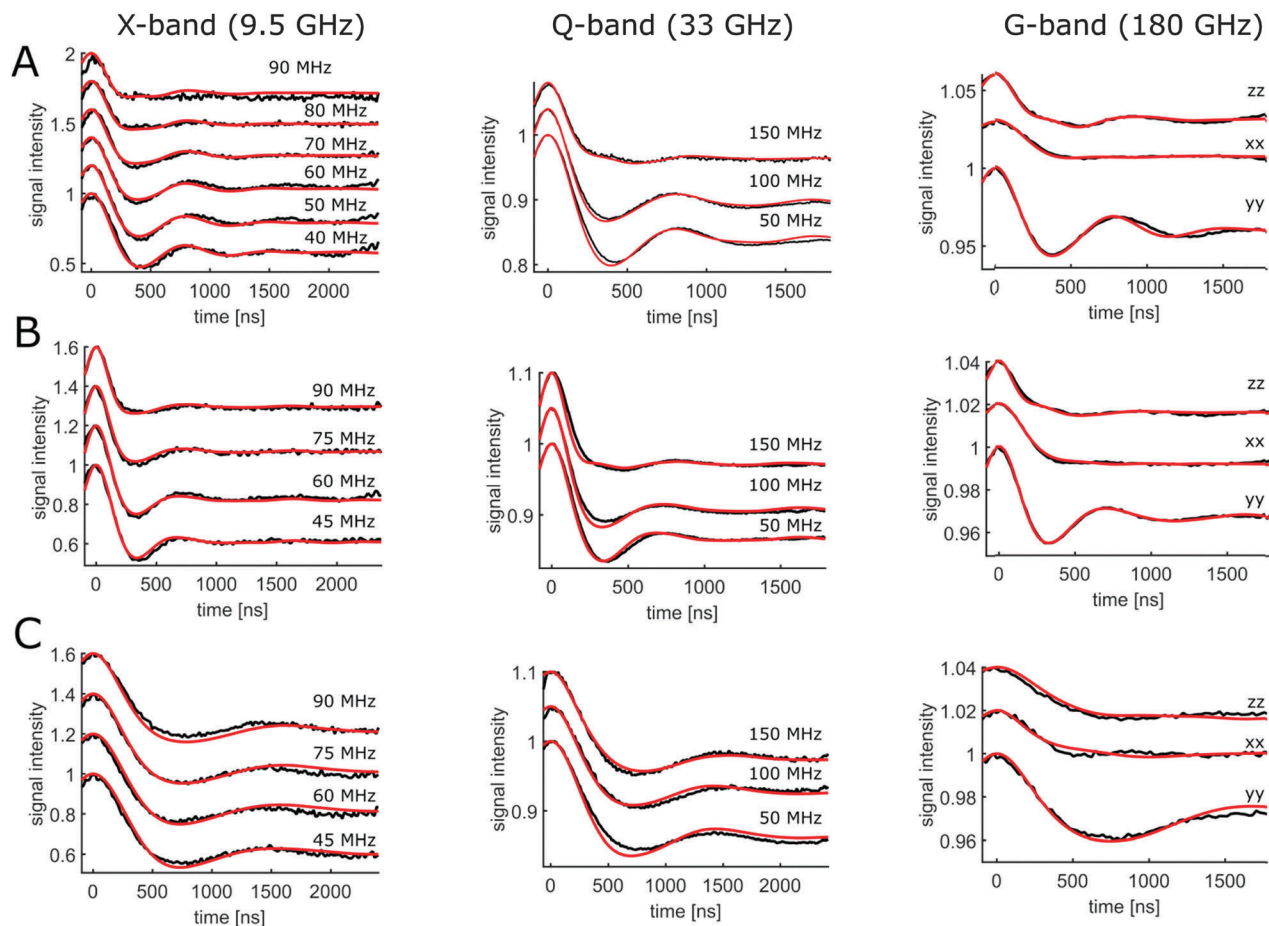


Fig. 5 Experimental (black) and simulated (red) PELDOR time traces. For X-band (right) and Q-band (middle) different offsets $\Delta\nu$ (in MHz) between probe and pump pulse frequency for DNA(1,9) with (A) ^{13}C (B) ^{15}O (C) ^{15}N spin label. G-band (left) PELDOR time traces at the three magnetic field positions corresponding to the main G-tensor components. In these experiments, the difference between pump and probe frequency was kept constant at $\Delta\nu = 60$ MHz.

Table 1 Result for the flexibility of the different spin labels in respect to their position at the DNA. The values represent the result of the global analysis over all frequencies. The numbers in brackets show the error. An example for error estimation is given in the ESI

	x-rotation	y-rotation	z-rotation
^{13}C -DNA(1,9)	5° (2)	14° (1)	5°
^{13}C -DNA(1,12)	5° (2)	20° (1)	5°
^{15}O -DNA(1,9)	10° (2)	18° (1)	5°
^{15}O -DNA(1,12)	10° (5)	22° (2)	5°
^{15}N -DNA(1,9)	90° (5)	12° (2)	5°
^{15}N -DNA(1,12)	90° (10)	16° (2)	5°

to be performed to investigate this further. Overall the spin label ^{13}C is somewhat better for orientation measurements, compared to the ^{15}O spin label.

The simulations that were performed were based on simplified models of the overall conformational motion of the DNA molecule and the spin label and, therefore, the question arises about the uniqueness of the solution and the accurateness of the obtained values. All rotation parameters for the spin label movement were estimated by comparison of the simulated and experimental data from measurements at X- and Q-band.

The y-axis rotation is already rather well defined by the X-band data, because it strongly influences the damping of the dipolar oscillations. For the x-axis rotation only an accuracy of about $\pm 10^\circ$ was possible with the X-band data alone. The effect of this rotation is mainly seen as a change in modulation depth of the X-band time traces for large offsets between pump and probe pulses. However at Q-band frequencies, variation of the x-axis rotation shows also more sensitive changes in the modulation period of the time trace with 15 MHz offset between pump and probe frequency. Despite the fact that these effects are quite small, it led to an enhanced precision of the determination of this important rotation angle to $\pm 3^\circ$. Additional experiments at G-band frequency were performed to take advantage of the fact that at high fields the anisotropy of the g- and A-tensor is fully spectrally resolved, allowing one to distinguish all orientations with high precision. Simulations using the (low field) optimized parameters were performed and compared with the experimental data, as depicted in Fig. S4 in the ESI.† A large deviation between experiment and prediction was observed, especially at the g_{xx} position. A small fixed rotation of the spin label of 9° around the x axis (N–O bond), before the rotation started, improves the fit without influencing the (low field) simulation

time traces. This reflects a slight tilting of the spin label plane with respect to the nucleobase plane. With this very small readjustment of the spin label position, very good predictions of the G-band PELDOR time traces taken at the canonical g -tensor positions could be achieved, indicating that our model with the optimized parameters can indeed be used to accurately model the spin labels. This rotation was also applied to the analysis of the other two spin labels, since they have the same geometry.

4. Conclusion

In this work orientation selective PELDOR experiments were performed at multiple magnetic fields (0.3 T, 1.2 T and 6.4 T) and allowed the determination of the flexibility of the isoindoline-derived spin labels $^{\text{ExIm}}\text{U}$, $^{\text{Im}}\text{U}$ and $^{\text{Ox}}\text{U}$, all of which were covalently attached to a dsDNA. For this purpose, the earlier proposed model for the dsDNA dynamics, consisting of a negative correlated twist-stretch motion with a radius change of the DNA^{21,31} was extended to include the intrinsic rotational freedom of the spin labels. Simulations were found to be in very good agreement with the experimental time traces, which verified the expected different degree of rotational freedom around the N–O axis for the conformationally unambiguous spin label $^{\text{ExIm}}\text{U}$ and the two semi-rigid spin labels, $^{\text{Im}}\text{U}$ and $^{\text{Ox}}\text{U}$. The spin labels showed some additional flexibility, which could be modeled by a 10–20° rotation around the y -axis of the nitroxide molecular axis system. The dependence of this parameter on the position of the spin label might indicate some additional DNA dynamics at the ends of the helix. The parameters describing the internal flexibility of the spin labels, which were obtained from X-band and Q-band PELDOR experiments, predicted very accurately the high-field PELDOR time traces at G-band frequencies. Thus, we believe that our parameterization of the intrinsic nitroxide dynamics is reliable and can be used also for modeling of more complex DNA structures. That will allow to use these new spin labels to study the conformational flexibilities of nucleic acids with respect to their specific sequence, the ionic strength and other parameters effecting their structure and dynamics.

Acknowledgements

We acknowledge financial support from the German Research Foundation (CRC902: Molecular Principles of RNA Based Regulation) and the Icelandic Research Fund (120001022).

References

- 1 D. Klostermeier and C. Hammann, *RNA Structure and Folding*, Walter de Gruyter GmbH, 2013.
- 2 H. M. Al and N. G. Walter, *Curr. Opin. Struct. Biol.*, 2008, **18**, 321–329.
- 3 B. Fürtig, C. Richter, J. Wöhnert and H. Schwalbe, *ChemBioChem*, 2003, **4**, 936–962.
- 4 J. Hennig and M. Sattler, *Protein Sci.*, 2014, **23**, 669–682.
- 5 A. Lapinaite, B. Simon, L. Skjaerven, M. Rakwalska-Bange, F. Gabel and T. Carlomagno, *Nature*, 2013, **502**, 519–523.
- 6 A. Reining, S. Nozinovic, K. Schlepckow, F. Buhr, B. Fürtig and H. Schwalbe, *Nature*, 2013, **499**, 355–359.
- 7 A. Iqbal, S. Arslan, B. Okumus, T. J. Wilson, G. Giraud, D. G. Norman, T. Ha and D. M. J. Lilley, *Proc. Natl. Acad. Sci. U. S. A.*, 2008, **105**, 11176–11181.
- 8 A. K. Wozniak, G. F. Schröder, H. Grubmüller, C. A. M. Seidel and F. Oesterhelt, *Proc. Natl. Acad. Sci. U. S. A.*, 2008, **105**, 18337–18342.
- 9 A. D. Milov, K. Salikhov and M. Shchirov, *Sov. Phys. Solid State*, 1981, **23**, 975–982.
- 10 A. D. Milov, A. Ponomarev and Y. D. Tsvetkov, *Lett. Chem. Phys.*, 1984, **110**, 67–72.
- 11 M. Pannier, S. Veit, A. Godt, G. Jeschke and H. W. Spiess, *J. Magn. Reson.*, 2011, **213**, 316–325.
- 12 T. Prisner, M. Rohrer and F. MacMillan, *Annu. Rev. Phys. Chem.*, 2001, **52**, 279–313.
- 13 G. W. Reginsson, S. A. Shelke, C. Rouillon, M. F. White, S. T. Sigurdsson and O. Schiemann, *Nucleic Acids Res.*, 2013, **41**, 1–10.
- 14 D. Margraf, B. E. Bode, A. Marko, O. Schiemann and T. F. Prisner, *Mol. Phys.*, 2007, **105**, 2153–2160.
- 15 W. L. Hubbell, D. S. Cafiso and C. Altenbach, *Nat. Struct. Biol.*, 2000, **7**, 735–739.
- 16 S. A. Shelke and S. T. Sigurdsson, *Angew. Chem., Int. Ed. Engl.*, 2010, **49**, 7984–7986.
- 17 N. Barhate, P. Cekan, A. P. Massey and S. T. Sigurdsson, *Angew. Chem.*, 2007, **119**, 2709–2712.
- 18 C. Höbartner, G. Sicoli, F. Wachowius, D. B. Gophane and S. T. Sigurdsson, *J. Org. Chem.*, 2012, **77**, 7749–7754.
- 19 T. F. Prisner, a. Marko and S. T. Sigurdsson, *J. Magn. Reson.*, 2015, **252**, 187–198.
- 20 A. Marko, D. Margraf, P. Cekan, S. T. Sigurdsson, O. Schiemann and T. F. Prisner, *Phys. Rev. E: Stat., Nonlinear, Soft Matter Phys.*, 2010, **81**, 1–9.
- 21 A. Marko, V. Denysenkov, D. Margraf, P. Cekan, O. Schiemann, S. T. Sigurdsson and T. F. Prisner, *J. Am. Chem. Soc.*, 2011, **133**, 13375.
- 22 C. M. Grytz, A. Marko, P. Cekan, S. T. Sigurdsson and T. F. Prisner, *Phys. Chem. Chem. Phys.*, 2016, **18**, 2993–3002.
- 23 D. B. Gophane and S. T. Sigurdsson, *Chem. Commun.*, 2013, **49**, 999–1001.
- 24 M. Sajid, G. Jeschke, M. Wiebcke and A. Godt, *Chem. – Eur. J.*, 2009, **15**, 12960–12962.
- 25 D. B. Gophane, B. Endeward, T. F. Prisner and S. T. Sigurdsson, *Chem. – Eur. J.*, 2014, **20**, 15913–15919.
- 26 Y. Polyhach, E. Bordignon, R. Tschaggelar, S. Gandra, A. Godt and G. Jeschke, *Phys. Chem. Chem. Phys.*, 2012, **14**, 10762.
- 27 G. Jeschke, V. Chechik, P. Ionita, A. Godt, H. Zimmermann, J. Banham, C. R. Timmel, D. Hilger and H. Jung, *Appl. Magn. Reson.*, 2006, **30**, 473–498.
- 28 M. M. Hertel, V. P. Denysenkov, M. Bennati and T. F. Prisner, *Magn. Reson. Chem.*, 2005, **43**, S248–S255.
- 29 M. Rohrer, O. Brüggemann, B. Kinzer and T. Prisner, *Appl. Magn. Reson.*, 2001, **21**, 257–274.
- 30 V. P. Denysenkov, T. F. Prisner, J. Stubbe and M. Bennati, *Appl. Magn. Reson.*, 2005, **29**, 375–384.
- 31 J. Gore, Z. Bryant, M. Nöllmann, M. U. Le, N. R. Cozzarelli and C. Bustamante, *Nature*, 2006, **442**, 836–839.

Supporting Information

Flexibilities of Isoindoline-Derived Spin Labels by Orientation Selective PELDOR

N. Erlenbach^a, B. Endeward^a, P. Schöps^a, D. B. Gophane^b, S. Th. Sigurdsson^{*b} and T. F. Prisner^{*a}

^a Institute of Physical and Theoretical Chemistry and Center of Biomolecular Magnetic Resonance, Goethe University, 60438 Frankfurt am Main, Max-von-Laue-Str. 9, Hessen, Germany

^b University of Iceland, Department of Chemistry, Science Institute, Dunhaga 3, 107 Reykjavik, Iceland

* To whom correspondence should be addressed. Email: prisner@chemie.uni-frankfurt.de, snorrissi@hi.is

Content

1. Final spin concentration
2. Original experimental PELDOR time traces in Q-Band
3. Original experimental PELDOR time traces in G-Band
4. Simulations for the Ç-DNA(1,9) and DNA(1,12)
5. Simulations using the (low field) optimized model
6. Simulation for DNA(1,12)
7. Error estimation

1. Final spin concentrations

Table 1 depicts the final spin concentrations of the samples for the PELDOR measurements. The spin concentrations of the samples are measured by CW-EPR measurements at X-Band. The integrated area is analysed by a calibration curve with nitroxide standards of different spin concentrations.

Tab. 1 Final spin concentration for the DNA samples

	spin concentration [μM]
ImU DNA(1,9)	197
ImU DNA(1,12)	191
OxU DNA(1,9)	178
OxU DNA(1,12)	180
ExImU DNA(1,9)	120
ExImU DNA(1,12)	136

2.Original experimental PELDOR time traces in Q-Band

Figure S1 contains the Q-Band PELDOR time traces, normalized and phase corrected (where necessary) with and without any background correction. The frequency of the pump pulse was fixed to the intensity maximum of the nitroxide powder spectrum to obtain maximum pumping efficiency. The probe frequency was chosen to 50, 100 or 150 MHz below this frequency.

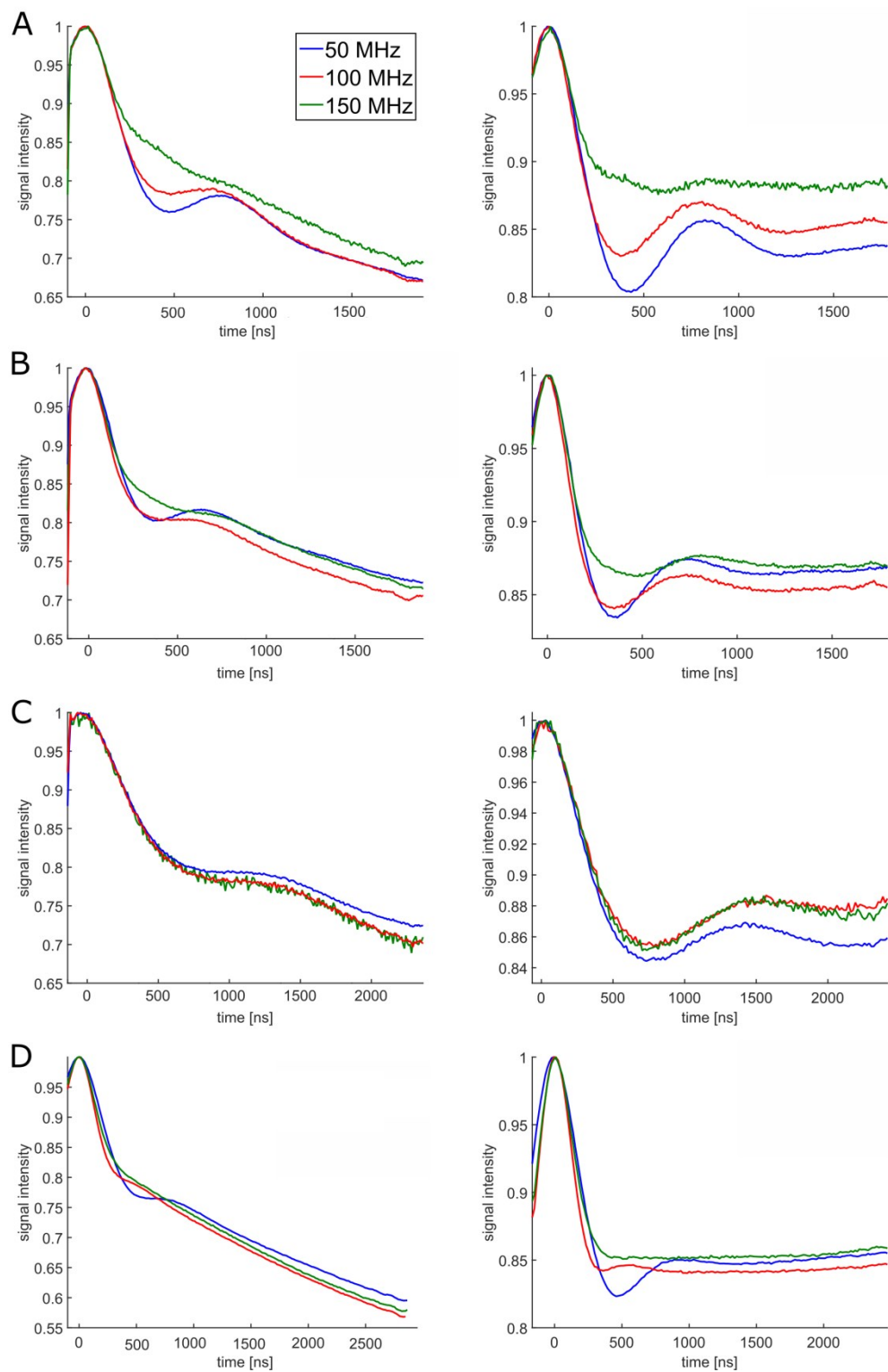


Fig. S1 Q-band PELDOR time traces before (left) and after (right) background correction for DNA (1,9). Offset is indicated. (A) ^{100}U – DNA(1,9) (B) ^{100}U – DNA(1,9) (C) ^{100}U – DNA(1,9) and (D) ^{100}U – DNA(1,12)

3. Original experimental PELDOR time traces in G-Band

Figure S2 contains the G-Band PELDOR time traces, normalized and phase corrected (where necessary) with and without any background correction. The field positions correspond roughly to $B \parallel g_{xx}$, $B \parallel g_{yy}$, and $B \parallel g_{zz}$. The probe frequency was set at a constant offset of 60 MHz above the pump frequency.

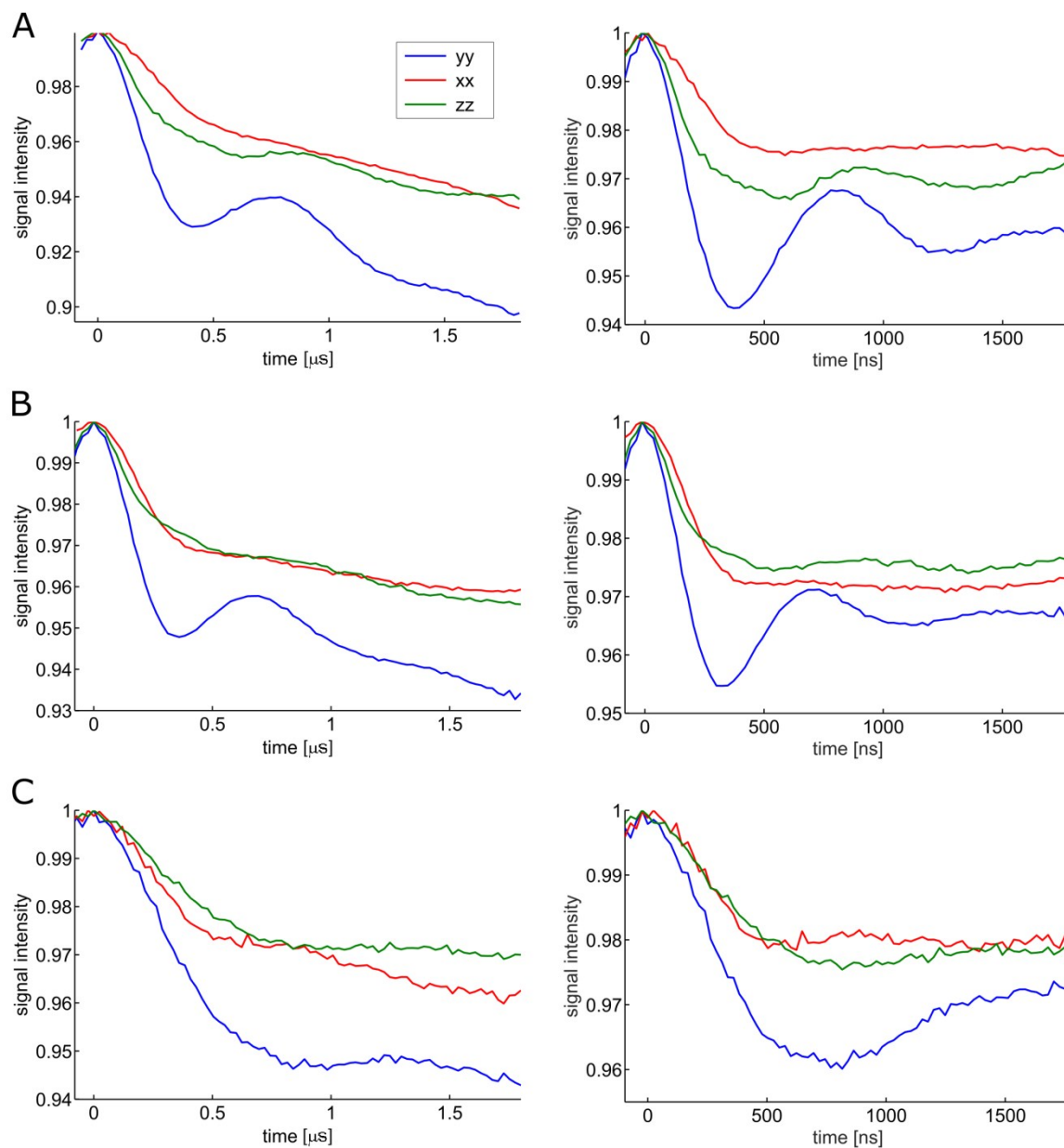


Fig. S2 G-band PELDOR time traces before (left) and after (right) background correction at the three magnetic field positions corresponding to the main G-tensor components for DNA (1,9) (A) ^{1m}U (B) ^{0x}U (C) ^{Exm}U

4. Simulations for the ζ -DNA(1,9) and DNA(1,12)

Figure S3 shows the comparisons between experimental and simulated time traces for X-Band and G-Band with the ζ -spin labels of DNA(1,9) and DNA(1,12). Since this spin label is assumed to be nearly rigid, no rotation around the x axis is used. Nevertheless, even this spin label shows a small own flexibility of 6° for the y rotation.

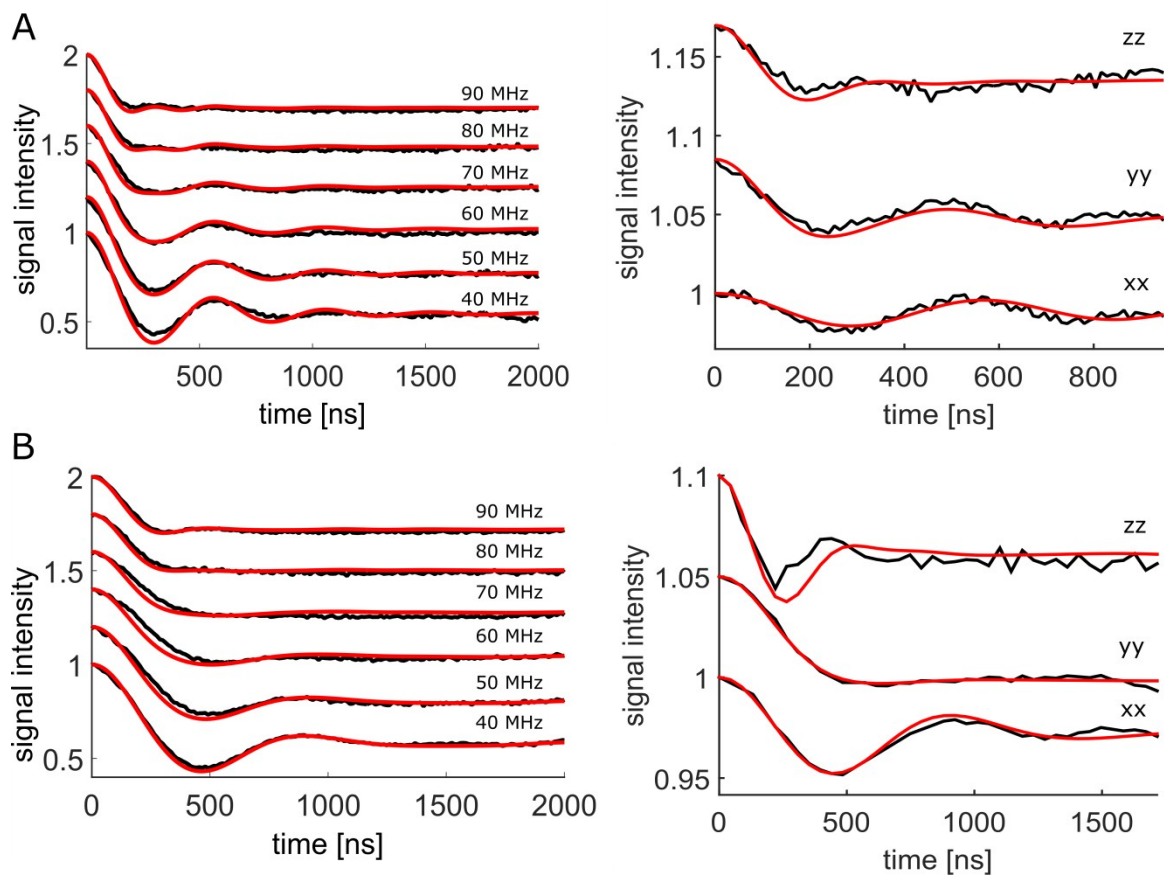


Fig. S3 Experimental (black) and simulated (red) PELDOR time traces for (A) ζ -DNA(1,9) and (B) ζ -DNA(1,12). On the left panel are the X-band time traces. The offset $\Delta\nu$ are indicated in the Figures. On the right panel are the G-band time traces at the three magnetic field positions corresponding to the main G-tensor components.

5. Simulations using the (low field) optimized model

The rotation parameters for the ^{19}F spin label movement were estimated by comparison of the simulated and experimental data from measurements at X- and Q-band. Simulations for G-Band, using this optimized model, were performed and compared with the experimental data. Especially in the region of $B \parallel g_{xx}$ a large deviation was observed.

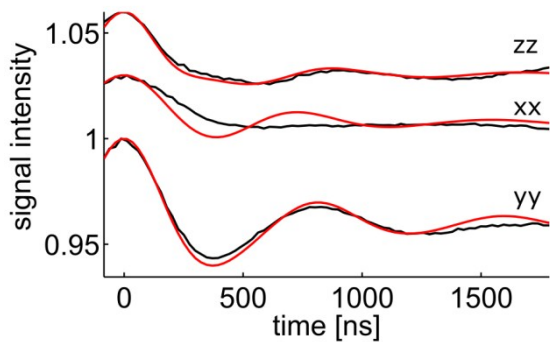


Fig. S4 Experimental (black) and simulated (red) G-band PELDOR time traces at the three magnetic field positions corresponding to the main G-tensor components for the ^{19}F -DNA(1,9). Simulations are based on the parameter estimated only at low fields

6. Simulation for DNA(1,12)

The comparisons between experimental and simulated time traces for all frequencies and spin labels of DNA(1,12). The parameter for the spin label flexibility are shown in Table 1 in the paper.

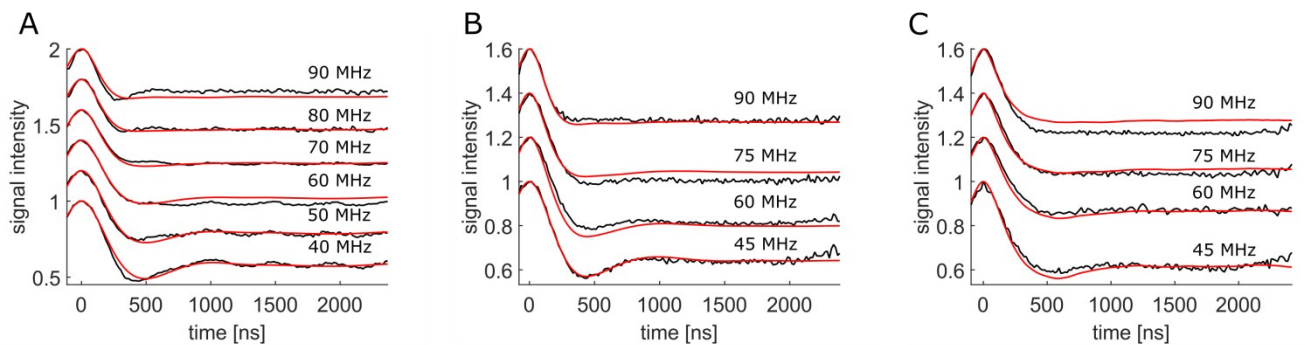


Fig. S5 Experimental (black) and simulated (red) X-band PELDOR time DNA(1,12). The offset $\Delta\nu$ are indicated in the Figures (A) ^{19}F (B) ^{19}F (C) ^{19}F .

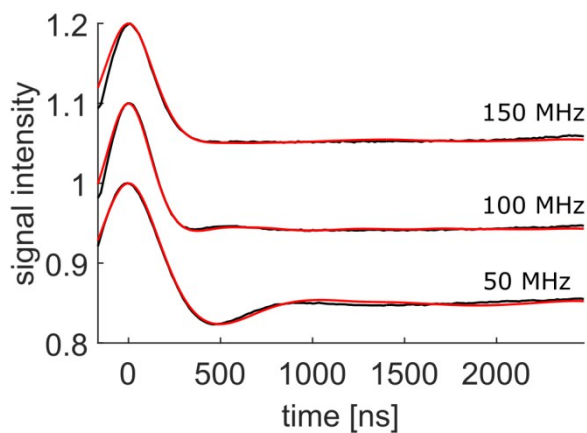


Fig. S6 Experimental (black) and simulated (red) Q-band PELDOR time DNA(1,12). The offsets $\Delta\nu$ are indicated in the Figures.

7. Error estimation

For an estimation of the error an example is given for the γ -rotation for the ^{13}C -DNA(1,9). On the left picture the summed RMSD value for all frequencies are shown against the γ -rotation. On the right picture a comparison for two different γ -rotation is given. The experimental time traces (black) are measured at Q-band. The red traces have a 14° rotation and the blue ones 18° . The damping of the signal increases significant with higher γ -rotation.

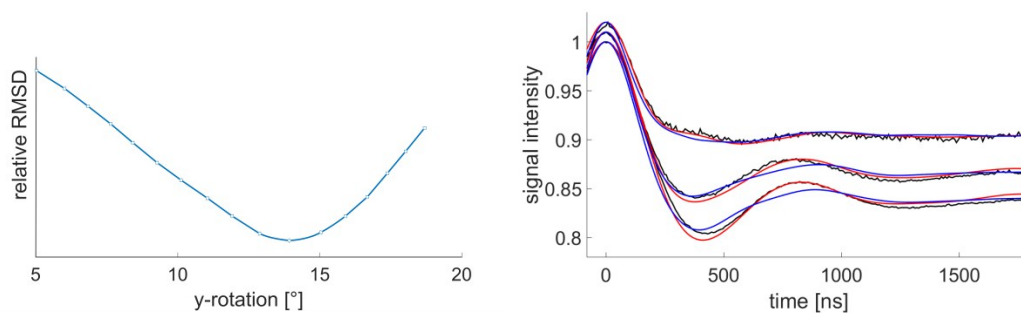


Fig. S7 Left: The summed RMSD values for the ^{13}C -DNA(1,9) for different γ -rotations. Right: Experimental (black) and with 14° γ -rotation (red) and 18° rotation Q-band PELDOR time DNA(1,9).

Resolving the Conformational Dynamics of DNA with Ångstrom Resolution by Pulsed Electron–Electron Double Resonance and Molecular Dynamics

Lukas S. Stelzl,^{†,¶,Ⓜ} Nicole Erlenbach,^{‡,¶,Ⓜ} Marcel Heinz,[†] Thomas F. Prisner,[‡] and Gerhard Hummer^{*,†,§,Ⓜ}

[†]Department of Theoretical Biophysics, Max Planck Institute of Biophysics, 60438 Frankfurt am Main, Germany

[‡]Institute of Physical and Theoretical Chemistry and Center of Biomolecular Magnetic Resonance, Goethe University Frankfurt, 60438 Frankfurt am Main, Germany

[§]Institute for Biophysics, Goethe University Frankfurt, 60438 Frankfurt am Main, Germany

Supporting Information

ABSTRACT: Pulsed electron–electron double resonance (PELDOR/DEER) experiments of nucleic acids with rigid spin labels provide highly accurate distance and orientation information. Here we combine PELDOR experiments with molecular dynamics (MD) simulations to arrive at an atomistic view of the conformational dynamics of DNA. The MD simulations closely reproduce the PELDOR time traces, and demonstrate that bending, in addition to twist–stretch motions, underpin the sub- μ s dynamics of DNA. PELDOR experiments correctly rank DNA force fields and resolve subtle differences in the conformational ensembles of nucleic acids, on the order of 1–2 Å. Long-range distance and angle measurements with rigid spin labels provide critical input for the refinement of computer models and the elucidation of the structure and dynamics of complex biomolecules.

The conformational dynamics of DNA is essential for its biological function and thus central to biochemistry. DNA double helices are often modeled as elastic rods,¹ but experiments demonstrated that the dynamics of DNA is more complex.^{2–6} DNA often stretches⁷ and bends to bind proteins. However, experiments have largely been interpreted in terms of geometric models,⁶ which capture the essential behavior of DNA, but do not provide an atomic-scale view of the dynamics. In this work we combine molecular dynamics (MD) simulations with pulsed electron–electron double resonance (PELDOR) experiments to arrive at a high-resolution view of the conformational motions of DNA.

MD simulations can resolve the dynamics of DNA in solution with atomic resolution.⁹ Very long MD simulations¹⁰ showed that DNA features complex dynamics on the sub- μ s time scale including bending motions, but dynamics are largely absent on the time scale of tens of μ s. Despite the successes, the quality of force fields remains a concern. Recently, two very promising DNA force fields have been released, AMBER parmbsc1 (bsc1)¹¹ and AMBER OL15 (OL15),^{12–14} which may supersede the well established AMBER parmbsc0 (bsc0)¹⁵ force field. In MD simulations, the new force fields capture key experimental properties,^{11,16–18} but further probes of long-range structural information are required.

PELDOR experiments,¹⁹ which are also often referred to as double electron–electron resonance (DEER), provide an exciting prospect for the validation and development of computational models because PELDOR provides long-range distance, orientation and dynamical information. PELDOR distance measurements on doubly spin-labeled²⁰ macromolecules are well established and have provided distance information on DNA with nm accuracy.²¹ Spin-label flexibility limits the information that can be extracted from PELDOR.²² PELDOR measurements with rigid spin labels can resolve distances with higher precision²³ and relative orientations.⁸

Here we show that the high-resolution long-range information from orientation-selective PELDOR can clearly distinguish between an older (bsc0¹⁵) and newer DNA force fields (OL15^{12–14} and bsc1¹¹). We compare MD simulations to previous PELDOR measurements⁶ of DNA labeled with the rigid ζ (Cspin) spin label^{24,25} (Figure 1A), which also provides an opportunity to interpret the data in greater detail than before. A key advantage of MD simulations in the analysis of PELDOR experiments is that no extraneous assumptions about the conformational dynamics have to be made. For a parameter-free direct comparison we calculated PELDOR time traces⁸ from the MD trajectories (SI text). The signal $S(T)$ is given by

$$S(T) = 1 + \int_0^{\pi/2} \lambda(\Theta) \left[\cos\left(\frac{D_{\text{dip}}}{r^3}(1 - 3\cos^2\Theta)T\right) - 1 \right] \times \sin\Theta d\Theta \quad (1)$$

where $D_{\text{dip}} = 52.16 \text{ MHz}\cdot\text{nm}^3$, T is the time, Θ is the orientation between the interspin vector and the external magnetic field, λ is the pump efficiency, which depends on the mutual orientation of the spins to each other, and r is the spin–spin distance. The mutual spin-label orientation and spin–spin distance were determined from MD simulations. As ζ is largely rigid, spin-positions were determined by mapping the ζ structure²⁶ onto the simulated conformations (SI Figure S5). This mapping approach neglects the influence of ζ on the DNA, which appears justified given the high level of agreement with experiment we obtained.

Received: May 24, 2017

Published: August 4, 2017

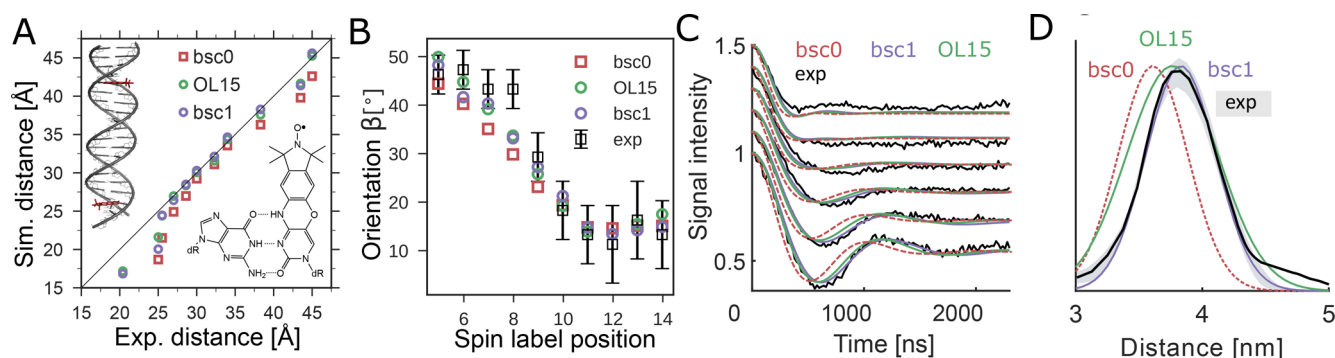


Figure 1. Comparison of orientation-selective PELDOR experiments (black) with MD simulations. (A) We analyzed PELDOR experiments (from ref 6) with 11 spin-label pairs and compared distances from experiments and MD. The spin label on one strand was kept at a fixed position, denoted as 1. The spin-label on the complementary strand was varied from positions 5 to 15. Left inset: DNA(1,14) with ζ residues in red. Right inset: ζ , a 2'-deoxycytidine analogue, base pairs with guanine. (B) Spin-label orientations from MD and PELDOR. The angle β describes the orientation between the vectors normal to the spin-label planes and the dipole–dipole vector.⁸ (C) Comparison of PELDOR signals calculated from MD to experiments for DNA(1,13). The PELDOR time traces were measured at X-band with different offsets ν_n between probe and pump pulse frequency from 40 MHz (lower time trace) to 90 MHz (upper time trace). (D) Spin–spin distance distributions for DNA(1,13) from Tikhonov regularization of PELDOR time traces and MD. Gray indicates the range of profiles obtained from resampling 20 PELDOR traces.

Even small differences between the MD ensembles have a marked effect on the PELDOR time traces calculated from the simulations. For the DNA(1,13) spin-label pair, the mean spin–spin distances were 36.3, 37.6, and 38.3 Å, respectively, for bsc0, OL15, and bsc1. Clearly, the PELDOR time traces calculated from the simulations with the latest force fields (Figure 1C), bsc1 and OL15, match the experiment substantially better than the time traces from the bsc0 simulation. For a direct comparison of distances (Figure 1A), we summed up all X-band time traces for a given spin-label pair and extracted distances²⁷ via Tikhonov regularization.^{28,29} For DNA(1,13), we find that the bsc0 simulation noticeably underestimates the experimental spin–spin distance of 38.3 Å, OL15 reproduces it very well, and bsc1 matches it exactly.

The PELDOR traces (SI Figure S6) and distances (Figure 1A) for the other ten spin-label pairs also agree better with bsc1 and OL15 than with the bsc0 simulations. Mean MD distances ≥ 25 Å agree with the PELDOR results typically within 1 Å. For the two spin-labels pairs, DNA(1,5) and DNA(1,6), where the spin labels are closest together, the agreement is not as good, which is also apparent from comparing the calculated and measured PELDOR traces. For DNA(1,6) the OL15 force field performs best (SI Figure S6B). At small separations, details of the conformations of the spin labels may play a larger role (SI Figure S5B,C). Short distances < 18 Å, outside the range accessible to highly accurate PELDOR measurements, are frequently sampled in the MD simulations for DNA(1,5) and DNA(1,6). Accounting for these short distances in the calculation of the PELDOR signals is challenging.³⁰

The calculated PELDOR time traces from the MD simulations take the orientation of the spin labels into account. The experimentally determined⁸ angle β of the spin labels relative to the spin–spin vector is well described by the simulations (Figure 1B), with larger angles for spins closer together and smaller angles for spins further apart. Measured and calculated angles agree in almost all cases within the experimental uncertainty (Figure 1B). For DNA(1,8), the agreement is not as good, with β underestimated by about 10° (OL15 and bsc1) or more (bsc0) in the MD simulations. Overall, the newer force fields perform somewhat better than bsc0, with better agreement for DNA(1,6) to DNA(1,9). High-field experiments are particularly sensitive to spin-label

orientations. Measurements for DNA(1,9) and DNA(1,12) give better agreement for the new OL15 and bsc1 force fields (SI Figure S8) than the bsc0 force field. Overall, the comparison ranks the bsc1 and OL15 force fields above bsc0, as judged by the mutual orientations and by distinguishing differences in the mean spin–spin distances as small as ≈ 1 –2 Å. We would thus expect an older force field to produce poorer PELDOR traces. Indeed, a simulation with parm94^{31,32} performs significantly worse than newer force fields (SI Figure S10), in particular concerning orientations (SI Figure S9C).

PELDOR experiments are sensitive to the distributions of the mutual spin-label orientations and distances, i.e., conformational flexibility. A broad conformational distribution dampens the oscillations of the PELDOR signals. In general, the oscillations in the experimental PELDOR traces are well reproduced, as evidenced for DNA(1,13) (Figure 1C). For DNA(1,9) and DNA(1,10), all MD simulations show more pronounced dampening of the oscillations than experiment. The small discrepancy may stem from neglecting the interactions between ζ and the DNA, which could affect dynamics.

Overall, the simulations yield distance distributions that agree well with distributions extracted from the summed PELDOR time traces, as evidenced, e.g., by Figure 1D. To confirm that we have captured the dominant dynamics of DNA, giving rise to the PELDOR signals, we extended a trajectory to 1 μ s and find equally good agreement (SI Figure S7).

A possible concern is that the PELDOR measurements were conducted at 40 K, whereas the MD simulations were run at room temperature. As the sample is cooled down, DNA molecules adjust their structures. However, below temperatures of 200–250 K no large scale rearrangements are possible and structures are trapped in local minima.³³ To explore the effect of sample freezing, we ran an additional set of MD simulations at 230 K. The agreement is on par with room temperature (Figure S11), suggesting that freezing has only a mild effect and preserves the overall dynamics, reminiscent of theoretical filtering methods.³⁴

The simulations with the novel OL15 and bsc1 force fields, validated by PELDOR, provide an updated view of the dynamics of DNA. The two most important motions, according to principal component analysis, were bending modes, which

have also been found in very long MD simulations.¹⁰ The third most important mode is a stretching motion. As the DNA twists, the helical rise increases and the DNA becomes more extended (SI Figure S13). This negative-twist stretch coupling has been identified in MD simulations,^{35,36} single-molecule experiments,⁷ and in the original analysis of the PELDOR data.⁶ Marko et al. analyzed the PELDOR data (Table 1) with a

Table 1. Dynamics of DNA from MD Simulations and the Analysis of PELDOR Experiments^a

	Marko et al. ⁶	MD
Helix pitch	33 ± 3.68 Å (A)	33 ± 1 Å
Helix radius	5.85 ± 0.65 Å (B)	6.3 ± 0.3 Å
Helix bending	≈ 25° (C)	≈ 19°

^aMarko et al.⁶ analyzed PELDOR experiments in terms of changes in helix pitch (model A), helix radius (model B), and bending (model C). The extent of bending was characterized by the mean bending angle $\langle\theta\rangle$ at a contour length of 49 Å (SI text). For helix pitch and radius, the mean and the standard deviation are reported to characterize their distributions.

stretching model with changes in helical pitch (Model A), or changes in helix radius (Model B), and a model of helix bending (Model C). Model B gave the best agreement with PELDOR. In MD simulation with bsc1, we find variations in the pitch of the helix ($\langle h_p \rangle = 33 \pm 1$ Å), in its radius ($\langle h_R \rangle = 6.3 \pm 0.3$ Å), and bending motions. The mean bending angle, $\langle\theta\rangle \approx 19^\circ$ (at a distance of 49 Å) agrees well with $\langle\theta\rangle = 25^\circ$ estimated from PELDOR experiments.⁸ A combination of these bending and stretching motions closely reproduces the PELDOR signals calculated from the MD simulations (SI Figure S14). The near quantitative agreement of the geometrical/mechanical model parametrized from MD shows that bending and twisting dominate the motions probed by PELDOR in the conformational ensemble of double-stranded DNA.

In summary, MD simulations with the most recent DNA force fields accurately report on the structure and conformational flexibility of DNA. Detailed investigations of, e.g., chromatin structure,³⁷ are thus feasible by combining MD and PELDOR. Conversely, our comparison shows that with rigid spin labels it is possible to use PELDOR to measure distances and angles with ≈ 1 Å and $\approx 5^\circ$ resolution. PELDOR was thus able to rank the bsc1 and OL15 force fields ahead of the older bsc0 force field, and all of them ahead of parm94, confirming the expectation of improvements. Orientation-selective PELDOR should be generally useful for the validation and refinement of computer models of biomolecules.

■ ASSOCIATED CONTENT

● Supporting Information

The Supporting Information is available free of charge on the ACS Publications website at DOI: 10.1021/jacs.7b05363.

Computational methods, comparison of MD simulations to all experimental PELDOR time traces, and geometrical/mechanical model of DNA helix dynamics (PDF)

■ AUTHOR INFORMATION

Corresponding Author

*gerhard.hummer@biophys.mpg.de

ORCID

Lukas S. Stelzl: 0000-0002-5348-0277

Gerhard Hummer: 0000-0001-7768-746X

Author Contributions

[†]These authors contributed equally

Notes

The authors declare no competing financial interest.

■ ACKNOWLEDGMENTS

We acknowledge financial support from the German Research Foundation (CRC902: Molecular Principles of RNA Based Regulation). L.S.S, M.H., and G.H were also supported by the Max Planck Society. Dr. Andriy Marko is thanked for providing his program for simulation of orientation-selective PELDOR signals. Drs. Andriy Marko, Vasyl Denysenkov, Dominik Margraf, Pavol Cekan, and Profs. Olav Schiemann and Snorri Th. Sigurdsson are thanked for their contributions to the original PELDOR measurements.

■ REFERENCES

- Hagerman, P. J. *Annu. Rev. Biophys. Biophys. Chem.* **1988**, *17*, 265–286.
- Cluzel, P.; Lebrun, A.; Heller, C.; Lavery, R.; Viovy, J.-L.; Chatenay, D.; Caron, F. *Science* **1996**, *271*, 792–794.
- Smith, S. B.; Cui, Y.; Bustamante, C. *Science* **1996**, *271*, 795–799.
- Marko, J. F. *Europhys. Lett.* **1997**, *38*, 183.
- Mathew-Fenn, R. S.; Das, R.; Harbury, P. A. B. *Science* **2008**, *322*, 446–449.
- Marko, A.; Denysenkov, V.; Margraf, D.; Cekan, P.; Schiemann, O.; Sigurdsson, S. T.; Prisner, T. F. *J. Am. Chem. Soc.* **2011**, *133*, 13375–13379.
- Gore, J.; Bryant, Z.; Nöllmann, M.; Le, M. U.; Cozzarelli, N. R.; Bustamante, C. *Nature* **2006**, *442*, 836–839.
- Marko, A.; Margraf, D.; Cekan, P.; Sigurdsson, S. T.; Schiemann, O.; Prisner, T. F. *Phys. Rev. E* **2010**, *81*, 1–9.
- Perez, A.; Castellazzi, C. L.; Battistini, F.; Collinet, K.; Flores, O.; Deniz, O.; Ruiz, M. L.; Torrents, D.; Eritja, R.; Soler-López, M.; Orozco, M. *Biophys. J.* **2012**, *102*, 2140–2148.
- Galindo-Murillo, R.; Roe, D. R.; Cheatham, T. E. *Nat. Commun.* **2014**, *5*, 5152.
- Ivani, I.; Dans, P. D.; Noy, A.; Pérez, A.; Faustino, I.; Hospital, A.; Walther, J.; Andrio, P.; Goñi, R.; Balaceanu, A.; Portella, G.; Battistini, F.; Gelpi, J. L.; González, C.; Vendruscolo, M.; Laughton, C. A.; Harris, S. A.; Case, D. A.; Orozco, M. *Nat. Methods* **2016**, *13*, 55–58.
- Krepl, M.; Zgarbová, M.; Stadlbauer, P.; Otyepka, M.; Banáš, P.; Koča, J.; Cheatham, T. E.; Jurečka, P.; Šponer, J. *J. Chem. Theory Comput.* **2012**, *8*, 2506–2520.
- Zgarbová, M.; Luque, F. J.; Šponer, J.; Cheatham, T. E.; Otyepka, M.; Jurečka, P. *J. Chem. Theory Comput.* **2013**, *9*, 2339–2354.
- Zgarbová, M.; Šponer, J.; Otyepka, M.; Cheatham, T. E.; Galindo-Murillo, R.; Jurečka, P. *J. Chem. Theory Comput.* **2015**, *11*, 5723–5736.
- Pérez, A.; Marchán, I.; Svozil, D.; Šponer, J.; Cheatham, T. E.; Laughton, C. A.; Orozco, M. *Biophys. J.* **2007**, *92*, 3817–3829.
- Galindo-Murillo, R.; Robertson, J. C.; Zgarbová, M.; Šponer, J.; Otyepka, M.; Jurečka, P.; Cheatham, T. E. *J. Chem. Theory Comput.* **2016**, *12*, 4114–4127.
- Dans, P. D.; Danilâne, L.; Ivani, I.; Dršata, T.; Lankaš, F.; Hospital, A.; Walther, J.; Pujagut, R. I.; Battistini, F.; Gelpi, J. L.; Lavery, R.; Orozco, M. *Nucleic Acids Res.* **2016**, *44*, 4052–4066.
- Dans, P. D.; Ivani, I.; Hospital, A.; Portella, G.; González, C.; Orozco, M. *Nucleic Acids Res.* **2017**, *45*, 4217.
- Milov, A.; Ponomarev, A.; Tsvetkov, Y. *Chem. Phys. Lett.* **1984**, *110*, 67–72.

- (20) Spaltenstein, A.; Robinson, B. H.; Hopkins, P. B. *Biochemistry* **1989**, *28*, 9484–9495.
- (21) Schiemann, O.; Piton, N.; Mu, Y.; Stock, G.; Engels, J. W.; Prisner, T. F. *J. Am. Chem. Soc.* **2004**, *126*, 5722–5729.
- (22) Jeschke, G. *Prog. Nucl. Magn. Reson. Spectrosc.* **2013**, *72*, 42–60.
- (23) Halbmaier, K.; Seikowski, J.; Tkach, I.; Hobartner, C.; Sezer, D.; Bennati, M. *Chem. Sci.* **2016**, *7*, 3172–3180.
- (24) Barhate, N.; Cekan, P.; Massey, A. P.; Sigurdsson, S. T. *Angew. Chem., Int. Ed.* **2007**, *46*, 2655–2658.
- (25) Cekan, P.; Smith, A. L.; Barhate, N.; Robinson, B. H.; Sigurdsson, S. T. *Nucleic Acids Res.* **2008**, *36*, 5946–5954.
- (26) Edwards, T. E.; Cekan, P.; Reginsson, G. W.; Shelke, S. A.; Ferre-D'Amare, A. R.; Schiemann, O.; Sigurdsson, S. T. *Nucleic Acids Res.* **2011**, *39*, 4419–4426.
- (27) Prisner, T.; Marko, A.; Sigurdsson, S. *J. Magn. Reson.* **2015**, *252*, 187–198.
- (28) Godt, A.; Schulte, M.; Zimmermann, H.; Jeschke, G. *Angew. Chem., Int. Ed.* **2006**, *45*, 7560–7564.
- (29) Jeschke, G.; Chechik, V.; Ionita, P.; Godt, A.; Zimmermann, H.; Banham, J.; Timmel, C. R.; Hilger, D.; Jung, H. *Appl. Magn. Reson.* **2006**, *30*, 473–498.
- (30) Banham, J.; Baker, C.; Ceola, S.; Day, I.; Grant, G.; Groenen, E.; Rodgers, C.; Jeschke, G.; Timmel, C. *J. Magn. Reson.* **2008**, *191*, 202–218.
- (31) Cornell, W. D.; Cieplak, P.; Bayly, C. I.; Gould, I. R.; Merz, K. M.; Ferguson, D. M.; Spellmeyer, D. C.; Fox, T.; Caldwell, J. W.; Kollman, P. A. *J. Am. Chem. Soc.* **1995**, *117*, 5179–5197.
- (32) Kollman, P.; Dixon, R.; Cornell, W.; Fox, T.; Chipot, C.; Pohorille, A. In *Computer Simulation of Biomolecular Systems: Theoretical and Experimental Applications*; van Gunsteren, W. F., Weiner, P. K., Wilkinson, A. J., Eds.; Springer Netherlands: Dordrecht, 1997; pp 83–96.
- (33) Jeschke, G.; Sajid, M.; Schulte, M.; Ramezani, N.; Volkov, A.; Zimmermann, H.; Godt, A. *J. Am. Chem. Soc.* **2010**, *132*, 10107–10117.
- (34) Meyer, T.; Ferrer-Costa, C.; Pérez, A.; Rueda, M.; Bidon-Chanal, A.; Luque, F. J.; Laughton, C. A.; Orozco, M. *J. Chem. Theory Comput.* **2006**, *2*, 251–258.
- (35) Liebl, K.; Drsata, T.; Lankas, F.; Lipfert, J.; Zacharias, M. *Nucleic Acids Res.* **2015**, *43*, 10143–10156.
- (36) Bao, L.; Zhang, X.; Shi, Y.-Z.; Wu, Y.-Y.; Tan, Z.-J. *Biophys. J.* **2017**, *112*, 1094–1104.
- (37) Pasi, M.; Lavery, R. *Nucleic Acids Res.* **2016**, *44*, 5450.

Supporting Information: Resolving the Conformational Dynamics of DNA with Ångstrom Resolution by Pulsed Electron-Electron Double Resonance and Molecular Dynamics

Lukas S. Stelzl,^{†,¶} Nicole Erlenbach,^{‡,¶} Marcel Heinz,[†] Thomas F. Prisner,[‡] and
Gerhard Hummer^{*,†,§}

[†]*Department of Theoretical Biophysics, Max Planck Institute of Biophysics, 60438
Frankfurt am Main, Germany*

[‡]*Institute of Physical and Theoretical Chemistry and Center of Biomolecular Magnetic
Resonance, Goethe University, 60438 Frankfurt am Main, Germany*

[¶]*These authors contributed equally*

[§]*Institute for Biophysics, Goethe University Frankfurt, 60438 Frankfurt am Main, Germany*

E-mail: gerhard.hummer@biophys.mpg.de

This document contains

1. Supplementary Methods

- (a) Molecular dynamics simulations of DNA and their analysis
- (b) DFT calculations
- (c) Calculation of orientation-selective PELDOR signals
- (d) Comparison of PELDOR time traces to MD simulations

2. Supplementary Results

- (a) Overall stability of the MD simulations
- (b) Testing the extraction of spin-positions from MD simulations
- (c) Comparison of X-band PELDOR time traces to MD simulations
- (d) Comparison of G-band PELDOR time traces to MD simulations
- (e) Comparison of MD simulation with parm94 to PELDOR
- (f) Effect of freezing on the determination the conformational ensemble by PELDOR
- (g) Geometrical analysis of DNA helix in the MD simulations
- (h) Comparison with a geometrical model of DNA helix dynamics

3. Supplementary References

4. Supplementary Figures (S1 to S14) with legends

Supplementary Methods

Molecular dynamics simulations of DNA and their analysis

Molecular dynamics (MD) simulations were run in GROMACS 4.6,¹ using the AMBER parm94,^{2,3} parmbsc0 (bsc0),^{4,5} OL15⁶⁻⁸ and parmbsc1 (bsc1)⁹ force fields. B-DNA helices were constructed using the Nucleic Acid Builder (NAB) webserver or NAB module in the AMBER suite,¹⁰ for the sequences studied by Marko *et al.*¹¹ OL15 and bsc1 simulations systems were set up with the help of ACPYPE.¹² To model the PELDOR experiments on the eleven different label combinations, we ran two simulations for each force field, one with the sequence used for experiments with the second spin labels at odd positions (positions 5 to 15), and one with the sequence featuring the second spin label at even positions (positions 6 to 14). We did not explicitly model the spin labels in our simulations, but reconstructed the mutual positions and orientations of the spin labels from the DFT-optimized structure of Ç (details below),¹³ taking advantage of its rigid structure and the essentially unperturbed base pairing geometry (details given below). The six simulations were run for 200 ns each. One simulation with bsc1 was extended to 1 μ s.

a)

5' GT - C₁AG -TCG - CG C - G CG - CG C - ATC 3'
3' CA - G TC -AGC₆- GC₈G - C₁₀GC₁₂- GC₁₄G - TAG 5'

b)

5' GT - C₁AG - TG C - G CG - CG C - G CG - ATC 3'
3' CA - G TC - AC₅G - C₇GC₉- GC₁₁G- C₁₃GC₁₅- TAG 5'

Fig. S1: The two DNA sequences studied in MD simulations. (A) Second spin-label at even positions (positions 6 to 14) and (B) second spin-label at odd positions (positions 5 to 15). A spin-label pair with Ç at, e.g., positions 1 and 13 is referred to as DNA(1,13) throughout this work.

Simulations were conducted using the TIP3P water model,¹⁴ periodic boundary conditions, and a NaCl concentration of 120 mM. In the OL15 and bsc1 simulations the updated ion parameters by Joung and Cheatham were employed.¹⁵ Simulation systems contained

≈ 59000 (bsc1, OL15) and ≈ 75000 (bsc0, parm94) atoms respectively. The experimental samples contained 20 % ethylene glycol as a cryoprotectant.¹¹ We assumed that the cryoprotectant does not disturb the conformational ensemble of the DNA and hence did not attempt to model its effect in the simulations. After setup, the simulation systems were energy minimized and equilibrated for 10 ns in the NPT ensemble without position restraints for the bsc1 and OL15 simulations and with position restraints for the bsc0 and parm94 simulations. Production simulations were run without restraints at 298.15 K and 1 bar for 200 ns for the AMBER parm94, bsc0, OL15 and the bsc1 force fields. The production simulations were kept in the NPT ensemble using the velocity rescaling thermostat by Bussi et al.¹⁶ with $\tau_t = 0.1$ ps and the Parrinello-Rahman barostat¹⁷ with $\tau_p = 4$ ps. Electrostatic interactions were treated using the Particle-Mesh-Ewald approach and van der Waals interactions were cut-off at 10 Å. A time step of 2 fs was used to integrate the equations of motion.

Simulation analysis built on the MDAnalysis Python library^{18,19} and 3DNA²⁰ using do_x3dna.²¹ Helix pitch, helix radius and bending, were extracted from a 200 ns trajectory (with the bsc1 force field).

DFT calculations

An initial C geometry was constructed by taking the 1.7 Å resolution crystal structure embedded in DNA¹³ (pdb: 3OT0). The surrounding residues were removed and the sugar moiety was substituted by a methyl group. Missing hydrogen atoms were added, resulting in a molecule containing 43 atoms. Geometry optimization was performed in Gaussian09²² at the PBE0²³/N07D^{24,25} level of theory, which was used in previous nitroxide studies.^{24,26,27} Analysis of the computed eigenvalues in the Hessian matrix reveals a minimum structure (i.e. all values are positive). The optimized atom coordinates are presented in Table S1.

Table S1: XYZ coordinates of the optimized ζ structure at the PBE0/N07D level of theory.

N	-0.413256	-8.238653	11.151577	C	-0.510058	-7.756990	9.824992
O	0.098728	-8.339476	8.946571	N	-1.294621	-6.650189	9.614902
C	-1.915993	-6.082668	10.612233	N	-2.687412	-4.986708	10.376451
H	-2.740023	-4.662661	9.421498	C	-1.837456	-6.546089	11.961285
C	-1.066280	-7.638084	12.183807	H	-0.946154	-8.062400	13.176020
C	-3.376000	-4.335587	11.397652	C	-3.264692	-4.832500	12.707444
O	-2.500157	-5.932748	12.994619	C	-3.928919	-4.222649	13.761103
H	-3.815863	-4.639127	14.759139	C	-4.714618	-3.102531	13.506019
C	-4.831536	-2.602294	12.212070	C	-4.165616	-3.213437	11.154675
H	-4.250138	-2.830466	10.138839	C	-5.725526	-1.390762	12.159147
N	-6.095184	-1.275389	13.589199	C	-5.513931	-2.294313	14.494173
O	-6.856714	-0.366868	14.009302	C	-6.640840	-3.090937	15.155948
H	-7.250676	-3.603761	14.405853	H	-6.226966	-3.839967	15.839578
H	-7.281707	-2.410767	15.725567	C	-4.648668	-1.603655	15.550956
H	-5.264308	-0.904603	16.125519	H	-4.222619	-2.343535	16.237066
H	-3.828707	-1.049143	15.084362	C	-6.988734	-1.606980	11.322447
H	-6.734600	-1.676471	10.259254	H	-7.501874	-2.527080	11.618442
H	-7.669574	-0.762255	11.466198	C	-4.996413	-0.119613	11.717453
H	-4.079852	0.027610	12.296893	H	-4.731601	-0.181114	10.656376
H	-5.650052	0.745415	11.866612	C	0.419071	-9.409096	11.360313
H	0.406719	-9.672090	12.420506	H	0.044866	-10.246282	10.764320
H	1.443956	-9.202093	11.039624				

Calculation of orientation-selective PELDOR signals

This section contains a brief introduction to orientation selective PELDOR and the calculation of PELDOR signals from conformations visited in a MD trajectory. A more detailed description of the calculation of PELDOR signals can be found in the literature.^{28,29} The PELDOR pulse sequence is given in Fig. S2A. PELDOR is a double frequency method, in which microwave-frequency pulses are applied at two different frequencies to excite electron spins resonant with these frequencies. Under certain conditions, samples with two spin labels of the same type, e.g., a pair of nitroxide spin labels, can be characterized. The \mathbf{g} -tensor describing the Zeeman interaction of the electron spin with the static magnetic field, and the tensor \mathbf{A} , describing the hyperfine interaction of the electron spin with the spin of the ^{14}N

nucleus, are both anisotropic and depend on the orientation of the spin labels to the magnetic field. Consequently, the distribution of the resonance frequencies in a powder sample, with randomly orientated molecules, will be broad. Two spin labels with different orientations with respect to the static magnetic field will differ in their resonance frequencies. Thus spin labels with different orientations and with different spin states can be excited independently. Typically PELDOR measurements are performed on biomolecules labeled with flexible spin labels such as TPA (2,2,5,5-tetramethyl-pyrrolin-1-oxyl-3-acetylene). The mutual orientations between the two spin labels will be random and the full Pake pattern gets excited. Therefore only the distance between the two spins can be extracted from the experiment. However for rigid spin labels such as C the mutual orientation between the two spin labels is no longer random and their relative orientation will be encoded in the measured PELDOR signals. The mutual orientation of the spin labels to each other are defined by Euler angles $(\alpha_1, \beta_1, \gamma_1) \equiv \mathbf{o}_1$ and $(\alpha_2, \beta_2, \gamma_2) \equiv \mathbf{o}_2$ (Fig. S2C), which describe the orientation of the coordinate axis of the spin label to the main axis system. The coordinate system of the spin label is chosen in such a way that the x-axis points along the NO axis and the z-axis is plane normal (Fig. S2B). The main axis system has its z-axis along the distance vector between the two radicals (Fig. S2D). The polar Φ and azimuth Θ angles describe the orientation of the distance vector to the external magnetic field.

From these definitions of the spin-label orientations and distances, the PELDOR signal for given conformation visited in an MD trajectory can be calculated. This calculation is essentially parameter free. The inputs are spin-label distances and orientations as determined from MD. Other inputs are experimental parameters, e.g., the pulse durations. To a first approximation, a PELDOR signal can be described as a modulation of the signal from the refocused Hahn-echo sequence (Fig. S2A). The Hahn-echo sequence is applied with the frequency ν_A and the modulation occurs due to the dipolar interaction between spins A and B. The dipolar modulation between two spins depends on the inversion of spin B by the pump pulse at the second frequency ν_B . A PELDOR signal $S(T)$ of a powder sample can

be calculated with eq 1 given in the main text,

$$S(T) = 1 + \int_0^{\pi/2} \lambda(\Theta) \left[\cos \left(\frac{D_{\text{dip}}}{r^3} (1 - 3 \cos^2 \Theta) T \right) - 1 \right] \sin \Theta d\Theta \quad (1)$$

where $D_{\text{dip}} = 52.16 \text{ MHz}\cdot\text{nm}^3$, T is the time, Θ is the orientation between the interspin vector and the external magnetic field, r is the spin-spin distance and λ is the pump efficiency. The pump efficiency λ depends on the mutual orientations of the spin labels to each other. The function λ is an averaged sum of the echo magnetization m_x formed by probe pulses, multiplied by the flip probability of the B-spin p achieved by the pump pulse

$$\lambda(\Theta) = \frac{1}{2V(\nu_A)} \sum_{m1, m2} \langle m_x(\omega_{r1}, \nu_a) p(\omega_{r2}, \nu_B) + m_x(\omega_{r2}, \nu_A) p(\omega_{r1}, \nu_B) \rangle_{\Phi, \delta b_1, \delta b_2} \quad (\text{S1})$$

with $V(\nu_A)$ the unmodulated Hahn echo signal. Importantly, both the flip probability p and the transversal echo magnetization m_x , depend on the resonance frequency for each nitroxide spin

$$\omega_r(\Theta, \Phi, \mathbf{o}, m) = \gamma_e \left(B_0 \frac{g_{\text{eff}}(\Theta, \Phi, \mathbf{o})}{g_e} + mA_{\text{eff}}(\Theta, \Phi, \mathbf{o}) + \delta b \right) \quad (\text{S2})$$

where γ_e denotes the gyromagnetic ratio of the electron, and the quantum number $m = -1, 0, 1$ accounts for the state of the nuclear spin. The angular dependence enters via the effective g-tensor g_{eff} for the Zeeman interaction and A_{eff} for the hyperfine interaction. Expressions for g_{eff} and A_{eff} can be founded in Marko et al.²⁸ Additionally the term δ_b reflects the inhomogeneous line broadening as shift due to for coupling to other nuclear spins or local field fluctuations. The flip probability

$$p(\omega_r, \nu_B) = \frac{1}{2} \left[\frac{\gamma_e B_{1B}}{\Omega_B(\omega_r)} \right]^2 (1 - \cos(\Omega_B(\omega_r) t_\pi^B)) \quad (\text{S3})$$

depends on the pulse length of the pump π pulse (t_π), magnitude of the microwave magnetic field B_{1B} and the Rabi frequency eq S4, which depends on the resonance frequency of the

B-spin. Specifically, the Rabi frequency

$$\Omega_B(\omega_r) = \sqrt{\gamma_e^2 B_{1B}^2 + (2\pi\nu_b - \omega_r)^2} \quad (\text{S4})$$

depends on ω_r , the resonance frequency, and B_1 the external magnetic field strength. The magnitude of the transversal magnetization after applying the three Hahn echo pulses

$$m_x(\omega_r, \nu_A) = \frac{1}{4} \left[\frac{\gamma_e B_{1B}}{\Omega_A(\omega_r)} \right]^5 \sin(\Omega_A(\omega_r) t_{\pi/2}^A) (1 - \cos(\Omega_A(\omega_r) t_{\pi}^A))^2 \quad (\text{S5})$$

is given by the product of the Rabi frequency and the pulse durations $t_{\pi/2}^A$ and t_{π}^A of the probe pulses. The resonance frequency ω_r encodes the orientation information.

Comparison of PELDOR time traces to MD simulations

We analyzed PELDOR time traces previously measured at X-Band frequency (0.3 T, 9.5 GHz) and G-band frequency (6.4 T, 180 GHz),¹¹ with different offsets between pump and probe pulse frequency. For rigid spin labels, the orientation dependence of the dipole-dipole interaction between the spin labels is not averaged out, unlike for flexible spin labels. Measured with different pulse frequencies, the time traces thus change as a function of orientation. The frequency of the pump pulse was fixed to the intensity maximum of the nitroxide powder spectrum to obtain maximum pumping efficiency. In X-band measurements, probe frequencies 40 to 90 MHz larger than the pump frequency were employed. In our quantitative comparison of X-band data to MD simulations, we took into account the frequency of the oscillations, the dampening and the relative modulation depths of the PELDOR time traces at different offsets. The depth variations between the set of X-band time traces measured at different offsets were not fitted. However, for the G-band data, due to uncertainties of the resonator performance and non-perfect calculations of the excitation profiles, the modulation depth was adjusted for each time trace. For simulating the PELDOR signal, 2000 regularly spaced structures (one for every 0.1 ns) were taken from the respective MD trajectories.

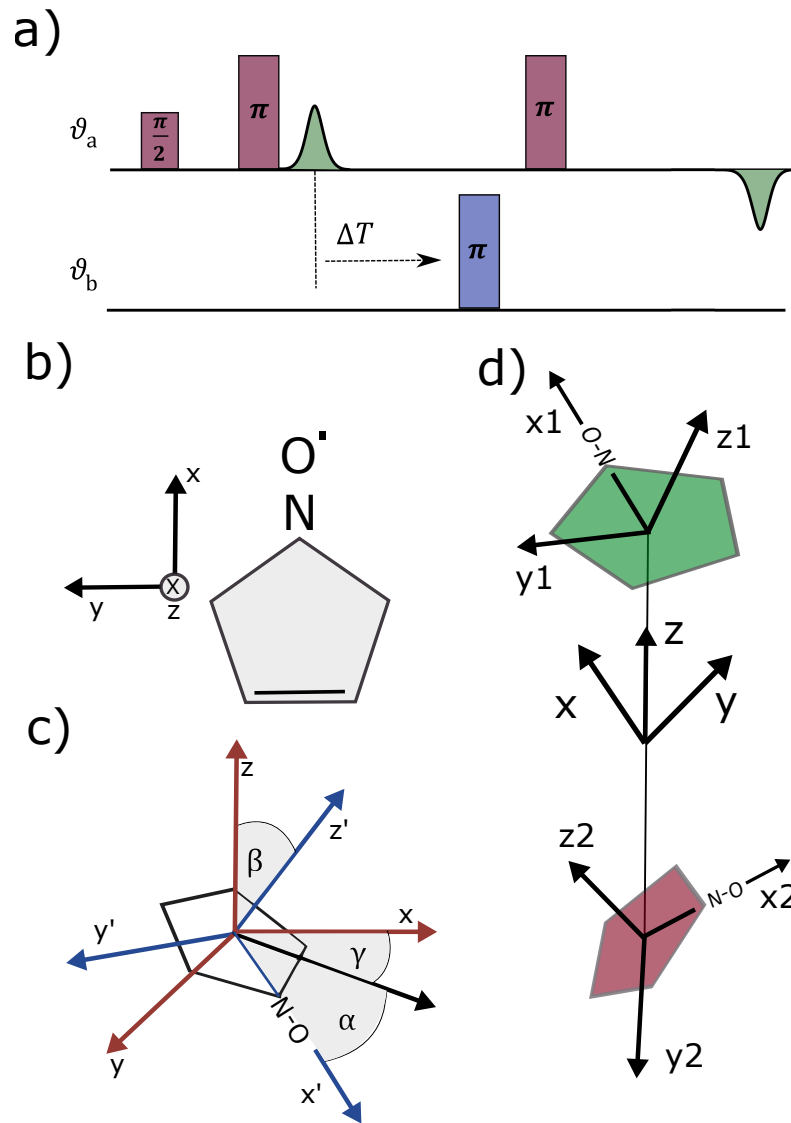


Fig. S2: Orientation-selective PELDOR experiments. (A) Four-pulse PELDOR sequence. ν_A and ν_B are probe and pump frequencies, respectively. (B) Axis system of a nitroxide spin label (C) Euler angles $(\alpha, \beta, \gamma)=0$ defining the orientation of the axis system $\{x', y', z'\}$ of the nitroxide in the main axis system frame $\{x, y, z\}$. (D) The three coordinate systems for the description of a rigid biradical. $\{x_1, y_1, z_1\}$ and $\{x_2, y_2, z_2\}$ frames correspond to the axes of the first and the second nitroxide, respectively. $\{x, y, z\}$ has the z axis coinciding with the interspin axis r and the x axis is perpendicular to both vectors z and z_1 .

Deviations of the simulated signals $V^{\text{sim}}(t_m)$ from the measured PELDOR signals $V^{\text{obs}}(t_m)$ were quantified by

$$\chi^2 = N^{-1} \sum_{m=1}^N \frac{[V^{\text{sim}}(t_m) - V^{\text{obs}}(t_m)]^2}{\sigma^2}. \quad (\text{S6})$$

The statistical error σ in the PELDOR experiments was determined from the standard deviation between the scaled experimental time trace and a ninth-order polynomial fit.³⁰ Values of $\chi^2 \leq 1$, indicate that, on average, the measured and calculated signals are within one standard deviation, ignoring errors in the MD simulations and correlations. To estimate the effect of the statistical uncertainty in the PELDOR experiments on the extracted distance distributions of, e.g., DNA(1,13), we have generated synthetic data based on the experimental time traces and their noise, and then repeated the Tikhonov regularization. The range of profiles from generating 20 synthetic PELDOR time traces is indicated in Fig. 1D in the main text.

Supplementary Results

Overall stability of the MD simulations

Calculating the root mean square deviation (RMSD)^{18,31,32} of the atomic positions demonstrated that all the MD trajectories were stable (Fig. S3). Here the RMSDs of atomic positions were calculated with respect to ideal B-helical structures generated with the NAB webserver and suite,¹⁰ which we used to set up the simulations. MD simulations with the older bsc0 force field relax to a RMSD of $\approx 4 \text{ \AA}$ to the reference B-helix. Simulations with the recently developed OL15 (Fig. S3C and D) and bsc1 (Fig. S3E and F) force fields settle at a RMSD of $\approx 3 \text{ \AA}$, with respect to the reference B-helix. In all simulations the DNA stayed close to the average structure adopted after relaxation for the remainder of the trajectories (Fig. S4). Extending one simulation with the bsc1 force field to 1 μs showed that current force fields enable stable simulations of B-DNA on the timescales of hundreds of ns

(Fig. S3F and Fig. S4F).

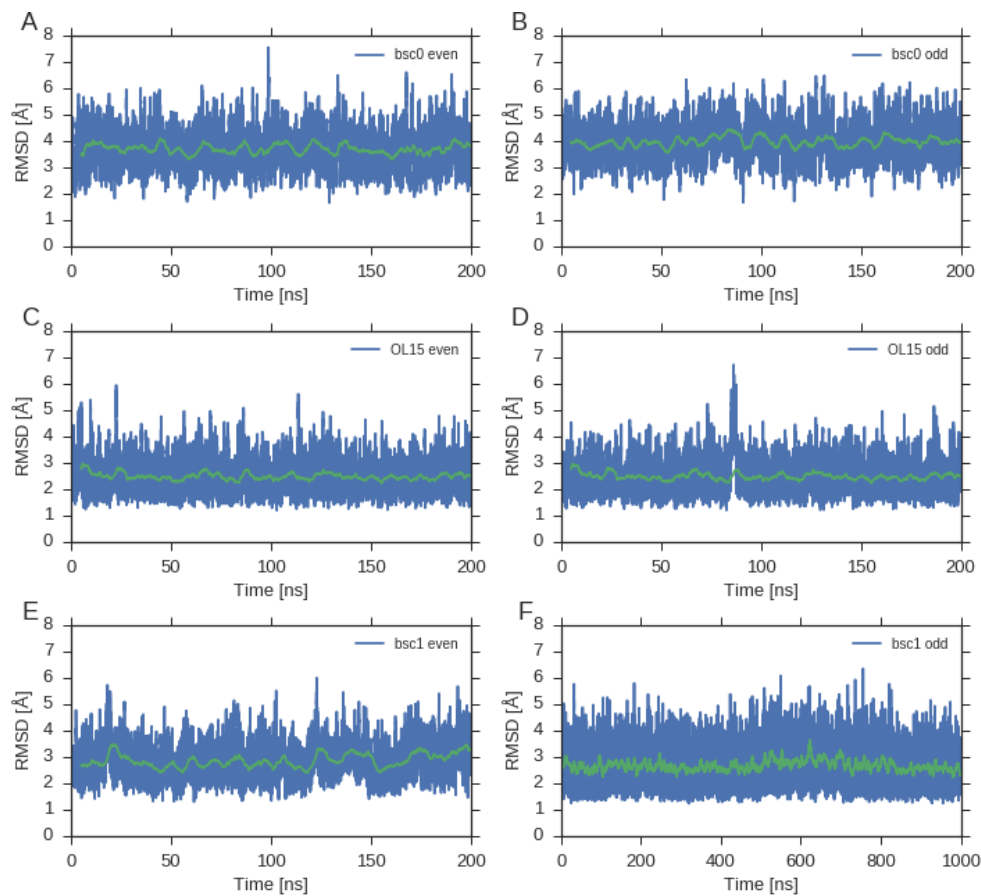


Fig. S3: RMSD from starting structure for MD simulations with the bsc0 (A and B), OL15 (C and D) and bsc1 (E and F) force fields. All heavy atoms were included in the RMSD calculation. The green curves correspond to 5 ns window averages.

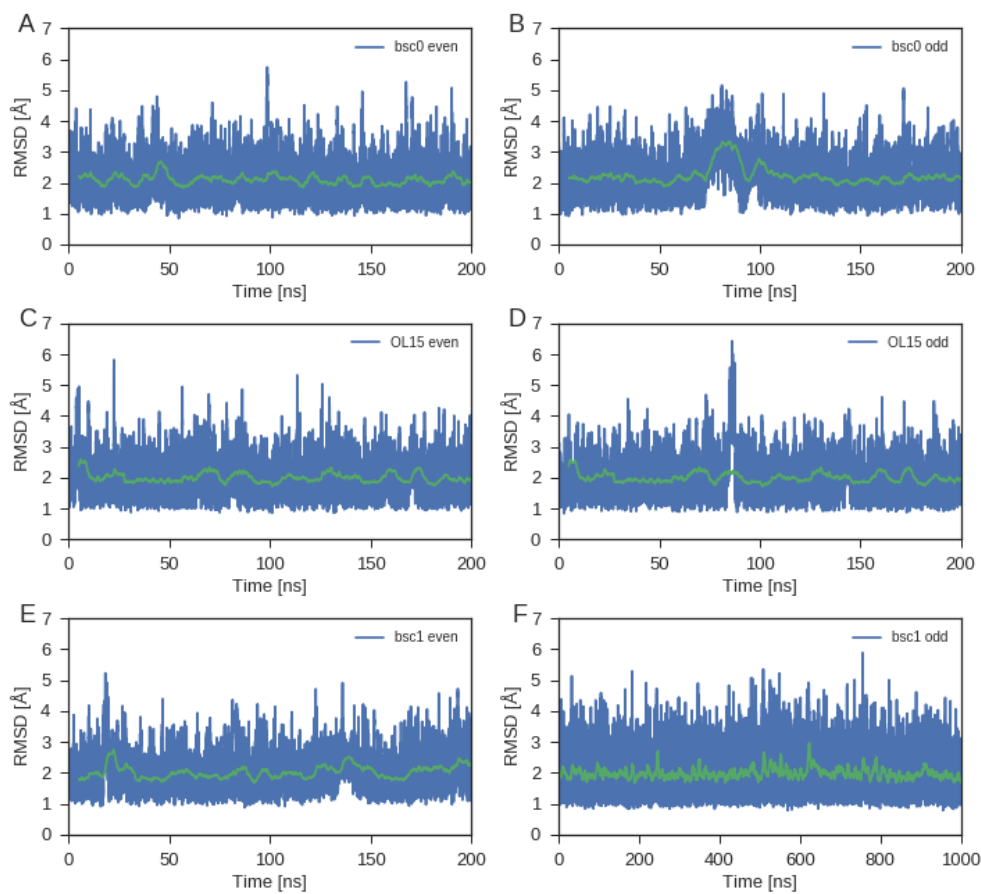


Fig. S4: RMSD from the average simulation structure for simulations with the bsc0 (A and B), OL15 (C and D) and bsc1 (E and F) force fields. All heavy atoms were included in the RMSD calculation. The green curves correspond to 5 ns window averages.

Testing the extraction of spin-positions from MD simulations

Since the MD simulations were run without the spin labels, the spin positions were determined according to the published structure of $\dot{\text{C}}^{13}$ in a mapping approach. The position of the unpaired electron was extrapolated from the cytosine ring (Fig. 1A in the main text), assuming a perfectly rigid and planar spin label. Specifically, the vector connecting the centers of C4-C5 and C2-N1 bonds of the cytosine ring was extrapolated to the position of the radical, as illustrated in Fig. S5F. This extrapolation over two aromatic ring systems (with the distance between the edge of the cytosine ring, the C4-C5 bond, and the unpaired electron 7.7 Å) may lead to uncertainties in the spin positions (Fig. S5) as the cytosine ring may deviate slightly from its ideal, planar structure due to thermal motions in MD and/or imperfections in the force field. Larger relative uncertainties in the spin positions would be expected for the spin-label pairs closer together, which may contribute to the trend we found in the comparison of experiment and simulation, with excellent agreement at large distances (e.g., DNA(1,13)), but worse agreement at the shortest distances (DNA(1,5) and DNA(1,6)). To test for possible uncertainties in the extracted spin positions, we also determined the spin positions by fitting the $\dot{\text{C}}$ coordinates onto cytosine at spin-labeled sites. Fig. S5D highlights cytosine at spin-labeled site 6 in a snapshot taken from a MD trajectory. The $\dot{\text{C}}$ is then RMSD fitted onto the heavy atoms of the cytosine ring (Fig. S5E). In the X-ray structure,¹³ the N-O featuring the paramagnetic center is not in the plane of the $\dot{\text{C}}$ ring system. Geometry optimizing the structure at the PBE0/N07D level of theory moved the N-O bond into the plane of $\dot{\text{C}}$. The resulting $\dot{\text{C}}$ structure is almost identical to the one Edwards et al. obtained at the B3LYP/6-31G* level of theory.

For both a short distance DNA(1,6), and a long distance, DNA(1,12), we find that fitting $\dot{\text{C}}$ to the respective cytosine in the MD trajectory leads to spin-spin distances virtually identical to the ones determined by extrapolation (Fig. S5B and C). The analysis suggests that high quality spin positions can be determined, simply by extrapolating from the cytosine positions. However, residual flexibility in $\dot{\text{C}}$ may further broaden the distance distribution.

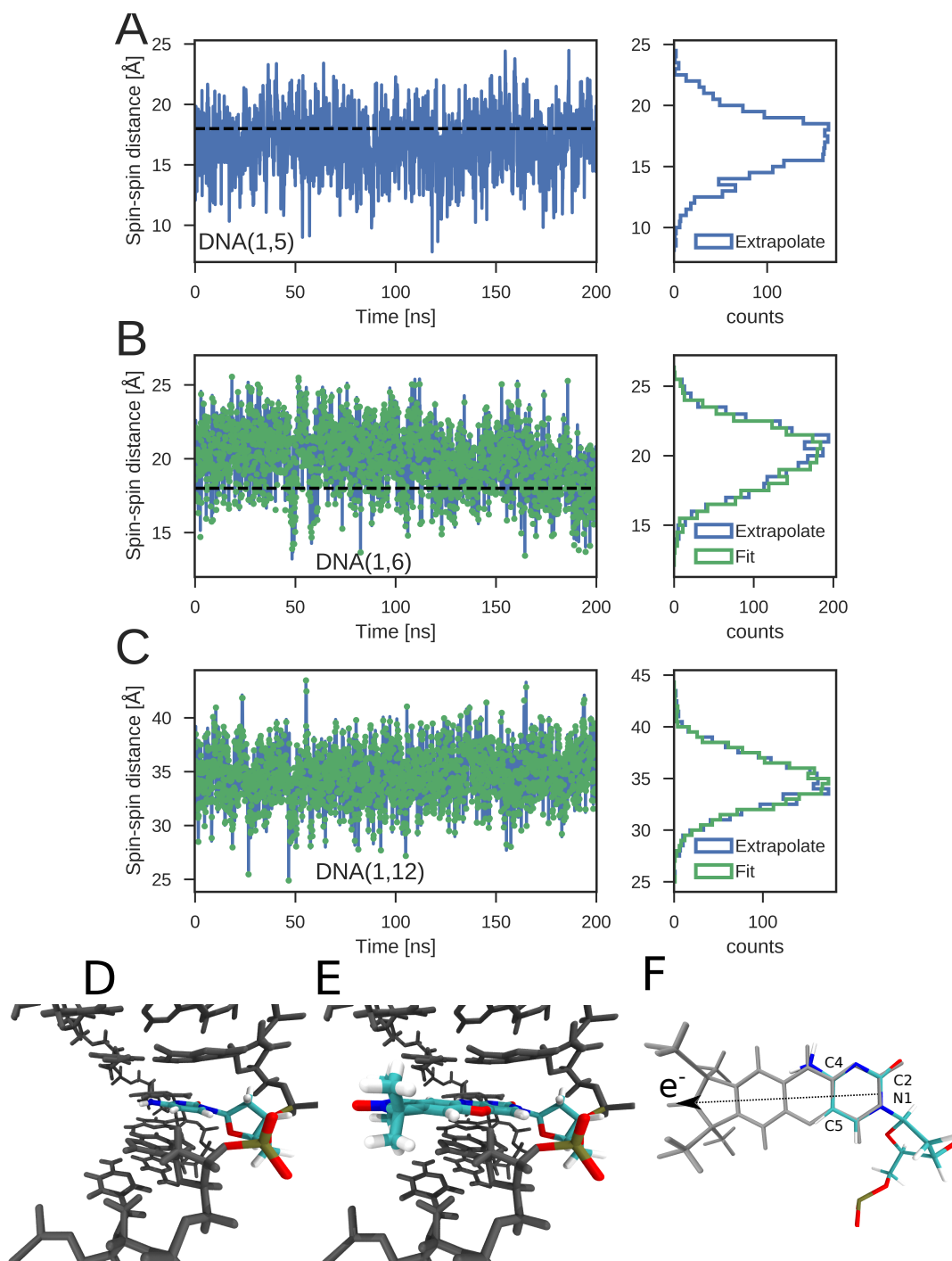


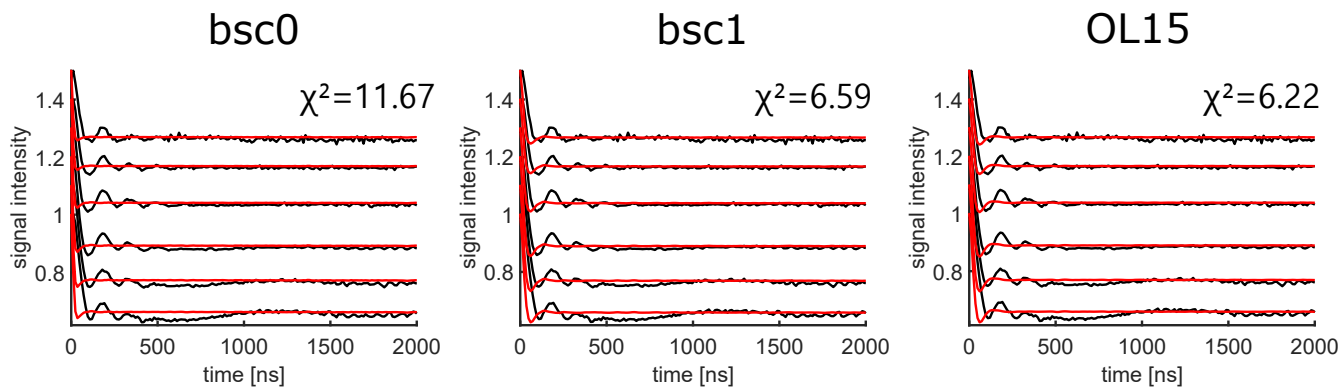
Fig. S5: Spin-spin distances from MD simulations. Timeseries are shown in the left and distributions in right panel. (A,B) For DNA(1,5) and DNA(1,6) short distances $< 18 \text{ \AA}$ outside the range accessible to high-resolution distance measurements by PELDOR were sampled in MD. Distances as determined from MD trajectories from extrapolation of spin positions (blue) are compared to RMSD fitting the DFT-optimized ζ X-ray structure (green) onto cytosines 1 and 6 (B) and 1 and 12 (C). (D) Cytidine at position 6 in a structure from MD. (E) ζ fitted onto the heavy atoms of the cytosine ring of cytosine 6. (F) Determining the spin-positions by extrapolation of the vector connecting the centers of the C4-C5 and C2-N1 bonds of the cytosine ring.

The time series for DNA(1,5) and DNA(1,6) also show that many distances shorter than 18 Å are sampled in MD, which is outside the range accessible to high-resolution PELDOR experiments. The contributions of these distances to the experimental signals³³ may not be fully captured by the theoretical formalism used here .

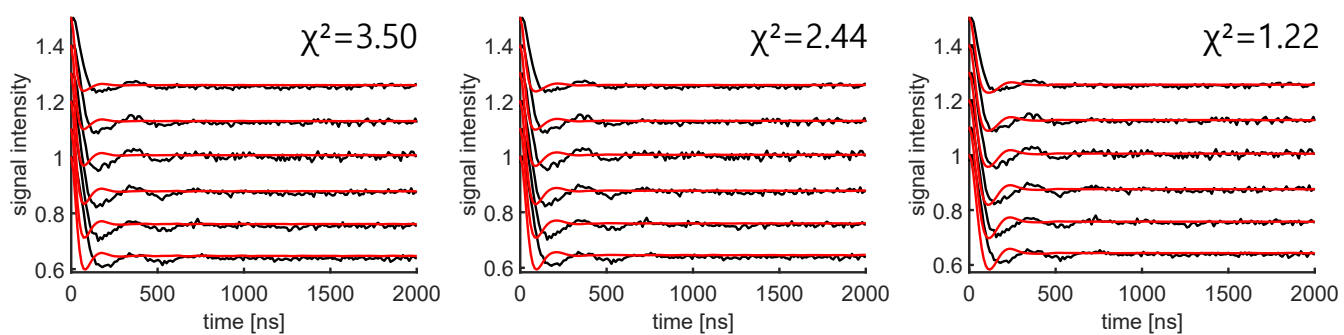
From the distance between the two spin labels and their mutual orientation, which is described by a set of five Euler angles, we calculated the PELDOR traces as described briefly above and in detail by Marko *et al.*²⁸

Comparison of X-Band PELDOR traces to MD simulations

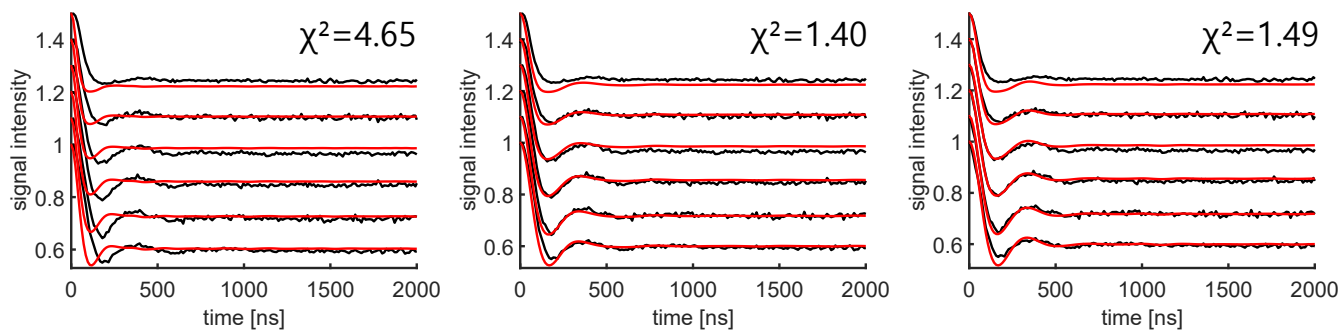
Overall the PELDOR signals calculated from MD simulations agree well with X-band experiments (Fig. S6), with the newer force fields marking a clear improvement over the established bsc0 force field as discussed in the main text. By extending a MD trajectory with the bsc1 force field to 1 μ s, we test whether we have captured the essence of the motions giving rise to the experimental PELDOR signal in our simulations. We find a similar level of agreement for the PELDOR signals calculated from the first (0 - 200 ns) and the second part (200 ns - 1 μ s) of the simulation, with e.g., the agreement improving somewhat for DNA(1,9) and DNA(1,13) (Fig. S7). This suggests (1) that the bsc1 force field is stable on the 100 ns - 1 μ s timescale, (2) that our simulations have captured the essence of the dynamics giving rise to the PELDOR signal, and correspondingly (3) that for our B-DNA sub- μ s motions largely determine the PELDOR signal.



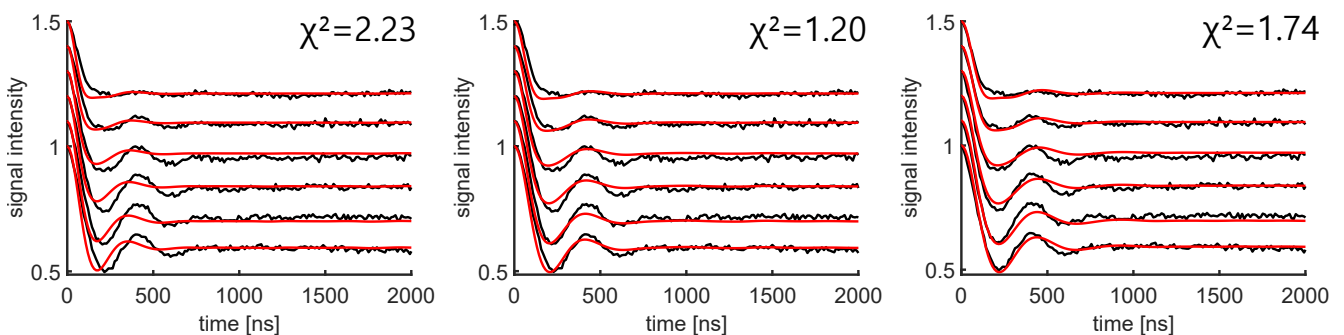
(a) DNA(1,5)



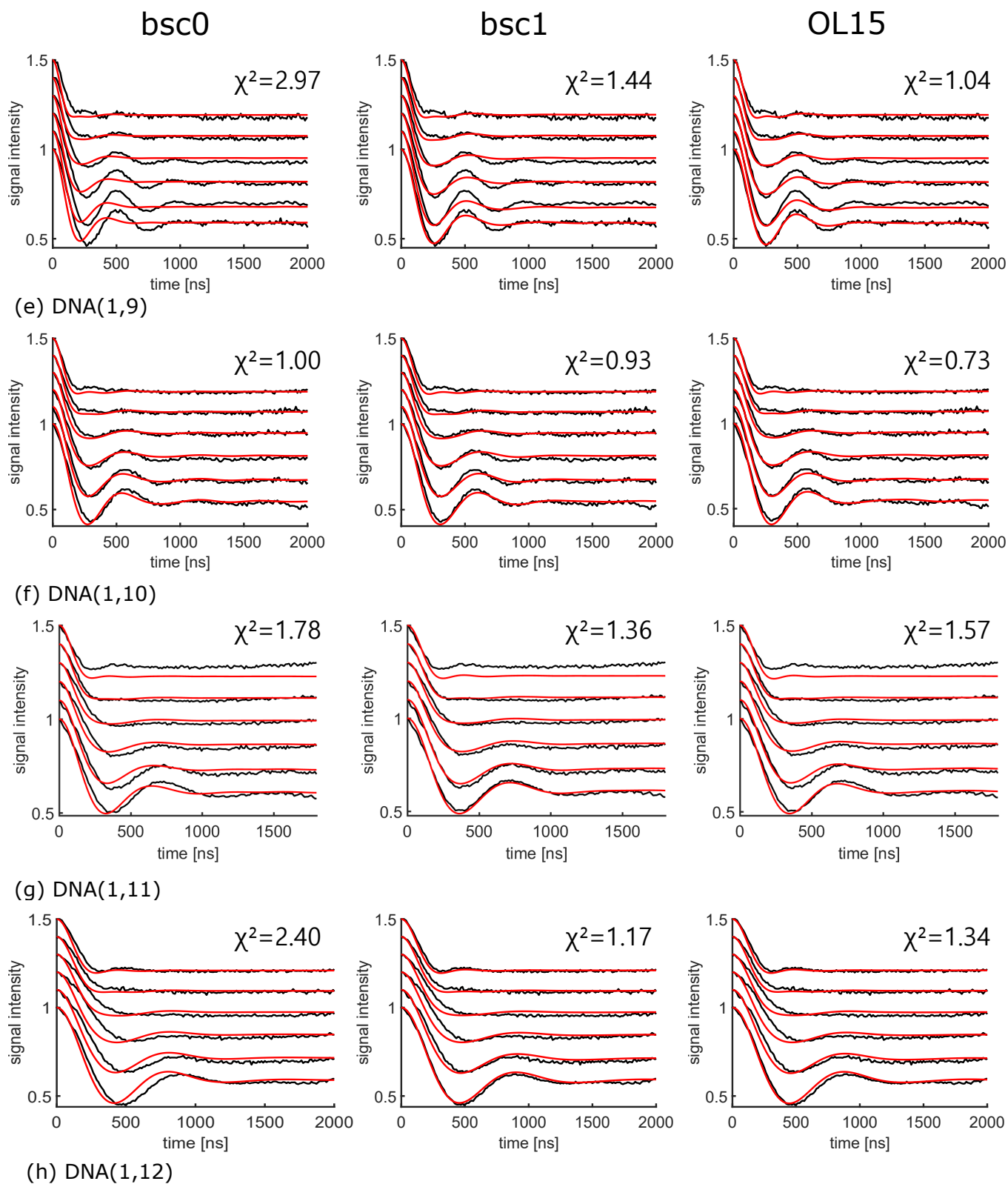
(b) DNA(1,6)



(c) DNA(1,7)



(d) DNA(1,8)



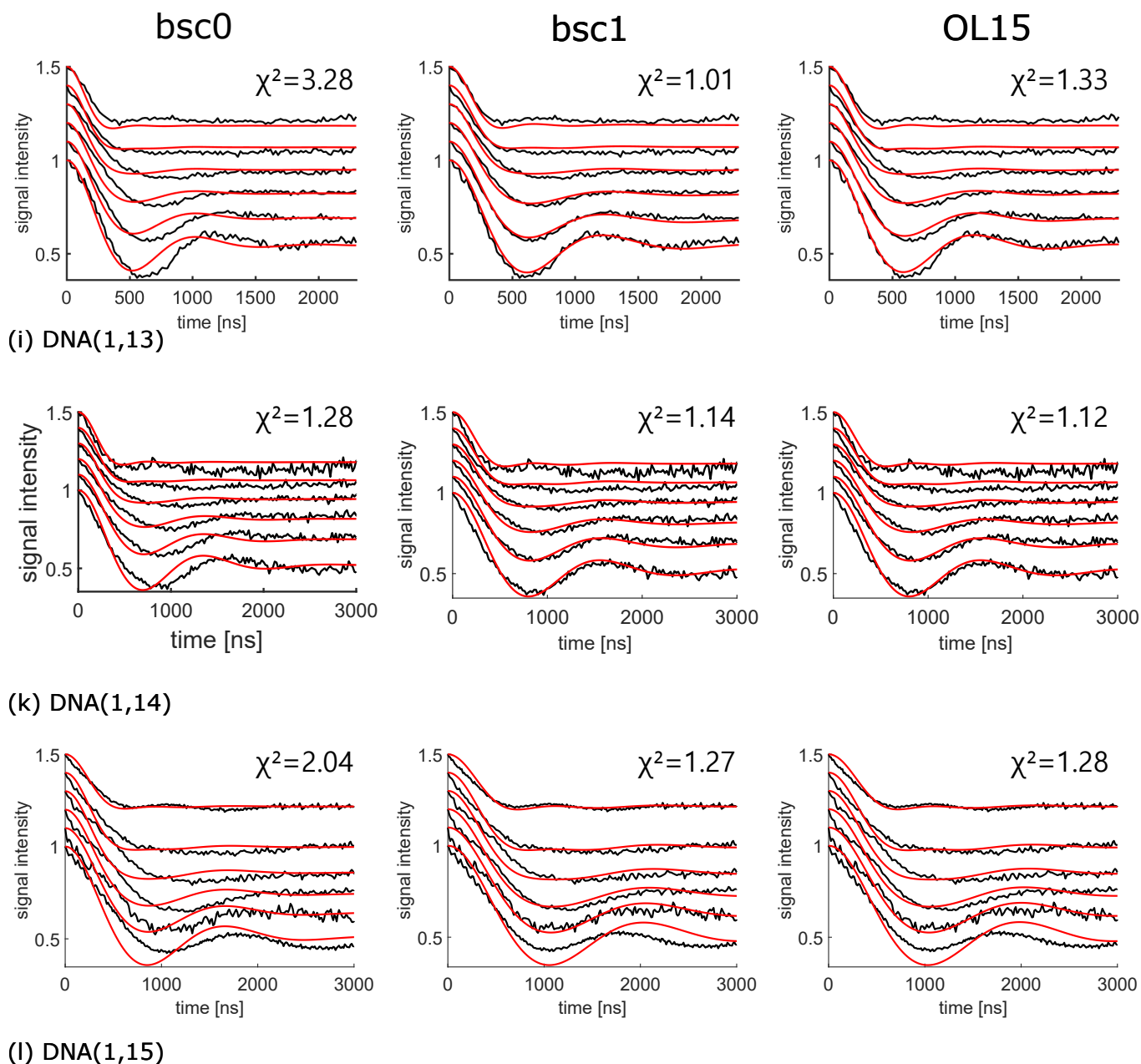


Fig. S6: Comparison of X-band PELDOR signals calculated from MD simulations (red) to experiment (black). The PELDOR time traces were measured at X-band with different offsets ν_n between probe and pump pulse frequency from 40 MHz (lower) to 90 MHz (upper time trace). Simulations with the bsc0 force field are shown on the left. The middle panel shows simulations with the bsc1 force field and the right panel with the OL15 force field. Each panel lists the χ^2 deviations averaged over the six traces.

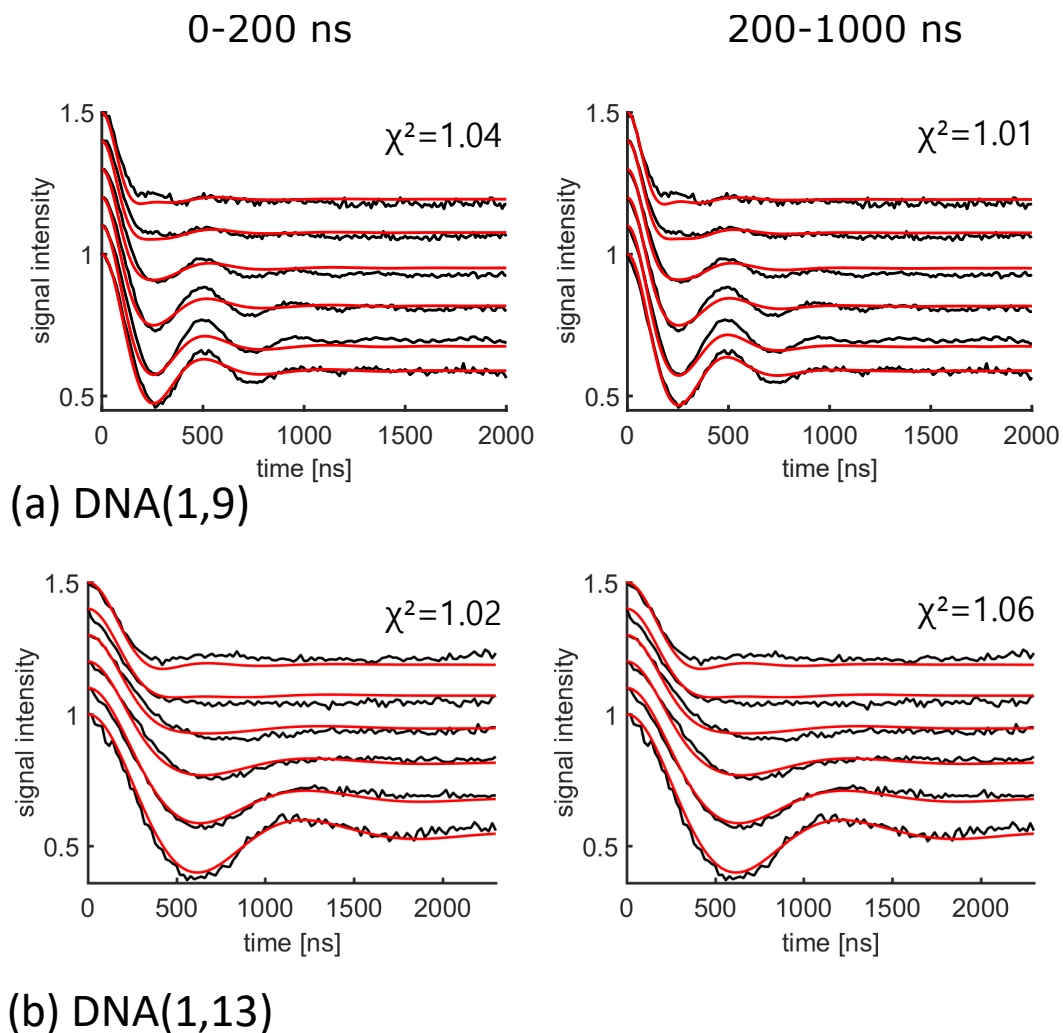


Fig. S7: Comparison of X-band PELDOR signals calculated from MD simulations with the bsc1 force field (red) to experiment (black) for trajectory extended to $1 \mu s$. Comparison for DNA(1,9) (a) and DNA(1,13) (b). The PELDOR time traces were measured at X-band with different offsets ν_n between probe and pump pulse frequency from 40 MHz (lower) to 90 MHz (upper time trace). Each panel lists the χ^2 deviations averaged over the six traces.

Comparison of G-band PELDOR time traces to MD simulations

PELDOR experiments were also recorded at G-Band frequency (6.4 T, 180 GHz),¹¹ which enables us to further probe spin-label orientations from MD (Fig. S8). G-band PELDOR experiments were recorded at different field positions, corresponding to $B||g_{xx}$, $B||g_{yy}$, and $B||g_{zz}$ positions. High-field G-band experiments are more sensitive to mutual orientation than X-band experiments, especially with respect to the orientation in the plane of the spin label. We compare the MD simulations to the experiments by calculating corresponding PELDOR traces²⁸ using the same procedure as for the X-band analysis. We find that the newer OL15 and bsc1 force fields yield better agreement with the G-Band PELDOR traces for DNA(1,9) and DNA(1,12) than the well-established bsc0 force field. Changes in the form of the traces, in particular for DNA(1,9), suggest that orientations are better captured in the simulations with the OL15 and bsc1 force fields.

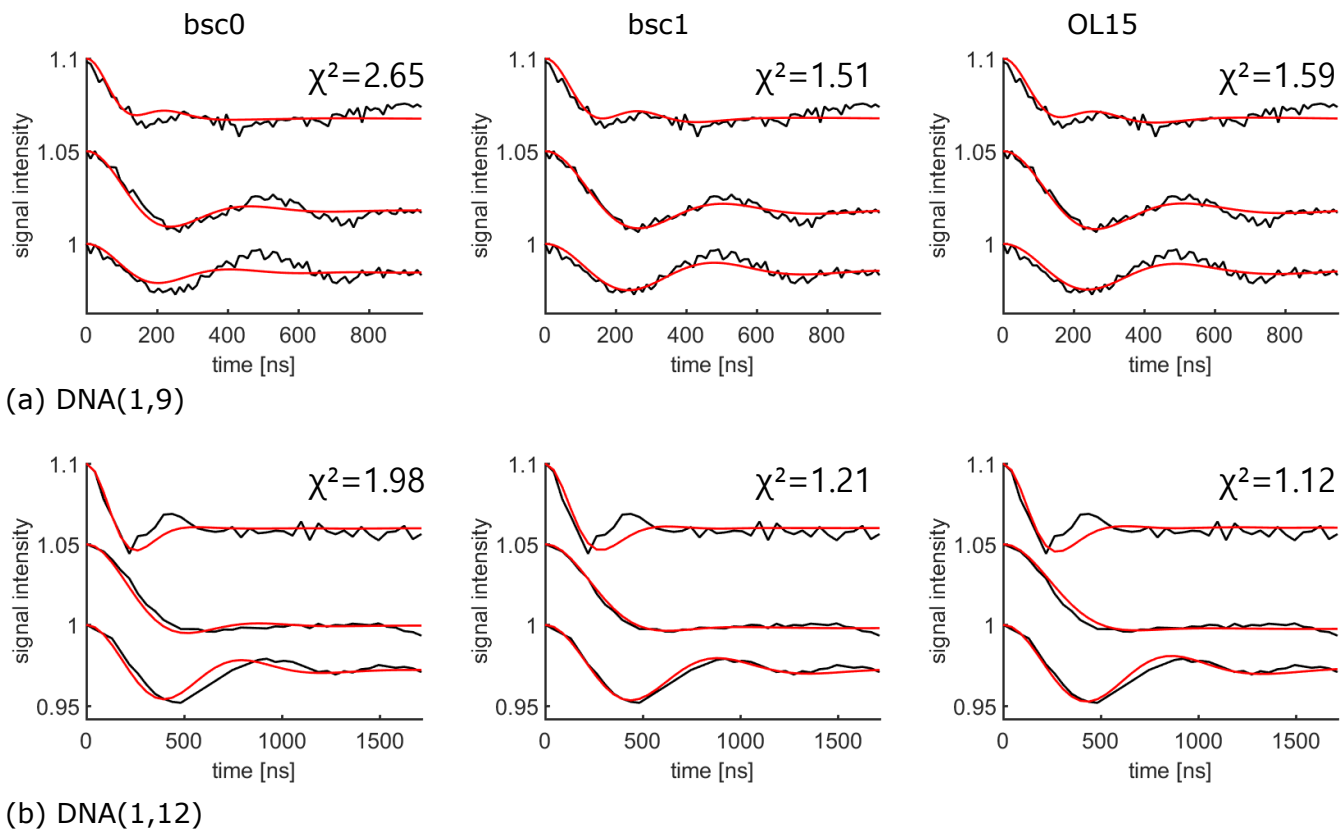


Fig. S8: Comparison of G-band PELDOR signals calculated from MD simulations (red) to experiment (black). (a) DNA(1,9) and (b) DNA(1,12). The PELDOR time traces were measured at G-band at different field position, corresponding to $B||g_{xx}$, $B||g_{yy}$, and $B||g_{zz}$ positions (top to bottom). Simulations with the bsc0, bsc1 and OL15 force fields are shown in the left, center, and right panels, respectively. Each panel lists the χ^2 deviations averaged over the three traces.

Comparison of MD simulation with parm94 to PELDOR

A simulation with the older force field parm94^{2,3} further confirmed that calculating PELDOR signals from MD simulations can rank the quality of simulations ensembles. The parm94 and parm99 force fields capture the structure of DNA relatively poorly, which necessitated the development of the bsc0 force field.⁴ We ran a 200 ns simulations with parm94 using the DNA sequence with the second spin label at odd-numbered positions (Fig. S1A). As expected the DNA structure moved away from the reference B-helix, with on average, a RMSD of > 6 Å over the last 50 ns of the simulation. Simulations with the bsc0, OL15 and bsc1 force fields stayed much closer to the reference helix as discussed above. Visual inspection also revealed degradation in helical structure and the helix radius (parm94: 7.3 ± 0.5 Å, bsc1: 6.3 ± 0.3 Å) and helix pitch (parm94: 31 ± 1 Å, bsc1: 33 ± 1 Å) also differed markedly from the bsc1 simulations.

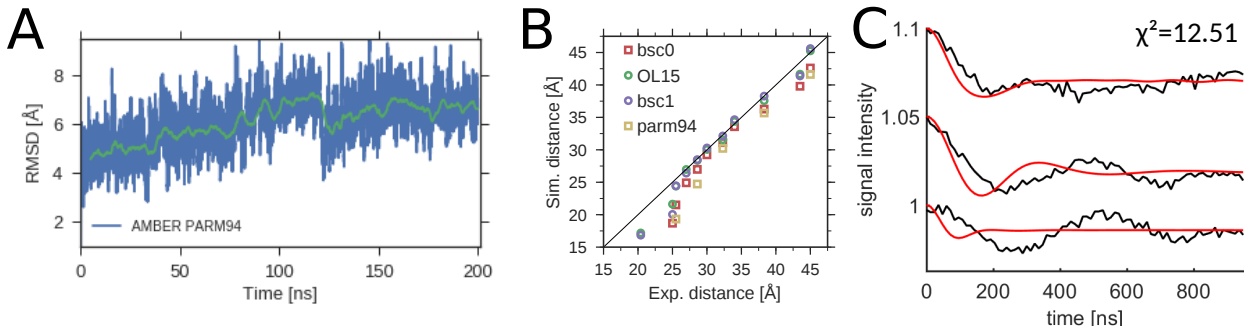


Fig. S9: Analysis of a MD simulations with parm94. (A) RMSD from starting structure, a reference B-helix. All heavy atoms were included in the RMSD calculation. (B) Mean spin-spin distances from the simulation with parm94 compared to the experimentally determined distances. The distances from the simulations with other force fields are shown for reference. (C) Comparison of calculated G-band PELDOR signals (red) for DNA(1,9) to experiment (black). The PELDOR time traces were measured at G-band at different field position, corresponding to $B||g_{xx}$, $B||g_{yy}$, and $B||g_{zz}$ positions (top to bottom). The χ^2 deviation averaged over the three traces is listed in the panel.

The agreement between the calculated PELDOR signals from the simulation with parm94 is significantly worse than for more recent force fields. The χ^2 values for the X-band measurements are larger than for the bsc0, OL15 and bsc1 simulations. The oscillatory frequencies in the calculated X-band traces differs markedly from experiment (Fig. S10), which indicates

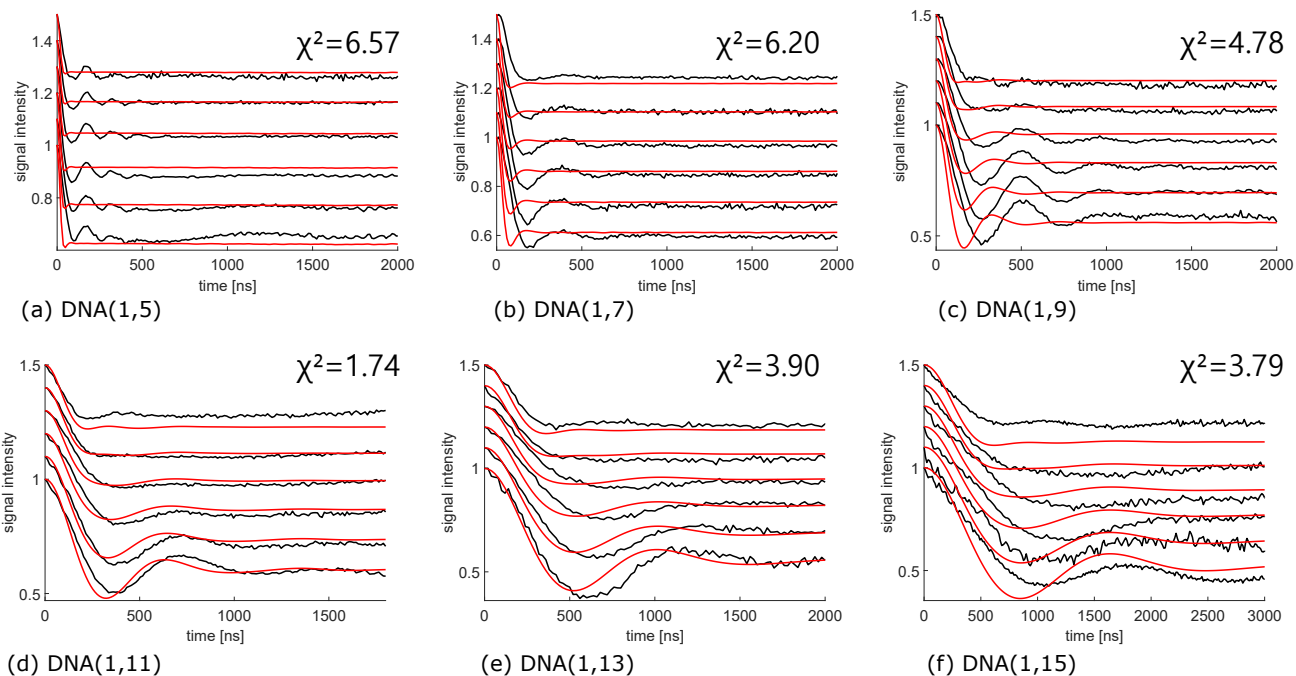


Fig. S10: Comparison of X-band PELDOR signals from MD simulation with parm94 (red) to experiment (black). The PELDOR time traces were measured at X-band with different offsets ν_n between probe and pump pulse frequency from 40 MHz (lower) to 90 MHz (upper time trace). Each panel lists the χ^2 deviations averaged over the six traces.

that the spin-spin distances extracted from the simulation are too short, as confirmed by comparing the experimental distances to the parm94 simulation in Fig. S9B. The disagreement is more much dramatic for the high-field G-band measurements for DNA(1,9) (Fig. S9), i.e., the orientations are poorly reproduced by the parm94 simulation. By contrast, the other force fields give much better agreement for the G-band measurements for DNA(1,9) (Fig. S8). The unique long-range orientation information from PELDOR is thus particularly useful in the evaluation of computer models of biomolecules.

Effect of freezing on the determination the conformational ensemble by PELDOR

PELDOR experiments are recorded at cryogenic temperatures and sample freezing might affect the comparison of the MD simulations run at room temperature. As the sample is

frozen, the system responds to cooling, but at some point most dynamics is frozen out^{34,35} and the system becomes trapped. This trapped ensemble is then probed by the PELDOR measurement.³⁶ The effect of freezing on the comparison between simulation and experiment can be investigated, for instance, by essential dynamics,³⁷ which is based on principal component analysis (PCA), to remove the effect of thermal fluctuations from room-temperature simulations or in low-temperature simulations. We ran an additional set of simulations at 230 K. This temperature should be close to the point where most of the dynamics is frozen out, according to previous work using a comparable simulation setup,³⁸ with DNA described with an AMBER force field (parm99³⁹) and water with the TIP3P model.

Given that at low temperature conformational transitions are expected to slow down and simulations will be trapped in local minima, generating a representative ensemble from a single trajectory would require exceedingly long simulation times. Hence we ran many (2000) short (100 ps) simulations started from structures sampled during a room temperature trajectory (bsc1, sequence with the second spin label at odd positions, Fig. S1B) to generate a representative ensemble. The PELDOR traces calculated for the low temperature ensemble give overall good agreement with experiment (Fig. S11).

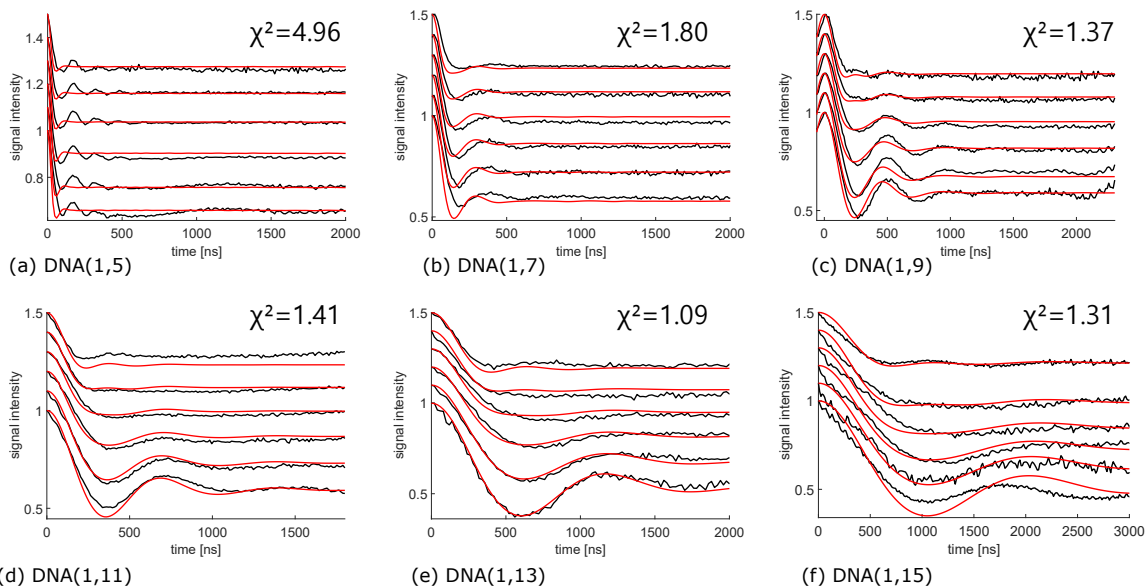


Fig. S11: Effect of freezing. Comparison of simulations at 230 K (red) to the experimental X-Band PELDOR data (black). At 230 K, we ran 2000 simulations for 100 ps each, starting from structures sampled at room temperature. The PELDOR time traces were measured at X-band with different offsets ν_n between probe and pump pulse frequency from 40 MHz (lower) to 90 MHz (upper time trace). Each panel lists the χ^2 deviations averaged over the six traces.

Geometrical analysis of DNA helix in the MD simulations

The DNA helix showed considerable bending in the MD simulations. Bending motions constituted the two most important principal component analysis (PCA) modes. To characterize the extent of bending in MD to parameterize a 3D vector model of helix dynamics (see below) we calculated the bending angle θ . To calculate θ , we first RMSD fitted the structures in a MD trajectory on a five base-pair segment at one end of the helix. Subsequently, we aligned a second five base-pair segment a distance L away from the first base-pair segment and determined the Euler angle θ , corresponding to a polar angle, from the rotation matrix. To reduce the error incurred by RMSD fitting to a flexible molecule, we used the average structure in the simulation as a reference. As expected we find small bending angles at close separation and larger angles at larger distance L . The mean bending angles from MD and the previous PELDOR study agree well (Table 1 in the main text).

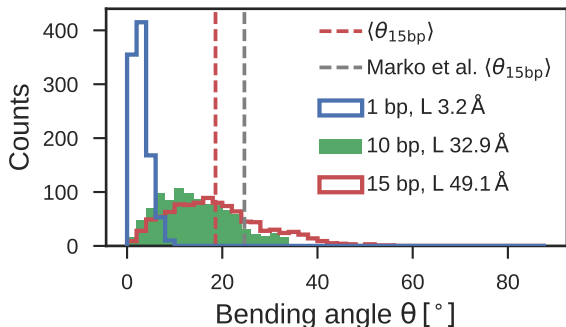


Fig. S12: Bending in MD. Distributions of θ at different center of mass distances/ contour lengths L , with the base pair distance between the centers of the segments indicated in the legend.

To further characterize the motions of the DNA, we calculated helix radius, helical rise and helical twist. The helix radius and rise (Table 1 in the main text) were averaged over the 12 central base pairs in order to remove noise from the more flexible base pairs at the ends of the DNA helix. From the correlation between the helical twist and the helical rise we determined the twist-stretch coupling, i.e., changes in the length of DNA as it twists (Fig. S13).^{40,41} We analyzed 2000 snapshots from the MD trajectories, spaced 0.1 ns apart,

using 3DNA.^{20,21} Because base pairs at the ends of a dsDNA strand are more flexible, we included only the central base pairs in the calculation and the data were smoothed by binning in intervals of 0.2° , following the approach taken by Liebl et al.⁴⁰ As expected, we find a correlation between the helical twist and rise. The considerable bending of the DNA in the MD simulations adds noise to the analysis. The bending motions give rise to a spread in the helical rise (the distance between two neighboring base pairs) for a given value of the helical twist.

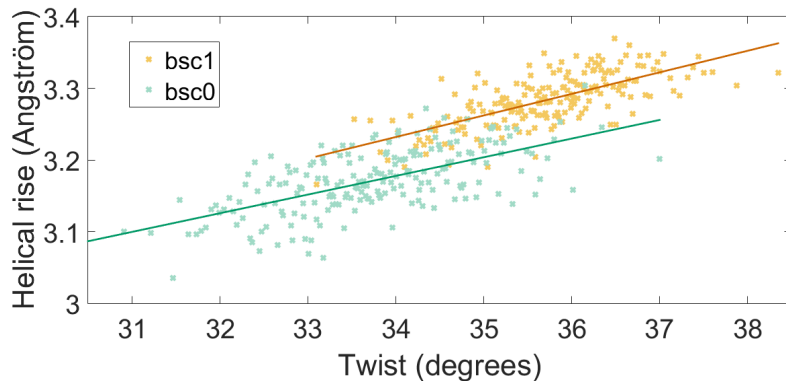


Fig. S13: Coupling of helical rise and helical twist for MD simulations with bsc0 (green) and bsc1 (yellow). The plots are generated for 2000 structures equally spaced in the 200 ns trajectories. The helical twist and helical rise is averaged over the 16 central base pairs. The slopes are $0.026 \text{ \AA deg}^{-1}$ (bsc0) and $0.03 \text{ \AA deg}^{-1}$ (bsc1). The data were binned in intervals of 0.2 deg following Ref. 40.

Comparison with a geometrical model of DNA helix dynamics

Previously the dynamics of spin-labeled DNA were analyzed with a geometrical/mechanical model,^{11,42} capturing the essence of the dynamics of double helical DNA, which we re-examined based on our MD simulations. This 3D vector model was parameterized according to the distributions of helical rise, helical twist and helix bending determined from a MD simulation with the bsc1 force field (Table 1 in the main text). The mean bending angle for a contour length of 64 Å was estimated to be 23° for the MD simulations by extrapolating with an exponential fit to the mean bending angles determined at different contour lengths (from 3.2 Å to 49.1 Å). The signals calculated from the MD ensemble are a bit more dampened (Fig. S14), reflecting additional motions not captured by the helix model. Nevertheless, good agreement was observed, confirming that bending and twist-stretch motions are the most important motions captured by the PELDOR experiments.

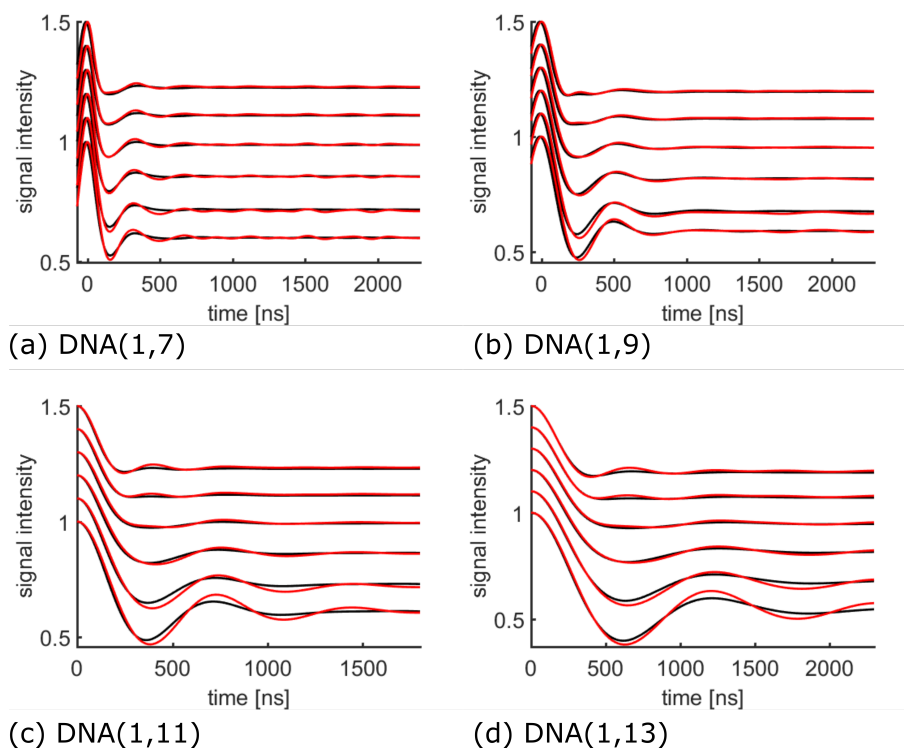


Fig. S14: Comparison of PELDOR signals calculated from MD (black) and a geometrical/mechanical model of the DNA (red). The PELDOR time traces were measured at X-band with different offsets ν_n between probe and pump pulse frequency from 40 MHz (lower) to 90 MHz (upper time trace). The mechanical model was parameterized to reproduce the helical dynamics observed in the MD simulations with the bsc1 force field.

References

- (1) Hess, B.; Kutzner, C.; van der Spoel, D.; Lindahl, E. *J. Chem. Theory Comput.* **2008**, *4*, 435–447.
- (2) Cornell, W. D.; Cieplak, P.; Bayly, C. I.; Gould, I. R.; Merz, K. M.; Ferguson, D. M.; Spellmeyer, D. C.; Fox, T.; Caldwell, J. W.; Kollman, P. A. *J. Am. Chem. Soc.* **1995**, *117*, 5179–5197.
- (3) Kollman, P.; Dixon, R.; Cornell, W.; Fox, T.; Chipot, C.; Pohorille, A. In *Computer Simulation of Biomolecular Systems: Theoretical and Experimental Applications*; van Gunsteren, W. F., Weiner, P. K., Wilkinson, A. J., Eds.; Springer Netherlands: Dordrecht, 1997; pp 83–96.
- (4) Pérez, A.; Marchán, I.; Svozil, D.; Sponer, J.; Cheatham, T. E.; Laughton, C. A.; Orozco, M. *Biophys. J.* **2007**, 3817–3829.
- (5) Guy, A. T.; Piggot, T. J.; Khalid, S. *Biophys. J.* **2012**, *103*, 1028 – 1036.
- (6) Krepl, M.; Zgarbová, M.; Stadlbauer, P.; Otyepka, M.; Banáš, P.; Koča, J.; Cheatham, T. E.; Jurečka, P.; Šponer, J. *J. Chem. Theory Comput.* **2012**, *8*, 2506–2520.
- (7) Zgarbová, M.; Luque, F. J.; Šponer, J.; Cheatham, T. E.; Otyepka, M.; Jurečka, P. *J. Chem. Theory Comput.* **2013**, *9*, 2339–2354.
- (8) Zgarbová, M.; Šponer, J.; Otyepka, M.; Cheatham, T. E.; Galindo-Murillo, R.; Jurečka, P. *J. Chem. Theory Comput.* **2015**, *11*, 5723–5736.
- (9) Ivani, I.; Dans, P. D.; Noy, A.; Pérez, A.; Faustino, I.; Hospital, A.; Walther, J.; Andrio, P.; Goñi, R.; Balaceanu, A.; Portella, G.; Battistini, F.; Gelpí, J. L.; González, C.; Vendruscolo, M.; Laughton, C. A.; Harris, S. A.; Case, D. A.; Orozco, M. *Nat. Methods* **2016**, *13*, 55–58.

- (10) Case, D. A.; Cheatham, T. E.; Darden, T.; Gohlke, H.; Luo, R.; Merz, K. M.; Onufriev, A.; Simmerling, C.; Wang, B.; Woods, R. J. *J. Comput. Chem.* **2005**, *26*, 1668–1688.
- (11) Marko, A.; Denysenkov, V.; Margraf, D.; Cekan, P.; Schiemann, O.; Sigurdsson, S. T.; Prisner, T. F. *J. Am. Chem. Soc.* **2011**, *133*, 13375–13379.
- (12) Sousa da Silva, A. W.; Vranken, W. F. *BMC Res. Notes* **2012**, *5*, 367.
- (13) Edwards, T. E.; Cekan, P.; Reginsson, G. W.; Shelke, S. A.; Ferre-D’Amare, A. R.; Schiemann, O.; Sigurdsson, S. T. *Nucleic Acids Res.* **2011**, *39*, 4419–4426.
- (14) Jorgensen, W. L.; Chandrasekhar, J.; Madura, J. D.; Impey, R. W.; Klein, M. L. *J. Chem. Phys.* **1983**, *79*, 926–935.
- (15) Joung, I. S.; Cheatham, T. E. *J. Phys. Chem. B* **2008**, *112*, 9020–9041.
- (16) Bussi, G.; Donadio, D.; Parrinello, M. *J. Chem. Phys.* **2007**, *126*, 014101.
- (17) Parrinello, M.; Rahman, A. *J. Appl. Phys.* **1981**, *52*, 7182–7190.
- (18) Michaud-Agrawal, N.; Denning, E. J.; Woolf, T. B.; Beckstein, O. *J. Comput. Chem.* **2011**, *32*, 2319–2327.
- (19) Gowers, R. J.; Linke, M.; Barnoud, J.; Reddy, T. J. E.; Melo, M. N.; Seyler, S. L.; Dotson, D. L.; Domański, J.; Buchoux, S.; Kenney, I. M.; Beckstein, O. *Proc. 15th Python Science Conf.* **2016**, 98–105.
- (20) Lu, X. J.; Olson, W. K. *Nucleic Acids Res.* **2003**, *31*, 5108–5121.
- (21) Kumar, R.; Grubmüller, H. *Bioinformatics* **2015**, *31*, 2583–2585.
- (22) Frisch, M. J.; Trucks, G. W.; Schlegel, H. B.; Scuseria, G. E.; Robb, M. A.; Cheeseman, J. R.; Scalmani, G.; Barone, V.; Mennucci, B.; Petersson, G. A.; Nakatsuji, H.;

Caricato, M.; Li, X.; Hratchian, H. P.; Izmaylov, A. F.; Bloino, J.; Zheng, G.; Sonnenberg, J. L.; Hada, M.; Ehara, M.; Toyota, K.; Fukuda, R.; Hasegawa, J.; Ishida, M.; Nakajima, T.; Honda, Y.; Kitao, O.; Nakai, H.; Vreven, T.; Montgomery, J. A., Jr.; Peralta, J. E.; Ogliaro, F.; Bearpark, M.; Heyd, J. J.; Brothers, E.; Kudin, K. N.; Staroverov, V. N.; Kobayashi, R.; Normand, J.; Raghavachari, K.; Rendell, A.; Burant, J. C.; Iyengar, S. S.; Tomasi, J.; Cossi, M.; Rega, N.; Millam, J. M.; Klene, M.; Knox, J. E.; Cross, J. B.; Bakken, V.; Adamo, C.; Jaramillo, J.; Gomperts, R.; Stratmann, R. E.; Yazyev, O.; Austin, A. J.; Cammi, R.; Pomelli, C.; Ochterski, J. W.; Martin, R. L.; Morokuma, K.; Zakrzewski, V. G.; Voth, G. A.; Salvador, P.; Dannenberg, J. J.; Dapprich, S.; Daniels, A. D.; Farkas, \tilde{A} .; Foresman, J. B.; Ortiz, J. V.; Cioslowski, J.; Fox, D. J. Gaussian 09 Revision D.01. Gaussian Inc. Wallingford CT **2009**.

(23) Adamo, C.; Barone, V. *J. Chem. Phys.* **1999**, *110*, 6158–6170.

(24) Barone, V.; Cimino, P. *Chem. Phys. Lett.* **2008**, *454*, 139 – 143.

(25) N07D basis set taken from <http://dreamsnet.sns.it/downloads>

Accessed June 26, **2017**. http://dreamsnet.sns.it/sites/default/files/download/gaussian/basis_sets/N07D_PBE0.gbs.

(26) Stendardo, E.; Pedone, A.; Cimino, P.; Cristina Menziani, M.; Crescenzi, O.; Barone, V. *Phys. Chem. Chem. Phys.* **2010**, *12*, 11697–11709.

(27) Hermosilla, L.; Prampolini, G.; Calle, P.; García de la Vega, J. M.; Brancato, G.; Barone, V. *J. Chem. Theory Comput.* **2013**, *9*, 3626–3636.

(28) Marko, A.; Margraf, D.; Cekan, P.; Sigurdsson, S. T.; Schiemann, O.; Prisner, T. F. *Phys. Rev. E* **2010**, *81*, 1–9.

(29) Prisner, T.; Marko, A.; Sigurdsson, S. *J. Magn. Reson.* **2015**, *252*, 187–198.

- (30) Akhmetzyanov, D.; Schöps, P.; Marko, A.; Kunjir, N. C.; Sigurdsson, S. T.; Prisner, T. F. *Phys. Chem. Chem. Phys.* **2015**, *17*, 24446–24451.
- (31) Theobald, D. L. *Acta Crystallogr., Sect. A: Found. Crystallogr.* **2005**, *61*, 478–480.
- (32) Liu, P.; Agrafiotis, D. K.; Theobald, D. L. *J. Comput. Chem.* **2010**, *31*, 1561–1563.
- (33) Banham, J.; Baker, C.; Ceola, S.; Day, I.; Grant, G.; Groenen, E.; Rodgers, C.; Jeschke, G.; Timmel, C. *J. Magn. Reson.* **2008**, *191*, 202 – 218.
- (34) Norberg, J.; Nilsson, L. *Proc. Natl. Acad. Sci. U. S. A.* **1996**, *93*, 10173–6.
- (35) Vitkup, D.; Ringe, D.; Petsko, G. A.; Karplus, M. *Nat Struct Mol Biol* **2000**, *7*, 34–38.
- (36) Jeschke, G.; Sajid, M.; Schulte, M.; Ramezani, N.; Volkov, A.; Zimmermann, H.; Godt, A. *J. Am. Chem. Soc.* **2010**, *132*, 10107–10117.
- (37) Meyer, T.; Ferrer-Costa, C.; Pérez, A.; Rueda, M.; Bidon-Chanal, A.; Luque, F. J.; Laughton, C. A.; Orozco, M. *J. Chem. Theory Comput.* **2006**, *2*, 251–258.
- (38) Nakagawa, H.; Yonetani, Y.; Nakajima, K.; Ohira-Kawamura, S.; Kikuchi, T.; Inamura, Y.; Kataoka, M.; Kono, H. *Phys. Rev. E* **2014**, *90*, 022723.
- (39) Wang, J.; Cieplak, P.; Kollman, P. A. *J. Comput. Chem.* **2000**, *21*, 1049–1074.
- (40) Liebl, K.; Drsata, T.; Lankas, F.; Lipfert, J.; Zacharias, M. *Nucleic Acids Res.* **2015**, *43*, 10143–10156.
- (41) Bao, L.; Zhang, X.; Shi, Y.-Z.; Wu, Y.-Y.; Tan, Z.-J. *Biophys. J.* **2017**, *112*, 1094 – 1104.
- (42) Erlenbach, N.; Endeward, B.; Schöps, P.; Gophane, D. B.; Sigurdsson, S. T.; Prisner, T. F. *Phys. Chem. Chem. Phys.* **2016**, *18*, 16196–16201.



Orientation Selective 2D-SIFTER Experiments at X-Band Frequencies

A. M. Bowen^{1,2} · N. Erlenbach¹ · P. van Os¹ · L. S. Stelzl³ · S. Th. Sigurdsson⁴ · T. F. Prisner¹ 

Received: 16 June 2018 / Revised: 6 September 2018 / Published online: 19 September 2018
© Springer-Verlag GmbH Austria, part of Springer Nature 2018

Abstract

Frequency-correlated 2D SIFTER with broadband pulses at X-band frequencies can be used to determine the inter-spin distance and relative orientation of nitroxide moieties in macromolecules when the flexibility of the spin-labels is restricted. At X-band frequencies the EPR spectrum of nitroxides is governed by the strongly anisotropic nitrogen hyperfine coupling. For rigid spin-labels, where the orientation of the inter-connecting vector R correlates to the relative orientations of the nitroxide labels, the dipolar oscillation frequency varies over the EPR spectral line shape. Broadband shaped pulses allow excitation of the complete nitroxide EPR spectra. In this case, Fourier transform of the echo signal gives both fast and direct access to the orientation dependent dipole coupling. This allows determination of not only the inter-spin distance R , but also their mutual orientation. Here, we show the application of the frequency-correlated 2D SIFTER experiment with broadband pulses to a bis-nitroxide model compound and to a double stranded DNA sample. In both molecules, there is restricted internal mobility of the two spin-labels. The experimental results are compared to orientation selective pulsed electron double resonance (PELDOR) experiments and simulations based on a simple geometrical model or MD simulations describing the conformational flexibility of the molecules. Fourier transformation of the SIFTER echo signal yields orientation selective dipolar time traces over the complete EPR-spectral range. This leads to an improved frequency resolution and either to a reduced experimental measurement time or a larger span of frequency offsets measured compared to orientation selective PELDOR experiments. The experimental potential and limitations of the 2D SIFTER method for samples containing rigid spin-labels will be discussed.

A. M. Bowen and N. Erlenbach contributed equally to this work.

✉ T. F. Prisner
prisner@chemie.uni-frankfurt.de

Extended author information available on the last page of the article

1 Introduction

Pulsed dipolar spectroscopy (PDS) methods measure the dipolar interaction between unpaired electron spins. It is an increasingly important set of techniques in biophysics for the determination of structure and structural flexibility in biomolecules. Example of PDS techniques include: pulsed electron double resonance (PELDOR [1, 2], also known as double electron–electron resonance, DEER) [3, 4], double quantum coherence (DQC) [5], relaxation induced dipolar modulation enhancement (RIDME) [6, 7], and the Single Frequency Technique for Refocusing dipolar couplings (SIFTER) [8]. All PDS techniques result in oscillating time traces, where the frequency of oscillation ω_{dd} can be related to the inter-spin distance R and, in cases of rigid radical moieties or spin-labels, to the orientation θ of the distance vector \mathbf{R} with respect to the external magnetic field direction.

$$\omega_{\text{dd}} = \frac{\mu_0 \mu_{\text{B}}^2}{4\pi \hbar} g_{\text{A}} g_{\text{B}} \frac{1 - 3 \cos^2 \theta}{R^3}. \quad (1)$$

Here, μ_0 is the magnetic susceptibility of a vacuum, μ_{B} is the Bohr magneton and \hbar is the reduced Planck constant. g_{A} and g_{B} are the effective g -factors of the two coupled spins (notated A and B).

Many biomolecules are inherently EPR silent; therefore, to study them spin-labels must be used. Frequently, these spin-labels are nitroxide based, due to their stability and ease of handling. In the case, that the nitroxide spin-labels are attached to the biomolecule via flexible tethers, all orientations of \mathbf{R} with respect to the external magnetic field (described by the angle θ) contribute to each resonance position within the EPR spectra. This is typically the case for the MTSSL (1-oxyl-2,2,5,5-tetramethylpyrroline-3-methyl methanethiosulfonate) spin-label covalently bound to cysteines of proteins, modified via site directed mutagenesis [9]. In this case, the Fourier transform of the dipolar time trace results in the well-known Pake pattern. This can be analysed purely in terms of the distance R between both spin-labels or a distance distribution $P(R)$ for flexible macromolecules [10].

In contrast, when rigid nitroxides are attached to the macromolecule such that they have limited motion, as is the case for the spin-labeled DNA molecule presented in this work, different angles θ contribute to the dipolar time trace, depending on the frequencies excited in the EPR spectrum. Currently, the most common method to probe orientation selection in PDS is 2D-PELDOR, a method where several one-dimensional time traces are recorded sequentially by varying the pump and/or detection pulse frequency or the external magnetic field strength to sample different orientations of the spin-label with respect to the external magnetic field. Commonly, for nitroxide spin-labels at X-band, this is achieved by positioning the pump pulse at the centre of the nitroxide spectrum and varying the detection pulse frequency offset.

For nitroxide spin-labels, when the system is fully rigid, a set of orientation selective X-band data set may allow full determination of the distance and relative

orientation between both spin-labels [11]. However, as most molecules have some degree of flexibility, an increased set of orientation selective PDS traces may provide a more stable solution.

A disadvantage of the 2D PELDOR methodology is that a number of different time traces must be collected to allow accurate analysis making the experiment time consuming. Furthermore, to sample the full range of orientations at X-band frequencies, the probe frequencies have to be offset up to 90 MHz, which due to the finite resonator bandwidth leads to varying microwave field strengths as a function of the offset frequency. This can lead to a variation of the excitation bandwidths and modulation depths as a function of the pump and probe frequencies. These experimental variations make the quantitative analysis of such 2D-PELDOR experiments more demanding.

For molecules with rigid spin-labels attached, it is, therefore, highly desirable to have a single two-dimensional experiment in which the complete spectrally resolved dipolar time traces can be detected simultaneously. This can be achieved by single frequency PDS methods, such as DQC and SIFTER, if the pulses that are used excite the whole nitroxide EPR spectrum, as already realized by Jack Freed in several very elegant and benchmarking experiments [12–14].

Whereas rectangular pulses need very high microwave field strengths and short pulse lengths to excite the whole nitroxide spectrum, broadband pulses shaped by a fast arbitrary waveform generator (AWG) can achieve such excitation bandwidths with more moderate microwave powers for prolonged pulse lengths [15, 16]. We have shown that such broadband pulses improve the quality of the 1D SIFTER pulse sequence considerably [16]. However, in the one-dimensional form, integrating over the echo signal has the effect of removing all orientation information [17]. Doll and Jeschke reported a frequency-correlated 2D-SIFTER recorded at Q-band frequencies (35 GHz) using broadband chirp pulses [18].

In this manuscript, we present two-dimensional frequency correlated 2D-SIFTER performed at X-band frequencies, where the spectrum asymmetry is governed by the hyperfine anisotropy. At this frequency band, orientation selection is more easily probed compared to Q-band frequencies, where the g-tensor and nitrogen hyperfine asymmetries have similar size. Additionally, it is often not possible to achieve sufficiently large frequency offsets to adequately sample all orientation selective data at Q-band frequencies without a special wide bandwidth resonator. We compare the 2D-SIFTER experiments with PELDOR experiments performed with several probe frequencies for a bis-nitroxide chemical compound and a double stranded DNA molecule with two rigid ζ spin-labels [19–22]. The optimization of the broadband SIFTER pulse sequence for orientation selective 2D experiments is described, and to validate the methodology, we show comparison of the frequency correlated 2D-SIFTER data recorded to the current gold standard of orientation selective PELDOR and explain the differences in the forms of the data. Finally, we show that it is possible to quantitatively simulate the spectrally resolved time traces using an analytical methodology [11] and compare the data with simulations based on geometrical models [21, 23] or MD simulations [24, 25].

2 Experimental Methods

2.1 Instrumentation and Experimental Conditions

Experiments were performed at X band (9.5 GHz) on a commercially available Bruker Elexsys E580 spectrometer. For experiments using broadband pulses this was modified with an ITS 8200 (innovative technical systems) arbitrary waveform generator (AWG) positioned before the 1 kW travelling wave tube (TWT) amplifier as described in [16]. An Oxford Instruments CF935 cryostat was used to cool the sample and resonator, a Bruker MS3 3 mm loop gap resonator. All experiments were performed at 50 K using a continuous flow of liquid helium and the temperature maintained using an Oxford Instruments ITC 503 temperature control unit.

Pulsed electron double resonance experiments used the four pulse DEER sequence [3, 4], with detection pulse lengths of 32 ns and pump pulse lengths of 16 ns. In all cases, the pump pulse frequency was set to be resonant with the maximum of the nitroxide spectrum and the detection pulses were offset from this frequency by 30 MHz or 40 MHz to 80 MHz or 90 MHz in 10 MHz increments. The bandwidth of the 16 ns pump pulse is sufficient to excite the complete central A_z hyperfine transition ($A_z, m_1=0$) of the nitroxide spectrum, and as a result excites all of the orientations of the nitroxide centre with respect to the magnetic field in this transition while exciting minimal amounts of the other A_z transitions. This results in a pump pulse that yields very little orientation selection. The frequency offsets of 30–90 MHz for the detection frequency was used as this allowed detection on the more intense $A_z, m_1=+1$ feature, a similar set of traces could be measured on the $A_z, m_1=-1$ feature with negative frequency offset between the pump and detection frequencies, however, this would yield traces of lower signal to noise. The lower limit of 30 MHz corresponds to the frequency at which overlap of the pump and detection pulses becomes significant and the upper limit of 80–90 MHz to the edge of the nitroxide spectrum.

To reduce the presence of nuclear modulations in the time traces a tau-averaging procedure of 8 steps with an increment of 56 ns (for deuterated solvent samples) were utilized. For the chemical model system in total 540 time steps with 640 averages per data point have been recorded, resulting in a total acquisition time of about 45 min per offset. The echo signal is integrated over a 32 ns time window. In the DNA system, the concentration of the sample was lower. Therefore, to detect a reasonable signal to noise ratio (SNR), the number of averages was varied for different pump pulse offsets.

The set of PELDOR experiments recorded on the DNA system were recorded keeping the pump pulse frequency constant at the centre of the resonator and the detection pulses were retuned at a different frequency offset for each subsequent experiment. This makes recording the data labour-intensive as retuning is required between each experiment. For the bis-nitroxide model compound an alternative approach was used, whereby the detection frequency was kept constant and the pump frequency and attenuation changed between each experiment.

Pulse length and field strength of the pump pulse were calibrated for each offset frequency of the overcoupled MS3 resonator to achieve same excitation efficiency for all PELDOR traces. This has been reliably achieved, as observed in the data in Figs. 2 and 3 where the modulation depths were in good agreement with the simulations using experimental methods.

For SIFTER we used broadband $\text{sech}(x)/\tanh(x)$ pulses [26] combined with a WURST, (wideband, uniform rate, smooth truncation) amplitude function [27], as previously employed [16]. Two forms of the experimental sequence using broadband pulses were trialed; one where all pulses had equal length (200 ns) and chirp rate, resulting in the relative amplitude of the pulses being ca. 0.4:1 for the $\pi/2$ (200 ns): π (200 ns) pulses; and another where the pulse length of the final π pulse used was 100 ns. The second sequence has the effect of refocusing the phase of all components of the echo at a fixed time [16], leading to the largest solid echo signal. However, it was found that using pulses of equal lengths (200 ns) yielded a better modulation depth, as the longer pulses possessed better excitation efficiency. All of the pulses were calibrated to have bandwidths of ca. 200 MHz, (sufficient to excite the complete nitroxide spectrum). In this optimised sequence the 200 ns π pulses used in the experiment had $\beta=9.3$ MHz, bandwidth parameter $=0.017 \times 2\pi$, $\omega_{1,\max}=25$ MHz, $\varphi=0$, $\beta_{\text{WURST}}=16$ MHz, $n=16$. The 200 ns $\pi/2$ pulses used had $\beta=9.3$ MHz, bandwidth parameter $=0.017 \times 2\pi$, $\omega_{1,\max}=10$ MHz, $\varphi=0$, $\beta_{\text{WURST}}=16$ MHz, $n=16$. For optimum performance, the bandwidth of the broadband pulses was set symmetrically to the edges of the nitroxide EPR spectrum, and thus the carrier frequency was offset from the maximum of the nitroxide spectrum. For our data analysis, a frequency dependent phasing of each time trace after Fourier transform of the echo was used to minimise the contributions in the imaginary channel.

SIFTER was recorded both as a one-dimensional experiment, which allows determination of the distance R by Tikhonov regularization, and as a two-dimensional one to enable orientation dependent analysis. As with the PELDOR sequence described above tau-averaging was incorporated in all of the SIFTER experiments by increasing each tau period by 56 ns over 8 steps to average over the deuterium nuclear oscillations from the deuterated solvents used.

2.2 Processing of Experimental Data

For PELDOR time traces an exponential background correction was performed using Deer Analysis to remove the background due to intermolecular dipolar interactions [10]. SIFTER backgrounds are known to contain components due to both inter molecular dipolar interactions and relaxation [29]. It is possible to remove the part due to relaxation by recording an additional experimental SIFTER traces under the same conditions with the second $\pi/2$ pulse removed [29]. The two systems presented here were optimised to maximise modulation depth and contributions from relaxation were minimized using deuterated solvents. This means that the data did not require any background correction.

In frequency correlated 2D-SIFTER the raw echo transients stored from the two dimensional experiments were apodized by a Gaussian function centred at

the centre of the echo in the direct time domain to suppress the noise at the edge of the echo transient. These data were then Fourier transformed in the direct time domain. After that the time traces for each offset frequency were phased individually using a 0th order correction to achieve a maximum signal in the real part at the time point $\tau_1 - \tau_2 = 0$.

2.3 Samples

Data were recorded on two samples: a bis-nitroxide model-compound [16] prepared at a concentration of 150 μM in deuterated toluene and a double stranded DNA molecule with two rigid spin-labels ζ at position 3 and 15 prepared in a deuterated solvent [21] (Fig. 1).

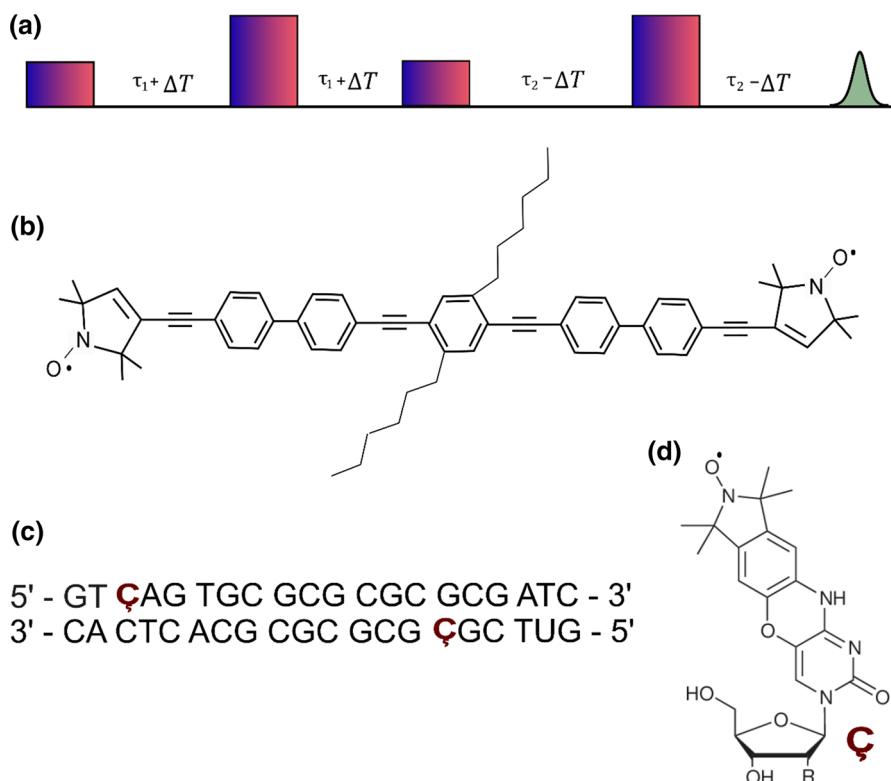


Fig. 1 **a** Broadband SIFTER pulse sequence with all pulses of equal length here. **b** Bis-nitroxide model compound used in this study. **c** Sequence of the dsDNA molecule used in this study. **d** Chemical structure of the cytidine analogue spin-label ζ incorporated into the dsDNA molecule

2.4 Simulation Methods

The simulation procedure of orientation dependent PELDOR time traces, based on the secular approximation of the dipolar interaction (Eq. 1), is described in detail in [11, 22]. This assumes that the dipolar coupling strength is smaller than the offset of pump and probe frequency in the PELDOR experiments. This approximation is not fulfilled for all possible spin-pairs in single-frequency dipolar experiments, such as DQC or SIFTER [8, 28], especially for very short distances (< 1.5 nm). The inter-spin distances in the two molecules used here are longer than 2 nm and the excellent agreement of the experimental SIFTER data with the simulations and PELDOR data show that the approximation is still sufficient here.

For the analytical simulations of the PELDOR and SIFTER dipolar time traces of the bis-nitroxide compound, the relative positions of the nitroxide N–O moieties and their conformational distribution is required. A geometric model was used, as described in [21] to provide this data. For the ds-DNA molecule, the MD simulation, detailed in [25], was directly used to determine the distances and relative orientations between the two ζ spin-labels for the quantitative simulation of the PELDOR and SIFTER time traces [23].

3 Experimental Results

3.1 Optimization of Pulse Settings for 2D-SIFTER

PDS experiments with rigid spin-labels can encode up to six parameters: the distance R , the three Euler angles describing the mutual orientation between both nitroxide spin-labels and the two polar angles describing the orientation of the \mathbf{R} vector with respect to one of the nitroxides. However, when the pump is orientation unselective, as is the case for PELDOR at X-band with a pump pulse that excited the complete central transition and frequency correlated SIFTER, only the distance and polar angles of each of the centres can be resolved, and in the case that the spin-centres are chemically identical the number of angles that can be resolved is further reduced. To unravel the unknown distance and orientation parameters quantitatively an X-band PELDOR data set, the pump pulse positioned at the nitroxide maximum and with detection-pump frequency offsets ranging from 30–40 up to 80–90 MHz with 10 MHz steps, can be used [22]. In a 2D frequency correlated technique, these frequencies are captured within a single experiment. The signal intensity of each dipolar trace will depend on the spectral intensity at each frequency, which is a feature of the radical species being studied, and on the degree of excitation at each frequency. The broadband pulses used in our experiments were designed to have a rectangular frequency profile across the whole EPR spectrum of the nitroxide. Therefore, the Fourier transform of the echo for zero dipolar evolution time should reproduce the EPR spectrum. Experimentally it was found that the measured profile did not always agree with expected nitroxide profile measured via an echo detected field sweep. There are several reasons for this: First, the exact shape of the Fourier transform will depend on the signal processing used; if a Gaussian apodization

window is used this improves SNR but may cause some broadening of the resulting spectrum. Second, the precise shape of the echo detected field sweep depends on the lengths of the pulses used, the excitation bandwidths of these pulses and the integration window used in detection. The broad bandwidth of short pulses can cause broadening of the spectrum from its expected form when the integration window used is less than ca. 200 ns; in all data sets recorded using rectangular time domain pulses the integration window used was set to the length of the π pulse. Finally, although the broadband pulses were designed to have equal excitation at all frequencies of the nitroxide spectrum, convolution of the pulses with the resonator bandwidth and the bandwidths of other components used in generation of the pulses and detection may cause a distortion of the spectrum observed. Specifically the video amplifier in the Bruker E580 has a bandwidth of only 200 MHz. Experiments conducted with the amplifier removed, while showing slight increase in the amplitudes of the signals at large frequency offsets from the carrier frequency did not show differences in the shape of the dipolar traces recorded at these offsets. While it is possible to compensate for the component bandwidths using compensated pulses, [29] as our analysis is based on the shape of the traces at different offsets, rather than the signal amplitude, this was not necessary for the experiments presented in this work and the experiments were conducted with the video amplifier in use as the overall signal to noise was marginally increased. Artefacts due to carrier frequency leakage in the pulse up-conversion process can also occur and show up in the frequency domain as sharp spikes. Although all these features may distort the frequency spectrum at zero dipolar evolution time of the experiment, they do not change the observed dipolar oscillations in the indirect time domain (although they can degrade the signal to noise of the traces at specific frequencies).

3.2 Comparison of Simulations with the Experimental Data

For a quantitative analytical simulation, the following spin parameters were used: $g = (2.0088, 2.0065, 2.0027)$ and nitrogen hyperfine coupling of $A[\text{MHz}] = (15, 15, 95)$. Orientation-selective PELDOR data were simulated using the experimental pulse lengths, field strengths and offset frequencies. The conformational model for the DNA system is based on a molecular dynamics simulation [25], and the conformers for the bis-nitroxide model compound were derived from a conical model simulating the allowed rotation of the nitroxide moieties and the bending of the linker unit as described before [11, 20, 23]. We achieved very good agreement between simulated and experimentally recorded PELDOR data sets for both molecules as demonstrated in Figs. 2, 3; bottom left plots.

Comparison of the orientation selective PELDOR data recorded with the pump pulse at the central maximum and the detection pulse offset by 30–80 MHz with individual traces from the 2D SIFTER data sets that were recorded at equivalent offsets from the nitroxide maximum as the detection frequency in the comparative PELDOR experiment showed small but reproducible differences in the shape of the time traces (Fig. 4). These differences can be assigned to the differences in the excitation profiles of the pulses used in the two different experiments. As previously

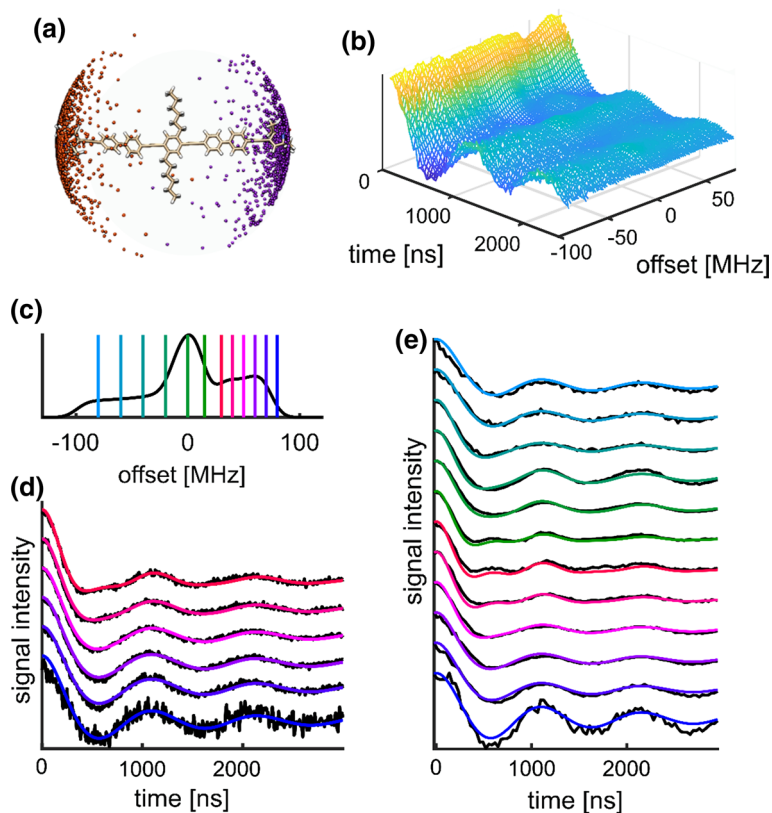


Fig. 2 Results for bis-nitroxide model system: **a** Spin-label orientations calculated using a cone model. **b** Normalised frequency correlated SIFTER dataset measured with all pulses 200 ns long presented in the time domain of the dipolar dimension; time is $\tau_1 - \tau_2$. **c** Echo detected field sweep of the system presented in the frequency domain relative to the spectral maxima with coloured lines showing the detection positions offsets for the PELDOR data presented in **d** and the frequency slice of the frequency correlated SIFTER data presented in **e**. **d** PELDOR time traces, experimental data (black lines) with corresponding simulations (coloured lines). **e** Slices from the frequency correlated 2D-SIFTER experiment (black lines) presented in **b** with corresponding simulations (coloured lines). Molecular graphics and analyses were performed with the UCSF Chimera package (colour figure online)

mentioned the experimental setup used for the PELDOR experiments results in a pump pulse that provides little orientation selection and, therefore, the orientation selection is provided mainly by the detection pulses. Likewise in SIFTER the orientation selection is provided only by the detection, thus a comparison of the traces provides an insight into the degree of selectivity of the detection mechanism and how sensitive the orientation of the labels are to this. As the shape of the traces is sensitive to the orientation of the two labels the degree of difference in the SIFTER and PELDOR traces detected at the same frequency offset from the nitroxide maximum.

In the remainder of the paper offset frequency is defined for PELDOR as the offset of the detection frequency from the nitroxide central maximum, where the pump

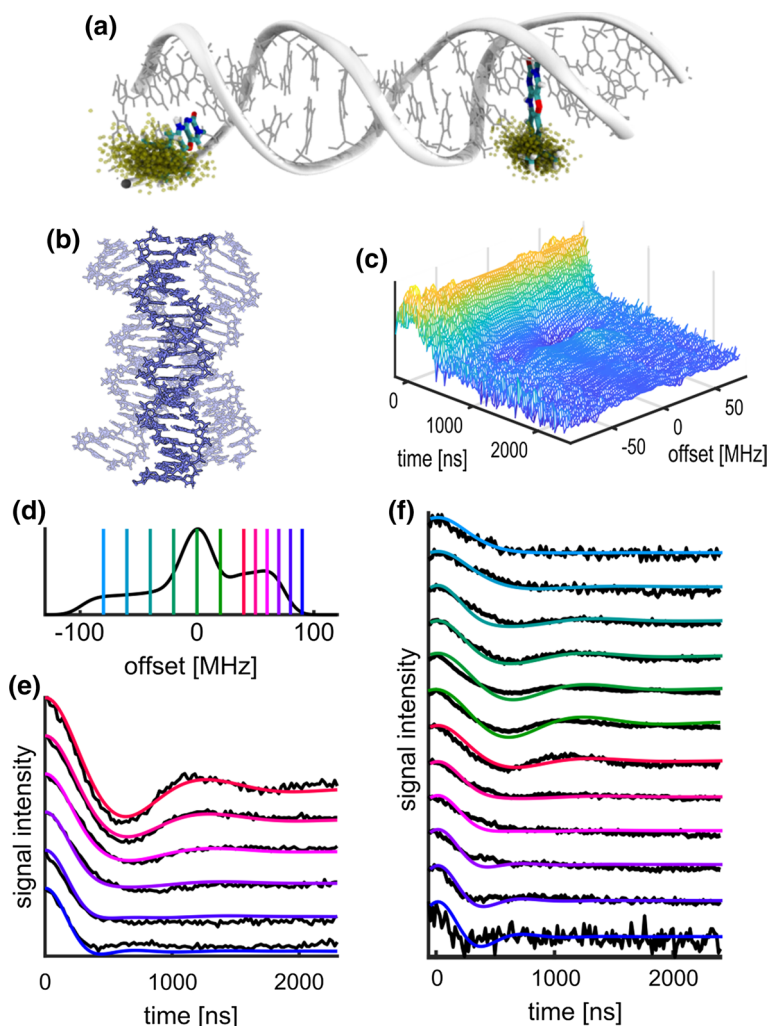


Fig. 3 Results for the ds-DNA molecule: **a** spin-label orientations from molecular dynamic (MD) simulations of DNA(1, 13), ζ structure from final frame from the MD trajectories shown as a stick representation relative to a ribbon representation of the DNA backbone. The positions of nitroxide spins over the course of a 200 ns MD trajectory are visualized as yellow spheres, showing 1000 spin positions per label, a subset of the 2000 orientations used in the simulation of the PDS traces. The distribution of the nitroxide spins results from the flexibility of the DNA backbone as shown with superimposed frames from the MD simulations in **b**. **c** Normalised frequency correlated SIFTER dataset presented in the time domain of the dipolar dimension; time is $\tau_1 - \tau_2$. **d** Echo detected field sweep of the system presented in the frequency domain relative to the spectral maxima with coloured lines showing the detection positions offsets for the PELDOR data presented in **e** and the frequency slice of the frequency correlated SIFTER data presented in **f**. **e** PELDOR time traces, experimental data (black lines) with corresponding simulations (coloured lines). **f** Slices from the frequency correlated SIFTER experiment (black lines) presented in **c** with corresponding simulations (coloured lines) (colour figure online)

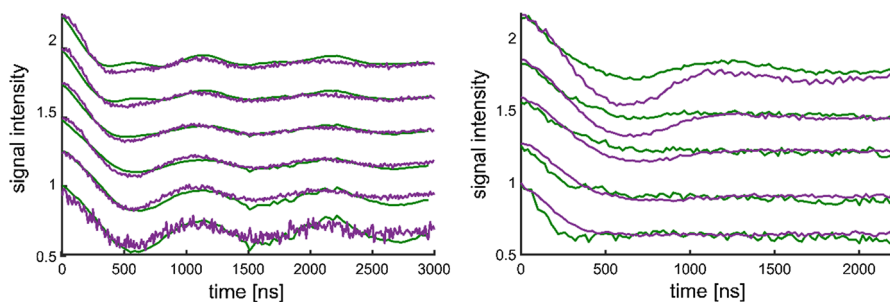


Fig. 4 Comparison of PELDOR (violet) and SIFTER (green) time traces for the bis-nitroxide model system (on the left) and for the DNA (on the right). For the bis-nitroxide molecule the PELDOR time traces have offsets between pump and detection pulse frequency varying from 80 MHz (lowest trace) to 30 MHz (uppermost trace) in 10 MHz steps. For the dsDNA molecule the PELDOR time traces have offsets between pump and detection pulse frequency varying from 80 MHz (lower) to 40 MHz (uppermost time trace) in 10 MHz steps. In both cases, the slices for the SIFTER time traces are taken at the same frequency offsets from the signal maximum as for the corresponding PELDOR time traces (colour figure online)

pulse is applied and in SIFTER experiments traces corresponding to the same offset frequency are classified as the frequency slice that has the same offset from the nitroxide maximum.

In the broadband SIFTER experiment at X-band, all pulses are designed to excite the whole nitroxide EPR spectrum, as visible by the large experimental modulation depth. This can be analytically simulated by a pump pulse efficiency of 100%. The ‘detection pulse’ bandwidth for the simulation of the 2D-SIFTER data was chosen as a Gaussian function to best fit the experimental frequency selective dipolar time traces obtained by Fourier transform of the SIFTER data set. The linewidth of 20 MHz obtained from this fitting procedure is about a factor of 2 smaller than the excitation bandwidth of the 32 ns detection pulse sequence used for the PELDOR data set. It is limited by the inhomogeneous linewidth broadening from unresolved hyperfine couplings, which has to be used to simulate the nitroxide EPR spectral shape. Additionally, the Gaussian window function used for filtering of the echo transient before Fourier transformation will add further broadening. Correspondingly, the orientation selection achieved with the 2D SIFTER experiment is higher compared to that observed in the PELDOR experiment, leading to more pronounced oscillations in some traces specifically for the bis-nitroxide model system at 50–30 MHz frequency offset. Taking the differences in excitation and detection bandwidth between both methods into account, it was possible to simulate the 2D SIFTER data quantitatively, as presented in Figs. 2 and 3 (right side).

It should be noted that to record data of comparable SNR significantly fewer averages (about a factor of 6) were needed for 1D SIFTER compared to PELDOR; this is a result of the fact that SIFTER allows both pumping and detection of the whole nitroxide spectrum. Although fewer averages are needed for 1D SIFTER the average time to acquire one average of a data point can be longer partly, partly because of the external triggering of sequence with the AWG pulses. Although the sequences for the 1D- and 2D SIFTER experiments are identical, the detection procedures

are not. In the 1D SIFTER experiment the solid echo is integrated over the central 50 ns time region whereas in 2D SIFTER a time trace with the full echo signal was recorded with a 1 ns time resolution and 512 points in the echo dimension. Within the Bruker hard- and software, recording the complete echo transient takes longer than integrating over the echo and, therefore, the time to acquire one average of a data point is increased. Comparing the SNR of the PELDOR data recorded to that of the 2D SIFTER it was found that approximately 4 times the number of averages were required for the 2D SIFTER compared to a single PELDOR experiment to yield time traces of comparable SNR. However, the 2D SIFTER experiment produces directly 100 individual time traces with a frequency spacing of approximately 2 MHz distributed over the whole EPR spectrum. Our analysis additionally showed that the bandwidth of contributing frequencies to each time trace of the 2D SIFTER data set is significantly narrower compared to the PELDOR time traces, where the bandwidth is determined by the strength of the detection pulses. Therefore, significantly higher SNR can be achieved with the 2D SIFTER method with the same number of acquisitions. While hard- and software limitations might reduce this gain if the overall measurement time is considered, it may be possible to overcome some of these limitations on homebuilt spectrometers built to a different design and specification.

4 Conclusions and Outlook

In this work, we have shown that it is possible to record a 2D frequency correlated SIFTER spectrum with broadband pulses at X-band frequencies on a bis-nitroxide model compound and a ds-DNA molecule containing two rigid $\dot{\text{C}}$ spin-labels. This could be achieved using broadband excitation pulses created by an AWG and implemented into a commercial spectrometer and resonator. For rigid spin-labels, this technique allows orientation selective datasets to be acquired reliably from a single 2D experiment in a reasonable amount of time.

As the information provided by both orientation dependent PELDOR traces and 2D SIFTER is comparable, the question arises as to which is the better method to use. We have shown that the spectral resolution of such frequency correlated 2D-SIFTER time traces is superior to datasets achieved by the PELDOR method with several probe frequencies under typical conditions. For this reason when the sample being studied has some flexibility, fitting to the complete 2D SIFTER dataset may be preferable to a collection of frequency offset dependent PELDOR traces as the 2D SIFTER provides a more complete and finer grain description of the dipolar orientation dependence. However, the offset dependent modulation depth of the 2D PELDOR data set, which also contains information on the geometry between both spin-labels, is lost in the 1D SIFTER experiment.

Based on our datasets it appears that approximately the same SNR is reached for a single time trace of the 2D SIFTER experiment compared to a PELDOR time trace with the same offset frequency (for the same number of averages per time step). However, the 2D SIFTER experiment can access all offsets over the full spectral range simultaneously with much higher spectral resolution compared to the

PELDOR experiment. Integration of the time traces over all offsets (as achieved also with the 1D SIFTER experiment) allows also a simple determination of the distance R and the distance distribution function $P(R)$ for samples with orientation selection [14].

We have also shown that the 2D-SIFTER data can be quantitatively simulated by the same analytical procedure used for the simulation of the orientation selective PELDOR time traces, taking the different excitation and detection bandwidth of both experiments into account. This is demonstrated here for a bis-nitroxide model compound, where the conformational ensemble of the spin system is obtained from a geometrical model, and for a double spin-labelled DNA molecule, where the conformational ensemble is derived from MD simulations. Of course it is well known that X-band data alone are not sufficient for an ab initio determination of all of the parameters describing the geometry between both spin-labels [11, 22]. This is especially true if a broad distribution of conformers exist. Therefore, taking additional data at high magnetic field strengths is important, as well as the incorporation of data from other spectroscopic, computational or structural methods. We believe that the frequency correlated 2D-SIFTER method with shaped broadband pulses at X-band frequencies is a very promising new technique and tool for the determination of structure and conformational flexibilities of macromolecules with rigid spin-labels.


Acknowledgements We acknowledge financial support from the German Research Foundation (CRC902: Molecular Principles of RNA Based Regulation and SPP1601: New Frontiers in Sensitivity for EPR Spectroscopy). L.S. S is grateful for support from the Max Planck Society. A.M.B was supported by the Marie Curie GOIN program, and gratefully acknowledges her current fellowship support from the Royal Society and EPSRC for a Dorothy Hodgkin Fellowship (DH160004). We thank Dr. Plackmeyer for the synthesis of the bis-nitroxide model compound.

References

1. A.D. Milov, K. Salikhov, M. Shchirov, *Sov. Phys. Solid State* **23**, 975 (1981)
2. A.D. Milov, A. Ponomarev, Y. Tsvetkov, *Chem. Phys. Lett.* **110**, 67 (1984)
3. R. Martin, M. Pannier, F. Diederich, V. Gramlich, M. Hubrich, H.W. Spiess, *Angw. Chemie Int. Ed.* **37**, 2833 (1998)
4. M. Pannier, S. Veit, A. Godt, G. Jeschke, H.W. Spiess, *J. Magn. Reson.* **142**, 331 (2000)
5. P.P. Borbat, J.H. Freed, *Chem. Phys. Lett.* **313**, 145 (1999)
6. L.V. Kulik, S.A. Dzuba, I.A. Grigoryev, Y.D. Tsvetkov, *Chem. Phys. Lett.* **343**, 315 (2001)
7. S. Milikisyants, E.J.J. Groenen, M. Huber, *J. Magn. Reson.* **192**, 275 (2008)
8. G. Jeschke, M. Pannier, A. Godt, H.W. Spiess, *Chem. Phys. Lett.* **331**, 243 (2000)
9. C. Altenbach, T. Marti, H. Khorana, W. Hubbell, *Science (80-)* **248**, 1088 (1990)
10. G. Jeschke, V. Chechik, P. Ionita, A. Godt, H. Zimmermann, J. Banham, C.R. Timmel, D. Hilger, H. Jung, *Appl. Magn. Reson.* **30**, 473 (2006)
11. A. Marko, T.F. Prisner, *Phys. Chem. Chem. Phys.* **15**, 619 (2013)
12. J. Gorcester, J.H. Freed, *J. Chem. Phys.* **88**, 60 (1988)
13. S. Saxena, J.H. Freed, *J. Phys. Chem. A* **101**, 181 (1997)
14. P.P. Borbat, J. H. Freed, in *EPR Spectroscopy: Fundamentals and Methods* (eMagRes Books), ed. by D. Goldfarb and S. Stoll, Chapt. 20 (Wiley, Chichester, 2018)
15. A. Doll, S. Pribitzer, R. Tschaggelar, G. Jeschke, *J. Magn. Reson.* **230**, 27 (2013)
16. P. Schöps, P.E. Spindler, A. Marko, T.F. Prisner, *J. Magn. Reson.* **250**, 55 (2015)

17. G.E. Merz, P.P. Borbat, A.J. Pratt, E.D. Getzoff, J.H. Freed, B.R. Crane, *Biophys. J.* **107**, 1669 (2014)
18. A. Doll, G. Jeschke, *Phys. Chem. Chem. Phys.* **18**, 33 (2016)
19. P. Cekan, A.L. Smith, N. Barhate, B.H. Robinson, S.T. Sigurdsson, *Nucl. Acids Res.* **36**, 5946 (2008)
20. O. Schiemann, P. Cekan, D. Margraf, T.F. Prisner, S.T. Sigurdsson, *Angew. Chemie Int. Ed.* **48**, 3292 (2009)
21. A. Marko, V. Denysenkov, D. Margraf, P. Cekan, O. Schiemann, S.T. Sigurdsson, T.F. Prisner, *J. Am. Chem. Soc.* **133**, 13375 (2011)
22. A. Marko, S.T. Sigurdsson, T.F. Prisner, *J. Magn. Reson.* **252**, 187 (2015)
23. D. Margraf, B. Bode, A. Marko, O. Schiemann, T.F. Prisner, *Mol. Phys.* **105**, 15 (2007)
24. A. Marko, D. Margraf, H. Yu, Y. Mu, G. Stock, T.F. Prisner, *J. Phys. Chem.* **130**, 6 (2009)
25. L.S. Stelzl, N. Erlenbach, M. Heinz, T.F. Prisner, G. Hummer, *J. Am. Chem. Soc.* **30**, 139 (2017)
26. M.S. Silver, R.I. Joseph, D.I. Hoult, *Phys. Rev. A* **31**, 2753 (1985)
27. Ě. Kupce, R. Freeman, *J. Magn. Reson. A* **117**, 246 (1995)
28. S.K. Misra, P.P. Borbat, J.H. Freed, *Appl. Magn. Reson.* **36**, 237 (2008)
29. P.E. Spindler, P. Schöps, A.M. Bowen, B. Endeward, T.F. Prisner, *eMagRes.* **5**, 1477 (2016)

Affiliations

A. M. Bowen^{1,2} · N. Erlenbach¹ · P. van Os¹ · L. S. Stelzl³ · S. Th. Sigurdsson⁴ · T. F. Prisner¹ 

¹ Institute of Physical and Theoretical Chemistry and Center of Biomolecular Magnetic Resonance, Goethe University, Max-von-Laue-Str. 7, 60438 Frankfurt am Main, Germany

² Present Address: Inorganic Chemistry Laboratory, Department of Chemistry, Centre for Applied Electron Spin Resonance, University of Oxford, South Parks Road, Oxford OX1 3QR, UK

³ Department of Theoretical Biophysics, Max Planck Institute of Biophysics, 60438 Frankfurt am Main, Germany

⁴ Department of Chemistry, Science Institute, University of Iceland, Dunhaga 3, 107 Reykjavík, Iceland

Conformational Dynamics

International Edition: DOI: 10.1002/anie.201803682

German Edition: DOI: 10.1002/ange.201803682

Dynamics of Nucleic Acids at Room Temperature Revealed by Pulsed EPR Spectroscopy

Markus Gränz, Nicole Erlenbach, Philipp Spindler, Dnyaneshwar B. Gophane, Lukas S. Stelzl, Snorri Th. Sigurdsson, and Thomas F. Prisner*

Abstract: The investigation of the structure and conformational dynamics of biomolecules under physiological conditions is challenging for structural biology. Although pulsed electron paramagnetic resonance (like PELDOR) techniques provide long-range distance and orientation information with high accuracy, such studies are usually performed at cryogenic temperatures. At room temperature (RT) PELDOR studies are seemingly impossible due to short electronic relaxation times and loss of dipolar interactions through rotational averaging. We incorporated the rigid nitroxide spin label ζ into a DNA duplex and immobilized the sample on a solid support to overcome this limitation. This enabled orientation-selective PELDOR measurements at RT. A comparison with data recorded at 50 K revealed averaging of internal dynamics, which occur on the ns time range at RT. Thus, our approach adds a new method to study structural and dynamical processes at physiological temperature in the $<10 \mu\text{s}$ time range with atomistic resolution.

Pulsed electron paramagnetic resonance (EPR) spectroscopy is established as a valued method for investigations of biomolecular structures and conformational flexibility, next to nuclear magnetic resonance (NMR) spectroscopy, X-ray crystallography, and optical or infrared spectroscopy. Most common are pulsed electron–electron double resonance (PELDOR, also called double electron–electron resonance/DEER)^[1,2] or double quantum coherence (DQC)^[3] experiments. These techniques rely on the detection of the magnetic dipolar interaction between unpaired electrons. For this purpose, two spin labels are covalently attached to specific sides of the system by side-directed spin labeling (SDSL).^[4] Such labeling can be performed either during the synthesis of a biopolymer or post-synthetically.^[5,6] PELDOR spectroscopy

in combination with SDSL is not limited by the size of the molecules under investigation and can determine distances in the 1.5–10 nm range for nucleic acids, proteins, and their complexes.^[7–9]

Due to the intrinsically fast echo dephasing time of nitroxide spin labels at higher temperatures, PELDOR experiments are usually carried out in frozen solutions at $\approx 50 \text{ K}$.^[10] Thus, such experiments report on a static frozen conformational ensemble, providing the full conformational accessible space of flexible biomolecules at the freezing temperature.^[11] However, freezing may trap biomolecules in specific conformations. Furthermore, cryo-protectants, necessary additives to form a good glass upon freezing, can also affect natural equilibria.^[12] Additionally, kinetics for dynamic processes are not accessible in frozen solution.

A longstanding goal is to relate PELDOR data acquired at low temperatures to physiological conditions. In order to perform PELDOR measurements at room temperature (RT), one needs to overcome two fundamental limitations which are not present in frozen solutions. First, the rotational motion of the molecules has to be inhibited to avoid averaging out the dipolar interaction. This can be achieved by, for example, immobilization on a solid support. Second, the transverse relaxation time T_2 of the spin label has to be long enough to obtain an appropriate time window for the evolution of the dipolar coupling.

A proof of concept for RT DQC experiments has been demonstrated using triarylmethyl (TAM, trityl) labels attached to a biotin-immobilized protein^[13] and on double-stranded DNA.^[14,15] As the echo-dephasing mechanism in the liquid phase is strongly driven by the anisotropy of the hyperfine- and g-tensor, the carbon-based trityl radicals with isotropic hyperfine couplings and very small g-tensor anisotropy are good candidates for RT experiments. However, incorporation of the bulky and hydrophobic trityl label into biomolecules is limited, for example, to end groups or loops and requires an adequate linker to overcome steric hindrance.^[16–19] Spirocyclohexyl-derived nitroxides have also been utilized as spin labels on DNAs^[15] and proteins^[21] to obtain distance information by PELDOR at RT. Here the absence of the rotating methyl groups on the carbon atoms adjacent to the nitroxide functional groups leads to longer relaxation times. Nevertheless, for both trityls and spirocyclohexyl nitroxides there are indications that the linkers and the attachment strategy still limit the transverse relaxation time T_2 .^[16] In the case of nitroxides, the molecules had to be immobilized in solid matrices to prevent the tumbling motion of the biomolecule and the nitroxide spin label. Polysugars, like trehalose and sucrose, exhibit great immobilization and

[*] M. Gränz, N. Erlenbach, Dr. P. Spindler, Prof. Dr. T. F. Prisner
Institute of Physical and Theoretical Chemistry and Center of
Biomolecular Magnetic Resonance, Goethe University Frankfurt
Max-von-Laue-Straße 7, 60438 Frankfurt am Main (Germany)
E-mail: prisner@chemie.uni-frankfurt.de

Dr. L. S. Stelzl
Department of Theoretical Biophysics
Max Planck Institute of Biophysics
Max-von-Laue-Straße 3, 60438 Frankfurt am Main (Germany)

Dr. D. B. Gophane, Prof. Dr. S. Th. Sigurdsson
Department of Chemistry, Science Institute
University of Iceland
Dunhaga 3, 107 Reykjavík (Iceland)

Supporting information and the ORCID identification number(s) for the author(s) of this article can be found under:
<https://doi.org/10.1002/anie.201803682>.

cryo-protection properties. However, the degree of dehydration affects the biomolecular structure^[19] and full immobilization requires very high sugar concentrations.^[22] Thus, the structure and especially the conformational flexibility of the biomolecules under investigation might be affected by this immobilization procedure.

Here we report the use of rigid spin labels for RT PELDOR. The rigid spin label ζ (“C-spin”)^[23] is a cytidine analogue where the nitroxide is fused to the base such that Watson–Crick base pairing to guanine is maintained (Figure 1). The spin label does not perturb the helical

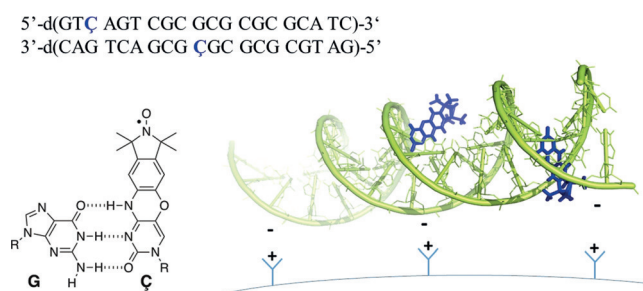


Figure 1. Sequence of the double-stranded 20mer DNA sample. Left: The rigid nitroxide spin label ζ base-paired with guanine (G). Right: Molecular model of the dsDNA molecule with nitroxide spin labels (blue) and electrostatic interaction to the silica beads (Nucleosil surface).

structure of dsDNA, as demonstrated by X-ray crystallography,^[24] and has been shown to be an excellent tool for PELDOR measurements of DNA^[25–27] as well as its ribo derivative ζ m for RNA.^[28,29] Moreover, the rigidity of ζ yields information on the mutual orientation between both spin labels, in addition to the distance. Due to this and its rigid attachment to the biomolecule, the conformational dynamics of nucleic acids can be observed with unprecedented precision.

We synthesized a duplex oligonucleotide containing two ζ spin labels with a distance of 2.65 nm for proof-of-principle experiments. This dsDNA had previously been characterized by PELDOR measurements at cryogenic temperature, which revealed the conformational flexibility of the DNA.^[23,26,27] The measurements reported on the ensemble of all possible conformations, yet this is fundamentally a static view. At RT, in contrast, the dynamics of the molecule will modulate the Larmor frequency of the spins within their evolution time and therefore affect the observed PELDOR time trace. Anisotropic couplings modulated by the dynamics that are much faster than their coupling strength will be averaged out.

Synthesis of the spin-labeled dsDNA was performed by phosphoramidite chemistry on controlled pore glass (CPG) as previously published.^[30] Subsequently, the spin-labeled dsDNA was adsorbed to functionalized silica surface beads (Nucleosil) through electrostatic interactions (Figure 1). Continuous wave (CW) EPR data proved that the dsDNA was immobilized upon binding to the Nucleosil (Figure S1). At 50 K, the transverse relaxation time T_2 of the DNA sample was found to be 3 μ s in protonated solvent and around 8 μ s in deuterated solvent (Figure S3). The relaxation time in

buffered solution at RT was too short to be measured. After immobilization on the Nucleosil surface T_2 was found to be around 550 ns. This time is similar to those obtained with nitroxides immobilized in glassy trehalose.^[16] As T_2 depends on the spectral position, the rates are measured on the maximum of the spectrum, represented in Figure S2. The Boltzmann population difference between the two-electron spin states decreases with increasing temperature, reducing the signal-to-noise ratio of the PELDOR experiment. Fortunately, the longitudinal relaxation rate T_1 also decreases, thus allowing faster signal averaging because of much shorter shot repetition times (SRT).

X-band PELDOR measurements of the spin-labeled dsDNA were performed at 50 K with and without binding to Nucleosil. The two time traces obtained with 45 MHz and 85 MHz offset between pump and probe pulses showed orientation selection^[27] but also revealed some differences (Figure 2). Attaching the dsDNA to the surface increases the

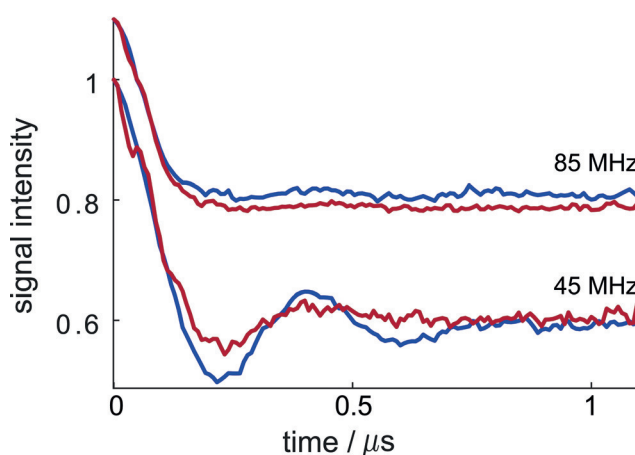


Figure 2. PELDOR time traces at 50 K of dsDNA in a 20% glycerol/water mixture (blue) and attached on Nucleosil surface (red). Traces were recorded with 45 MHz (lower trace) and 85 MHz (upper trace) frequency offset between pump and probe pulses. The pump pulse was set resonant to the maximum of the nitroxide spectrum.

dampening of the time traces (Figure 2 red line, Figure S4). This is presumably a consequence of the electrostatic interaction between the positively charged Nucleosil surface and the negatively charged backbone (Figure 1), leading to a somewhat larger conformational distribution of the dsDNA.

When the temperature is increased to 295 K, orientation selection remains visible in the PELDOR time traces at both offset frequencies (Figure 3 A, Figure S5). Additionally, the RT traces of Nucleosil-immobilized dsDNA samples show a reduced dampening of the dipolar oscillations compared to the 50 K measurements. This goes in line with the assumed averaging of fast conformational dynamics at RT. MD simulations^[31] (at RT) of this specific dsDNA revealed bend and twist-stretch dynamics which reflect the conformational ensemble probed by PELDOR at cryogenic temperatures very well. This conformational flexibility is responsible for the dampening of the PELDOR oscillations at low temperature. As these dynamics have a correlation time shorter than 0.5 ns

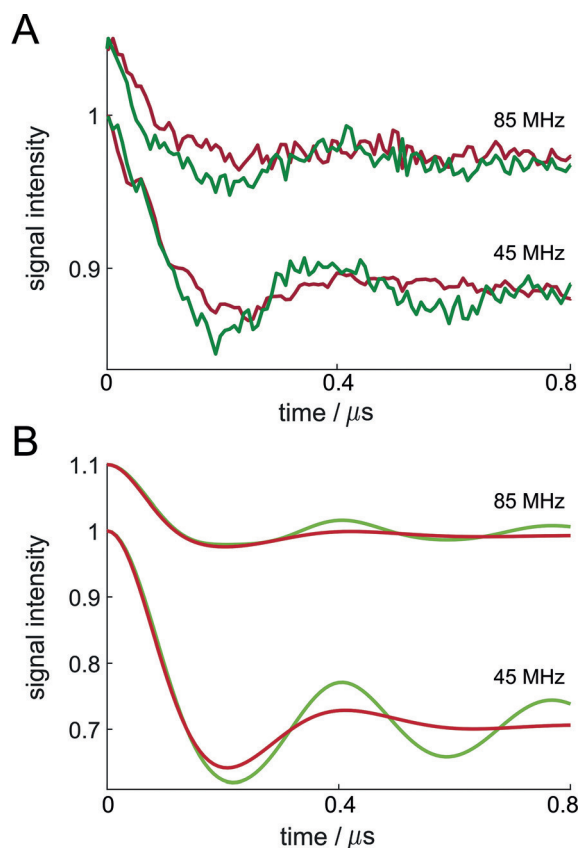


Figure 3. PELDOR time traces of dsDNA adsorbed on Nucleosil. The traces were recorded with 45 MHz (lower traces) and 85 MHz (upper traces) offset between pump and probe pulse. The probe pulse was set to the maximum of the nitroxide spectrum to gain higher signal to noise (S/N) ratio. A) Experimental PELDOR time traces at 50 K (red) and at RT (green). B) Calculated PELDOR time traces from MD trajectories for 50 K (red) and for RT (green). For simulation details see the Supporting Information.

at room temperature, the modulation of the dipolar interaction arising from these dynamics is averaged out (Figure 3B).

For both frequency offsets, the dynamic-averaged ensemble calculated from MD trajectories is in qualitative agreement with the experimental observed PELDOR time traces at RT, whereas the full ensemble of MD structures corresponds well with the low-temperature PELDOR experiments, as previously reported.^[31] Slight changes of the low-temperature PELDOR time traces of the dsDNA sample with Nucleosil reveals structural modifications introduced by the electrostatic interaction. Nevertheless, the damping of the oscillations in the PELDOR time traces stays the same. Therefore, we conclude that binding of the dsDNA to Nucleosil does not inhibit its internal dynamics, leading to the more pronounced dipolar oscillations at room temperature.

In conclusion, we have demonstrated that ζ is very well suited for PELDOR investigations on DNA molecules performed at physiological temperatures. Since ζ is a rigid spin label, the overall immobilization of the dsDNA is sufficient to obtain a long enough transversal relaxation

time T_2 for RT PELDOR measurements. This guarantees minimum distortion of the structure and conformational dynamics of the DNA molecule. The additional orientation information obtained with this rigid spin label enables sensitive detection of even small changes of these properties. Our measurements showed that the attachment to the silica beads (Nucleosil) not only prevents the overall tumbling of the DNA molecule but also changes the conformational distribution slightly. Furthermore, the orientation-selective PELDOR data at RT show for the first time the effect of the dynamic averaging of fast internal motions. The orientation-selective PELDOR time traces are in full agreement with predictions based on MD simulations. Such details are not accessible with flexible spin labels. Thus, our approach offers direct access to structural and dynamical investigations under physiological conditions on such molecules.

Acknowledgements

This work was supported by the German Research Foundation (CRC902: Molecular Principles of RNA-Based Regulation) and the Icelandic Research Fund (120001021; 141062051). L.S.S. was also supported by the Max Planck Society. We thank Dr. Andriy Marko and Prof. Dr. Gerhard Hummer for fruitful discussions.

Conflict of interest

The authors declare no conflict of interest.

Keywords: conformational dynamics · DEER spectroscopy · DNA · EPR spectroscopy · PELDOR spectroscopy

How to cite: *Angew. Chem. Int. Ed.* **2018**, *57*, 10540–10543
Angew. Chem. **2018**, *130*, 10700–10703

- [1] A. D. Milov, K. M. Salikhov, M. D. Shchirov, *Sov. Phys. Solid State* **1981**, *23*, 975–982.
- [2] M. Pannier, S. Veit, A. Godt, G. Jeschke, H. Spiess, *J. Magn. Reson.* **2000**, *142*, 331–340.
- [3] P. P. Borbat, H. S. Mchaourab, J. H. Freed, *J. Am. Chem. Soc.* **2002**, *124*, 5304–5314.
- [4] W. L. Hubbell, A. Gross, R. Langen, M. A. Lietzow, *Curr. Opin. Struct. Biol.* **1998**, *8*, 649–656.
- [5] S. A. Shelke, S. T. Sigurdsson in *Modified Nucleic Acids* (Eds.: K. Nakatani, Y. Tor), Springer International Publishing, Cham, **2016**, pp. 159–187.
- [6] S. A. Shelke, S. T. Sigurdsson, *Eur. J. Org. Chem.* **2012**, 2291–2301.
- [7] B. Joseph, V. M. Tormyshev, O. Y. Rogozhnikova, D. Akhmetzyanov, E. G. Bagryanskaya, T. F. Prisner, *Angew. Chem. Int. Ed.* **2016**, *55*, 11538–11542; *Angew. Chem.* **2016**, *128*, 11710–11714.
- [8] O. Schiemann, T. F. Prisner, *Q. Rev. Biophys.* **2007**, *40*, 1–53.
- [9] O. Duss, M. Yulikov, G. Jeschke, F. H.-T. Allain, H. Paulsen, *Nat. Commun.* **2014**, *5*, 279–295.
- [10] G. Jeschke, *Annu. Rev. Phys. Chem.* **2012**, *63*, 419–446.
- [11] G. Jeschke, Y. Polyhach, *Phys. Chem. Chem. Phys.* **2007**, *9*, 1895.
- [12] E. R. Georgieva, A. S. Roy, V. M. Grigoryants, P. P. Borbat, K. A. Earle, C. P. Scholes, J. H. Freed, *J. Magn. Reson.* **2012**, *216*, 69–77.

- [13] Z. Yang, Y. Liu, P. Borbat, J. L. Zweier, J. H. Freed, W. L. Hubbell, *J. Am. Chem. Soc.* **2012**, *134*, 9950–9952.
- [14] G. Y. Shevelev, O. A. Krumkacheva, A. A. Lomzov, A. A. Kuzhelev, O. Y. Rogozhnikova, D. V. Trukhin, T. I. Troitskaya, V. M. Tormyshev, M. V. Fedin, D. V. Pyshnyi, et al., *J. Am. Chem. Soc.* **2014**, *136*, 9874–9877.
- [15] A. A. Kuzhelev, D. V. Trukhin, O. A. Krumkacheva, R. K. Strizhakov, O. Y. Rogozhnikova, T. I. Troitskaya, M. V. Fedin, V. M. Tormyshev, E. G. Bagryanskaya, *J. Phys. Chem. B* **2015**, *119*, 13630–13640.
- [16] A. A. Kuzhelev, R. K. Strizhakov, O. A. Krumkacheva, Y. F. Polienko, D. A. Morozov, G. Y. Shevelev, D. V. Pyshnyi, I. A. Kirilyuk, M. V. Fedin, E. G. Bagryanskaya, *J. Magn. Reson.* **2016**, *266*, 1–7.
- [17] Z. Yang, M. D. Bridges, C. J. López, O. Y. Rogozhnikova, D. V. Trukhin, E. K. Brooks, V. Tormyshev, H. J. Halpern, W. L. Hubbell, *J. Magn. Reson.* **2016**, *269*, 50–54.
- [18] M. V. Fedin, G. Y. Shevelev, D. V. Pyshnyi, V. M. Tormyshev, G. Jeschke, M. Yulikov, E. G. Bagryanskaya, *Phys. Chem. Chem. Phys.* **2016**, *18*, 29549–29554.
- [19] O. Krumkacheva, E. Bagryanskaya, *J. Magn. Reson.* **2017**, *280*, 117–126.
- [20] A. Rajca, V. Kathirvelu, S. K. Roy, M. Pink, S. Rajca, S. Sarkar, S. S. Eaton, G. R. Eaton, *Chem. Eur. J.* **2010**, *16*, 5778–5782.
- [21] V. Meyer, M. A. Swanson, L. J. Clouston, P. J. Boratyński, R. A. Stein, H. S. Mchaourab, A. Rajca, S. S. Eaton, G. R. Eaton, *Biophys. J.* **2015**, *108*, 1213–1219.
- [22] M. Malferrari, A. Savitsky, W. Lubitz, K. Möbius, G. Venturoli, *J. Phys. Chem. Lett.* **2016**, *7*, 4871–4877.
- [23] N. Barhate, P. Cekan, A. P. Massey, S. T. Sigurdsson, *Angew. Chem. Int. Ed.* **2007**, *46*, 2655–2658; *Angew. Chem.* **2007**, *119*, 2709–2712.
- [24] T. E. Edwards, P. Cekan, G. W. Reginsson, S. A. Shelke, A. R. Ferre-D'Amare, O. Schiemann, S. T. Sigurdsson, *Nucleic Acids Res.* **2011**, *39*, 4419–4426.
- [25] O. Schiemann, P. Cekan, D. Margraf, T. F. Prisner, S. T. Sigurdsson, *Angew. Chem. Int. Ed.* **2009**, *48*, 3292–3295; *Angew. Chem.* **2009**, *121*, 3342–3345.
- [26] C. M. Grytz, A. Marko, P. Cekan, S. T. Sigurdsson, T. F. Prisner, *Phys. Chem. Chem. Phys.* **2016**, *18*, 2993–3002.
- [27] A. Marko, V. Denysenkov, Margraf, Dominik, P. Cekan, O. Schiemann, S. T. Sigurdsson, T. F. Prisner, *J. Am. Chem. Soc.* **2011**, *133*, 13375–13379.
- [28] C. Höbartner, G. Sicoli, F. Wachowius, D. B. Gophane, S. T. Sigurdsson, *J. Org. Chem.* **2012**, *77*, 7749–7754.
- [29] I. Tkach, S. Pornsuwan, C. Höbartner, F. Wachowius, S. T. Sigurdsson, T. Y. Baranova, U. Diederichsen, G. Sicoli, M. Bennati, *Phys. Chem. Chem. Phys.* **2013**, *15*, 3433–3437.
- [30] P. Cekan, A. L. Smith, N. Barhate, B. H. Robinson, S. T. Sigurdsson, *Nucleic Acids Res.* **2008**, *36*, 5946–5954.
- [31] L. S. Stelzl, N. Erlenbach, M. Heinz, T. F. Prisner, G. Hummer, *J. Am. Chem. Soc.* **2017**, *139*, 11674–11677.

Manuscript received: March 27, 2018

Revised manuscript received: May 6, 2018

Accepted manuscript online: June 2, 2018

Version of record online: July 13, 2018

Supporting Information

Dynamics of Nucleic Acids at Room Temperature Revealed by Pulsed EPR Spectroscopy

*Markus Gränz, Nicole Erlenbach, Philipp Spindler, Dnyaneshwar B. Gophane, Lukas S. Stelzl, Snorri Th. Sigurdsson, and Thomas F. Prisner**

anie_201803682_sm_miscellaneous_information.pdf

Supporting Information

Table of Contents

Sample preparation for EPR measurements.....	2
Continuous wave EPR analysis of duplex DNA.....	3
Echo-detected field sweep.....	4
Hahn echo decay curve	5
PELDOR Experiments.....	6
Comparison of cold temperature in solution and RT measurements on Nucleosil.....	9
Simulation of time dependence of the dsDNA dynamics	10
References.....	12

Sample preparation for EPR measurements

The spin-labeled DNA sample was prepared by annealing 10 nmol of each strand in 100 μL of 10 mM phosphate buffer, pH 7.0, 100 mM NaCl and 0.1 mM EDTA, followed by evaporation of the water. The dried sample was dissolved in degassed D_2O (100 μL) and 24 μL of this stock solution with additional 6 μL of d_8 -Glycerol were added to prewashed Nucleosil particles (5 mg). Nucleosil $^{\text{C}}$ (5 μm in size, CS Chromatographie Service GmbH) is a silica gel, whose surface is functionalized with dimethyl amino (DMA) residues. As a solid phase Nucleosil is commonly used for nucleic acid separation with HPLC. DMA groups on the silica beads are protonated at neutral pH and were washed before usage as described elsewhere.¹

The sample mixture was transferred in a 1.6 mm outer diameter (OD) quartz EPR tube (Suprasil, Wilmad LabGlass) under argon atmosphere, followed by spinning with a hand-driven rotor. The supernatant was separated from the settled particles and measured individually for non-bound DNA left-overs. No EPR signal was detected for the supernatant, indicating full adsorbance on the Nucleosil surface. For pulsed X-band measurements the 1.6 mm OD quartz capillary was taken into a 2.8 mm OD quartz tube (Suprasil, Wilmad LabGlass).

Continuous wave EPR analysis of duplex DNA

Continuous wave (cw) EPR measurements at RT were performed at X-band frequency (9.54 GHz) using a Bruker E500 spectrometer equipped with a TE102 cavity. Experimental parameters were set to 100 kHz modulation frequency, 0.1 mT modulation amplitude, 0.2 mW microwave power, 40.96 ms time constant, 40.96 ms conversion time, 1024 points, 6 mT sweep width and 20-100 scans.

The cw EPR spectra were recorded as the first derivative of the absorption spectra. For spin counting the baseline was corrected by a 2nd order polynomial fit to remove a zero offset of the single integrated spectra. Nitroxide spin concentration was determined by comparing the intensity of the double integrated spectra with those of standard sample with known concentration (200 μ M of 4-Hydroxy-2,2,6,6-tetramethylpiperidinyloxy (TEMPO) in buffered solution). The spin concentration of the samples was $180 \pm 20 \mu$ M. The cw-EPR data proved full immobilization upon binding to the Nucleosil (Fig. S1).

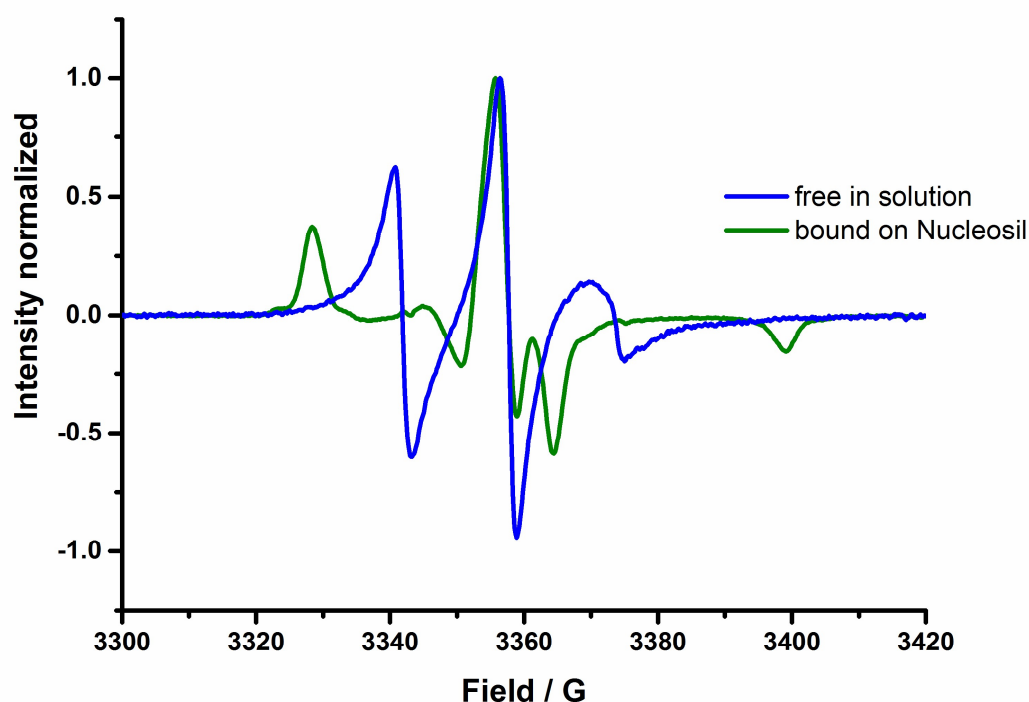


Figure S1: Continuous wave EPR spectra of dsDNA free in buffered solution (blue) and bound on Nucleosil particle (green). The spectra were normalized to the middle peak. For calculation of spins, double integral intensities were determined and compared to calibrated standard.

Echo-detected field sweep

Field-sweep experiments were performed by using the Hahn echo sequence ($\pi/2$ - τ - π) with 32 ns $\pi/2$ and π pulses both at RT and 50 K. The time τ between the pulses was set to 400 ns at 50 K and to 200 ns at RT. Echo integration was done in a 60 ns window and the shot repetition time (SRT) was 300 μ s at RT and 4000 μ s at 50 K. For the RT PELDOR measurements, the probe pulse was set to the maximum of the nitroxide spectrum (Fig. S2). Selective orientations were pumped by inversion pulses 45 MHz and 85 MHz offset to the probe pulses. The distorted shape of the field sweep spectrum obtained at room temperature is due to the fast and anisotropic transversal relaxation time, most probably due to small angle motions of the nitroxide spin labels.

Due to the strongly anisotropic phase memory time at RT PELDOR time traces at non-canonical orientations are very difficult to acquire. Thus the positions of pump and probe pulses have been interchanged here. The probe pulse was set to the center of the nitroxide spectra, where hardly any orientation selection occurs and the pump pulses were set to 45 or 85 MHz offset. For pump pulses the orientation dependent T_2 relaxation time is not important, as long as the excitation width of the pump pulse exceeds the homogeneous linewidth.

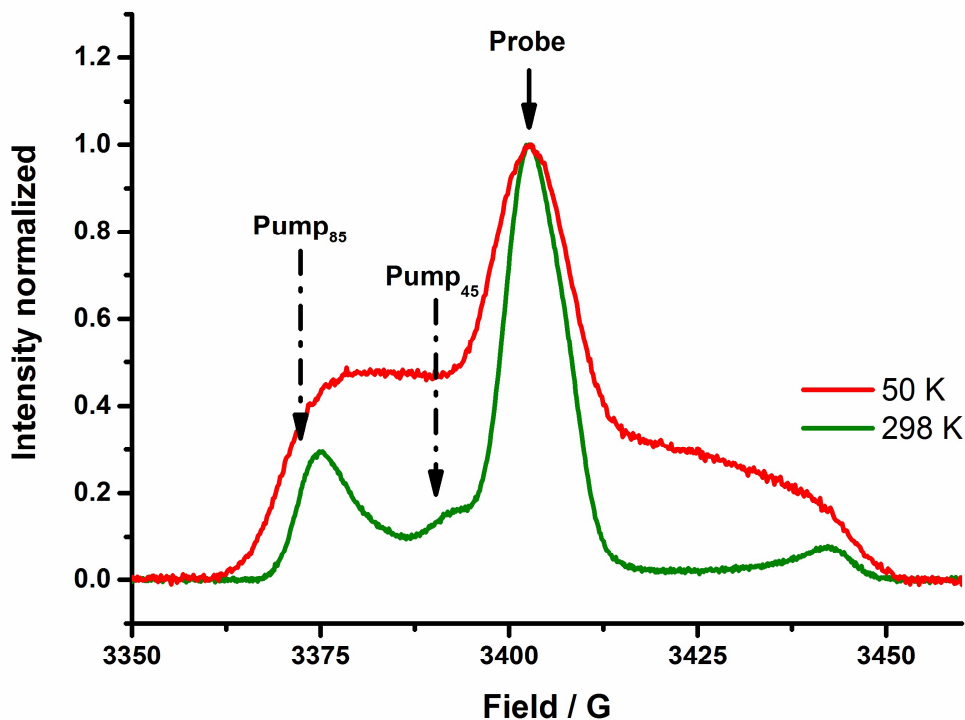


Figure S2: Echo-detected field sweep EPR data of dsDNA bound to Nucleosil at X-band frequency. Spectra are normalized to the same maximum intensity; RT (298 K) spectrum is shown in green, the spectrum obtained at 50 K is shown in red. Pump and probe pulse positions for the RT PELDOR measurements are indicated by black arrows.

Hahn echo decay curve

The transverse relaxation times (T_2) were measured by a Hahn echo sequence as a function of the inter-pulse delay, starting from a value of 200 ns and increasing in steps of 8 ns. Figure S3 shows the echo decay function measured at the field position corresponding to the maximum of the EPR spectrum. Deuterium or proton electron spin echo modulation (ESEEM) was prominent in the 50 K spectra, but not at RT. The relaxation curve at RT has two components. The PELDOR measurements at RT were measured with $\tau_2 = 900$ ns (indicated with dotted line, Fig. S3).

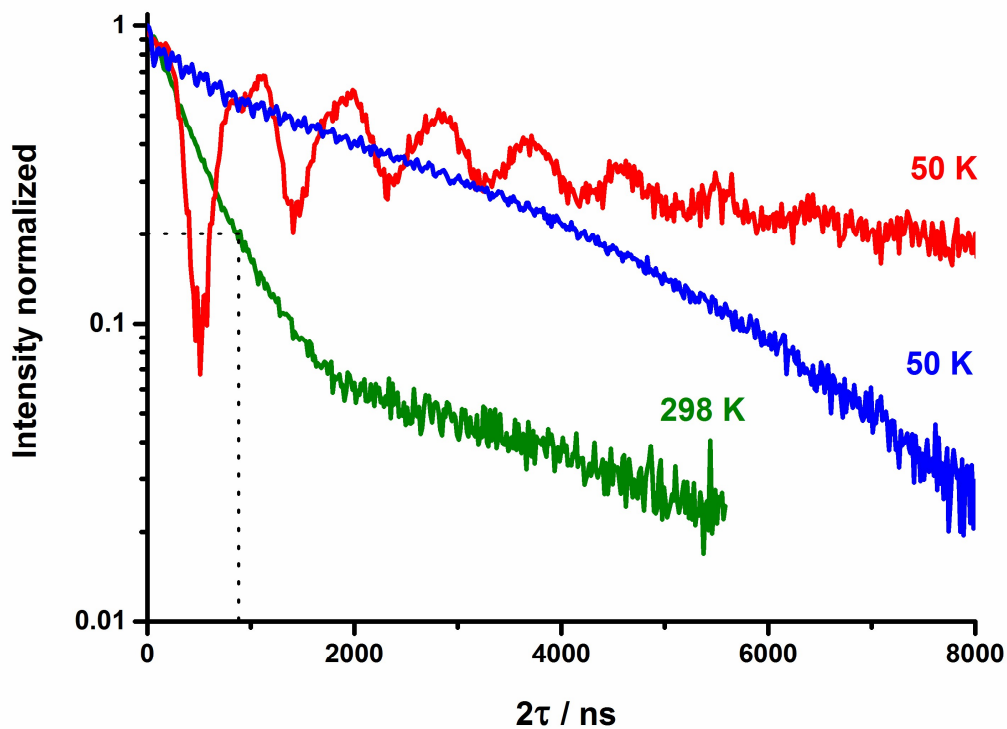


Figure S3: Hahn echo decay curve of dsDNA absorbed on Nucleosil at 50 K buffered in D_2O (red) and at 298 K / RT shown in green. Supplementary, the measurement at 50 K in H_2O without Nucleosil is shown in blue.

PELDOR Experiments

X-band frequency (9.5 GHz) experiments were performed with a BRUKER ER4118X-MS3 resonator equipped with a continuous-flow helium cryostat (CF935, Oxford Instruments) and a temperature control system (ITC 502, Oxford Instruments). For PELDOR experiments, the conventional dead-time free four-pulse sequence was used.² All pulses were amplified with a 1 kW traveling wave tube amplifier (Applied Systems Engineering 117X) and pump pulses were generated by an arbitrary waveform generator (AWG, SP devices SDR14). A 4-step phase cycle (0° , 90° , 180° , 270°) was performed on the coherent pump pulse, in addition to the phase cycle of the PELDOR detection pulses (incoherent; on x, -x, y channels). Shot repetition time was set to 4000 μs at 50 K and 300 μs at 298 K.

The 12 ns long pump pulse was applied to the maximum of the spectrum for the 50 K PELDOR time traces (Fig. S4). The probe pulses ($\pi/2$ and π) were set to 32 ns and applied with a frequency offset of ~ 45 MHz and 85 MHz above the pump pulse frequency. For the measurements on the Nucleosil at 50 K and at RT (Fig. S5) this setting was changed. Here the length of the pump pulse was set to 32 ns applying at the left shoulder with 45 MHz and 85 MHz off. While setting the probe pulses with 12 ns at the maximum this leads to a switch of the pump and probe positions (see depicted in Fig. S2). This setting is different from typical experiments at 50 K. It optimizes the detection time window and signal-to-noise ratio of the signal at room temperature, at the expense of the modulation depth of the PELDOR time trace.

The delay time between the first two pulses of the primary echo sequence was varied between 100 ns and 164 ns in 8 ns steps in order to reduce the ^1H nuclear modulation contributions to the PELDOR signal. The length of the PELDOR time trace evolution is limited by the transversal relaxation time T_2 . At RT, the maximum length of the time trace that could be measured with a good signal-to-noise ratio was around 900 ns. Primary experimental data were background-corrected by fitting an exponential decay function to the time trace and dividing the experimental time trace by this background function to remove the intermolecular contribution. The measurement time for RT experiments was around 12 hours.

PELDOR data without background correction on Nucleosil

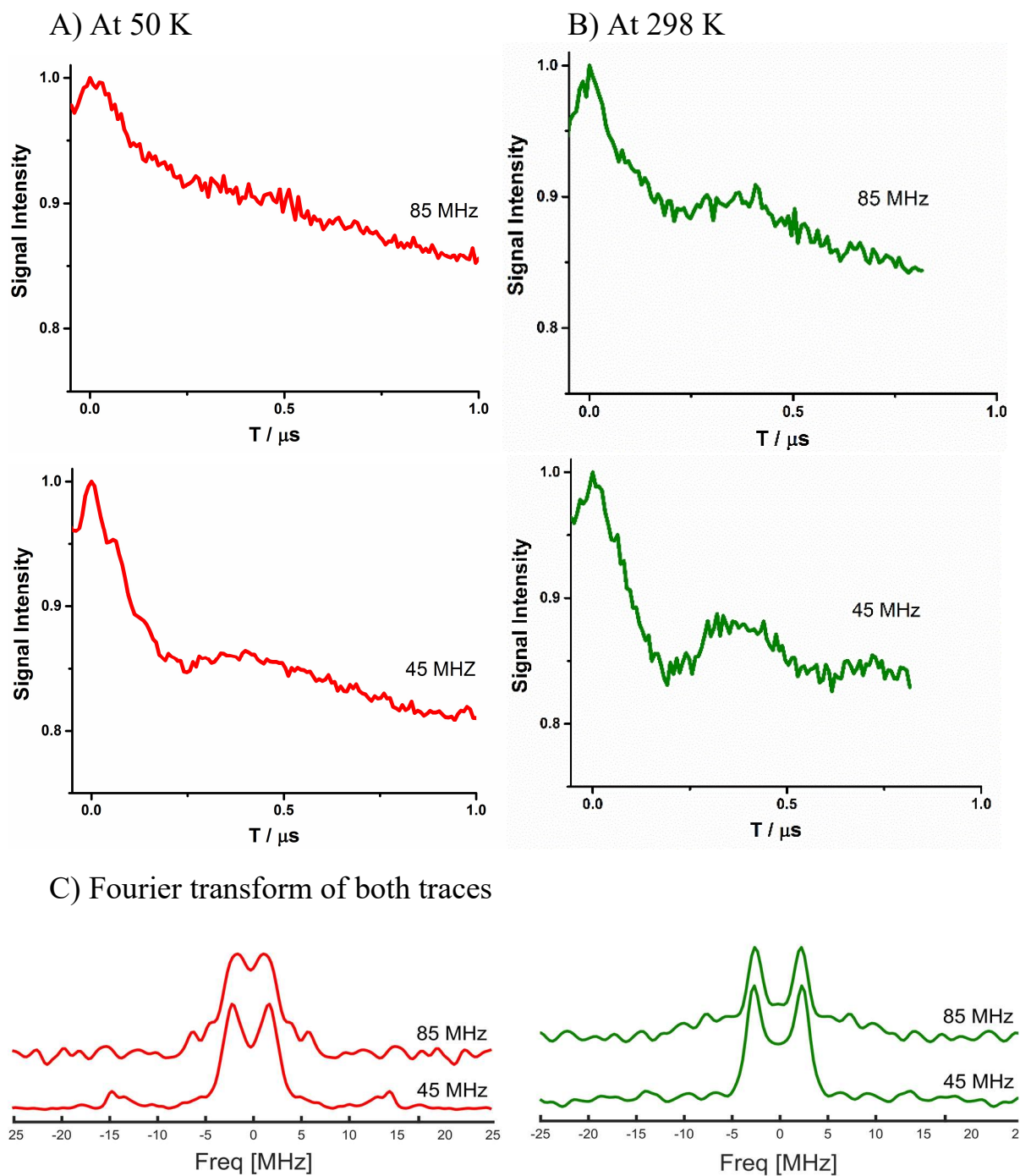


Figure S5: PELDOR time traces of dsDNA on Nucleosil at designated pump-probe frequency offsets at 50 K (A) and 298 K (B). The probe pulse was set to the maximum of the nitroxide spectrum to achieve higher signal-to-noise ratio. Modulation depth is thereby smaller comparing to traces in Fig. S4. C) Fourier transform of both traces. . The small peaks observed at about 14 MHz arise from proton hyperfine couplings.

Direct comparison of room temperature PELDOR time traces of dsDNA with Nucleosil with low temperature measurements in frozen solution of dsDNA without Nucleosil

The room temperature PELDOR time traces of dsDNA adsorpt on silica beads show more pronounced modulation (Figure S6), consistent with our hypothesis that the electrostatic interaction with the Nucleosil particles inhibit the rotational motion of the dsDNA molecule but do not suppress their internal dynamics.

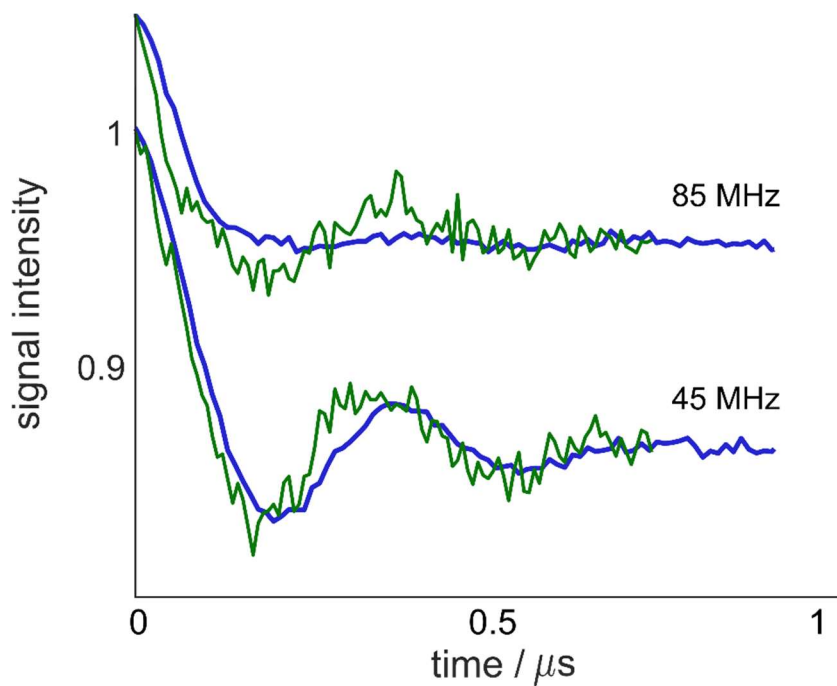


Figure S6: PELDOR time traces of dsDNA at RT on Nucleosil (green) compared to dsDNA buffered in solution at 50 K (blue). The time traces are rescaled in modulation depth for better comparison.

Simulation of time dependence of the dsDNA dynamics

An MD simulation with the state-of-the-art parambsc1 force field³ was used to generate an ensemble of conformers which were used to calculate the PELDOR time traces. The sum of the PELDOR time traces calculated from the ensemble of conformers represents the experimental situation at cryogenic temperature (Fig. 3B). A 200 ns long MD simulation with 0.1 ns steps was used to generate such an ensemble, resulting in 2000 structures. The atomistic MD simulation in explicit water was run without explicitly representing the spin label and the Nucleosil. However, for the rigid spin label ζ the position of each of the two spin labels can be extrapolated from the planar cytosine ring, as discussed in detail in Ref 4. The mutual spin-label orientations and spin – spin distances were determined analytically from the coordinates and used to simulate the PELDOR time traces. Details regarding the MD and PELDOR simulation procedure are described elsewhere.^{4,5} In this static ensemble, the resulting PELDOR time traces are an average over all structures present in the MD simulation.

At room temperature the Larmor frequency of the observer spin as well as the dipolar coupling frequency between both spins will fluctuate due to the conformational dynamics of the dsDNA molecule. For a 3-pulse PELDOR sequence this leads to a phase fluctuation given by:

$$\varphi(2\tau) = \int_0^T \omega_r(t) \pm \omega_{dd}(t) dt + \int_T^\tau \omega_r(t) \mp \omega_{dd}(t) dt - \int_\tau^{2\tau} \omega_r(t) \mp \omega_{dd}(t) dt$$

with the resonance frequency ω_r describing the electron Zeeman interaction and the hyperfine interaction of the observed spin, the time T were the pump pulse is applied and ω_{dd} the dipolar coupling between both spins. The dipolar coupling frequency is usual given by

$$\omega_{dd}(t) = \frac{D}{r(t)^3} (1 - 3\cos^2(\theta(t)))$$

with $r(t)$ the distance between both spin-labels and $\theta(t)$ the angle between the distance vector and the external magnetic field. The dipolar coupling constant is $D = 2\pi \cdot 54.07 \text{ MHz} \cdot \text{nm}^3$.

The only part which is dependent on the time T of the inversion pulse is given by:

$$\varphi(T) = \int_0^T \omega_{dd}(t) dt$$

For frozen solutions ω_{dd} is not a function of t, resulting in the usual formula for the PELDOR signal:

$$S(T) = \langle \langle \cos(\omega_{dd} T) \rangle_\theta \rangle_N$$

with a sum over all the conformers N in the sample and all possible orientation of the magnetic field with respect to the dipolar axis. At room temperature the dipolar coupling is modulated by the internal dynamics of the dsDNA, therefore the PELDOR time trace is given by:

$$S(T) = \langle \langle \cos\left(\int_0^T \omega_{dd}(t) dt\right) \rangle_\theta \rangle_N$$

For the dsDNA system investigated here, we used the dipolar coupling strength $\omega_{dd}(t)$ obtained from the MD simulation.⁵ Trajectory segments were used to calculate a conformational ensemble, where the windows moved by 2 ns further for each segment. The ensemble is then represented by N=100 trajectory segments. Since the PELDOR experiment reports on the internal dynamics rather than diffusion of the DNA, we fitted the trajectory to a reference structure, removing the rotational diffusion from the MD simulations for subsequent analysis. To calculate the orientation selection of the dsDNA, the pump pulse efficiency, also called orientation intensity function $\lambda(\theta(T))$, was calculated according to Ref. 5. The orientation-selective PELDOR time traces for the dsDNA at RT (Fig. 3) is calculated as followed:

$$\mathbf{S}(T) = \left\langle \mathbf{1} + \int_0^{\frac{\pi}{2}} \lambda(\theta(T)) \left(\cos \left(\int_0^T \omega_{dd}(t) dt \right) - \mathbf{1} \right) \sin\theta d\theta \right\rangle_N$$

References

1. Shevelev, G. Y. *et al.* Physiological-Temperature Distance Measurement in Nucleic Acid using Triarylmethyl-Based Spin Labels and Pulsed Dipolar EPR Spectroscopy. *J. Am. Chem. Soc.* **136**, 9874–9877 (2014).
2. Pannier, M., Veit, S., Godt, A., Jeschke, G. & Spiess, H. Dead-Time Free Measurement of Dipole–Dipole Interactions between Electron Spins. *J. Magn. Reson.* **142**, 331–340 (2000).
3. Ivani, I.; Dans, P. D.; Noy, A.; Pérez, A.; Faustino, I.; Hospital, A.; Walther, J.; Andrio, P.; Goñi, R.; Balaceanu, A.; Portella, G.; Battistini, F.; Gelpí, J. L.; González, C.; Vendruscolo, M.; Laughton, C. A.; Harris, S. A.; Case, D. A.; Orozco, M., *Nat. Methods*, **13**, 55– 58 (2016).
4. Stelzl, L. S., Erlenbach, N., Heinz, M., Prisner, T. F. & Hummer, G. Resolving the conformational dynamics of DNA with Ångstrom Resolution by PELDOR and Molecular Dynamics. *J. Am. Chem. Soc.* **139**, 11674-11677 (2017).
5. Marko, A. & Prisner, T. F. An algorithm to analyze PELDOR data of rigid spin label pairs. *Phys. Chem. Chem. Phys.* **15**, 619–627 (2013).

“End-to-end” stacking of small dsRNA

NICOLE ERLNBACH,¹ CHRISTIAN GRÜNEWALD,² BISERA KRSTIC,¹ ALEXANDER HECKEL,²
and THOMAS F. PRISNER¹

¹Institute of Physical and Theoretical Chemistry, Center of Biomolecular Magnetic Resonance, Goethe University, D-60438 Frankfurt am Main, Germany

²Institute of Organic Chemistry and Chemical Biology, Goethe University, D-60438 Frankfurt am Main, Germany

ABSTRACT

PELDOR (pulsed electron–electron double resonance) is an established method to study intramolecular distances and can give evidence for conformational changes and flexibilities. However, it can also be used to study intermolecular interactions as for example oligerimization. Here, we used PELDOR to study the “end-to-end” stacking of small double-stranded (ds) RNAs. For this study, the dsRNA molecules were only singly labeled with the spin label TPA to avoid multispin effects and to measure only the intermolecular stacking interactions. It can be shown that small dsRNAs tend to assemble to rod-like structures due to π – π interactions between the base pairs at the end of the strands. On the one hand, these interactions can influence or complicate measurements aimed at the determining of the structure and dynamics of the dsRNA molecule itself. On the other hand, it can be interesting to study such intermolecular stacking interactions in more detail, as for example their dependence on ion concentration. We quantitatively determined the stacking probability as a function of the monovalent NaCl salt and the dsRNA concentration. From these data, the dissociation constant K_d was deduced and found to depend on the ratio between the NaCl salt and dsRNA concentrations. Additionally, the distances and distance distributions obtained predict a model for the stacking geometry of dsRNAs. Introducing a nucleotide overhangs at one end of the dsRNA molecule restricts the stacking to the other end, leading only to dimer formations. Introducing such an overhang at both ends of the dsRNA molecule fully suppresses stacking, as we demonstrate by PELDOR experiments quantitatively.

Keywords: EPR; PELDOR/DEER; dsRNA; stacking

INTRODUCTION

In 1958 it was recognized that the hydrogen bonds between the complementary base pairs in double-stranded nucleic acids (dsNA) (Fonseca Guerra et al. 1999) cannot be the only interaction stabilizing the secondary structure of duplexes (Sturtevant et al. 1958). An additional effect of parallel aromatic stacking by London dispersion forces between the base pairs above and below each other was found, also known as π – π interaction (van de Waal 1986; Mignon et al. 2005). This intramolecular interaction was studied intensively in the last decade using experimental and computational methods (Hunter and Sanders 1990; Gellman et al. 1996; Florián et al. 1999; Brown et al. 2015; Häse and Zacharias 2016; Kilchherr et al. 2016; Šponer et al. 2018). However, this inter-residue interaction is not only an intramolecular effect; it can also be observed as intermolecular interaction between two duplexes. In such cases, the short dsNAs stack spontaneously into rod-like structures, which were first observed for DNA in liquid crys-

tals (Nakata et al. 2007). The “end-to-end” stacking was the only possible way to explain the axial ordering in these crystals. Previous studies had primarily focused on “side-by-side” forces between long dsDNA (Oosawa 1968; Allahyarov et al. 2004; Maffeo et al. 2010; Wong and Pollack 2010).

Rod-like stacking can play an important role in RNA–protein interactions, as shown by Ryter and Schulz (1998). They studied the interaction between a dsRNA-binding domain and two ten base pair long dsRNAs. These dsRNAs stacked with each other to form a pseudo-continuous helix. The stacking expanded the major groove, which seemed to create the binding site for the protein.

The Pollack group (Qiu et al. 2006; Pollack 2011) studied “end-to-end” stacking of dsDNA with small angle X-ray scattering (SAXS). They were able to differentiate between repulsion and attraction of two dsNA, and they studied the

Corresponding author: prisner@chemie.uni-frankfurt.de

Article is online at <http://www.majournal.org/cgi/doi/10.1261/rna.068130.118>.

© 2019 Erlenbach et al. This article is distributed exclusively by the RNA Society for the first 12 months after the full-issue publication date (see <http://majournal.cshlp.org/site/misc/terms.xhtml>). After 12 months, it is available under a Creative Commons License (Attribution-NonCommercial 4.0 International), as described at <http://creativecommons.org/licenses/by-nc/4.0/>.

contribution of salt concentration, of DNA concentration and of the number of base pairs to the attraction and repulsion forces between short dsDNA (Qiu et al. 2007). In the case of dsRNA, they found that the nearby divalent Mg^{2+} ion distribution shields the negative charge of the nucleic acids more effectively compared to dsDNA. They also found that for dsRNAs the π - π attraction plays an important role even at low salt concentrations (Pabit et al. 2009).

Another method to study these interactions is electron paramagnetic resonance spectroscopy (EPR). Pulsed electron-electron double resonance spectroscopy (PELDOR/DEER) (Milov et al. 1984; Martin et al. 1998) is a method for measuring distances in a range of 2–10 nm (Fig. 1). However, paramagnetic reporter groups attached to the biomolecule are required for such measurements. Commonly used modified nucleic acids are aminoxyl radicals based spin labels, called nitroxides. The well-established spin-label 2,2,5,5-tetramethyl-pyrrolin-1-oxyl-3-acetylene (TPA, chemical structure depicted in Fig. 2A) is used for dsNA (Spaltenstein et al. 1989) and produces reliable distances (Schiemann et al. 2007). Such measurements were performed to obtain information about structure and about dynamic and conformational changes of different kinds of NAs (Krstić et al. 2010; Romainczyk et al. 2011). The experimental PELDOR time trace (Fig. 1C) can be described as a product of the specific intramolecular interaction between the two spin labels on the RNA molecule (giving rise to a well-defined oscillation) and the nonspecific intramolecular interaction between all molecules in the sample (resulting in an exponential decaying background function). After background division and normalization (to the signal intensity for $\Delta t = 0$) of the PELDOR time trace (Fig. 1D), Tikhonov regularization can be used to extract from the oscillations of the time trace the distance distribution function $P(r)$ between both spin labels (Fig. 1E).

However, the PELDOR method is not limited to intramolecular interactions. Wherever specific intermolecular

distances in the 2–10 nm range appear, for example in oligomerization of membrane proteins (Endeward et al. 2009) or “end-to-end” stacking of RNA, these distances can be measured by this method. Such distances have already been observed in previously published PELDOR measurements of NAs (Piton et al. 2007; Romainczyk et al. 2011; Halbmaier et al. 2016; Weinrich et al. 2017) and were especially pronounced for RNA molecules. Whereas only one distinct distance was expected for short dsRNAs with two spin labels, additional distances were observed. Compared with dsRNA models, it was clear that these additional distances could only be explained by “end-to-end” stacking between dsRNA molecules. However, a detailed analysis of the intramolecular distances is more difficult in such cases, because more than two coupled spins contribute to the PELDOR signal (Bode et al. 2007).

In addition to information on distances, a PELDOR time trace also provides information about the number of spins interacting within an ~ 10 nm sphere. The modulation depth Δ of the background corrected and normalized PELDOR signal (Fig. 1D) reports on the number of interacting spins. This was recognized by Milov et al. (1998) and used for spin counting in multispin molecules (Bode et al. 2007). However, this method is not only useful in determining the number of spins per macromolecule but also in assessing the stacking of singly spin-labeled dsRNA molecules. In this case, a direct correlation of the experimental easy accessible modulation depth Δ and the dsRNA stacking probability P exists, allowing a quantitative determination of the thermodynamic equilibrium between stacked and unstacked dsRNA molecules.

In this paper, we investigated the influence of the monovalent NaCl salt concentration and of dsRNA concentration itself on the stacking probability p . For this specific purpose, the dsRNAs were only mono-labeled with the TPA spin label. Hence, only intermolecular distances arising

from stacking of the dsRNAs are visible in our PELDOR measurements. From the distance distribution functions $P(r)$ derived from the PELDOR time traces the end-to-end stacking geometry could be deduced. The influence of dsRNA concentration and of the salt concentration was studied by PELDOR spectroscopy. The stacking probability could be quantitatively determined from the modulation depth Δ , as a function of NaCl salt and dsRNA concentration. From this, the dissociation constant K_d of the stacking could be calculated. Additionally, we could demonstrate that stacking of short dsRNAs can be quantitatively avoided by

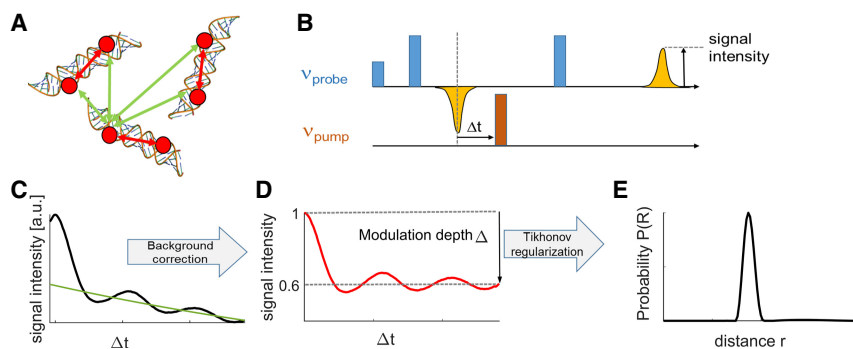


FIGURE 1. (A) Cartoon of possible intramolecular (red) and intermolecular (green) interactions in doubly labeled dsRNA molecules. (B) Four-pulse PELDOR sequence. (C) Raw PELDOR time trace (black) with intermolecular mono-exponential background (green). (D) Background corrected PELDOR time trace with only intramolecular interaction. The modulation depth Δ is indicated in the figure. (E) Distance distribution derived from a Tikhonov regularization of the background corrected PELDOR time traces.

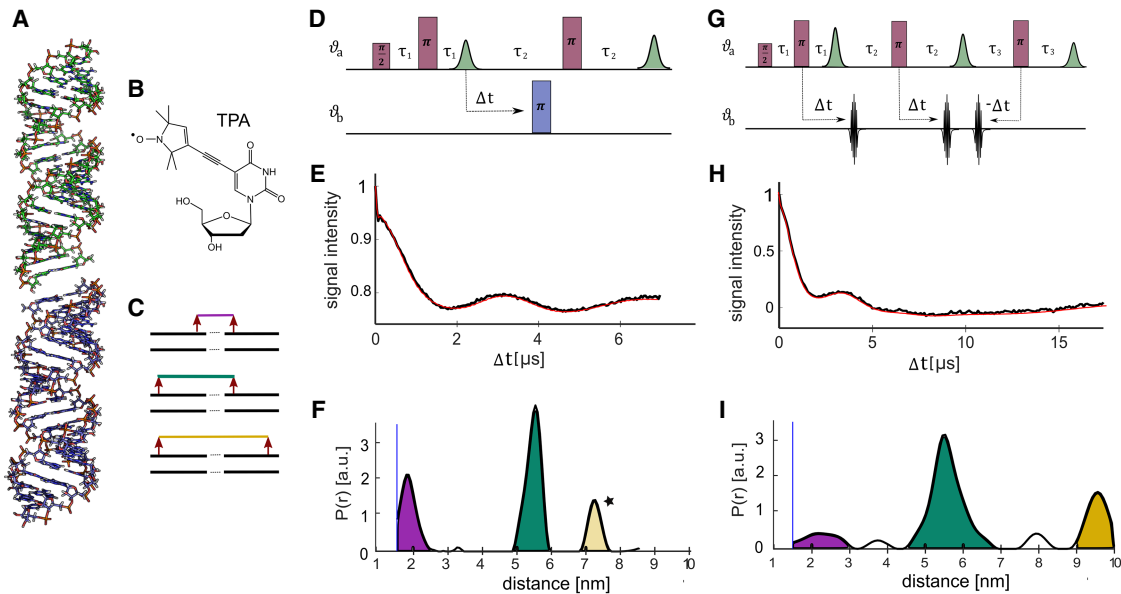


FIGURE 2. (A) Model of a stacked dsRNA dimer. (B) Chemical structure of TPA. (C) Three stacking possibilities, which relate to three different measurable distances in a singly labeled dsRNA sample. (D) Pulse sequence of the four-pulse PELDOR experiment. (E) Background corrected four-pulse PELDOR time trace for a stacked singly labeled dsRNA. (F) Distance distribution from the four-pulse PELDOR measurements obtained by Tikhonov regularization. (G) Sequence of the seven-pulse-CP-PELDOR experiment. (H) Background corrected seven-pulse-CP-PELDOR time trace for a stacked singly labeled RNA. (I) Distance distribution from the seven-pulse-CP-PELDOR measurements obtained by Tikhonov regularization.

introducing an overhang of one nucleotide at both ends of the dsRNA.

RESULTS AND DISCUSSION

Our PELDOR measurements performed on singly labeled dsRNAs (Fig. 2) confirm that additional distances observed previously on doubly labeled dsRNAs (Piton et al. 2007; Romainczyk et al. 2011; Halbmaier et al. 2016; Weinrich et al. 2017) are due to "end-to-end" stacking. PELDOR measurements with single-labeled dsRNAs exclusively show distances that result from intermolecular attraction between nucleic acids. This means that only stacked dsRNA molecules contribute to the modulation depth of the PELDOR signal after background division. As the stacking can occur at both ends of the strands, three different distances can be measured, as depicted in the cartoon in Figure 2C. Two distances can clearly be identified in the four-pulse PELDOR time traces (Fig. 2E,F). An additional higher distance peak (Fig. 2F, marked with a star) indicates the possible presence of a longer distance, but it is already beyond the distance range accessible with the maximum achievable four-pulse sequence time window of 7 μ sec.

To be able to reliably observe the expected long distance seven-pulse-CP-PELDOR measurements were performed. With the Carr–Purcell (CP) pulse sequence (Fig. 2G), the length of the time traces can be significantly extended to more than 17 μ sec. Therefore, distances up to 10 nm can be measured. The seven-pulse-CP-PELDOR mea-

surements confirm the shorter distances and show the expected additional distance at around 9 nm (Fig. 2H,I).

These distance distributions have been used for a simple geometrical interpretation of the orientations between two stacked dsRNA molecules, with each dsRNA molecule represented as a rigid cylinder. Assuming a rise per base pair of 0.28 nm, which is in full agreement with previous PELDOR measurements on doubly labeled dsRNA molecules (Halbmaier et al. 2016), the mean values of all three measured intermolecular distances fit very well with a parallel end-to-end alignment of the dsRNA molecules (bend angle $\theta = 0$). To model the width of the experimental observed distance peaks, we used a Gaussian distribution of the bend angle θ :

$$P(\theta) = \frac{1}{\sqrt{2\pi}\sigma} e^{-\frac{\theta^2}{2\sigma^2}}. \quad (1)$$

Comparison of the experimental distance distribution widths for all three distance peaks resulted in a standard deviation σ of about 40° – 50° for the kink angle distribution.

To inhibit the stacking, a nucleotide overhang was added to one end of one RNA strand during the solid phase synthesis. This prevents the possibility of a π – π interaction between the dsRNAs at one end; therefore, stacking can only lead to dimers with a single distinct distance as shown in the cartoon in Figure 3A. PELDOR measurements fully validated our expectations as they show only the high frequency oscillation corresponding to the short distance

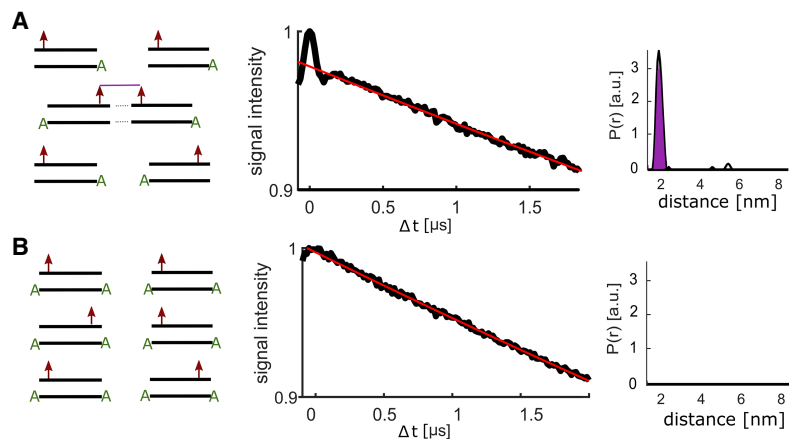


FIGURE 3. (A) dsRNA with a single nucleotide overhang at one end. (B) dsRNA with an overhang at both ends of the dsRNA. (Left) Schematic picture of stacking possibilities; (middle) raw four-pulse-PELDOR data; (right) Tikhonov derived distance distribution.

between the spin labels (Fig. 3A). In a second step, overhangs were added to both ends of one RNA strand. This led to the absence of any PELDOR oscillation, which indicates that there is no distinct distance and therefore a lack of stacking between the dsRNAs. The monotonous decay of the PELDOR signal in this case originates solely from the background signal arising from randomly distributed dsRNA molecules in the frozen solution sample (Fig. 3B).

Samples with different Na^+ concentrations were prepared to investigate the dependency of stacking on the concentration of monovalent counterions. The monovalent sodium concentration was varied between 50 and 800 mM, while keeping the dsRNA concentration constant at 200 μM . The overall shape of the PELDOR time traces remained constant (Supplemental Fig. S3A), but the modulation depth Δ systematically increased as a function of the salt concentration. The modulation depth Δ depends on the excitation efficiency λ of the nitroxide spin label by the microwave pump pulse and on the fraction of coupled spins. The excitation efficiency is given by the microwave field strength (given by the pulse length) and the spectral position (defined by the microwave frequency and magnetic field strength) and can be easily calibrated with nitroxide model compounds (Bode et al. 2007). For samples with a nucleotide overhang on only one end (Fig. 3A) only dimers and monomers can occur. In this case, the relation between the stacking probability P and the modulation depth Δ is especially simple:

$$\Delta = \lambda * P, \quad (2)$$

with the stacking probability P defined as

$$P = \frac{2(D)}{(M) + 2(D)} = \frac{2(D)}{(\text{RNA})}. \quad (3)$$

Thus, the stacking probability P can be directly computed from the experimentally observed modulation depth Δ for the different salt concentrations (blue squares in Fig. 4A). For samples without any overhang higher oligomeric states can also occur. This leads to larger modulation depths for these samples (see Supplemental Fig. S3B). However, these samples yield the same stacking probability P , if statistics for the higher oligomeric states are taken into account (green diamonds in Fig. 4A, see Supplemental Material for details). The straight line in the diagram of Figure 4A serves only as an empirical correlation for the experimentally accessed salt concentration range. With Equation 3 and the thermodynamic definition of the dissociation constant K_d , the dissociation constant can be easily calculated for all salt concentrations from the derived stacking probabilities P and the known RNA concentration:

$$K_d = \frac{M^2}{D} = 2(\text{RNA}) \frac{(1 - P)^2}{P}. \quad (4)$$

The dissociation constant K_d varies between 0.2 and 1.2 mM (Fig. 4B) for the experimentally accessed NaCl salt concentration, ranging from 50 to 300 mM. It should be mentioned that the dissociation constant itself is of course not a function of the RNA concentration; this factor is compensated by the intrinsic RNA concentration dependence of the stacking probability P , directly derived from the experiment (Fig. 4A).

In a second series of experiments, we measured the modulation depth as a function of the RNA concentration

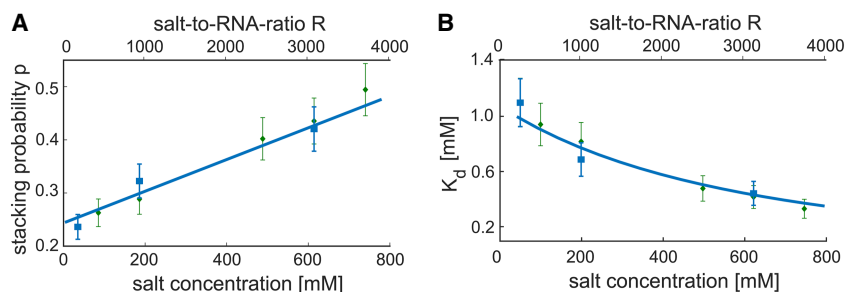


FIGURE 4. (A) Stacking probability of dsRNA in relation to the monovalent salt concentration of NaCl and to the salt-to-RNA ratio, for a RNA concentration of 200 μM . In blue for samples with one overhang and in green for samples without overhang but taking oligomers and multi-spin effects into account. The error was estimated to be 10%. (B) Dimerization constant K_d for the “end-to-end” stacking for different salt-to-RNA ratios. In blue for samples with one overhang and in green for samples without overhang but taking trimers and multi-spin effects into account. The error was estimated to be 10%.

(ranging between 50 and 300 μM). These experiments were performed for two NaCl concentrations (200 and 500 mM). Surprisingly, no dependency of the stacking probability P on the RNA concentration itself was found (Fig. 5A).

Solving Equation 4 for the stacking probability P leads to the following expression:

$$P = 1 + C - \sqrt{C(C + 2)}. \quad (5)$$

with

$$C = \frac{K_d}{4(\text{RNA})}. \quad (6)$$

The second solution of the quadratic equation for P can be ignored because it would lead to values of $P > 1$. The stacking probability P calculated from Equation 5 for a NaCl concentration of 200 mM is shown in Figure 5B as dotted line. As expected, this curve shows increasing stacking probability for higher RNA concentrations, but it does not fit our experimentally determined stacking probabilities. On the other hand, our experimental findings can be successfully described by Equation 5 if we define the K_d values in Figure 4B not as a function of the absolute NaCl salt concentration but as a function of the ratio R between the NaCl salt and the RNA concentration. Whereas the overall NaCl concentration does not vary significantly for the experimentally accessed RNA concentration range between 50 and 300 μM , the ratio R does range from 4500 to 650. In this case, our experimental findings that P does not vary with RNA concentration can easily be rationalized by two counteracting effects. On the one hand, P increases with the RNA concentration (dotted line in Fig. 5B), but on the other hand P decreases because of the strongly reduced salt-to-RNA ratio R . The calculated P values taking $K_d(R)$ explicitly into account are shown as a solid black line in Figure 5B and

fits our experimental determined values within experimental error.

Our finding that the dissociation constant K_d does not depend on the absolute NaCl concentration, but rather on the ratio R between the absolute NaCl concentration and the overall RNA concentration is an interesting experimental observation. It is further supported by the fact that we find the expected dependence of P as a function of the RNA concentration with a constant K_d if we keep R constant (Supplemental Fig. S5) and vice versa that we get only a K_d value independent of the RNA concentration for one ratio R (Supplemental Fig. S6). Thus, all our experimental results are consistently described by Equation 5 and by taking K_d as a function of R .

Conclusions

In this work, "end-to-end" stacking of small dsRNA was studied by PELDOR spectroscopy. We synthesized 20mer dsRNAs containing one spin-label TPA per dsRNA molecule and performed four-pulse PELDOR and seven-pulse-CP-PELDOR measurements. The distinct dipolar modulations of the PELDOR time traces arise from the magnetic dipole-dipole interaction between two spin labels belonging to two stacked dsRNA molecules. The extracted distances confirm that the dsRNA stack "end-to-end" via π - π interaction of bases at the end of the strands. The kink angle distribution width of the stacked molecules could be estimated from the widths of the observed distance peaks.

The influence of monovalent NaCl salt concentration and of the dsRNA concentration itself on the stacking probability was investigated by the PELDOR signal modulation depth parameter Δ . Our measurements show that the stacking probability P and the dissociation constant K_d depend strongly on the overall NaCl to RNA concentration ratio R . Higher R ratios increase the stacking probability and decrease the dissociation constant. Varying the dsRNA concentration in a range between 50 and 300 μM for a constant sodium concentration therefore does not alter the stacking probability due to the simultaneous decrease of the salt-to-RNA-ratio. It should be stressed that the ratio R does not reflect on the local number of the salt ions per RNA molecule and that our experimental findings only have validity in NaCl and RNA concentration ranges tested in our experiments. An interpretation of our macroscopic findings in terms of the local ion atmosphere and screening around the dsRNA molecules (see, for example, Lipfert et al. 2014) is not part of this study. Nevertheless, we believe that our experimental

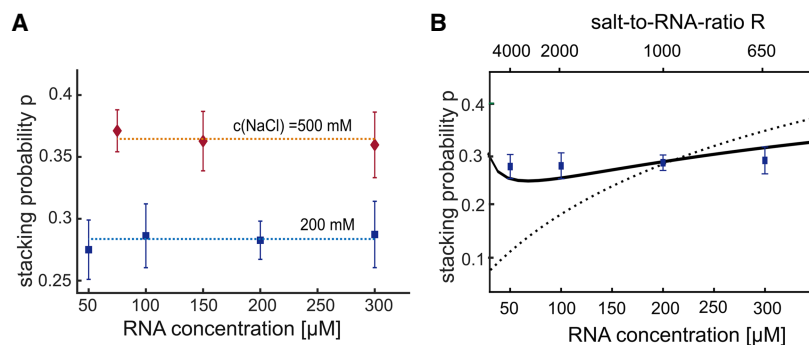


FIGURE 5. (A) Stacking probability of dsRNA in relation to the RNA concentration for 200 mM NaCl (blue) and 500 mM NaCl (orange). The error bars are statistical σ values of five measurements each. (B) Stacking probability of dsRNA in relation to the RNA concentration and the respective salt-to-RNA ratio for 200 mM NaCl concentration (blue data points). The dotted line indicates the expected behavior with a constant K_d and the black line with a K_d dependent on the salt-to-RNA ratio R .

results and findings will be interesting for theoretical modeling of such local properties and optimization of MD simulations for these molecules. Similar experiments for dsRNA molecules in a cellular environment will be interesting and are on our agenda.

Further, we could prove by the PELDOR method that stacking of dsRNA molecules can be efficiently avoided by the addition of a nucleotide overhang at both ends of the dsRNA. For these experiments, an additional base was added during the solid-state synthesis of the individual strands at one end of the dsRNA or at both ends. While a base at one end still leads to a dimerization of dsRNA molecules, bases at both ends of the double strands fully inhibit stacking. This strategy is important for future investigations of the internal dynamics of dsRNA molecules by PELDOR spectroscopy currently in progress in our laboratory.

MATERIALS AND METHODS

Sample preparation

Spin-label TPA (2,2,5,5-Tetramethylpyrrolin-1-yloxy-3-acetylene, structure depicted in Fig. 2B) was synthesized according to the literature (Schiemann et al. 2007; Azarkh et al. 2011). Oligonucleotide synthesis was performed using an Expedite Nucleic Acid Synthesis System from PerSeptive Biosystems and TBDMS-strategy amidites and standard protocols. The deprotection agent was dichloroacetic acid in dichloromethane, the coupling agent was 0.5 M ethylthiotetrazole, capping was performed using acetic anhydride in THF and *N*-methylimidazole in THF/pyridine, respectively. The oxidizing agent was iodine in THF/pyridine/H₂O. Since both the detritylation agent and oxidation agent are known to partially redox deactivate the spin label, the spin label was placed at the 5'-end of the oligonucleotide, and special care was taken to separate redox-deviated spin-labeled oligonucleotides. Oligonucleotide synthesis was stopped after the incorporation of the 5-iodouridine. Subsequently, TPA was coupled to the oligonucleotide by site-specific Sonogashira coupling to the 5-iodouracil base on solid support applying reported protocols (Schiemann et al. 2003; Grünwald et al. 2008). After the Sonogashira coupling, oligonucleotide synthesis was completed. For deprotection of phosphates and cleavage from solid support, cpg was removed from the column, suspended in 2 mL of a 3:1 mixture of 37% aq. ammonia/ethanol and incubated at 37°C for 18 h. Afterwards the supernatant was separated, the cpg material was washed two times with water and combined fractions were evaporated to dryness. TBDMS deprotection was performed by adding 300 μ L of *N*-methylpyrrolidone/triethylamine (TEA)/TEA*3HF 6/3/4/v/v/v and incubating at 65°C for 90 min. Precipitation with 1.2 mL butanol at -20°C and subsequent centrifugation yielded a pellet of crude oligonucleotide product.

The crude RNA was purified by AE-HPLC (A: water, B: 1 M LiCl; gradient: 0%–49% B for 30 min; flow 5 mL/min) on a JASCO LC-800. Further purification as well as concurrent desalting was typically accomplished by RP-HPLC (A: 1M TEAA buffer, B: water, C: acetonitrile; gradient: constant 10% A, 0%–45% C within

30 min; flow 4 mL/min) on a JASCO-2000 system including three times evaporation with water to remove buffering salt using a SpeedVac device.

Oligonucleotide concentrations were determined via UV spectrometry measurement on a nanodrop2000 (Thermo Scientific) applying the Lambert–Beer law. Extinction coefficients were determined by a nearest neighbor model according to the literature (Puglisi and Tinoco 1989; Gray et al. 1995). For that purpose, modified bases were considered correspondent to natural bases.

For all purification steps and resuspension, we used Milli-Q water that had been treated with 0.1% DEPC overnight and had been subsequently autoclaved.

The following oligonucleotides have been synthesized:

5'-GU XAG UCG CGC GCG CGC AUC-3' (X = spin-labeled C)
 3'-CA GUC AGC GCG CGC GCG UAG-5' (no overhang)
 3'-CA GUC AGC GCG CGC GCG UAG A-5' (5'-overhang)
 3'-ACA GUC AGC GCG CGC GCG UAG A-5' (3',5'-overhang)

EPR samples were prepared by resuspending the single strands in pure water, mixing the intended duplex of spin labeled oligonucleotide with counter strands with or without overhang and evaporation to dryness by SpeedVac. The oligonucleotide duplex was resuspended in buffer. Buffers used were phosphate buffer with different defined salt concentrations. Duplex concentration was set to 200 μ M in a total volume of 30 μ L if not otherwise stated. EPR samples contained 20% D8-glycol as cryoprotectant. For the determination of the intermolecular distances between the spin labels of dsRNA samples without overhang (Fig. 2) water was replaced by D₂O. This was necessary for increasing the transversal relaxation time T_2 of the spin label, allowing the recording of time traces with sufficient length. Before measurements, all samples were frozen in liquid nitrogen.

PELDOR methodology

The four-pulse PELDOR method was used to measure the distance between the spin labels and to measure the stacking probability of the dsRNA molecules. The pulse sequence is shown in Figure 1B. Pulses applied in PELDOR experiments have two distinct frequencies. The pump pulse frequency is typically set to be resonant with spins at the maximum of the nitroxide EPR spectra. This gives an optimal excitation efficiency λ , which depends on the applied microwave power and the chosen pulse length (for a π -pulse typically inversely related to the microwave power).

A refocused Hahn echo created by the probe pulses is used to monitor the magnetic dipole–dipole interaction between the nitroxide spins. The probe frequency is chosen 70 MHz below the pump frequency to avoid the pump and probe pulses affecting the same spins (typically called A and B spins affected by the probe and pump pulses, respectively). The flip of the B spin by the pump pulse shifts the Larmor frequency of the probed A spin, due to the dipolar spin–spin coupling. This reduces the intensity of the refocused Hahn echo, depending on the time Δt at which the pump pulse is applied. Recording the refocused Hahn echo intensity as a function of this time Δt results in the PELDOR time trace, which oscillates with the dipolar coupling frequency ω_{dd} .

PELDOR distances above 6 nm are challenging to measure, due to the limited observation time window of the four-pulse

PELDOR sequence. We also used a seven-pulse-Carr-Purcell (CP)-PELDOR sequence here, recently developed in our laboratory, to extend the time window of the PELDOR measurement (Spindler et al. 2015). In the seven-pulse-CP-PELDOR experiment, three refocusing π pulses are applied at the probe frequency (as depicted in Fig. 2F), leading to a slower decay of the transversal magnetization of the observed A spin. A matching number of pump pulses on spin B have to be used to obtain the maximum evolution time window for observation of the dipolar coupling. Sech/tanh pulses were used as pump pulses to suppress artifacts arising from the nonuniform inversion efficiencies of rectangular pulses. Nevertheless, a parameter describing the nonquantitative inversion of the adiabatic inversion pulses has to be taken into account when analyzing the seven-pulse-CP-PELDOR signals. Artifact and background corrections were performed as described before (Spindler et al. 2015) and are shown in the Supplemental Material.

The PELDOR time traces were analyzed in terms of distances and modulation depth after background division, which was performed using the DeerAnalysis software (Jeschke et al. 2006).

Q-Band measurements

A Bruker Elexsys E580X/Q-band spectrometer equipped with an Oxford CF935 cryostat and a phase unlocked PELDOR frequency unit was used. Microwave pulses were amplified by a 10 W solid-state Q-band amplifier. Thirty-two nanoseconds ($\pi/2$ and π)-pulses were used for detection and a 16 nsec (π) pump pulse was used for the four-pulse PELDOR experiments. The delay between the first and second probe pulse was 132 nsec. The frequency of the pump pulse was fixed to the intensity maximum of the nitroxide powder spectrum to obtain optimal pumping efficiency. The probe frequency was chosen to be 70 MHz below this frequency.

In the seven-pulse-CP-PELDOR experiment, a sech/tanh pulse with a pulse length of 400 nsec and a bandwidth of 60 MHz was used as the pump pulse. All experiments were carried out at a temperature of 50 K.

SUPPLEMENTAL MATERIAL

Supplemental material is available for this article.

ACKNOWLEDGMENTS

We acknowledge financial support from the German Research Foundation (CRC902: Molecular Principles of RNA Based Regulation). The authors thank Professor S. Sigurdsson for fruitful discussions and Dr. P. Spindler and Dr. A. Collauto for their contribution to the seven-pulse-CP-PELDOR experiments.

Received July 17, 2018; accepted November 6, 2018.

REFERENCES

Allahyarov E, Gompper G, Löwen H. 2004. Attraction between DNA molecules mediated by multivalent ions. *Phys Rev E Stat Nonlin Soft Matter Phys* **69**: 041904. doi:10.1103/PhysRevE.69.041904

Azarkh M, Okle O, Eyring P, Dietrich DR, Drescher M. 2011. Evaluation of spin labels for in-cell EPR by analysis of nitroxide reduction in

cell extract of *Xenopus laevis* oocytes. *J Magn Reson* **212**: 450–454. doi:10.1016/j.jmr.2011.07.014

Bode BE, Margraf D, Plackmeyer J, Dürner G, Prisner TF, Schiemann O. 2007. Counting the monomers in nanometer-sized oligomers by pulsed electron–electron double resonance. *J Am Chem Soc* **129**: 6736–6745. doi:10.1021/ja065787t

Brown RF, Andrews CT, Elcock AH. 2015. Stacking free energies of all DNA and RNA nucleoside pairs and dinucleoside-monophosphates computed using recently revised AMBER parameters and compared with experiment. *J Chem Theory Comput* **11**: 2315–2328. doi:10.1021/ct501170h

Endeward B, Butterwick J, MacKinnon R, Prisner TF. 2009. Pulsed electron–electron double-resonance determination of spin-label distances and orientations on the tetrameric potassium ion channel KcsA. *J Am Chem Soc* **131**: 15246–15250. doi:10.1021/ja904808n

Florián J, Šponer J, Warshel A. 1999. Thermodynamic parameters for stacking and hydrogen bonding of nucleic acid bases in aqueous solution: ab initio/Langevin dipoles study. *J Phys Chem* **103**: 884–892. doi:10.1021/jp983699s

Fonseca Guerra C, Bickelhaupt FM, Snijders JG, Baerends EJ. 1999. The nature of the hydrogen bond in DNA base pairs: the role of charge transfer and resonance assistance. *Chem Eur J* **5**: 3581–3594. doi:10.1002/(SICI)1521-3765(19991203)5:12<3581::AID-CHEM3581>3.0.CO;2-Y

Gellman SH, Haque TS, Newcomb LF. 1996. New evidence that the hydrophobic effect and dispersion are not major driving forces for nucleotide base stacking. *Biophys J* **71**: 3523–3526. doi:10.1016/S0006-3495(96)79547-4

Gray DM, Hung SH, Johnson KH. 1995. Absorption and circular dichroism spectroscopy of nucleic acid duplexes and triplexes. *Methods Enzymol* **246**: 19–34. doi:10.1016/0076-6879(95)46005-5

Grünewald C, Kwon T, Piton N, Förster U, Wachtveitl J, Engels JW. 2008. RNA as scaffold for pyrene excited complexes. *Bioorg Med Chem* **16**: 19–26. doi:10.1016/j.bmc.2007.04.058

Halbmaier K, Seikowski J, Tkach I, Höbartner C, Sezer D, Bennati M. 2016. High-resolution measurement of long-range distances in RNA: pulse EPR spectroscopy with TEMPO-labeled nucleotides. *Chem Sci* **7**: 3172–3180. doi:10.1039/C5SC04631A

Häse F, Zacharias M. 2016. Free energy analysis and mechanism of base pair stacking in nicked DNA. *Nucleic Acids Res* **44**: 7100–7108.

Hunter CA, Sanders JKM. 1990. The nature of π - π interactions. *J Am Chem Soc* **112**: 5525–5534. doi:10.1021/ja00170a016

Jeschke G, Chechik V, Ionita P, Godt A, Zimmermann H, Banham J, Timmel CR, Hilger D, Jung H. 2006. DeerAnalysis2006—a comprehensive software package for analyzing pulsed ELDOR data. *Appl Magn Reson* **30**: 473–498. doi:10.1007/BF03166213

Kilchherr F, Wachauf C, Pelz B, Rief M, Zacharias M, Dietz H. 2016. Single-molecule dissection of stacking forces in DNA. *Science* **353**: aaf5508. doi:10.1126/science.aaf5508

Krstić I, Frolov O, Sezer D, Endeward B, Weigand JE, Suess B, Engels JW, Prisner TF. 2010. PELDOR spectroscopy reveals preorganization of the neomycin-responsive riboswitch tertiary structure. *J Am Chem Soc* **132**: 1454–1455. doi:10.1021/ja9077914

Lipfert J, Doniach S, Das R, Herschlag D. 2014. Understanding nucleic acid-ion interactions. *Annu Rev Biochem* **83**: 813–841. doi:10.1146/annurev-biochem-060409-092720

Maffeo C, Schöpflin R, Brutzer H, Stehr R, Aksimentiev A, Wedemann G, Seidel R. 2010. DNA–DNA interactions in tight supercoils are described by a small effective charge density. *Phys Rev Lett* **105**: 158101. doi:10.1103/PhysRevLett.105.158101

Martin RE, Pannier M, Diederich F, Gramlich V, Hubrich M, Spiess HW. 1998. Determination of end-to-end distances in a series of TEMPO

- diradicals of up to 2.8 nm length with a new four-pulse double electron resonance experiment. *Angew Chem Int Ed Engl* **37**: 2833–2837. doi:10.1002/(SICI)1521-3773(19981102)37:20<2833::AID-ANIE2833>3.0.CO;2-7
- Mignon P, Loverix S, Steyaert J, Geerlings P. 2005. Influence of the π - π interaction on the hydrogen bonding capacity of stacked DNA/RNA bases. *Nucleic Acids Res* **33**: 1779–1789. doi:10.1093/nar/gki317
- Milov AD, Ponomarev AB, Tsvetkov YD. 1984. Electron-electron double resonance in electron spin echo: model biradical systems and the sensitized photolysis of decalin. *Chem Phys Lett* **110**: 67–72. doi:10.1016/0009-2614(84)80148-7
- Milov AD, Maryasov AG, Tsvetkov YD. 1998. Pulsed electron double resonance (PELDOR) and its applications in free-radicals research. *Appl Magn Reson* **15**: 107–143. doi:10.1007/BF03161886
- Nakata M, Zanchetta G, Chapman BD, Jones CD, Cross JO, Pindak R, Bellini T, Clark NA. 2007. End-to-end stacking and liquid crystal condensation of 6 to 20 base pair DNA duplexes. *Science* **318**: 1276–1279. doi:10.1126/science.1143826
- Oosawa F. 1968. Interaction between parallel rodlike macroions. *Biopolymers* **6**: 1633–1647. doi:10.1002/bip.1968.360061108
- Pabit SA, Qiu X, Lamb JS, Li L, Meisburger SP, Pollack L. 2009. Both helix topology and counterion distribution contribute to the more effective charge screening in dsRNA compared with dsDNA. *Nucleic Acids Res* **37**: 3887–3896. doi:10.1093/nar/gkp257
- Piton N, Mu Y, Stock G, Prisner TF, Schiemann O, Engels JW. 2007. Base-specific spin-labeling of RNA for structure determination. *Nucleic Acids Res* **35**: 3128–3143. doi:10.1093/nar/gkm169
- Pollack L. 2011. SAXS studies of ion–nucleic acid interactions. *Annu Rev Biophys* **40**: 225–242. doi:10.1146/annurev-biophys-042910-155349
- Puglisi J, Tinoco I. 1989. Absorbance melting curves of RNA. *Methods Enzymol* **180**: 304–325. doi:10.1016/0076-6879(89)80108-9
- Qiu X, Kwok LW, Park HY, Lamb JS, Andresen K, Pollack L. 2006. Measuring inter-DNA potentials in solution. *Phys Rev Lett* **96**: 138101. doi:10.1103/PhysRevLett.96.138101
- Qiu X, Andresen K, Kwok LW, Lamb JS, Park HY, Pollack L. 2007. Inter-DNA attraction mediated by divalent counterions. *Phys Rev Lett* **99**: 1–4.
- Romainczyk O, Endeward B, Prisner TF, Engels JW. 2011. The RNA–DNA hybrid structure determined by EPR, CD and RNase H1. *Mol Biosyst* **7**: 1050–1052. doi:10.1039/c0mb00258e
- Ryter JM, Schultz SC. 1998. Molecular basis of double-stranded RNA–protein interactions: structure of a dsRNA-binding domain complexed with dsRNA. *EMBO J* **17**: 7505–7513. doi:10.1093/emboj/17.24.7505
- Schiemann O, Piton N, Mu Y, Stock G, Engels JW, Prisner TF. 2003. A PELDOR-based nanometer distance ruler for oligonucleotides. *J Am Chem Soc* **126**: 5722–5729. doi:10.1021/ja0393877
- Schiemann O, Piton N, Plackmeyer J, Bode BE, Prisner TF, Engels JW. 2007. Spin labeling of oligonucleotides with the nitroxide TPA and use of PELDOR, a pulse EPR method, to measure intramolecular distances. *Nat Protoc* **2**: 904–923. doi:10.1038/nprot.2007.97
- Spaltenstein A, Robinson BH, Hopkins PB. 1989. Sequence- and structure-dependent DNA base dynamics: synthesis, structure, and dynamics of site, and sequence specifically spin-labeled DNA. *Biochemistry* **28**: 9484–9495. doi:10.1021/bi00450a036
- Spindler PE, Waclawska I, Endeward B, Plackmeyer J, Ziegler C, Prisner TF. 2015. Carr–Purcell pulsed electron double resonance with shaped inversion pulses. *J Phys Chem Lett* **6**: 4331–4335. doi:10.1021/acs.jpcllett.5b01933
- Šponer J, Bussi G, Krepl M, Banáš P, Bottaro S, Cunha RA, Gil-Ley A, Pinamonti G, Poblete S, Jurečka P, et al. 2018. RNA structural dynamics as captured by molecular simulations: a comprehensive overview. *Chem Rev* **118**: 4177–4338. doi:10.1021/acs.chemrev.7b00427
- Sturtevant JM, Rice SA, Geiduschek EP. 1958. The stability of the helical deoxyribonucleic acid (DNA) molecule in solution. *Disc Faraday Soc* **25**: 138–149. doi:10.1039/df9582500138
- van de Waal BW. 1986. Computed structure of small benzene cluster. *Chem Phys Lett* **123**: 69–72. doi:10.1016/0009-2614(86)87017-8
- Weinrich T, Gränz M, Grünewald C, Prisner TF, Göbel MW. 2017. Synthesis of a cytidine phosphoramidite with protected nitroxide spin label for EPR experiments with RNA. *Eur J Org Chem* **2017**: 491–496. doi:10.1002/ejoc.201601174
- Wong GC, Pollack L. 2010. Electrostatics of strongly charged biological polymers: ion-mediated interactions and self-organization in nucleic acids and proteins. *Annu Rev Phys Chem* **61**: 171–189. doi:10.1146/annurev.physchem.58.032806.104436

Supporting Information

‘End-to-End’ stacking of small dsRNA

Erlenbach, Nicole¹, Grünewald, Christian², Krstic, Bisera¹, Heckel, Alexander² and

Prisner, Thomas F.^{1,*}

¹ Institute of Physical and Theoretical Chemistry and Center of Biomolecular Magnetic Resonance,
Goethe University, D-60438 Frankfurt am Main, Germany

² Institute of Organic Chemistry and Chemical Biology, Goethe-University Frankfurt, D-60438 Frankfurt
am Main, Germany

4-PULSE PELDOR BACKGROUND CORRECTION	2
7-PULSE CP-PELDOR BACKGROUND CORRECTION	3
DETERMINATION OF MODULATION DEPTHS PARAMETER	4
DETECTION OF THE EXCITATION EFFICIENCY	6
STACKING PROBABILITY P AND DISSOCIATION CONSTANT K_D FOR SAMPLES WITH DIFFERENT RNA CONCENTRATIONS	7
CALCULATION OF STACKING PROBABILITY FOR SAMPLES WITHOUT OVERHANG	8

4-pulse PELDOR background correction

Original 4-pulse PELDOR time trace and the assumed non-specific background function for the time trace of Figure 2e in the manuscript is depicted in Figure S1.

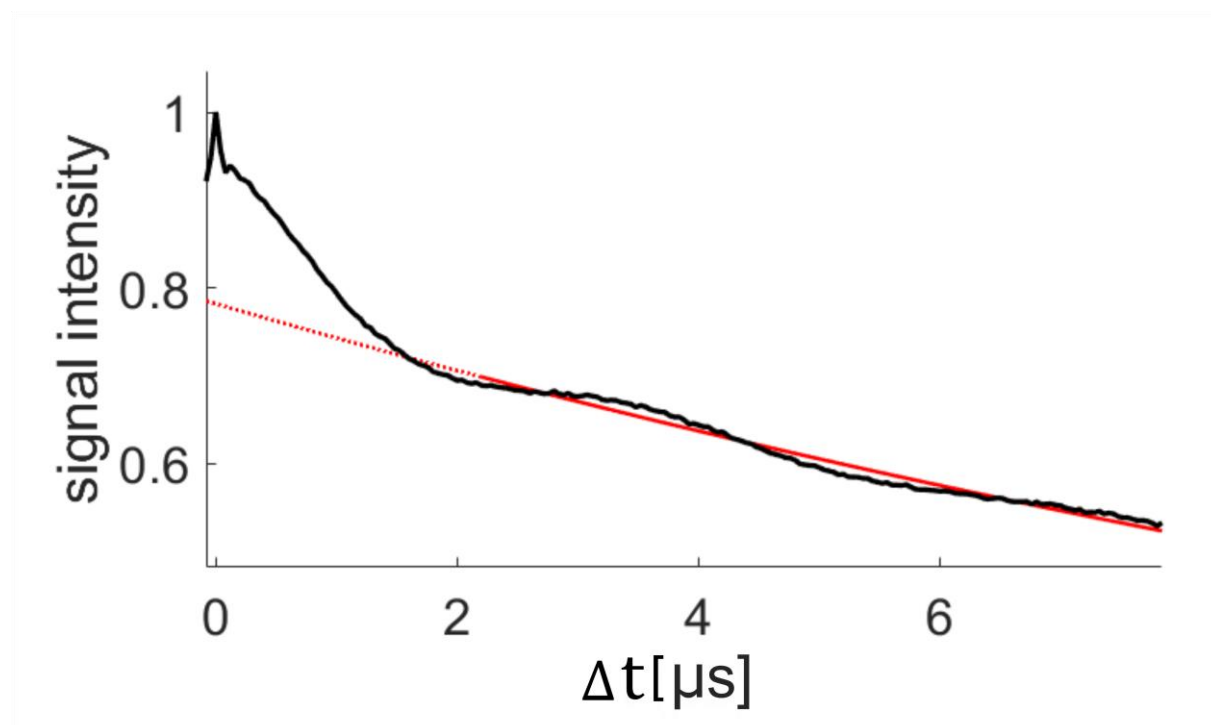


Figure S1 Background correction for the 4-Pulse PELDOR time traces of singly labelled dsRNA without overhang

7-pulse CP-PELDOR background correction

The 7-pulse CP-PELDOR experiments (Figure 2g) exhibit three inversion pulses for the coupled spin. Despite the fact that adiabatic sech/tanh inversion pulses are applied, the inversion efficiency is not perfect. This leads to unwanted signal contributions arising from spins where two or one of the inversion pulses only inverts the coupled spin. With our published procedure (Spindler et al. 2015) an undisturbed time trace (Figure 2h) can be derived. All correction steps to obtain the final dipolar time trace shown in Figure 2h are depicted in Figure S2.

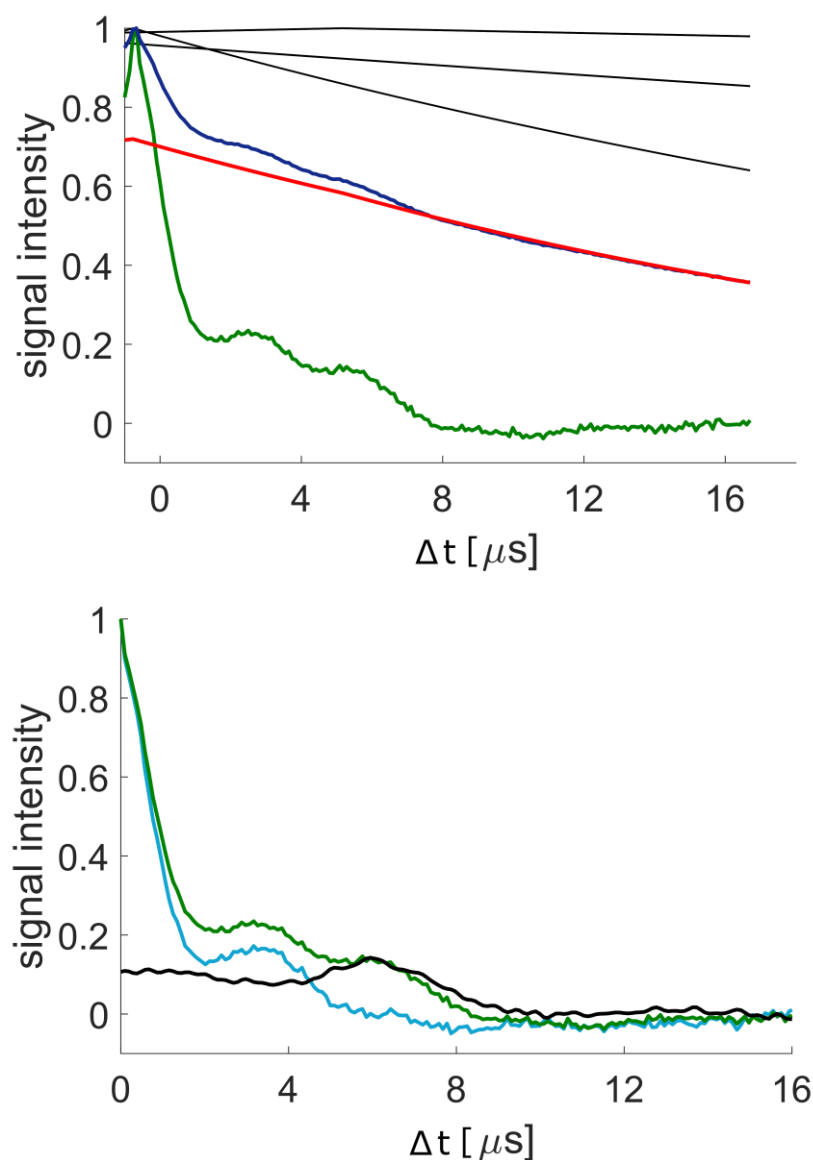


Figure S2 7-pulse CP-PELDOR data of singly labelled dsRNA without overhang. Top figure: The experimental raw time trace is shown in blue. In black are shown the decay functions for the different possible dipolar pathways. The product of all of them is shown in red. The background corrected dipolar signals after subtraction of the unmodulated part and renormalization is shown in green. Bottom figure: Background corrected PELDOR time trace in green and the artefact corrected time trace (light blue). The sum of all artefacts is shown in black.

Determination of modulation depths parameter Δ

The modulation depths reported in Figure 3 and 4 of the main text were extracted from the following raw PELDOR time traces (Figure S3).

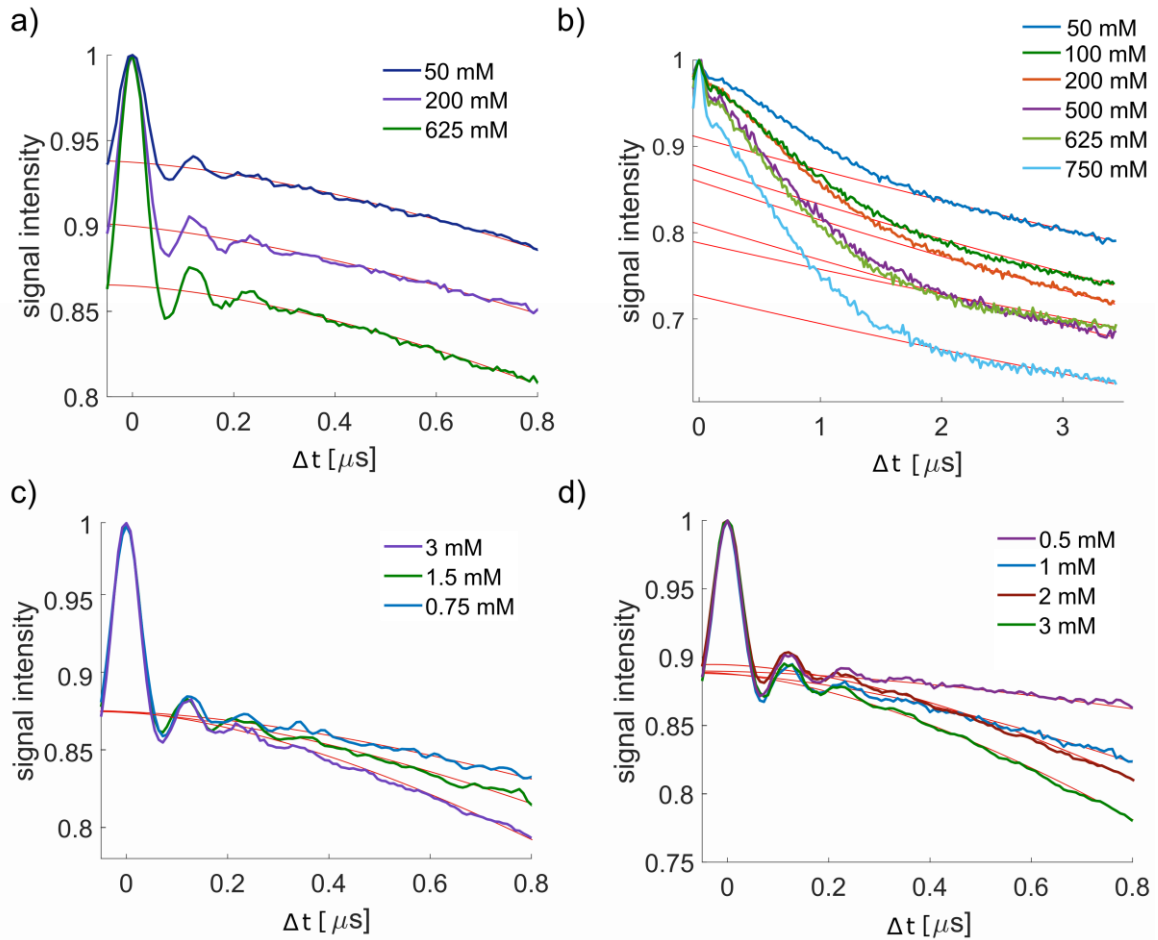


Figure S3 Raw 4-pulse-PELDOR traces of singly labelled dsRNA. a) Time traces of dsRNA samples with one nucleotide overhang for three different monovalent NaCl salt concentration as depicted in the figure legend. b) Time traces of dsRNA samples without any overhang for six different salt concentration as depicted in the figure legend. c) and d) Time traces of dsRNA samples with one nucleotide overhang for different RNA concentrations as depicted in the figure legends. c) Experiments for a salt concentration of 500 mM and d) for a salt concentration of 200 mM.

For short times $\Delta t < 0.8 \mu\text{s}$, the background deviated slightly from a straight exponential. Therefore, for the singly labelled dsRNA with one nucleotide overhang a higher dimensional ($D=4$) background was used. This higher dimensional background might be due to a very small remnant stacking probability between the protected ends or to an excluded volume effect. As demonstrated in Figure S4, such uncertainties in the determination of the background function does only very weakly influence the determination of the modulation depth parameter Δ . This uncertainty was taken into account and reflects the error bars of the stacking probabilities ρ shown in all figures.

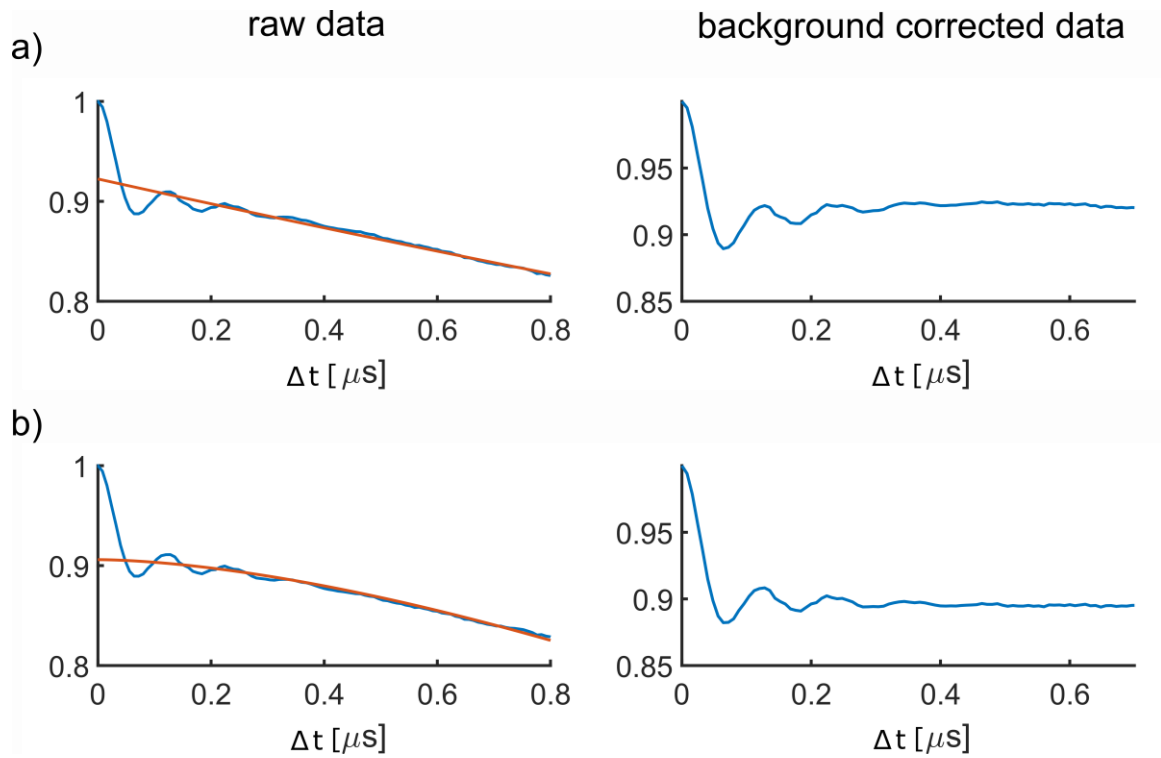


Figure S4 Background correction for the 4-pulse PELDOR time traces of singly labelled dsRNA with one overhang. On the left side, the original experimental data are shown in blue and the background in red. On the right side, the background corrected form factors are depicted. Background correction was done with DeerAnalysis in a) with a three dimensional background and in b) with a four dimensional background. As can be seen the chosen background dimensionality does only slightly affect the value for the modulation depth (<5%).

Detection of the excitation efficiency λ

To detect the excitation efficiency λ a nitroxide biradical (Schöps et al. 2015, structure depicted in Figure S5) was measured with the same pulse parameter than the dsRNA samples. As for the model compound all spins are quantitatively dipolar coupled, the modulations depth only depends on the excitation frequency. An excitation efficiency of 0.36 ± 0.05 was determined from three independent measurements (Figure S5).

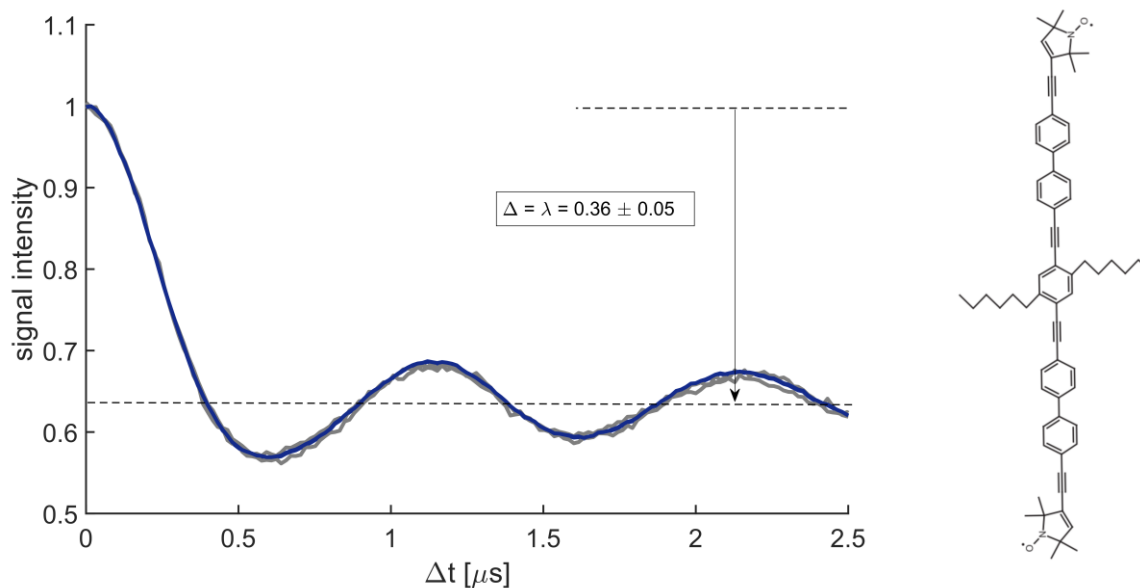


Figure S5 Three background corrected 4-pulse-PELDOR time traces (two shown in gray and one in blue) measured with the binitroxide model compound shown on the right.

Stacking probability p and dissociation constant K_d for samples with different RNA concentrations

To confirm that K_d only depends on the salt-to-RNA ratio R and not the absolute salt concentration, we have measured two samples with an equal salt-to-RNA ratio of 2000 but with different RNA concentrations. The signal time trace for the sample with higher RNA concentration (blue PELDOR time trace, Figure S6a) has an increased modulation depth Δ and therefore a higher stacking probability p compared to the time trace with lower RNA concentration (black curve). Both data points for p fit within experimental error to equation [5], described in the manuscript for a dissociation constant $K_d = 460 \mu\text{M}$. This dissociation constant was read-off from Figure 4b for a fixed salt-to-RNA ratio of $R=2000$.

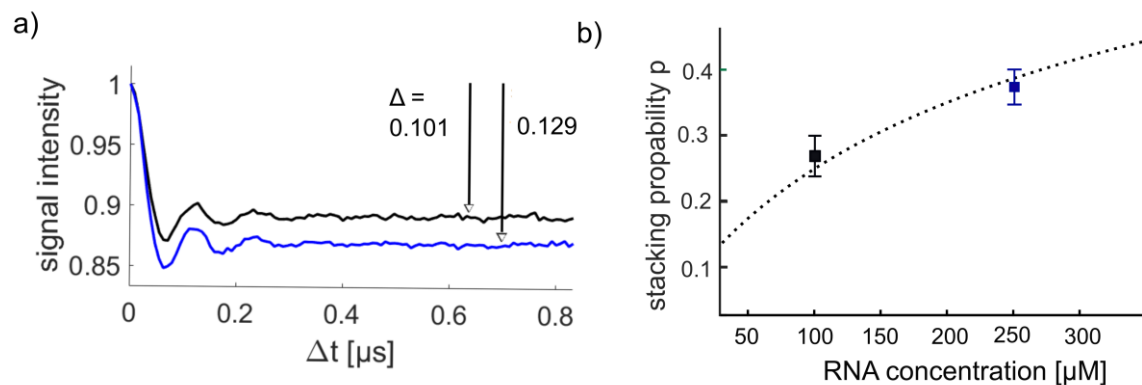


Figure S6 (a) PELDOR measurements with RNA duplexes having one overhang. Both samples are different in their RNA concentration but identical in their salt-to-RNA ratio. Black: $c(\text{RNA}) = 100 \mu\text{M}$; $c(\text{NaCl}) = 200 \text{ mM}$. Blue: $c(\text{RNA}) = 250$; $c(\text{NaCl}) = 500 \text{ mM}$ (b) Stacking probability of dsRNA in relation to the RNA concentration. The dotted line indicate the expected behaviour following equation [5] from the main text with a constant K_d of $460 \mu\text{M}$ (corresponding to a salt-to-RNA ratio of 2000, see Figure 4 main text).

Moreover it can be shown that also all the measurements with varying RNA concentrations (shown in the main text in Figure 5a) fall onto the curve $K_d(R)$ extracted from the measurements with varying salt concentration and a constant RNA concentration (Figure 4b main text). The results are shown in Figure S7.

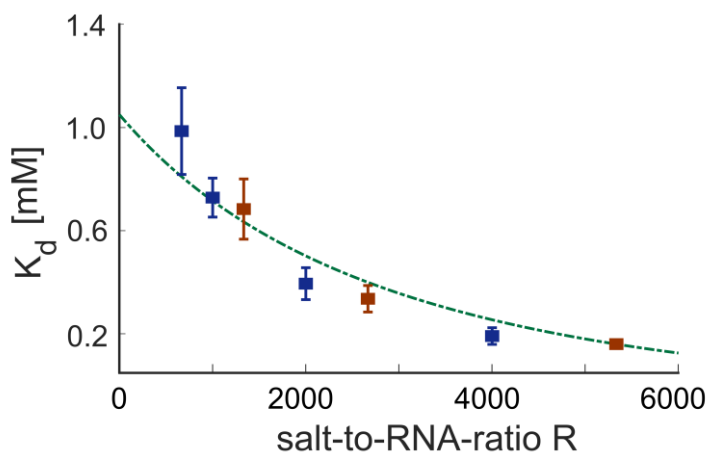


Figure S7 Dissociation constant K_d derived from experiments with different RNA concentrations and two constant salt concentration (200 mM NaCl (blue) and 500 mM NaCl (orange)). The dotted line is the K_d dependency on R extracted from measurements with a constant RNA concentration and different salt concentrations (Figure 4b of the main text).

Calculation of stacking probability for samples without overhang

For samples with one overhang, only dimerization of the dsRNAs is possible. However, dsRNAs without any overhang are able to form higher oligomers. As stated in the main text the modulation depth Δ depends on the excitation efficiency λ of the nitroxide spin label and the number of coupled spins n . If higher oligomers occur, more than two spin labels are coupled to each other. For n spins coupled, the modulation depth can be calculated to (Bode et al. 2005)

$$\Delta = 1 - (1 - \lambda)^{n-1} \quad [S1]$$

with λ being the excitation efficiency defined before.

The probability for a specific oligomeric state $P(n)$ depend on the stacking probability p of the dsRNA duplex and is given by:

$$P(n) = M p^{n-1} \quad [S2]$$

with M being the probability of the monomer. The normalization condition $\sum P(n)=1$ and the convergence of the geometric series leads to

$$P(n) = (1 - p)p^{n-1} \quad [S3]$$

Therefore, the overall modulation depth for dsRNA molecules without overhang can be written as:

$$\Delta = (1 - p) \sum_{n=1}^{\infty} (1 - (1 - \lambda)^{n-1}) p^{n-1} \quad [S4]$$

Again, the infinite sum can be written as two geometric series, leading to the following solution:

$$p = \frac{\Delta}{(\Delta + \lambda - \lambda \Delta)} \quad [S5]$$

The experimental modulation depth Δ for measurements with (blue) and without (green) overhangs are shown in Figure S8a. The resulting stacking probabilities p (Figure S8b) for samples with overhang can be calculated with $p=\Delta/\lambda$. For the samples without overhang, the stacking probability was calculated according equation S5. As can be seen, both samples lead to the same 'end-to-end' stacking probabilities p .

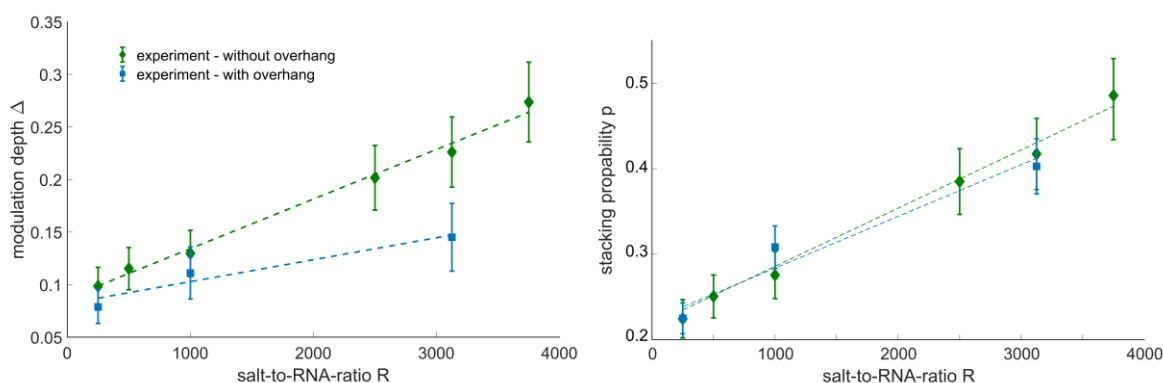


Figure S8 Dependence of the stacking probability to the salt-to-RNA ratio. Left side: Modulation depth Δ extracted from the PELDOR time traces. Green data points represents the measurements without overhang while the blue rectangles show the experiments from samples with one overhang. The error of the determined modulation depth was estimated to be 10 % (see above). Right side: Calculated stacking probabilities p for the samples with one overhang (blue) and without overhang (green). For the calculation of p the respective formulas were used (see above).

Literature

Bode BE, Margraf D, Plackmeyer J, Dürner G, Thomas F, Prisner A, Olav Schiemann. 2007. Counting the Monomers in Nanometer-Sized Oligomers by Pulsed Electron–Electron Double Resonance. *J Am Chem Soc* **129**: 6736–6745.

Schöps P, Spindler PE, Marko AM, Prisner TP. 2015. Broadband spin echoes and broadband SIFTER in EPR. *J Magn Res.* **250**: 55-62

Spindler PE, Waclawska I, Endeward B, Plackmeyer J, Ziegler C, Prisner TF. 2015. Carr–Purcell Pulsed Electron Double Resonance with Shaped Inversion Pulses. *J Phys Chem Lett* **6**: 4331–4335.

Orientation Selective EPR Measurements of RNA and DNA with Non-Covalent G Spin Label

Marcel Heinz,^{†,||} Nicole Erlenbach,^{‡,||} Lukas S. Stelzl,[†] Grace Thierolf,[‡] Snorri Th.
Sigurdsson,[¶] Thomas F. Prisner,^{*,‡} and Gerhard Hummer^{*,†,§}

[†]*Department of Theoretical Biophysics, Max-Planck-Institute of Biophysics,
Max-von-Laue-Straße 3, 60438 Frankfurt am Main, Germany*

[‡]*Institute of Physical and Theoretical Chemistry and Center of Biomolecular Magnetic Resonance,
Goethe University Frankfurt, Max-von-Laue-Straße 7, 60438 Frankfurt am Main, Germany*

[¶]*Department of Chemistry, Science Institute, University of Iceland,
Dunhaga 3, 107 Reykjavík, Iceland*

[§]*Institute for Biophysics, Goethe University Frankfurt, Max-von-Laue-Straße 1, 60438 Frankfurt
am Main, Germany*

^{||}*Contributed equally to this work*

E-mail: prisner@chemie.uni-frankfurt.de; gerhard.hummer@biophys.mpg.de

Abstract

Pulsed EPR experiments, among them most prominently pulsed electron-electron double resonance experiments (PELDOR/DEER), resolve the conformational dynamics of nucleic acids with high resolution. The wide application of these powerful experiments is limited by the synthetic complexity of some of the best-performing spin labels. The recently developed \dot{G} (G-spin) label, a isoindoline-nitroxide derivative of guanine, can be incorporated non-covalently into DNA and RNA via Watson-Crick base pairing in an abasic site. We used PELDOR and molecular dynamics (MD) simulations to characterize \dot{G} , obtaining excellent agreement between experiments and time traces calculated from MD of RNA and DNA double helices labeled with explicitly modeled \dot{G} . The MD simulations reveal stable hydrogen bonds between the spin label molecules and the paired cytosine. The abasic site has only minor influence on the helical structure. \dot{G} remains rigidly bound to helical RNA, but exhibits dynamics in helical DNA, which explains why strong orientation-selection is seen in PELDOR measurements on RNA but not DNA. Distance distributions are not substantially broadened by spin label motions and agree between experiment and MD. \dot{G} and similar non-covalently attached spin label, promise high-quality distance and orientation information, also for larger nucleic acid complexes.

Introduction

Pulsed EPR experiments can resolve the global structure characteristics and flexibility of nucleic acids with high resolution.¹ DNA and RNA carry the genetic information of the cell and RNA plays countless regulatory roles. The biological function of nucleic acids can often be understood by elucidating their structure and dynamics. Pulsed EPR experiments and in particular pulsed electron-electron double resonance experiments² (PELDOR also referred to as DEER) complement structure determination by X-ray crystallography,³ nuclear magnetic resonance (NMR)⁴⁻⁶ and Cryo-EM experiments.^{7,8} PELDOR provides highly

accurate information on distances and angles even in highly dynamic systems, where traditional structure determination is not possible, reporting also on the conformational flexibility of proteins and nucleic acids. Typically, PELDOR experiments require the introduction of a pair of spin labels. The nature of the spin label is a critical issue. Flexible spin labels complicate the determination of high-resolution distances⁹ and do not permit the extraction of angular information. By contrast, the rigid spin label ζ ^{10,11} (C-spin) enables highly accurate distance and angle measurements on, e.g., DNA. However, the synthesis of the ζ itself and especially ζ labeled nucleic acids remains difficult, limiting the wide applicability of high-resolution pulsed EPR experiments on nucleic acids.

A number of different spin labels were developed in the last years,¹²⁻¹⁵ but there is still a lack of spin labels that can be employed with little synthetic effort. One way to reduce the synthetic effort, which is particularly relevant for larger nucleic acids of biological interest, is to incorporate the spin label non-covalently. There, the challenge is to achieve high-affinity and high specificity binding to the nucleic acid target molecule.¹⁶⁻¹⁸ Only recently we were able to show that the \hat{G} (G-spin) incorporates with high affinity and specificity into abasic sites in double-stranded RNA (dsRNA) and dsDNA.¹⁹ Furthermore, first measurements of labeled dsRNA revealed orientation selection in the measured PELDOR time traces, which permits the extraction of angular information. However, use of this labels for the analysis of nucleic acid structure and flexibility requires an understanding of the detailed structure and dynamics.

Molecular dynamics (MD) simulations can provide a deeper understanding of the impact of non-native residues on nucleic acid structure and dynamics. It has been shown, that native DNA,²⁰ as well as larger photolabile protecting groups covalently attached at DNA bases,²¹ can be well described by state-of-the art MD simulations. For RNAs, despite the fact that current RNA force fields do not fully reflect experimental observations for single-stranded RNAs,²² native and protonated bases in double stranded RNAs are described well.²³⁻²⁶ Short MD simulations of a covalently attached EPR spin label (TEMPO)

in RNA double helices were already compared with experimentally determined distance distributions and revealed promising agreement.²⁷

With the methods on hand to calculate the PELDOR time traces from MD simulation^{1,28} and to explicitly model the spin-label in the MD simulations of DNA and RNA for a direct comparison with PELDOR experiments, we elucidate the influence of the non covalently attached $\dot{\text{G}}$ on dsRNA and dsDNA structure and dynamics. Conversely, we validate state of the art nucleic acid force fields with the new PELDOR data.

Results

The spin label $\dot{\text{G}}^{19}$ consists of an isoindoline derivative with an aminoxyl radical and an aromatic purine scaffold part (Fig. 1C). Both geometrical planes are connected via a rotatable nitrogen bridge, which allows a rotation with respect to each other. A DFT relaxed surface scan of the dihedral angle $\mathbf{d1}$ (depicted in Fig 1C , marked in red) was done at B3LYP-GD3BJ/cc-pVTZ and PBE0/N07D level of theories (s. Fig. 1B). Both scans reveal a global minimum at 0° and a local minimum at 180° , indicating two favored conformations of the $\dot{\text{G}}$ molecule in the gas phase without the nucleic acid.

We then proceeded to study the conformations of $\dot{\text{G}}$ in a double stranded DNA (dsDNA) helix and found it to be stably incorporated. During 1 μs of Molecular Dynamics (MD) simulation the purine end of the $\dot{\text{G}}$ molecule is located at the position of a native guanine base and forms hydrogen bonds with the corresponding cytidine in the complementary strand, mimicking a native base (s. Fig. 2). An additional hydrogen bond was observed between the nitrogen (N9) of the $\dot{\text{G}}$ molecules and the oxygen (O4') of the abasic site. The isoindoline aminoxyl radical end of the $\dot{\text{G}}$ molecule is positioned inside the minor groove of the helix.

The abasic sites and $\dot{\text{G}}$ molecules slightly perturb the helical dsDNA structure and its dominant dynamics. Individual averages over all characteristic backbone torsion angles

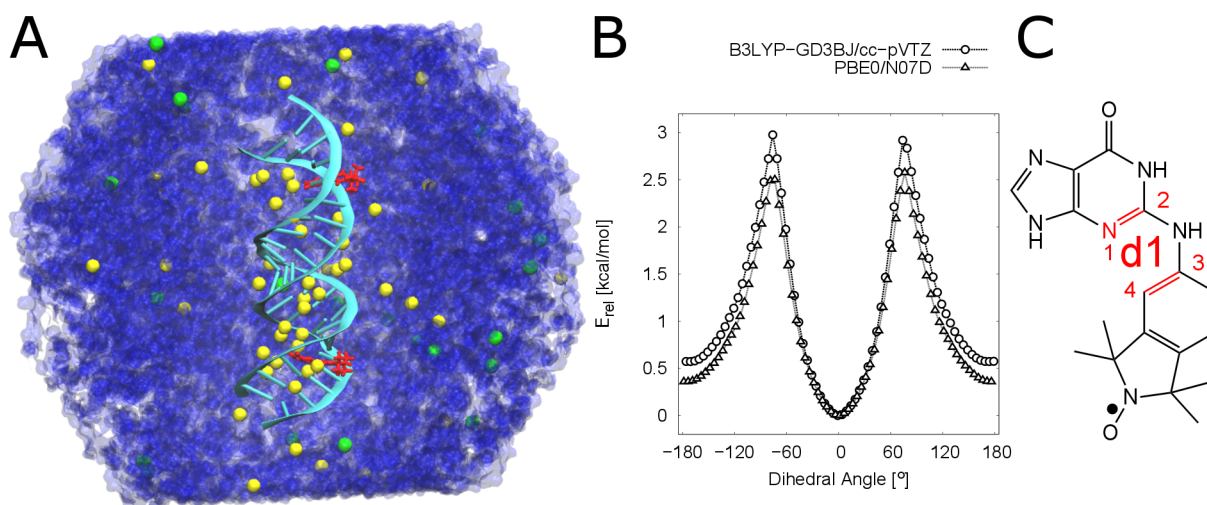


Figure 1: (A) Simulation system with two \dot{G} molecules (red) incorporated in the RNA helix (lime), solvated in a periodic truncated octahedral box of water (blue) with Na^+ (yellow) and Cl^- ions (green). (B) DFT relaxed surface scans of the dihedral angle $\mathbf{d1}$ in the \dot{G} molecule at B3LYP-GD3BJ/cc-pVTZ and PBE0/N07D level of theories. The scans reveal two energetical minima orientations of the aromatic purine scaffold to the covalently attached isoindoline nitroxide at 0° and 180° in vacuo. Energies are relative to the minimum energy structure of each scan. (C) Lewis structure of the \dot{G} molecule corresponding to a dihedral angle $\mathbf{d1}$ of 0° (syn), the global minimum.

were calculated for a native dsDNA and the complementary \dot{G} labeled dsDNA. The difference between the dihedral angles reveal fluctuation of the ζ torsion angle of up to 35° close to the spin label position or -27° directly at the spin label position (s. Fig. 3A). The δ torsion angle of the corresponding cytidine in the complementary strand is also perturbed with a deviation up to 32° . Visual inspection of the MD trajectory reveal that the abasic site sometimes rotates slightly out of a native-like helix structure. However, the overall helical structure stays intact during these short events. The heavy-atom position RMSD of the \dot{G} -labeled dsDNA to an ideal B-helical structure is only $\approx 1 \text{ \AA}$ larger than for a native dsDNA simulation (Fig. 3B).

The spin flexibility does not significantly impact spin-spin distance distributions, which agree well with the PELDOR experiments. Single rotations in the MD simulation around the dihedral angle $\mathbf{d1}$ in both \dot{G} molecules were observed (Fig. 4A), capturing three out of four possible states, i.e. (i) both \dot{G} molecules in syn configurations (syn-syn), (ii) one

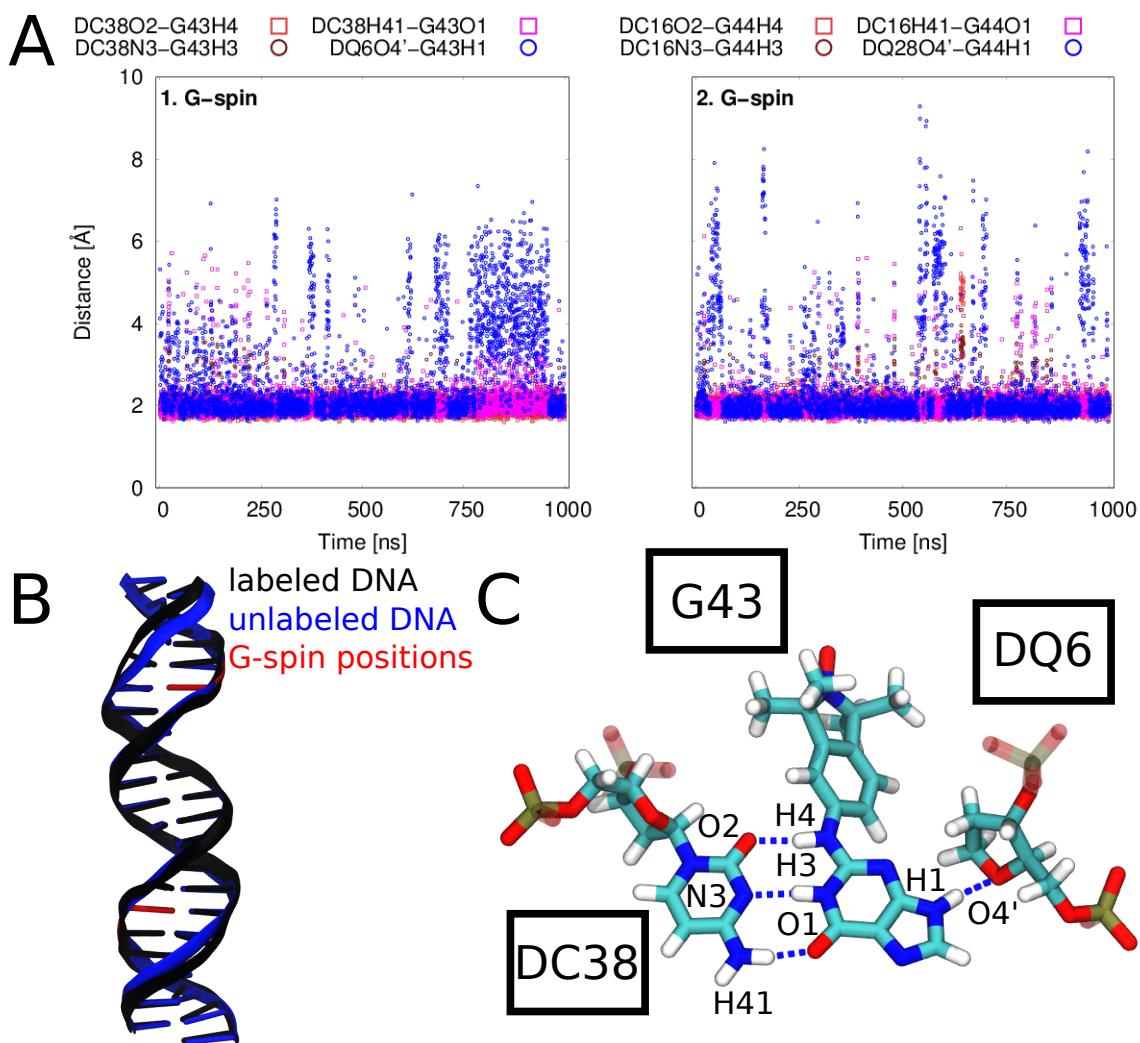


Figure 2: Hydrogen bonds between the two \hat{G} molecules and the complementary cytidines and the abasic sites in dsDNA. (A) The three stable Watson-Crick H-bonds are shown with their distances during the simulations (1. G-spin: DC38O2-G43H4, DC38H41-G43O1, DC38N3-G43H3; 2. G-spin: DC16O2-G44H4, DC16H41-G44O1, DC16N3-G44H3). Additional hydrogen bonds between \hat{G} molecules and the O4' of the abasic sites are depicted in blue and remain stable within the simulations (1. G-spin: DQ6O4'-G43H1; 2. G-spin: DQ28O4'-G44H1). (B) Average structures of the labeled and native dsDNA simulations. The position of the \hat{G} molecules and abasic sites are depicted in red at the native structure. (C) H-bonds between \hat{G} (G43), the abasic site (DQ6) and the cytidine (DC38) are depicted in dashed lines.

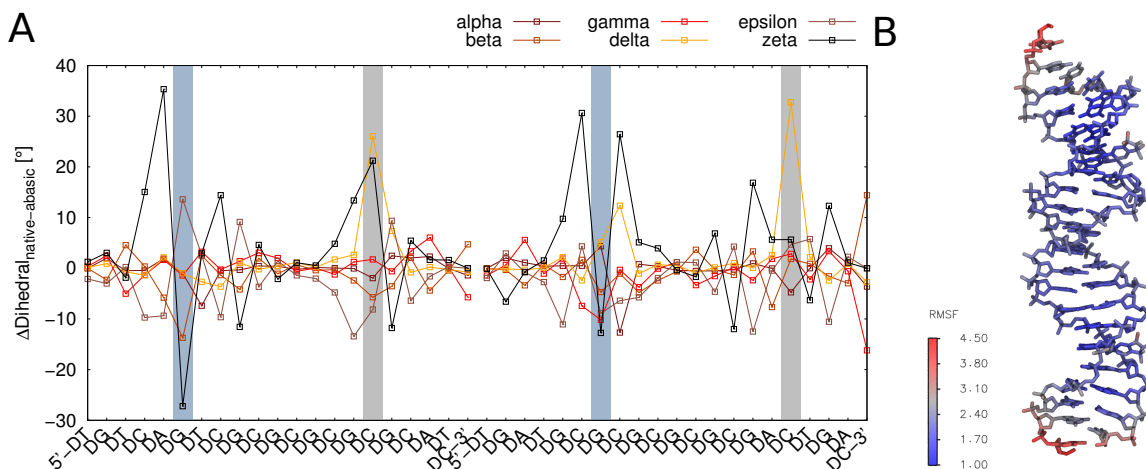


Figure 3: Structural and dynamical differences between native and \dot{G} labeled DNA. (A) difference of the average backbone dihedral angles in native and labeled DNA. Abasic sites (6,28) are highlighted in gray and the corresponding residue in the complementary strand (16,38) in light-gray. (B) Heavy atom position RMSF of the labeled MD simulation with respect to an ideal A-helical structure.

molecule has rotated into anti configuration (anti-syn) and (iii) both spin labels have rotated into anti configuration (anti-anti). A syn to anti rotation inside the minor groove reveal the parallel orientation of the isoindoline plane to the backbone (Fig. 4B). To compare the MD simulation with the PELDOR data, the experimental interspin distance distribution was extracted via a Tikhonov regularisation over the sum of all X-band (0.3 T/ 9 GHz) time traces of the orientation selective PELDOR data, following the protocol from Prisner et al.²⁹ The distance distribution is still very narrow and the different rotational states are indistinguishable within the overall distance distribution (s. Fig. 5C). The summed PELDOR traces show a distinct oscillation frequency (s. SI), revealing a narrow distance distribution. This distribution show a main population at 37.2 Å with a small shoulder at 33.9 Å, whereas the MD simulation reveals a major population centered around 36.8 Å with almost exact overlap to the experimental distribution (s. Fig. 5C). A comparison between the covalently attached and rigid spin label \dot{C}^1 to the non-covalently attached \dot{G} molecule at the same dsDNA sequence do not show a broadening in the inter spin distance distribution (FWHM: \dot{C} 0.633 nm to \dot{G} 0.675 nm) as determined by Tikhonov regularisation from the experimental data.

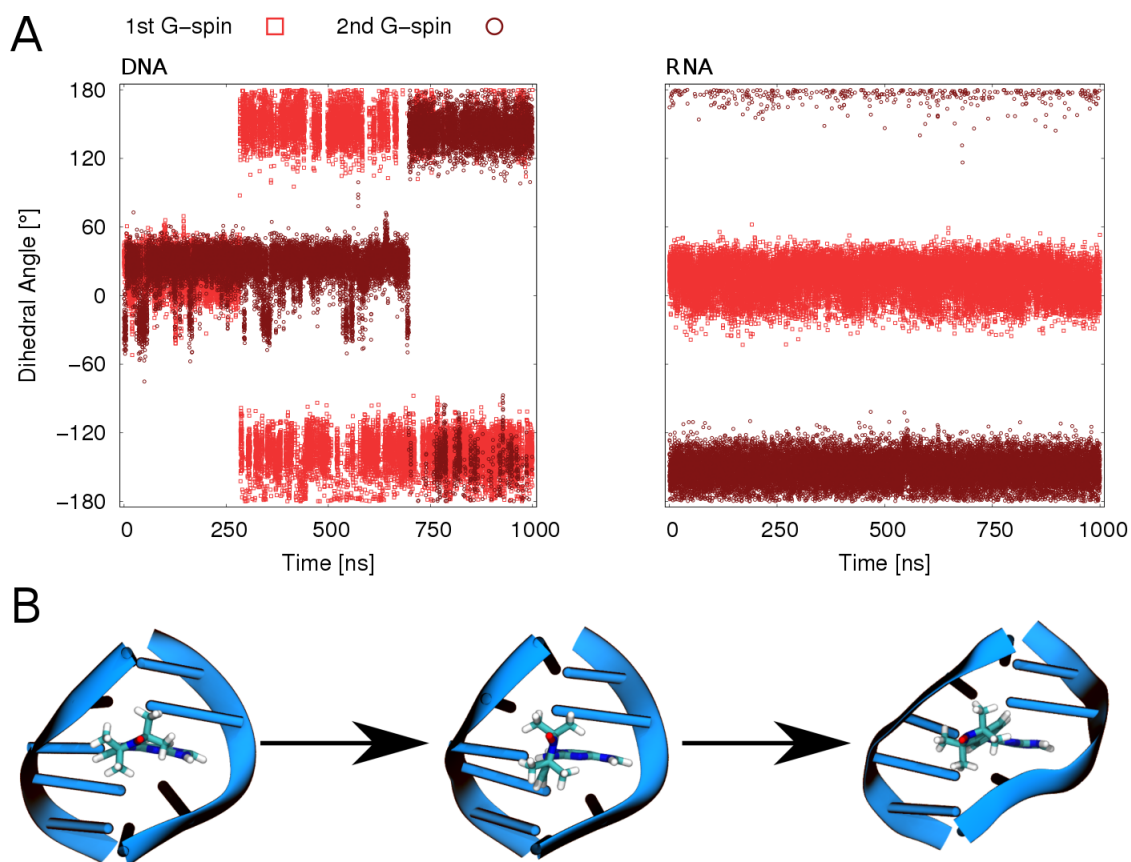


Figure 4: (A) Dihedral angle $d1$ between the aromatic purine scaffold and the isoindoline nitroxide plane of the two \dot{G} s in DNA and RNA during the molecular dynamic simulations. (B) Core bases around one \dot{G} in dsDNA with an observed rotation from syn to anti conformation of dihedral angle $d1$.

Low field X-band (0.3 T/ 9 GHz) measurements are dominated by the hyperfine anisotropy, i.e., by the axis perpendicular to the nitroxide plane (z-component (s. Fig. 5A,D)), revealing the out-of-plane orientations of the spin labels with respect to each other. Since the PELDOR time traces measured with different frequency offsets are identical in their dampening and oscillation frequency, there are no orientation selective effects observable, meaning no distinct out-of-plane orientation for the \dot{G} molecule, which goes in line with the observed rotations in the MD simulations. High field G-band (180 Ghz/6.4 T) data are dominated by the fully resolved g-tensor of the electron Zeeman interaction of the electron spin to the nitrogen spin, resolving additionally the in-plane orientations of the nitroxide planes (i.e., x- and y-components s. Fig.5D). The rotations around the dihedral angle $\mathbf{d1}$ does not change the spatial position of the spin label, and with it the x- and y- orientation of the spin label to each other. Therefore the rigidity of the spin label is still preserved, resulting in orientation selection effects in the measured G-band PELDOR time traces, i.e, differences in dampening and oscillation frequency in the PELDOR traces measured at different field positions (s. Fig. 5B).

A quantitative comparison of the measured and calculated PELDOR time traces for dsDNA shows excellent agreement. The PELDOR time traces are directly calculated^{1,28} from the coordinates of the spin labels of the MD simulation and compared to the measured PELDOR time traces (s. Fig. 5A,B). The low field X-band and high field G-band PELDOR time traces are excellently captured in the MD simulation, suggesting that the simulation reflects the observed experimental behavior and that latest DNA force fields describe B-helix dynamics well.¹

The MD simulation of two \dot{G} molecules non-covalently attached into a double stranded RNA (dsRNA) helix reveal an intact helical structure (s. Fig. 1A). Structurally, the \dot{G} molecule shows similar behavior in dsRNA as in dsDNA. The purine parts of the \dot{G} molecules are located inside the A-helix, forming hydrogen bonds to the complementary cytidine in the opposite strand, mimicking a similar behavior as a native guanine base (s.

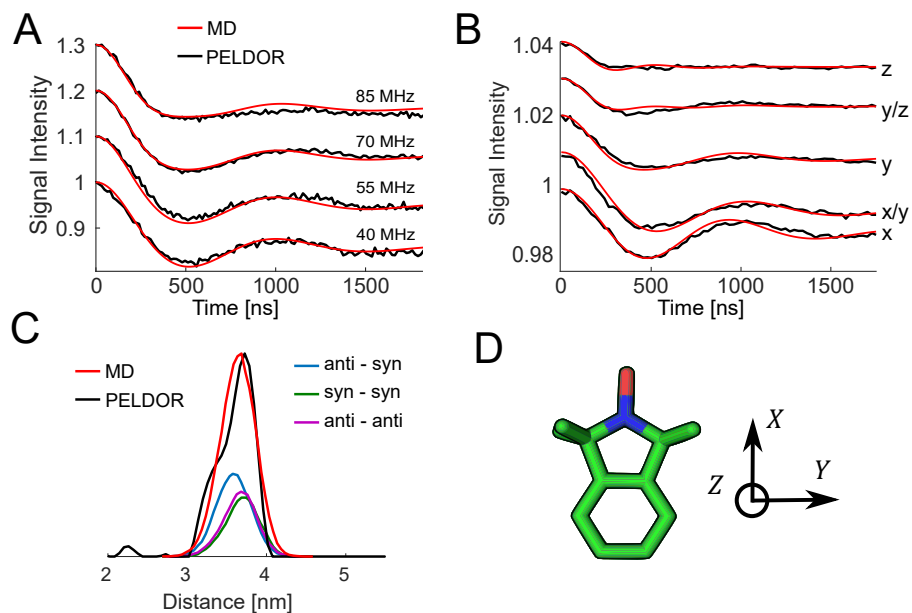


Figure 5: Comparison of PELDOR signals calculated from MD (red) to experiments (black) for DNA(1,10). (A) PELDOR time traces measured at X-band with different offsets ν_n between probe and pump pulse frequency from 40 MHz (lower time trace) to 85 MHz (upper time trace). (B) PELDOR time traces measured at G-band at different field positions with a constant offset of 60 MHz. The field positions are corresponding to $B \parallel g_{xx} - B \parallel g_{zz}$ (C) Distance distribution from PELDOR measurements obtained by Tikhonov regularisation (black) and distance from the MD simulation (red) and the corresponding populations with respect to the dihedral angle $\mathbf{d1}$ of both $\dot{\mathbf{G}}$ molecules. (D) Axis system of a nitroxide spin label.

Fig. 6). A hydrogen bond is additionally formed between the purine nitrogen (N9) and the oxygen (O4') of the abasic site sugar, where more fluctuations are observed than in dsDNA. The isoindoline aminoxyl radical part points into the minor groove, as already proposed previously.¹⁹

The abasic sites and \dot{G} molecules do not significantly effect the overall dsRNA structure and dominant dynamics. The backbone torsion angles of the dsRNA were calculated for a native dsRNA and \dot{G} molecule labeled dsRNA simulation. The differences between native and labeled dsRNA in each individual torsion angle reveal a small perturbation directly at the abasic site and the corresponding cytidine in the complementary strand (s. Fig. 7A). Nonetheless, the overall structure stays intact and the perturbation is negligibly small with an overall heavy atom position RMSD to an ideal A-helix of $3.3 \pm 0.7 \text{ \AA}$ compared to a native dsRNA simulation with an RMSD of $2.9 \pm 0.7 \text{ \AA}$ (s. Fig. 7B).

Within the MD simulation time of $1 \mu\text{s}$ no rotations of the \dot{G} around the dihedral angle **d1** were observed (Fig. 4), explaining the orientation selection observed in low field PELDOR experiments (s. Fig. 8). The differences in damping of the X-band PELDOR time traces give a strong evidence for a highly preserved out-of-plane orientation of the \dot{G} in dsRNA. Also in the high field G-band data, strongly pronounced orientation-selective effects could be measured (s. Fig. 8). Both orientation selections are strongly supported with the observed rigidity of the spin labels in the MD simulations of doubly labeled dsRNA, without a rotation around dihedral angle **d1**.

Comparison of measured and calculated PELDOR time traces, and the interspin distances for labeled dsRNA show very good agreement. Excellent agreement is achieved for the low field X-band data (s. Fig. 8). The high field G-band reveal a good agreement in the in-plane orientation in the measured and calculated PELDOR time traces. The extracted distance population of the PELDOR data have a main distance population at 37.5 \AA , while the direct extracted distances from the MD simulation tend to longer distances with a main population at 38.9 \AA . The small difference between experiment and simulation of labeled

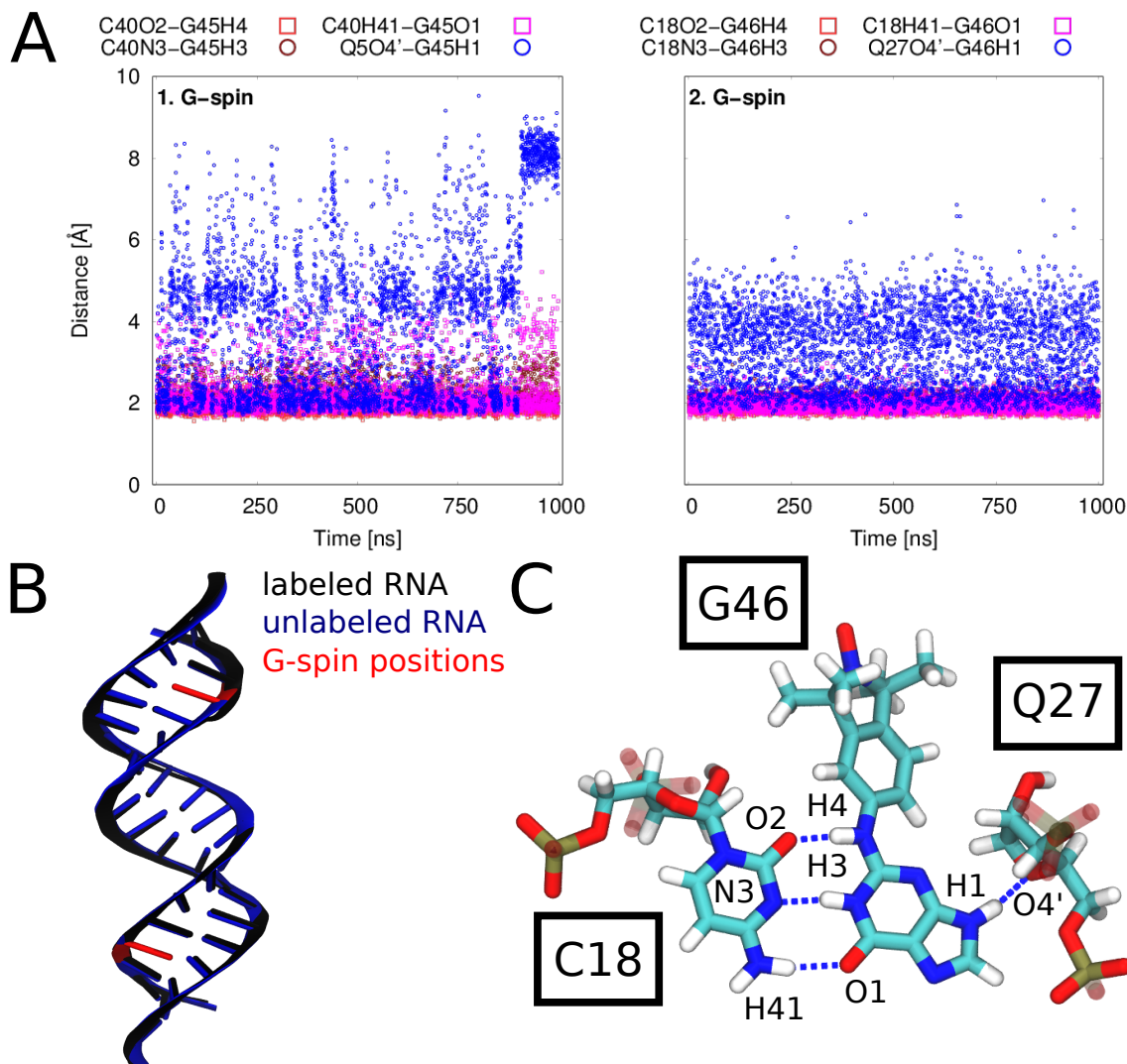


Figure 6: Hydrogen bonds between the two \hat{G} molecules and the complementary cytidines and the abasic sites in dsRNA. (A) The three stable Watson-Crick H-bonds are shown with their distances during the simulations (1. G-spin: C40O2-G45H4, C40H41-G45O1, C40N3-G45H3; 2. G-spin: C18O2-G46H4, C18H41-G46O1, C18N3-G46H3). Additional hydrogen bonds between \hat{G} molecules and the O4' of the abasic sites are depicted in blue and remain stable within the simulations (1. G-spin: Q5O4'-G45H1; 2. G-spin: Q27O4'-G46H1). (B) Average structures of the labeled and native dsRNA simulations. \hat{G} molecule and abasic site positions are depicted in red at the corresponding native structure position. (C) Involved H-bonds between \hat{G} (G46), the abasic site (Q27) and the cytidine (C18) are depicted in dashed lines.

dsRNA of 1.8 Å is still remarkably good. The comparison to PELDOR, which reports on long-range distances and angles, shows that the structure and dynamics of RNA A-helices are described well by the ParmBSC0+ χ_{OL3} force field.

Discussion

The comparison between our MD simulations and PELDOR experiments on $\dot{\mathbf{G}}$ labeled dsRNA and $\dot{\mathbf{G}}$ labeled dsDNA reveal that both systems are highly suited for further distance measurements using PELDOR. The simulated $\dot{\mathbf{G}}$ molecule distance distributions are on par with the PELDOR experiment in dsDNA and in excellent agreement for dsRNA. In both labeled nucleic acid helices, the helical structure remained intact. Small, local perturbations are introduced into the system with the abasic site and the $\dot{\mathbf{G}}$ molecule, which were very small in dsDNA and almost negligible in dsRNA. Both helices kept the $\dot{\mathbf{G}}$ molecules at their corresponding purine positions while for the $\dot{\mathbf{G}}$ molecule itself, intramolecular rotations around the dihedral angle $\mathbf{d1}$ were only observed in dsDNA. These rotations explain the absence of orientation selectivity in PELDOR experiments of the $\dot{\mathbf{G}}$ in dsDNA. By contrast, $\dot{\mathbf{G}}$ has a distinct orientation selection in dsRNA. A projection of the labeled trajectory onto the eigenvectors of the native trajectory demonstrate that the dominant helical motions, i.e., bending, are almost unperturbed with a slightly more prominent perturbation in dsDNA than in dsRNA. Interestingly, the non covalently attached $\dot{\mathbf{G}}$ molecule does not significantly effect the width of the distance distribution and is comparable to a completely rigid and covalently attached spin label $\dot{\mathbf{C}}$,¹ which requires a much higher synthetic effort to incorporate in nucleic acids.

The direct comparison to PELDOR measurements provides highly accurate information to evaluate current state of the art force fields for nucleic acids. Both force fields, ParmBSC1 for DNA and ParmBSC0+ χ_{OL3} for RNA, are able to describe double stranded, helical nucleic acids well. For dsDNA there is almost no difference discernable between the

experimental PELDOR data and PELDOR time traces computed from the MD simulation. The excellent agreement for ParmBSC1 confirms our previous conclusion that state-of-the-art force fields (including OL15) describe the dynamics of dsDNA well.¹ By contrast, the discrepancies between experiment and simulation were somewhat larger for dsRNA, though still small. The well-established ParmBSC0+ χ_{OL3} force field for RNA seems to describe the dynamics of dsRNA well. The MD interspin distance distribution is slightly shifted by 1.8 Å towards longer distances and the calculated PELDOR time traces from the MD simulations matches well with the PELDOR data, but further improvement is possible. As new RNA force fields are developed, we envisage that PELDOR data will provide a valuable reference for validation by providing highly accurate long-range distance information.

Computational Details

Relaxed surface scans of the dihedral angle $\mathbf{d1}$ in the \mathbf{G} molecule were performed using the Gaussian09 program package³⁰ at a PBE0/N07D^{31,32} level of theory, which was used in previous nitroxide studies.¹ An additional relaxed surface scan was performed with a dispersion correction (GD3BJ³³), an increased basis set of triple- ζ quality (cc-pVTZ³⁴) and the more commonly used B3LYP³⁵ functional. The dihedral angle between the aromatic purine scaffold and the isoindoline nitroxide plane was scanned with a step size of 5° in forward and backward direction. The final energy surface was constructed with the lowest energy for a given point in forward or backward direction.

MD simulations were performed with the Amber16 program package.³⁶ Native nucleic acid helices were constructed with the Nucleic Acid Builder (NAB³⁷). Double stranded RNA (5'-CGAGGAUCGCGCGCGAUCUCG-3') was built in the characteristic A-helical form. The dsDNA was constructed in B-helical form with an additional T base overhang at the 5' end of each strand (i.e., 5'-TGTCAGTCGCGCGCGCGCATC-3' and 5'-

TGATGCGCGCGCGCGACTGAC-3'). Partial charges of the abasic site were newly determined, based on a restrained electrostatic potential fit (RESP³⁸) as implemented in the R.E.D. Tools Version III.52.³⁹ Therefore, the abasic site was saturated with a methoxy group at the phosphate group at the 5' end. An additional monomethyl phosphate group was attached at the 3' oxygen, resulting in a net charge of -2 e. The partial charges of the abasic moiety atoms were determined and the additional attached substituents removed, afterwards. To obtain a net charge of -e at the abasic site, the remaining charges were distributed over all remaining atoms in this residue. The new partial charges were assigned to the abasic site (SI). Native and abasic site for DNA were described with the parmbsc1 force field⁴⁰ and RNA residues were described with the parmbsc0 force field including the χ_{OL3} correction.⁴¹⁻⁴³ The \hat{G} molecule is described with GAFF,⁴⁴ following the parameterization work flow as stated elsewhere⁴⁵ (SI).

The MD system was prepared with the tleap module as part of the AmberTools14 program package.⁴⁶ A layer of at least 15 Å TIP3P water⁴⁷ molecules separated the solute from the edges of the periodic, truncated octahedral box. System was neutralized and additional NaCl⁴⁸ was added to mimic a salt concentration of 100 mM. The system contained approximately 60,000 atoms in the RNA simulations and approximately 68,000 atoms in the DNA simulations.

After energy minimization and equilibration (s. SI), production runs were performed using the pmemd.cuda engine in Amber16. Continuous trajectories of 1 μ s length were simulated for RNA and DNA in 10 ns segments, where coordinates, velocities and box information were taken from the previous run. The written out coordinates were wrapped into a primary box. Temperature was kept at 300 K using Langevin dynamics ($\gamma = 1.0$ ps⁻¹). To prevent the simulation for "synchronization" artifacts,⁴⁹ caused by the thermostat, a random seed was set at every restart, which affects the set of pseudo-random values used for Langevin dynamics. Covalent bond lengths of hydrogen atoms were maintained with the SHAKE⁵⁰ algorithm. The pressure was kept at 1 atm with isotropic position scaling

and a relaxation time of 2 ps for the Berendsen barostat.⁵¹

Due to the limited number of atom types in the general amber force field (GAFF), the \dot{G} nitroxide atoms (N–O) are not optimally described, i.e., the oxygen atom was always out-of the isoindoline plane during the MD simulations. The oxygen was therefore virtually positioned in the isoindoline plane for the presented analysis and comparison of the MD to PELDOR data.

The covariance matrix of the atom fluctuations and the corresponding eigenvectors and eigenvalues were computed with the GROMACS (version 5.1.3⁵²) program `gmx covar`. Afterwards, the trajectories were projected onto the eigenvectors using `gmx ana eig`.

X-band measurements

A Bruker Elexsys E580 X/Q-band spectrometer equipped with an Oxford CF935 cryostat was used with a Bruker MS3 3mm loop gap resonator. Microwave pulses were amplified by a 1 kW Travelling Wave Tube (TWT). 32 ns ($\frac{\pi}{2}$ and π)-pulses were used for detection and a 20 ns (π) pump pulse. The delay between the first two probe pulses was 132 ns. The separation to the second π -probe pulse was 1.8 μ s. The repetition time of the experiment was 6 ms. The frequency of the pump pulse was fixed to the intensity maximum of the nitroxide powder spectrum to obtain maximum pumping efficiency. The probe frequency was chosen to be 40/55/70/85 MHz (DNA) and 40/50/60/75/90 MHz (RNA) above this frequency. All experiments were performed at 50K using a continuous flow of liquid helium and the temperature maintained using an Oxford Instruments ITC 503 temperature control unit.

G-band measurements

All G-band EPR experiments were performed with an in house built G-band spectrometer equipped with two independent frequency sources.⁵³ The probe pulse lengths were between 32–40 ns for the $\frac{\pi}{2}$ -pulse, 60–70 ns for the π -pulse. The pump inversion pulse was 30–38 ns. The pulse separation between the first probe pulses was 220 ns and 1.8 μ s to the next probe π -pulse. The repetition time of the experiment was 6 ms. All experiments were carried out at a temperature of 40 K. Every set of experiments consisted of around 40–120 time traces averaged with 100 shots per point and were recorded at different field positions across the EPR spectrum, corresponding roughly to the $B \parallel g_{xx}$, $B \parallel g_{yy}$, $B \parallel g_{zz}$ and two additional position in between. The probe frequency was set in all cases at a constant offset of 60 MHz above (DNA)/below (RNA) the pump frequency.

Acknowledgement

We acknowledge financial support from the German Research Foundation (CRC902: Molecular Principles of RNA Based Regulation). L.S.S., M.H., and G.H. were also supported by the Max Planck Society. Dr. Jürgen Köfinger is thanked for insightful discussions. We thank Dr. Vasyl Denysenkov for his help by the G-band measurements.

Supporting Information Available

Computational details for minimization and equilibration, G-spin and abasic sites atom types and partial charges, PELDOR time traces

References

- (1) Stelzl, L. S.; Erlenbach, N.; Heinz, M.; Prisner, T. F.; Hummer, G. J. *Am. Chem. Soc.* **2017**, *139*, 11674–11677.
- (2) Milov, A. D.; Ponomarev, A. B.; Tsvetkov, Y. D. *Lett. Chem. Phys.* **1984**, *110*, 67–72.
- (3) Peselis, A.; Gao, A.; Serganov, A. *Methods Mol. Biol.* **2016**, *1320*, 21–36.
- (4) Nozinovic, S.; Fürtig, B.; Jonker, H. R. A.; Richter, C.; Schwalbe, H. *Nucleic Acids Res.* **2010**, *38*, 683–694.
- (5) Fürtig, B.; Richter, C.; Wöhnert, J.; Schwalbe, H. *ChemBioChem* **2003**, *4*, 936–62.
- (6) Hennig, J.; Sattler, M. *Protein Sci.* **2014**, *23*, 669–682.
- (7) Bai, X.-c.; Martin, T. G.; Scheres, S. H. W.; Dietz, H. *Proc. Natl. Acad. Sci. U. S. A.* **2012**, *109*, 20012–20017.
- (8) Topf, M.; Lasker, K.; Webb, B.; Wolfson, H.; Chiu, W.; Sali, A. *Structure* **2008**, *16*, 295–307.
- (9) Reichel, K.; Stelzl, L. S.; Köfinger, J.; Hummer, G. J. *Phys. Chem. Lett.* **2018**, *9*, 5748–5752.
- (10) Barhate, N.; Cekan, P.; Massey, A.; Sigurdsson, S. *Angew. Chem.* **2007**, *119*, 2709–2712.
- (11) Sicoli, G.; Wachowius, F.; Bennati, M.; Höbartner, C. *Angew. Chem. Int. Ed.* **2010**, *49*, 6443–6447.
- (12) Shevelev, G. Y.; Krumkacheva, O. A.; Lomzov, A. A.; Kuzhelev, A. A.; Trukhin, D. V.; Rogozhnikova, O. Y.; Tormyshev, V. M.; Pyshnyi, D. V.; Fedin, M. V.; Bagryan-skaya, E. G. *J. Phys. Chem. B* **2015**, *119*.
- (13) Haugland, M. M.; Anderson, E. A.; Lovett, J. E. *Electron Paramagn. Reson.* **2017**, *25*, 1–34.

- (14) Kerzhner, M.; Abdullin, D.; Więcek, J.; Matsuoka, H.; Hagelueken, G.; Schiemann, O.; Famulok, M. *Chem. - A Eur. J.* **2016**, *22*, 12113–12121.
- (15) Gophane, D. B.; Endeward, B.; Prisner, T. F.; Sigurdsson, S. T. *Org. Biomol. Chem.* **2018**, *16*, 816–824.
- (16) Hong, S.; Piette, L. H. *Cancer Res.* **1976**, *36*, 1159–71.
- (17) Belmont, P.; Chapelle, C.; Demeunynck, M.; Michon, J.; Michon, P.; Lhomme, J. *Bioorg. Med. Chem. Lett.* **1998**, *8*, 669–674.
- (18) Shelke, S. A.; Sigurdsson, S. T. *European J. Org. Chem.* **2012**, 2291–2301.
- (19) Kamble, N. R.; Gränz, M.; Prisner, T. F.; Sigurdsson, S. T. *Chem. Commun.* **2016**, *52*, 14442–14445.
- (20) Dans, P. D.; Ivani, I.; Hospital, A.; Portella, G.; González, C.; Orozco, M. *Nucleic Acids Res.* **2017**, *45*, 4217–4230.
- (21) Seyfried, P.; Heinz, M.; Pintér, G.; Klötzner, D.-P.; Becker, Y.; Bolte, M.; Jonker, H. R. A.; Stelzl, L. S.; Hummer, G.; Schwalbe, H.; Heckel, A. *Chem. Eur. J.* **2018**, *24*, 17568–17576.
- (22) Grotz, K. K.; Nueesch, M. F.; Holmstrom, E. D.; Heinz, M.; Stelzl, L. S.; Schuler, B.; Hummer, G. *J. Phys. Chem. B* **2018**, *122*, 11626–11639, PMID: 30285443.
- (23) Mlýnský, V.; Banáš, P.; Hollas, D.; Réblová, K.; Walter, N. G.; Šponer, J.; Otyepka, M. *J. Phys. Chem. B* **2010**, *114*, 6642–6652.
- (24) Beššeová, I.; Banáš, P.; Kührová, P.; Košinová, P.; Otyepka, M.; Šponer, J. *J. Phys. Chem. B* **2012**, *116*, 9899–9916, PMID: 22809319.
- (25) Liebl, K.; Drsata, T.; Lankas, F.; Lipfert, J.; Zacharias, M. *Nucleic Acids Res.* **2015**, *43*, 10143–10156.

- (26) Šponer, J.; Bussi, G.; Krepl, M.; Banáš, P.; Bottaro, S.; Cunha, R. A.; Gil-Ley, A.; Pinamonti, G.; Poblete, S.; Jurečka, P.; Walter, N. G.; Otyepka, M. *Chem. Rev.* **2018**, *118*, 4177–4338.
- (27) Halbmaier, K.; Seikowski, J.; Tkach, I.; Höbartner, C.; Sezer, D.; Bennati, M. *Chem. Sci.* **2016**, *7*, 3172–3180.
- (28) Marko, A.; Margraf, D.; Cekan, P.; Sigurdsson, S. T.; Schiemann, O.; Prisner, T. F. *Phys. Rev. E* **2010**, *81*, 021911.
- (29) Prisner, T. F.; Marko, A.; Sigurdsson, S. T. *J. Magn. Reson.* **2015**, *252*, 187–198.
- (30) Frisch, M. J. et al. Gaussian 09 Revision D.01. Gaussian Inc. Wallingford CT **2009**.
- (31) Adamo, C.; Barone, V. *J. Chem. Phys.* **1999**, *110*, 6158–6170.
- (32) Barone, V.; Cimino, P. *J. Chem. Theory Comput.* **2009**, *5*, 192–199.
- (33) Grimme, S.; Ehrlich, S.; Goerigk, L. *J. Comput. Chem.* **2011**, *32*, 1456–1465.
- (34) Dunning, T. H. *J. Chem. Phys.* **1989**, *90*, 1007–1023.
- (35) Becke, A. D. *J. Chem. Phys.* **1993**, *98*, 5648–5652.
- (36) Case, D. et al. AMBER 16. 2016; University of California, San Francisco.
- (37) Macke, T.; Case, D. Modeling unusual nucleic acid structures. In *Molecular Modeling of Nucleic Acids*, N. B. Leontes and J. SantaLucia, Jr., eds. (Washington, DC: American Chemical Society, 1998), 379–393.
- (38) Bayly, C. I.; Cieplak, P.; Cornell, W.; Kollman, P. A. *J. Phys. Chem.* **1993**, *97*, 10269–10280.
- (39) Dupradeau, F.-Y.; Pigache, A.; Zaffran, T.; Savineau, C.; Lelong, R.; Grivel, N.; Lelong, D.; Rosanski, W.; Cieplak, P. *Phys. Chem. Chem. Phys.* **2010**, *12*, 7821–7839.
- (40) Ivani, I. et al. *Nat. Methods* **2016**, *13*, 55–58.

- (41) Pérez, A.; Marchán, I.; Svozil, D.; Sponer, J.; Cheatham, T. E.; Laughton, C. A.; Orozco, M. *Biophys. J.* **2007**, *92*, 3817 – 3829.
- (42) Banáš, P.; Hollas, D.; Zgarbová, M.; Jurečka, P.; Orozco, M.; Cheatham, T. E.; Šponer, J.; Otyepka, M. *J. Chem. Theory Comput.* **2010**, *6*, 3836–3849.
- (43) Zgarbová, M.; Otyepka, M.; Šponer, J.; Mládek, A.; Banáš, P.; Cheatham, T. E.; Jurečka, P. *J. Chem. Theory Comput.* **2011**, *7*, 2886–2902.
- (44) Wang, J.; Wolf, R. M.; Caldwell, J. W.; Kollman, P. A.; Case, D. A. *J. Comput. Chem.* **2004**, *25*, 1157–1174.
- (45) Vögele, M.; Köfinger, J.; Hummer, G. *Faraday Discuss.* **2018**, *209*, 341–358.
- (46) Case, D. et al. AMBER 14. 2014; University of California, San Francisco.
- (47) Jorgensen, W. L.; Chandrasekhar, J.; Madura, J. D.; Impey, R. W.; Klein, M. L. *J. Chem. Phys.* **1983**, *79*, 926–935.
- (48) Joung, I. S.; Cheatham, T. E. *J. Phys. Chem. B* **2008**, *112*, 9020–9041.
- (49) Sindhikara, D. J.; Kim, S.; Voter, A. F.; Roitberg, A. E. *J. Chem. Theory Comput.* **2009**, *5*, 1624–1631.
- (50) Ryckaert, J.-P.; Ciccotti, G.; Berendsen, H. J. *J. Comput. Phys.* **1977**, *23*, 327 – 341.
- (51) Berendsen, H. J. C.; Postma, J. P. M.; van Gunsteren, W. F.; DiNola, A.; Haak, J. R. *J. Chem. Phys.* **1984**, *81*, 3684–3690.
- (52) Abraham, M. J.; Murtola, T.; Schulz, R.; Páll, S.; Smith, J. C.; Hess, B.; Lindahl, E. *SoftwareX* **2015**, *1-2*, 19 – 25.
- (53) Denysenkov, V. P.; Prisner, T. F.; Stubbe, J.; Bennati, M. *Appl. Magn. Reson.* **2005**, *29*, 375–384.

Supporting Information:

Orientation Selective EPR Measurements of RNA and DNA with Non-Covalent G Spin Label

Marcel Heinz,^{†,||} Nicole Erlenbach,^{‡,||} Lukas S. Stelzl,[†] Grace Thierolf,[‡] Snorri Th.
Sigurdsson,[¶] Thomas F. Prisner,^{*,‡} and Gerhard Hummer^{*,†,§}

*†Department of Theoretical Biophysics, Max-Planck-Institute of Biophysics,
Max-von-Laue-Straße 3, 60438 Frankfurt am Main, Germany*

*‡Institute of Physical and Theoretical Chemistry and Center of Biomolecular Magnetic Resonance,
Goethe University Frankfurt, Max-von-Laue-Straße 7, 60438 Frankfurt am Main, Germany*

*¶Department of Chemistry, Science Institute, University of Iceland,
Dunhaga 3, 107 Reykjavík, Iceland*

*§Institute for Biophysics, Goethe University Frankfurt, Max-von-Laue-Straße 1, 60438 Frankfurt
am Main, Germany*

||Contributed equally to this work

E-mail: prisner@chemie.uni-frankfurt.de; gerhard.hummer@biophys.mpg.de

Supporting Information

MD simulations

Energy minimizations were carried out in the sander program as implemented in Amber16. Firstly, the solvent and ions were relaxed by 500 steps of steepest descent minimization and by 500 steps of conjugate gradient minimization. The nucleic acid atom positions and the \dot{G} atom positions were restrained with a force constant of $500 \text{ kcal}\cdot\text{mol}^{-1}\cdot\text{\AA}^{-1}$ during this step. Non-bonded interactions were treated with a cut-off of 12 \AA . Relaxations were performed with constant box volume. Secondly, the restraints were exclusively kept at the nucleic acid atoms, while relaxing the rest of the system. Thirdly, the whole system was free to relax with 1000 steps of steepest descent minimization and 1500 steps of conjugate gradient minimization.

The system was equilibrated in 50,000 steps with a time step of 2 fs ($\cong 100 \text{ ps}$). Weak atom position restraints ($10 \text{ kcal}\cdot\text{mol}^{-1}\cdot\text{\AA}^{-1}$) were applied at the atoms of the nucleic acid atoms. The solvent, ions and \dot{G} molecules were free to equilibrate. Random velocities were drawn from a Maxwell-Boltzmann distribution. Long-range electrostatic interactions were treated with the particle-mesh Ewald summation and a cut-off of 12 \AA was applied for non-bonded real-space interactions. Hydrogen containing bonds were constrained with the SHAKE algorithm. Langevin dynamics with a collision frequency of 1.0 ps^{-1} slowly heated the system up from 0 K to 300 K . In a second equilibration step, we switched from the sander to the pmemd.cuda engine in Amber16. The complete system was relaxed in 500 ps with a constant temperature of 300 K using Langevin dynamics ($\gamma = 1.0 \text{ ps}^{-1}$). Isotropic position scaling with a relaxation time of 2 ps ensured an average pressure of 1 atm . A random seed was set at the restart. Non-bonded interactions were truncated after 12 \AA and hydrogen atoms were constraint with SHAKE.

Table 1: Atoms, atom types and partial charges (δ) of the native and abasic site in RNA after the RESP fit. The table only contains the atoms of the abasic site, so not all native atoms are shown (i.e. purine atoms are missing). Native partial charges are taken from the parmbsc0+ χ_{OL3} force field for comparison.

atom	abasic atom type	native residue δ [a.u.]	abasic residue δ [a.u.]
P	P	1.166 200	1.150 865
OP1	O2	-0.776 000	-0.790 585
OP2	O2	-0.776 000	-0.790 585
O5'	OS	-0.498 900	-0.404 835
C5'	CI	0.055 800	0.013 465
H5'	H1	0.067 900	0.060 165
H5''	H1	0.067 900	0.060 165
C4'	CT	0.106 500	0.128 465
H4'	H1	0.117 400	0.074 065
O4'	OS	-0.354 800	-0.465 635
C1'	CT	0.019 100	0.064 865
H1'	H1	0.200 600	0.038 965
H1''	H1	/	0.038 965
C3'	CT	0.202 200	0.067 265
H3'	H1	0.061 500	0.110 765
C2'	CT	0.067 000	0.307 565
H2'	H1	0.097 200	0.050 765
O2'	OH	-0.613 900	-0.748 535
HO2'	HO	0.418 600	0.459 365
O3'	OS	-0.524 600	-0.425 535
		$\sum \delta = -0.8963$	$\sum \delta = -1.0000$

Table 2: Atoms, atom types and partial charges (δ) of the native and abasic site in DNA after the RESP fit. The table only contains the atoms of the abasic site, so not all native atoms are shown (i.e. purine atoms are missing). Native partial charges are taken from the parmbsc1 force field for comparison.

atom	abasic atom type	native residue δ [a.u.]	abasic residue δ [a.u.]
P	P	1.165 900	1.084 847
OP1	O2	-0.776 100	-0.782 353
OP2	O2	-0.776 100	-0.782 353
O5'	OS	-0.495 400	-0.308 753
C5'	CI	-0.006 900	-0.118 353
H5'	H1	0.075 400	0.090 846
H5''	H1	0.075 400	0.090 846
C4'	CT	0.162 900	0.154 747
H4'	H1	0.117 600	0.060 947
O4'	OS	-0.369 100	-0.447 753
C1'	CT	0.035 800	0.010 547
H1'	H2	0.174 600	0.056 246
H1''	H2	/	0.056 246
C3'	CE	0.071 300	0.119 547
H3'	H1	0.098 500	0.096 447
C2'	CT	-0.085 400	-0.013 253
H2'	HC	0.071 800	0.031 847
H2''	HC	0.071 800	0.031 847
O3'	OS	-0.523 200	-0.432 153
		$\Sigma \delta = -0.9112$	$\Sigma \delta = -1.0000$

Table 3: Atoms, GAFF atom types, partial charges (δ), x-,y- and z-coordinates of the G-spin atoms.

atom	atom type	δ [a.u.]	coordinates		
			x	y	z
N1	na	-0.348 400	-3.661 000	2.136 000	0.774 000
H1	hn	0.338 900	-2.946 000	2.773 000	1.041 000
C1	cc	0.250 800	-4.729 000	0.373 000	0.120 000
N2	nc	-0.564 100	-5.683 000	1.326 000	0.398 000
C2	cd	0.183 900	-5.019 000	2.348 000	0.781 000
H2	h5	0.144 900	-5.435 000	3.287 000	1.083 000
C3	cd	0.164 400	-3.474 000	0.865 000	0.350 000
N3	nd	-0.474 800	-2.275 000	0.251 000	0.203 000
C4	cc	0.548 400	-2.380 000	-0.963 000	0.212 000
N4	n	-0.497 200	-3.575 000	-1.562 000	0.479 000
H3	hn	0.336 200	-3.599 000	-2.494 000	0.835 000
C5	c	0.484 200	-4.859 000	-0.978 000	0.350 000
O1	o	-0.535 200	-5.821 000	-1.625 000	0.628 000
N5	nh	-0.480 200	-1.290 000	-1.747 000	0.427 000
H4	hn	0.328 300	-1.466 000	-2.717 000	0.562 000
C6	ca	0.137 000	0.061 000	-1.417 000	0.157 000
C7	ca	-0.275 900	0.610 000	-0.204 000	0.546 000
H5	ha	0.202 500	-0.006 000	0.532 000	1.022 000
C8	ca	0.011 000	1.949 000	0.031 000	0.294 000
C9	ca	0.038 500	2.746 000	-0.925 000	0.313 000
C10	ca	-0.339 600	2.201 000	-2.140 000	0.685 000
H6	ha	0.203 900	2.801 000	-2.897 000	1.158 000
C11	ca	-0.084 200	0.857 000	-2.378 000	0.457 000
H7	ha	0.127 600	0.421 000	-3.313 000	0.762 000
C12	c3	0.196 200	2.734 000	1.283 000	0.626 000
C13	c3	-0.272 100	2.233 000	2.518 000	0.130 000
H8	hc	0.082 400	2.169 000	2.320 000	1.194 000
H9	hc	0.082 400	1.249 000	2.807 000	0.224 000
H10	hc	0.082 400	2.914 000	3.346 000	0.027 000
C14	c3	-0.263 800	2.809 000	1.563 000	0.130 000
H11	hc	0.080 900	3.150 000	0.687 000	0.670 000
H12	hc	0.080 900	3.500 000	2.375 000	0.319 000
H13	hc	0.080 900	1.833 000	1.843 000	0.514 000
N6	n3	0.163 000	4.060 000	0.892 000	0.123 000
O2	o	-0.398 500	5.043 000	1.662 000	0.197 000
C15	c3	0.257 600	4.173 000	-0.448 000	0.475 000
C16	c3	-0.237 200	4.603 000	-0.329 000	0.194 000
H14	hc	0.068 200	4.677 000	-1.311 000	0.397 000
H15	hc	0.068 200	3.887 000	0.256 000	0.507 000
H16	hc	0.068 200	5.570 000	0.154 000	0.004 000
C17	c3	-0.258 400	5.181 000	-1.288 000	0.316 000
H17	hc	0.072 600	6.157 000	-0.819 000	0.285 000
H18	hc	0.072 600	4.876 000	-1.384 000	0.135 000
H19	hc	0.072 600	5.264 000	-2.283 000	0.110 000

PELDOR experiments

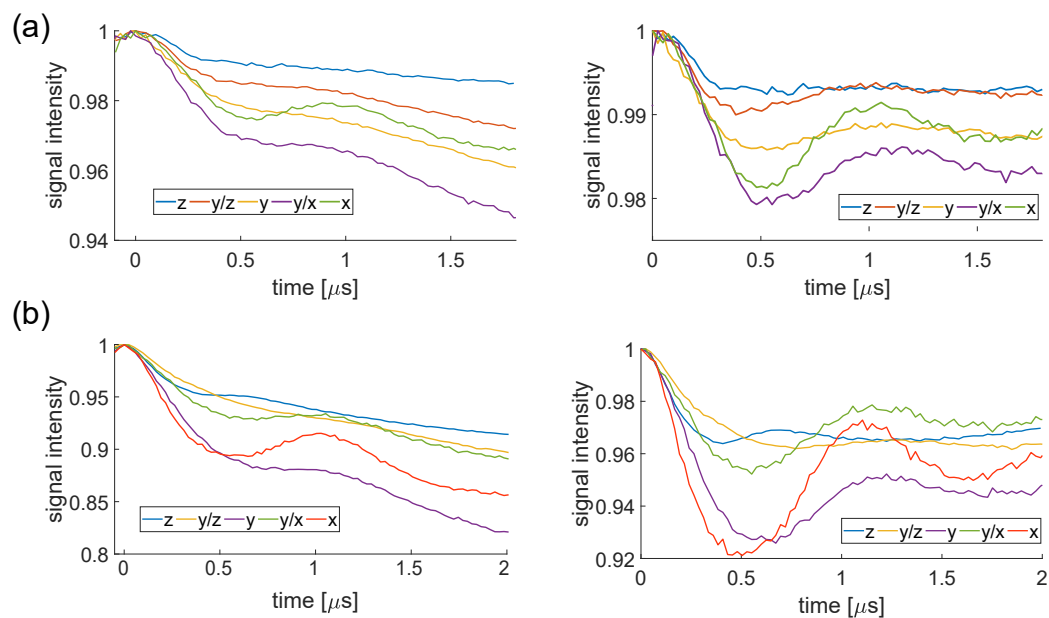


Figure 1: G-band PELDOR time traces before (left) and after (right) background correction at the magnetic field positions corresponding to the main G-tensor components for (a) DNA (b) RNA

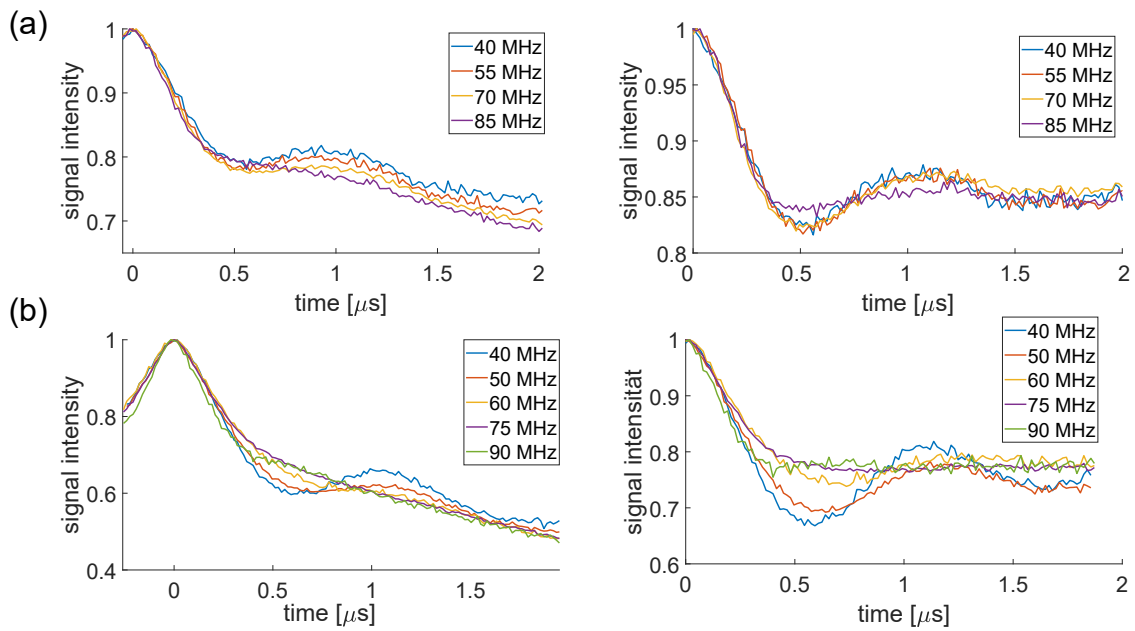


Figure 2: X-band PELDOR time traces before (left) and after (right) background correction for (a) DNA and (b) RNA. Offset is indicated

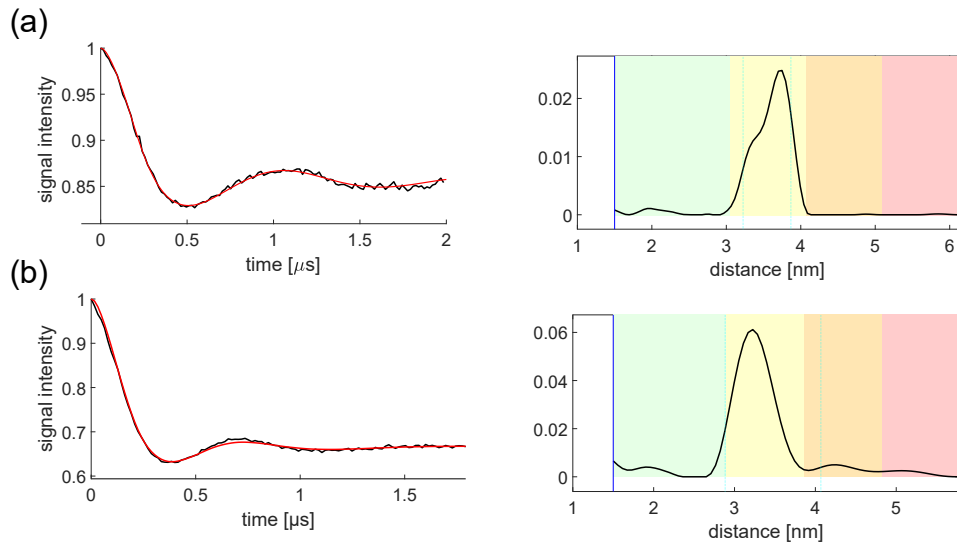


Figure 3: (left) Summed PELDOR time traces (black) with the Tikhinov fit (red) (right) the correspondet distance distribution. Distances were derived with DeerAnalysis.¹

References

- (1) Jeschke, G.; Chechik, V.; Ionita, P.; Godt, A.; Zimmermann, H.; Banham, J.; Timmel, C. R.; Hilger, D.; Jung, H. *Appl. Magn. Reson.* **2006**, *30*.